Ultracold Molecules from Ultracold Atoms: Interactions in Sodium and Lithium Gas

by

Caleb A Christensen

B.S. Physics, Iowa State University (2005)

Submitted to the Department of Physics
in Partial Fulfillment of the Requirements for the Degree of

Doctor of Philosophy

at the

Massachusetts Institute of Technology

June 2011

Signature of Author .....
Department of Physics
May 20, 2011

Certified by .....
Wolfgang Ketterle
John D. MacArthur Professor of Physics
Thesis Supervisor

Certified by .....
David E. Pritchard
Cecil and Ida Green Professor of Physics
Thesis Supervisor

Accepted by .....
Krishna Rajagopal
Professor of Physics, Associate Department Head for Education

Ultracold Molecules from Ultracold Atoms: Interactions in Sodium and Lithium Gas

by

Caleb A Christensen

Submitted to the Department of Physics
on May 20, 2011, in partial fulfillment of the
requirements for the degree of
Doctor of Philosophy

Abstract

The thesis presents results from experiments in which ultracold Sodium-6 and Lithium-23 atomic gases were studied near a Feshbach resonance at high magnetic fields. The enhanced interactions between atoms in the presence of a molecular state enhance collisions, leading to inelastic decay and loss, many-body dynamics, novel quantum phases, and molecule formation. Experimental data is presented alongside relevant theory and numerical models. Results are presented for both homonuclear Na_2 and Li_2 molecules, as well as heteronuclear NaLi resonances, although we were unable to isolate and measure NaLi molecules. Furthermore, experiments and theories related to strongly-correlated quantum phases such as Stoner model ferromagnetism, Bose mediated Fermi interactions, and Bose-Fermi mixtures are presented as applicable to Na and Li gases. Conclusions are presented regarding the feasibility of producing deeply bound, dipolar NaLi molecules, as well as future prospects for strongly interacting atomic gases of Na and Li.

Thesis Supervisor: Wolfgang Ketterle
Title: John D. MacArthur Professor of Physics

Thesis Supervisor: David E. Pritchard
Title: Cecil and Ida Green Professor of Physics

3

to Abby

Acknowledgments

Science cannot occur in a vacuum. Of course I mean a metaphorical social vacuum devoid of support or human contact; every experiment I've done in the last 6 years took place in a literal vacuum.

Ultracold atomic experiments such as ours require development by generations of graduate students, support and guidance from experienced supervisors, and continuous, extensive maintenance from several talented scientists. All those scientists also require support from caring, responsible friends, family, and university staff or they would quickly be found unresponsive in a dark corner of a laboratory.

In the following pages, I will attempt to give credit where credit is due, but I cannot express the extent of support I have received from the people around me during my training as a scientist and my time at MIT.

I'd first like to thank my parents Bill and Laurie, and my sisters Mariah and Tess, for convincing me as a young child that not only could I accomplish the things that I love, but that I was surprisingly good at them.

I thank every science and math teacher I've ever had for getting me started on a rewarding career, particularly Bob Steinke, Jan Quinlivan and Dan Gilpin, who went above and beyond in seeking out new challenges for me outside the classroom.

I thank my professors at Iowa State University, especially Kai-Ming Ho, Gary Tuttle, and Jim Cochran, who not only taught me amazing physics but trusted me to build and operate their experiments.

I thank Dave Pritchard for taking a chance by personally contacting me to work in the 2nd floor hallway of building 26, and for always having an array of impossible questions ready when I thought that I understood a thing or two about physics, or the world in general.

I thank Wolfgang Ketterle, for teaching me everything I know about atomic physics, and most of what I know about doing science.

I thank the 2005 class of first year MIT physics grad students who helped me study for and survive the intimidating graduate physics courses and qualifying exams.

I thank Eleanor Barish and Joanna Keseberg for protecting me from the confusing world of university bureaucracy and for providing smiling, human faces in a hallway otherwise occupied by physicists.

I thank Tom Pasquini for teaching me everything I know about the making the Science Chamber work, from RF boxes to dye lasers to fiber coupling to vacuum components. Tom has been my best example for how to have a good work ethic in grad school without sacrificing my relationships with friends and family.

I thank Michele Saba for showing me how to encourage a team of scientists to not only work hard, but to work together.

I thank Yong-Il Shin for teaching me the black magic of squeezing good data out of a complicated and messy machine, as well as the precise science of understanding BEC dynamics in ultracold gases.

I thank Gyu-boong Jo for his continuous, diligent labor which produced most of the successful experiments in the Science Chamber during my time there, and for his relaxed confidence which is directly responsible for my own scientific attitudes in the lab.

I thank Sebastian Will for doing most of the development work on the project which has been my only first-authored paper at MIT, and also for the excellent times we've had in Cambridge and abroad at conferences.

I thank Ye-ryoung Lee for working beside me every step of my thesis, both in classes, studying for qualifiers and in the laboratory for the entire time I've been an active member of the Science Chamber. Her scientific talents and her warm personality have been an unwavering source of support in all of my efforts.

I thank Jae Choi for his open, assertive personality and determined efforts in the lab. He was a dominant force in my personal and professional life, and he was there for most of the experiments reported in this thesis.

I thank Tony Kim for being a very close friend. I also thank him for his astonishing technical skills and his remarkable ability to seemingly effortlessly accomplish the most challenging tasks he could find, in the lab and outside it.

I thank Tout Wang for his eagerness to try any new idea, no matter how intimidating (or even foolish) it might seem, and for his bright optimism in science and in life. I particularly thank Tout for doing the hard work producing a number of figures and results in this thesis.

I thank Gregory Lau for his curiosity and ambition as an undergrad working in our lab. He has also provided some of the most important data and figures presented in this thesis.

I thank Myoung-Sun Heo for his fast friendship, his charming personality and his genuine interest in not only the things I've done in the lab but also many aspects of my life outside the lab.

I thank Timur Rvachov, the newest member of the Science Chamber, for bringing some new excitement to the lab and for keeping my mind and hands in practice during the final months of my lab work by asking me questions about all the things I had taken for granted as a tired old grad student.

I thank Martin Zwierlein for his example of how to succeed wildly as a grad student and as a professor by knowing the answer to absolutely every question I could ever ask him and by tirelessly conquering every practical and theoretical challenge he encountered as an atomic physicist.

I thank everybody on the 2nd floor of building 26. I couldn't begin to list all the people who have enriched my experience and enabled the success I have had at MIT.

I'd like to thank Anton Zavriyev at MagiQ Technologies for having enough confidence in me to offer me a great job, and for giving me valuable advice and encouragement as I make the shocking transition from a grad student into a career scientist.

And finally, I thank Abby Christensen, my wife. She trusted me enough to follow me across the country after dating me for only a year, she kept me fed, sheltered and clothed during a time when I may have ended up sleeping on couches in building 26, she

is the main reason I still have a social life after 6 years of grad school, and she has patiently remained supportive of me through all of our struggles together. I couldn't have held myself together without her holding my hand.

Table of Contents

Acknowledgements 4

1 Introduction 14

1.1 A Physicist's Motivation to study simple molecules 14

1.2 A Scientist's motivation to produce ultracold molecules 16

1.3 Recent history of the field 17

1.3.1 Molecular spectroscopy 17

1.3.2 Ultracold atoms 20

1.4 Molecule formation in gases of Na and Li 21

2 Basic Molecular Physics 23

2.1 Interatomic interactions 23

2.2 The Born-Oppenheimer approximation 25

2.2.1 Energies and Schrodinger's equations 25

2.2.2 Numerical solutions and model potentials 29

2.2.3 Long-range interatomic forces 32

2.3 Quantum states of molecules 34

2.3.1 Nuclear rotation and vibration 34

2.3.2 Spectroscopy notation for molecular states 36

2.4 Important considerations for experiments 37

2.4.1 Molecular transitions 37

2.4.2 Molecules in an electric field 40

3 Molecule Formation: Collisions and Feshbach Resonances 44

3.1 Atomic collisions and molecule formation 44

3.1.1 Inelastic collisions 45

3.1.2 Useful Inelastic collisions with ultracold atoms 47

3.2 Collisions and losses in dilute ultracold gases 48
3.2.1 3-body atomic losses 49
3.2.2 2-body molecular losses 50
3.2.3 Scattering coefficients 52
3.3 Feshbach resonances 56
3.3.1 Coupling between atomic and molecular states 56
3.3.2 Experimental parameters of Feshbach resonances 61
3.3.3 Scaling of loss coefficients with scattering length 63
3.3.4 Comparison of energy scales 66
3.4 Adiabatic molecule formation 70
3.4.1 Effects of phase-space density on molecule formation 72
3.4.2 Landau-Zener formula for non-adiabatic formation 76
3.4.3 Combined formula for non-adiabatic, finite temperature sweeps 78
3.4.4 Application to NaLi experiments 80
4 Experimental Apparatus for Ultracold Molecules 82
4.1 Ultracold atomic physics in the science chamber 82
4.1.1 Slowing atomic beams 85
4.1.2 Dual magneto-optical Traps 88
4.1.3 Quantum states of Na and Li 90
4.1.4 State preparation and evaporation of Na and Li 93
4.1.5 Optical dipole traps 96
4.1.6 Density Distributions and Imaging 98
4.2 RF techniques for preparation and study of Feshbach resonances 101
4.2.1 High Power RF Amplifiers 103
4.3 Precision control of High Magnetic Fields 104
4.3.1 High current hardware 104
4.3.2 Precision control of current 108
4.4 Techniques to measure ultracold molecules 113
4.4.1 Adiabatic sweeps for molecule formation 114
4.4.2 RF association of molecules 117
5 Feshbach Resonances in Sodium and Lithium 123

5.1 Feshbach resonances in Na and Li gases 123
5.1.1 New heteronuclear resonances between Na and Li 123
5.1.2 Search for the wide singlet NaLi resonance 127
5.1.3 Homonuclear resonances in Na and Li 132
5.2 Measured loss rates in Na and Li mixtures 133
5.2.1 3-body atomic losses near NaLi Feshbach resonances 133
5.2.2 2-body molecular losses near a Feshbach resonance 134
6 Ultracold Molecule Formation Experiments 137
6.1 Requirements for long-lived molecules 137
6.1.1 Stern-Gerlach separation 137
6.1.2 Resonant processes for separation 139
6.1.3 Unwanted resonant processes affecting molecules 140
6.2 Experimental results for Na and Li gases 142
6.2.1 Results from Na2 and Li2 145
6.3 Further considerations for molecule experiments 147
6.3.1 Empirical optimization of molecules 147
6.3.2 Molecular transitions in weakly bound NaLi 149
7 Modeling Practical Molecule Formation 151
7.1 Model of real Feshbach Association procedures 151
7.1.1 Assumptions of model 151
7.1.2 Description of model 152
7.2 Application to Na2 experiments 155
7.3 Application to NaLi experiments 156
7.4 Conclusions regarding NaLi molecules 159
7.4.1 Comparison to RbK 160
7.5 General procedure for optimized molecule formation 165
8 Many-body physics near a Feshbach Resonance 167
8.1 Ferromagnetism vs. molecule formation in Li mixture 168
8.1.1 Itinerant Ferromagnetism in a Fermi Gas of Ultracold Atoms 168
8.1.2 Comparison of molecule formation and ferromagnetic ordering 175

8.1.3 Further study 177
8.2 Interesting Phases of Bose-Fermi mixtures 181
8.2.1 Bose-mediated Fermi-Fermi interactions 182
8.2.2 Quantum phases of Bose-Fermi mixtures 183
9 Conclusions 186
9.1 Choosing the right molecules for the right reasons 187
9.2 Possibilities for NaLi 190
9.3 Coda: the motivations of a scientist 192

Appendices
A. Diode laser system for Lithium-6 195
B. Phase Sensitive Recombination of Two Bose-Einstein Condensates on an Atom Chip 197
C. Matter-Wave Interferometry with Phase Fluctuating Bose-Einstein Condensates 202
D. Trapping of Ultracold Atoms in a Hollow-core Photonic Crystal Fiber 207
E. Itinerant ferromagnetism in a Fermi gas of ultracold atoms 212
Bibliography 218

Table of Figures

1 Molecular spectra on photographic film 19
2 Definition of molecular coordinates 26
3 Effective potentials of the NaLi molecule 30
4 Turning-point method for Franck-Condon Factors 39
5 Atomic energy levels in an electric field 42
6 Comparison of 2-body and 3-body loss processes 54
7 Square well model for Feshbach resonances 58
8 Measured molecular losses in RbK 66
9 Binding energy vs. B-field for NaLi and RbK 69
10 Adiabatic states across a Feshbach resonance 71
11 Feshbach resonance in a QHO 73
12 Maximum conversion efficiency vs. phase-space density 75
13 BEC3 apparatus (The Science Chamber) 84
14 Dual species oven for Na and Li 86
15 Hyperfine states of Na and Li in a magnetic field 91
16 Na and Li level structure with cooling and pumping transitions 94
17 Circuit diagram for precision high-field control 106
18 Blasting method of isolating molecules from atoms 115
19 RF association of molecules 118
20 RF spectrum of RbK molecules 120
Table 1: Observed Feshbach resonances in NaLi 125
21 Loss measurements near NaLi Feshbach resonances 127
22 Asymptotic bound state calculation of NaLi resonances 131
23 3-body loss curve near a NaLi resonance 133
24 Predicted transitions in weakly-bound NaLi molecules 141
25 Asymmetric sweep results for Na-Na, Li-Li, and NaLi resonances 144

Table 2: Parameters of resonances used for molecule formation 145
26 Image of Na2 molecules 146
27 Comparison of model with Na2 observations 156
28 Model of surviving NaLi molecules 157
29 Model of surviving Na and Li atoms 158
30 Possible states of repulsively interacting fermions 170
31 Atomic loss rate suggesting ferromagnetic ordering 173
32 Thermodynamic data suggesting ferromagnetic ordering 174
33 Possible configurations of Ferromagnetic states 179
34 Diode laser system for Li-6 196

1

Introduction

1.1 A physicist's motivation to study simple molecules

The world is made of molecules. Most biological, chemical, and physical processes depend on the properties of molecules. The periodic table of elements is an elegant chart which lays out the properties and patterns of atoms in an informative, intuitive shorthand; yet it is far from a blueprint of nature. Without knowledge of the way atoms work together, there is no way to explain such basic phenomenon as the freezing and melting of water, the release of energy during oxidation of carbon, or the strength of the triple bond in diatomic nitrogen. But these processes which involve no more than two elements have profound effects on nature.

To a chemist, molecules are the starting points and ending points of most processes. To a physicist, molecules are a special case of a difficult problem: What happens when particles interact? Neutrons interact with protons to form stable nuclei, nuclei interact with electrons to form stable atoms, and atoms interact with each other to form molecules. A physicist would claim to understand the basic forces behind the

interactions, and might even offer simple examples where problems of two or three particles can be explicitly solved to explain observable phenomena. However, ask a physicist to calculate the mass of an arbitrary nucleus, and they will invoke approximations such a mean-field theories, shell models, or semi-empirical mass formulas[1], none of which are accurate enough to account for all observed nuclei, let alone unstable nuclei that may not have been accurately measured.

Likewise, exact *a priori* calculations are impossible for the interactions of some of the electronically simplest atoms, sodium and lithium, in a very simple molecular configuration, a covalently bound diatomic molecule with large internuclear separation[2,3]. The understanding of this simple system is evolving even today as new data become available and new modifications to the theory account for them[4,5]. The last three years of my thesis work studying NaLi molecules have been full of open questions regarding the dynamics of this system, and many questions remain unanswered.

The availability of ultracold atoms in recent decades has led to unprecedented accuracy in timekeeping[6,7], the first indisputable evidence of atomic Bose-Einstein Condensates[8,9], and tests of long-held theories on the foundations of superconductivity and ferromagnetism[10-16]. The recent ability to form and measure simple ultracold molecules[4,17-32]could allow a completely new approach to study molecular physics by connecting the precision and elegance of ultracold atoms to the richness and mystery of tightly bound molecules.

However, forming and isolating long-lived ultracold molecules for use in spectroscopy and ultracold chemistry, despite being a major research goal of several talented atomic physics groups[26,30,33-39], has proven to be a difficult and uncertain task.

This thesis describes the efforts of our research group to perform this feat with Sodium-23 and Lithium-6, which also happen to be the atoms which have achieved the lowest temperatures, largest BECs, and largest degenerate Fermi gases[40-42]. The thesis also contains a primer in understanding basic molecular physics, a presentation of current theories on the few-body atomic processes involved in molecule formation and destruction, and a framework for understanding the practical challenges encountered in an experiment on ultracold molecule formation.

1.2 A scientist's motiviation to produce ultracold molecules

The most direct benefit of ultracold molecule studies is the ability to study molecules with the same precision as ultracold atoms. By reducing the temperatures, it is possible to improve the knowledge of interatomic potentials by orders of magnitude simply by allowing more accurate spectroscopy. With the elimination of Doppler broadening it is possible to directly measure binding energies, tunneling barriers to dissociation, and relaxation rates by putting the entire sample of molecules into one quantum state and observing as they transition to another[43-45].

Heteronuclear molecules with a large electric dipole moment are particularly interesting. With a dense, cold sample of polarized molecules, the long-range effects of the anisotropic electric dipole-dipole interaction could be observed directly in the shape of a molecular cloud, although this feat has not been achieved as of the writing of this thesis[35,46].

Careful study of ultracold polar molecules could even provide insight into super-symmetric string theories and CP (charge-parity symmetry) violation, two very exciting fields in high-energy physics which would seem to have nothing in common with the zero-energy science normally favored by atomic physicists. However, precision spectroscopy of cold molecules has provided the strongest constraints to date on the electron electric dipole moment (EDM)[36].

A final application of ultracold molecules could equip computer scientists and mathematicians with a feasible, scalable platform for quantum computation. The existence of an electric dipole and long-lived, low-energy transitions between rotational states in a molecule could provide reliable qubit registers. Interactions between qubits could enable universal quantum gates, and an electric field gradient combined with precision RF sources could enable single qubit addressability within a register[47-49]. Given a cold sample of molecules, such a system can be created with optical lattices, high-voltage capacitors, and RF synthesizers; all widely used laboratory technologies.

1.3 Recent history of the field

1.3.1 Molecular spectroscopy

Although one could say that chemistry dates back to the discovery of fire, and the idea that molecules are made up of atoms can be attributed to John Dalton[50] and proven by Jean Baptiste Perrin[51], the atomic and molecular spectroscopists of the early-20th century can be given credit for developing our understanding of molecular structure and

interactions[52-57]. By producing a sample of a given molecule and studying it's absorption or emission of light, the energies and relative strengths of possible transitions could be identified. These transitions would then be compared to theories of the structure and dynamics of simple molecules.

At first the spectra took the form of arrays of lines and dense bands on photographic film (see figure 1). By improving gratings and eventually using tunable lasers, the bands resolved into lines, which could be interpreted by analogy to discrete atomic spectra.

Improvements were made in the accuracy of these measurements each time the molecular sample was prepared with a more controlled state population, or in an environment with lower pressure and effective temperature[58].

Methods starting with chemically stable molecules in thermal equilibrium could only produce deeply bound molecules, and as such the spectroscopy provided information mostly on short range interactions due to electrons redistributing among atoms. Some molecules, particularly weakly-bound diatomic molecules, will not even form at room temperature. For example, NaLi in the triplet electronic state has a binding energy of 325 K[59], meaning it will quickly dissociate at room temperature.

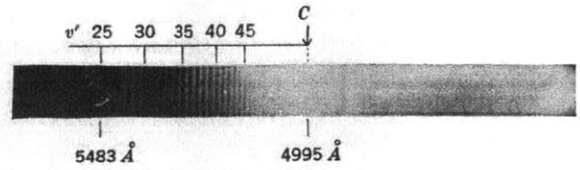

FIG. 15. **Absorption Spectrum of I_2 Vapor.** The arrow denoted by C indicates the position of the convergence limit of the bands, where a continuous absorption joins on.

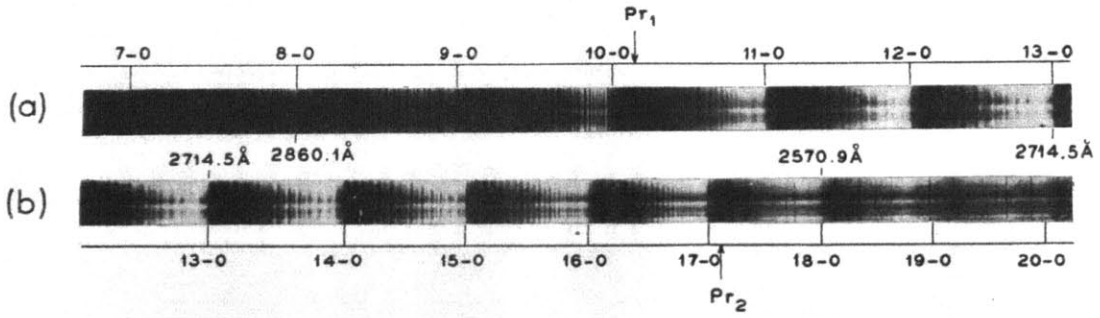

FIG. 16. **Absorption Spectrum of S_2 Vapor.** (a) and (b) give two adjacent parts of the same original spectrogram; they overlap slightly (13–0 band). The arrows denoted by *Pr* indicate the positions at which the bands become diffuse. The emission lines at the right in (b) are lines of H_2 (first order overlapping the second order spectrum).

figure 1: Examples of molecular spectra recorded on photographic film. This was the preferred method of recording and studying molecular spectra for decades. The top spectrum is from diatomic iodine, the bottom two spectra from diatomic sulfur. Images reproduced from Herzberg (1945).

Further information could be gleaned from atomic and molecular collisions, where careful measurements of collision rates could be interpreted to provide information on long-range interactions or weakly bound states[60-62]. Another development was photoassociation spectroscopy[63-66] where atoms are driven with a laser to produce excited state molecules which decay into ground state molecules. Such

methods can measure transitions among weakly-bound states, leading to information on the longer-range Van der Waals forces neutral atoms at long distances.

A recent advance in understanding molecules has been Feshbach resonances between atoms. These allow low energy transitions from free atoms into the most weakly-bound molecular states, providing a source of ultracold molecules in pure quantum states. This has already been used to refine the knowledge of the structure of diatomic molecules[67,68].

Chapter 2 will be an introduction to the theories that have been developed to understand the details of molecular dynamics.

1.3.2 Ultracold atoms

The systematic progress in molecular science can be contrasted with the leaps and bounds in ultracold atomic physics in the last few decades. Laser cooling and trapping in the 1980s[69-71], magnetic trapping and evaporation to BEC in the 1990s[8,9], and optical lattices and ultracold fermions in the 2000s[10,15,41,72,73] have lead to a revolution in atomic physics and experimental quantum physics in general.

The explosion in ultracold atomic physics of the last two decades has been a dizzying, confusing ride even for those physicists like myself who have been lucky enough participate. For the adventurous reader, or for any scientist wishing to join the ultracold community, I recommend a few particularly good textbooks and review papers[31,74-79].

Although direct cooling of broad classes of molecules is a rich field with some major recent advances[80-83], and there is currently an interesting proposal for laser cooling and trapping of SrF[39], these techniques have not yet been able to rival the low temperatures and quantum state control of ultracold atoms.

Feshbach association maintains ultracold atomic temperatures of 100 nK or less, even maintaining quantum degeneracy[25,29], and it is the method used by our research group as well as several others to maintain coherent control over all degrees of freedom. By using all coherent processes, the final molecules produced are guaranteed to maintain the pure quantum state and low entropy of the initial atoms, thus allowing the molecules to directly inherit the great precision of modern atomic physics. Feshbach resonances, along with a discussion of collisions related to molecule formation, will be presented in chapter 3.

1.4 Molecule formation in gases of Na and Li

My thesis work has been centered around attempts to form molecules from ultracold gases of Na-23 and Li-6. If formed and driven to deeply bound states, the result would be a gas of polar, fermionic molecules at temperatures of around 100 nK. In Chapter 4, I describe the experimental apparatus and techniques used in this pursuit.

Finding suitable Feshbach resonances for NaLi molecules is an ongoing challenge. A few resonances were observed in advance[4], others had been predicted[5], but we located and measured properties of several new resonances ourselves. The currently

known NaLi resonances, as well as Na_2 and Li_2 resonances, are presented in chapter 5.

In addition to forming molecules, Feshbach resonances allow control over collisions and many-body interactions in ultracold atomic gases. These have been the most scientifically fruitful characteristic of Feshbach resonances to the rest of atomic physics, and to condensed matter physics as well. A rich review of the previous advances in many-body, strongly correlated physics due to tunable Feshbach interactions can be found elsewhere[31], but a few interesting applications unique to mixtures of bosons and fermions like Na-23 and Li-6 will be addressed in Chapter 8.

In the course of my thesis, I have learned many things about the interactions of atoms and molecules, but the original goal, forming a long-lived gas of NaLi molecules, has eluded me. In the conclusion in Chapter 9, further possibilities are presented which could overcome some of the challenges currently encountered in NaLi. The conclusion also contains a discussion of the various techniques for studying Feshbach molecules, and suggestions from theory and lab experience for choosing the right molecules for the right reasons.

The quantum science of molecular physics requires the precise techniques of atomic physics informed by the proven, practical knowledge of chemistry. There has always been a desire to take the first principles from physics and combine them in the right ways to make predictions of the behavior of molecules, but in practice this is challenging and uncertain. However, with continued effort, the blind spot between physics and chemistry will shrink, and science will undoubtedly advance in the process.

2

Basic Molecular Physics

2.1 Interatomic interactions

Any stable bound structure in physics is made up of particles which are able to lower their total energy by coming close together. Regardless of the number of particles, the physical origins of the interactions involved, or the quantum states of the particles, this somewhat trivial statement will remain true.

One recurring theme in studying molecules is the separation of energy scales. When energy scales of different processes are widely different, most other properties are significantly different, from length scales to time scales to the tools used to manipulate and measure the processes. These differences are particularly useful because they also allow the Schrodinger equations for different degrees of freedom to be solved one at a time.

When considering molecules, the core electrons of each atom, which are part of a closed shell, can be solved while ignoring interatomic forces (to first order), because

they will remain localized near their nucleus and require very large energies to remove or dramatically perturb. The valence electrons, part of an incomplete shell, will adapt drastically different orbits, because their weaker binding energy can be overcome by the electrostatic interaction with an approaching nucleus at typical molecular length scales of several Bohr radii ($a_0 = 5 \times 10^{-11}$). As an example, consider a lithium atom. With two electrons filling the first shell (the 1S state), and one electron in the second shell (2S state), the outer electron can be ionized with 5.4 eV, a second electron (a core electron) can only be removed with an extra 75.6 eV[84].

In the ionic bonds in table salt (or more precisely, in gaseous NaCl), a chlorine atom strips the valence electron off a sodium atom, and the nuclei bind due to the electrostatic forces between the Na+ and Cl- ions, with only weak perturbation of the electron orbits in each ion. At the other extreme, homonuclear diatomic molecules such as H_2 have perfect symmetry between the two nuclei, so both electrons are equally likely to be near one nucleus as the other. The covalent binding energy comes from the fact that the electronic orbits around the two nuclei are lower in total energy than the independent electron orbits around a single nucleus[85]. Most diatomic molecules fall somewhere in between these cases, with strongly perturbed orbits that have some polar character caused by the more electronegative nucleus attracting the electron more strongly.

A unified, general theory of all possible atomic binding phenomena is not only beyond the scope of this thesis, it doesn't even exist! Such a theory would have to incorporate the exact 4 body problem of a the protons and electrons in H_2, the delicate balancing acts of organic chemical reactions and protein folding, and the highly

empirical sciences describing physical properties of alloys and inhomogeneous minerals. Even the relatively simple problem of *a priori* calculations of energy levels in Li2 is currently intractable; useful calculations involve approximations and the construction of effective potentials from empirical data[86].

However, there must be a place to start; a way to model simple molecules that starts with electrons and nuclei, combined with experiments that can compare the accuracy of different approximations and the importance of all the possible interactions between subatomic particles that make up molecules. The remainder of this chapter is dedicated to the theory of diatomic molecules, particularly bi-alkali molecules due to the ability to cool and precisely measure alkali atoms with lasers.

2.2 The Born-Oppenheimer approximation

2.2.1 Energies and Schrodinger's equations

The first step in reducing the complexity of the task is possible because of another separation in energy scales. The optical energies of electron dynamics (typically on the order of a few eV (100s of THz)), are much larger than the energies of nuclear motion (vibrational energy levels are spaced by 1 THz at most for tightly bound molecules).

In the Born-Oppenheimer Approximation, the electron wavefunctions and eigenvalues are found for a given nuclear configuration[58]. The approximation is approached by defining the basis of many-body wavefunctions to be

1 $$\Psi_{i,v}^{BO}=\Phi_i(r;R)\chi_v(R,\theta,\phi)$$

Φ and χ are the many-body electronic and nuclear wavefunctions, respectively, with indices i and v iterating over all combinations of relevant quantum numbers.

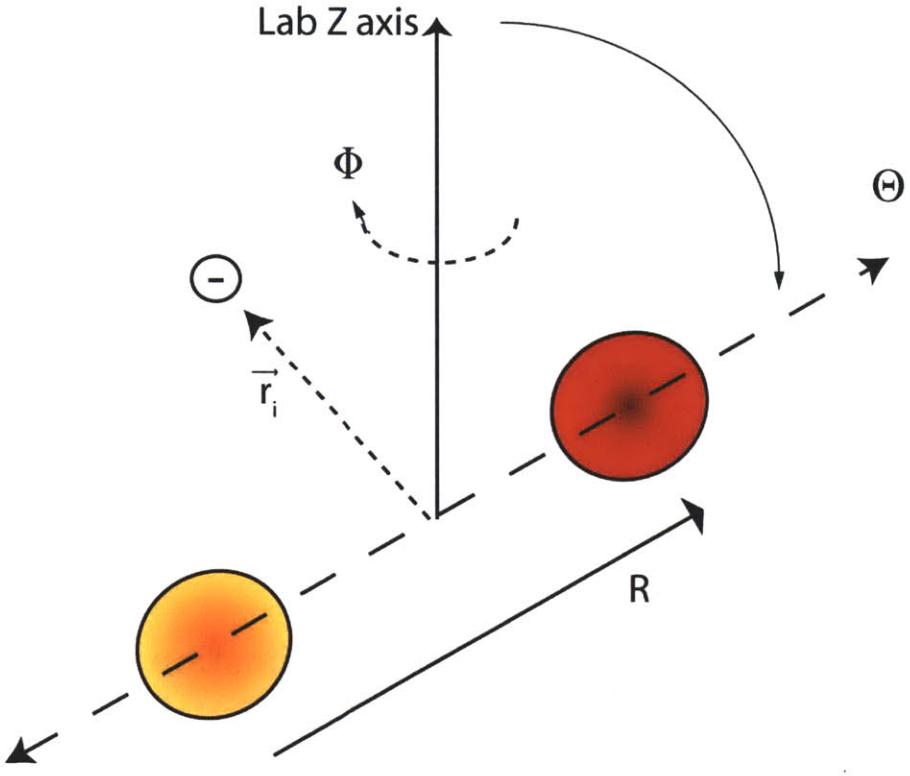

figure 2: definition of coordinates used in molecular wavefunctions

The coordinates in this wavefunction are illustrated in figure 2. In terms of these coordinates, the Hamiltonian can be written

2 $$\boldsymbol{H} = \boldsymbol{T}^N(R,\theta,\phi) + \boldsymbol{T}^e(r) + V(r,R)$$

Here $\mathbf{T}^N$ is the nuclear kinetic energy operator, $\mathbf{T}^e$ is the electronic kinetic energy operator, and V is the electrostatic potential energy. If a full many-body treatment is being used, V includes all electron-electron, electron-nucleus, and nucleus-nucleus terms. If only the valence electrons are explicitly solved, it includes the valence

electron-electron terms and screened electron-nucleus and nucleus-nucleus terms. The kinetic energy terms have the form:

$$3 \quad \boldsymbol{T}^{e}(r)=\frac{-\hbar^2}{2\mathrm{m}}\sum_i \nabla_i^2 ; \boldsymbol{T}^{N}(R,\theta,\phi)=\frac{-\hbar^2}{2\mu R^2}\left[\frac{\partial}{\partial R}\left(R^2\frac{\partial}{\partial R}\right)+\frac{1}{\sin\theta}\frac{\partial}{\partial\theta}\left(\sin\theta\frac{\partial}{\partial\theta}\right)+\frac{1}{\sin^2\theta}\frac{\partial^2}{\partial\phi^2}\right]$$

Note that $\mathbf{T}^{N}$ uses the reduced nuclear mass μ, and is written to show the possibility of separation of motion along R (vibrations) from motion along θ and φ (rotations)

The first approximation occurs by assuming $\mathbf{T}^{N}$ will be much smaller than $\mathbf{T}^{e}$, and neglecting it when considering the electronic motion. At this point we are ignoring terms such as spin-orbit coupling, spin-spin coupling, hyperfine interactions involving nuclear spin, etc. These terms may be included in the zero-order Hamiltonian, or they may be treated perturbatively or ignored all together, depending on the molecule and the desired precision. By assuming the nuclei are clamped at a fixed R for time-scales relevant to electronic motion, we write:

$$4 \quad [\boldsymbol{T}^{e}(r)+V(r,R)]\Phi_i(r;R)=E_i^{el}(R)\phi_i(r;R)$$

Which can be solved to obtain functions $E^{el}(R)$. We now write the full Schrodinger equation

$$5 \quad \boldsymbol{H}\Psi_{i,v}^{BO}=[\![\boldsymbol{T}^{N}(R,\theta,\phi)+\boldsymbol{T}^{e}(r)+V(r,R)]\!]\Phi_i(r;R)\chi_v(R,\theta,\phi)$$

and multiply by the hermitian conjugate of Φ

$$6 \quad E^{total}\langle\Phi_i|\Phi_i\rangle\chi_i\approx\langle\Phi_i|[\![\boldsymbol{T}^{e}(r)+V(r,R)]\!]|\Phi_i\rangle\chi_v(R,\theta,\phi)+\boldsymbol{T}^{N}(R,\theta,\phi)\langle\Phi_i|\Phi_i\rangle\chi_i$$

If electron wavefunctions are normalized, the inner products of Φ equal 1, and by using equation 4

$$7 \quad E^{total}\chi_v\approx E_i^{el}(R)\chi_v+\boldsymbol{T}^{N}(R,\theta,\phi)\chi_v$$

Which is now a Schrodinger equation for the nuclear motion, where $E^{el}(R)$ acts as an

effective potential experienced by the nuclei.

Quantum numbers specifying the particular electronic state include Λ, the projection of the electronic orbital angular momentum on $\hat{R}$, S, the total electron spin angular momentum, and Σ, the projection of S on $\hat{R}$. These are good quantum numbers as long as the Born-Oppenheimer approximation is valid, they rely only on the symmetry of the potential experienced by the electrons due to stationary nuclei separated by R. There will be multiple solutions to equation 4 of increasing energy for any combination of these quantum numbers, just as in atoms, and the electron wavefunction subscript i distinguishes between all such distinct wavefunctions.

When two electronic wavefunctions with different quantum numbers are nearly degenerate at a given value of R, the BO approximation breaks down because the energy of nuclear motion can be as large as the energy difference between the two electronic states. However, the BO wavefunctions form a complete orthogonal basis, so any exact solution can be expressed as a linear combination of BO states. This is convenient, as "presently, Ψ^{BO} is the only available type of complete, rigorously definable basis set" for molecular wavefunctions[58]. In most circumstances, no more than two BO wavefunctions will be needed, but for highly excited electronic states, many states can simultaneously cross, making such states very difficult to analyze.

Eqs. 4 and 7 demonstrate the usefulness of the Born-Oppenheimer approximation. The electron motion can be solved with R as a fixed parameter, producing $E^{el}(R)$. At that point, the nuclear motion can be solved using $E^{el}(R)$ as an effective potential. This separates the many-body 3-d problem of nuclear and electronic motion into a 1-D 1-body problem for reduced nuclear motion, and the electronic

problem. The electronic problem is still 3-D and many-body, but can be solved using methods similar to those developed to study atoms[57,58,85,87-89].

2.2.2 Numerical solutions and model potentials

At this point we will diverge from a traditional treatment of molecular dynamics. A traditional treatment would consider the relative importance of neglected terms in the Hamiltonians, which angular momenta are conserved and which are not under different circumstances (also known as Hund's cases), and ways to solve or approximate En(R). Initially, spectroscopic features are identified and given phenomenological parameters (also known as Dunham coefficients[52,53]), an appropriate basis is considered for solving the electronic equations, and the parameters (such as the exact form of the electrostatic potential or angular momenta coupling terms) are refined until adequate agreement is obtained between theoretical energy levels and experimental spectra of molecular transitions. As this chapter is intended to be a primer to molecules for ultracold atomic physics, we will leave the hard work to the molecular guys.

With computers, numerical solutions can be obtained to Schrodinger's equations, and the iterative process of fitting accurate potentials $E_{el}(R)$ to observations is often feasible. A plot of the lowest electronic levels of the NaLi molecule, solved numerically by Mabrouk and co-workers[59] is given in figure 3. However, it is also instructive to consider model potentials, where $E_{el}(R)$ takes the form of a closed formula or a convergent series[2].

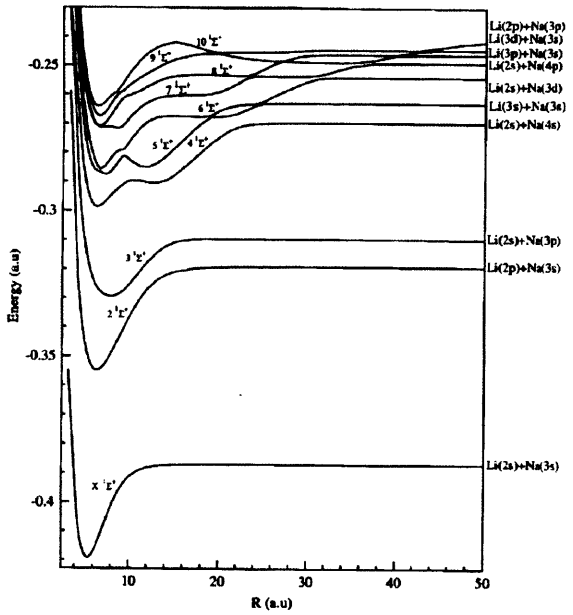

Figure 1. Potential energy curves of the ten lowest $^1\Sigma^+$ states of NaLi

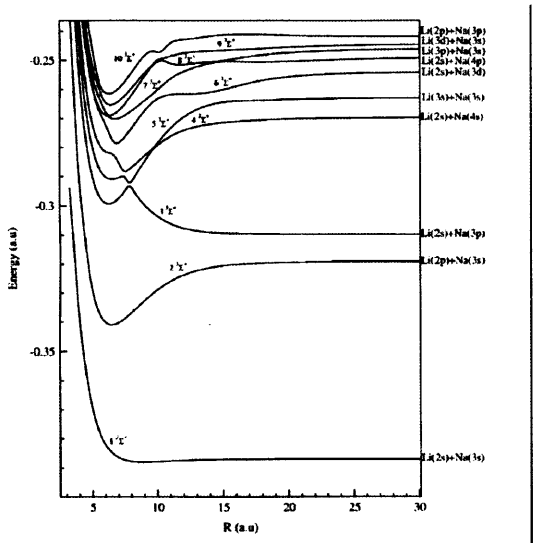

Figure 2. Potential energy curves of the ten lowest $^1\Sigma^+$ states of NaLi

figure 3: Plots of the lowest singlet and triplet potentials of the NaLi molecule. Note that the two figures have been rescaled and positioned so that the vertical axes approximately match up. Reproduced from Mabrouk et. al, J. Phys. B 41, 155101 (2008)

Perhaps the simplest model potential is that of the quantum harmonic oscillator, centered at the equilibrium separation R_e. The minimum potential energy and the stiffness of the oscillator are set so that the lowest few energy levels are accurately matched to empirical data. Anharmonic corrections can be applied to match higher energy levels, but even qualitative features of the harmonic oscillator are clearly unphysical, such as infinite bound vibrational levels. Therefore more accurate model potentials are needed to draw meaningful conclusions about molecules.

A realistic model potential should satisfy a few important requirements. First, it should reach a constant, finite value as $R \rightarrow \infty$. This asymptotic value should be equal to the total energy of the two free atoms in an electronic configuration that connects adiabatically to the molecular state of interest. Second, it should have a minimum at $R = R_e$. Third, it should become infinite (or at least very large relative to dissociation) as $R \rightarrow 0$, due to the repulsion between nuclei as they approach each other[2].

One satisfactory option is the Morse potential[90,91]. This potential is described by the function:

8 $$E^{el}(R) = D_e\left[1 - e^{-a(R-R_e)}\right]^2$$

where D_e is the Dunham coefficient representing the depth (below dissociation) of the potential minimum.

The Morse potential can be solved analytically under some conditions, making it a historically important development. It has a finite number of bound energy levels, gives accurate predictions for the first several low-lying levels, and allows for anharmonic phenomena such as overtone ($\Delta v > 1$) transitions. Many model potentials have been proposed over the decades, each with their own advantages and disadvantages[2].

The value of model potentials is not just the ability to obtain computationally easy solutions, but the ability to gain an intuitive picture of the molecule to plan a course of action for further study. The collections of parameters that make up accurate numerical potentials are hard to visualize, but approximate curves can help develop intuition about transitions and molecular states.

2.2.3 Long-range interatomic forces

The most important part of the potential for determining the behavior of weakly-bound molecules is at long-range. For large separations, the electron wavefunctions are very similar to the unperturbed atomic solutions, so the zero-order Born-Oppenheimer solutions are not particularly enlightening. Here the interatomic interaction is mostly due to the Van der Waals force between two polarizable particles[65].

Van der Waals forces can be interpreted as an attractive force between quantum fluctuations of the electronic dipoles of each atom. Although ground state atoms have zero expectation value for the dipole moment $\langle \boldsymbol{d} \rangle = \langle \Phi_g | e\boldsymbol{r} \cdot \hat{\boldsymbol{z}} | \Phi_g \rangle$, there is a non-zero variance

$$(\Delta \boldsymbol{d})^2 = \langle \Phi_g | (e\boldsymbol{r} \cdot \hat{\boldsymbol{z}})^2 | \Phi_g \rangle - (\langle \Phi_g | e\boldsymbol{r} \cdot \hat{\boldsymbol{z}} | \Phi_g \rangle)^2 = \langle \Phi_g | (e\boldsymbol{r} \cdot \hat{\boldsymbol{z}})^2 | \Phi_g \rangle + 0 \neq 0 \qquad (9)$$

which can be interpreted as fluctuations of the instantaneous dipole moment of either atom. These instantaneous dipoles will "induce" a dipole moment in the other atom, leading to weak dipole-dipole attraction.

More rigorously, by introducing a term in the Hamiltonian representing dipole-dipole coupling between two atoms a and b:

$$\boldsymbol{H}' = \frac{1}{4\pi\epsilon_0} \frac{\boldsymbol{d}_a \cdot \boldsymbol{d}_b - 3(\boldsymbol{d}_a \cdot \hat{\boldsymbol{R}})(\boldsymbol{d}_B \cdot \hat{\boldsymbol{R}})}{R^3} \qquad (10)$$

we obtain no first order perturbation to the ground state, but in second order perturbation theory

11 $$\Delta E^{(2)}=\frac{[\langle \Phi_g|\boldsymbol{H}'|\Phi_e\rangle]^2}{E_g-E_e}=\frac{C_6}{R^6}$$

Where C_6 is the standard notation for the constant associated with the R^6 interaction. For excited states, the treatment is the same unless the atoms are indistinguishable (i.e. homonuclear molecules) and in different states, in which case the atoms are in the superposition $\Phi_{coupled}=[|g_a e_b\rangle \pm |e_a g_b\rangle]/\sqrt{2}$. If this is the case, there can be the first order perturbation

12 $$\Delta E^{(1)}=\langle \Phi_{coupled}|\boldsymbol{H}'|\Phi_{coupled}\rangle=\pm 2\langle g_a e_b|\boldsymbol{H}'|e_a g_b\rangle \propto \frac{C_3}{R^3}$$

So in homonuclear molecules, the exited state has a much longer-range than the ground state.

The R3 and R6 terms are only the first terms in the long-range interatomic potential; relativistic considerations weaken the dipole-dipole correlations at longer range[92], resulting in a "retarded Van der Waals" term which varies as R^7, and potentials will even display higher order terms which can be significant for accurate knowledge of weakly-bound states[60-62].

One specific opportunity in current atomic and molecular physics is the study of Feshbach resonances, to addressed in more detail in chapter 3. These require accurate knowledge of the most weakly bound vibrational states of molecules, but such states were very hard to identify in traditional molecular spectroscopy, which starts with molecules in the lowest energy states and drives transitions among low vibrational states[3,93-97,97]. However, once a few Feshbach resonances are identified in ultracold gases they can be used to greatly refine the knowledge of the long range molecular potential[5].

This knowledge can be used to better predict transitions from these states to excited states, which can then be measured with precise spectroscopy, further refining the knowledge of the molecule[67].

2.3 Quantum states of molecules

2.3.1 Nuclear rotation and vibration

Regardless of the effective potential, the eigenfunctions form recognizable patterns and allow for further approximations to simplify the naming of energy levels and identifying spectroscopic lines with particular transitions. The first approximation is to separate rotation of the nuclei about the center of mass from vibrations in the nuclear spacing. Referring back to the form of $\mathbf{T}^N$ (equation 3), for diatomic molecules we can separate the terms into

13 $$\boldsymbol{T}^N(R,\theta,\phi)=\boldsymbol{T}^N(R)+\boldsymbol{H}^{ROT}$$

where $\mathbf{H}^{ROT}$ contains all terms with angular dependence.

Energy of rotation about the nuclei is quantized as usual for angular degrees of freedom. Introducing the operator for nuclear rotation **R** (not to be confused with R, the scalar value of the internuclear separation).

14 $$\boldsymbol{H}^{ROT} = \frac{1}{2\mu R^2}\boldsymbol{R}^2 = \frac{1}{2\mu R^2}(\boldsymbol{R}_x^2+\boldsymbol{R}_y^2) = \frac{1}{2\mu R^2}[(\boldsymbol{J}_x-\boldsymbol{L}_x-\boldsymbol{S}_x)^2+(\boldsymbol{J}_y-\boldsymbol{L}_y-\boldsymbol{S}_y)^2]$$

The far right side of equation 14 represents the fact that rotational motion of the nuclei is coupled to electron orbit and spin, so R is not necessarily a good quantum

number. The rotational operator $\mathbf{J} = (\mathbf{R}+\mathbf{S}+\mathbf{L})$ gives J and $m_{J,}$, which are good quantum numbers due to the symmetry of the Born-Oppenheimer potentials. Because the **S** and **L** operators apply only to electronic wavefunctions, $\mathbf{H}^{ROT}$ produces a well-defined, R dependent energy which is independent of the vibrational motion. A detailed treatment of these terms is beyond the scope of this thesis, but once the hard work is done[58], equation 7 for nuclear motion can be rewritten as

$$E^{total}\chi_v = \left[\boldsymbol{T}^N(R) + E_i^{el}(R) + \frac{\hbar^2}{2\mu R^2}(J(J+1) - \Omega^2)\right]\chi_v \qquad 15$$

where $\Omega = \Lambda + \Sigma$. Now the effects of nuclear rotation are encapsulated in perturbations to E^{el} and the rightmost term in the Hamiltonian, often called the centrifugal term. This Schrodinger equation can be used to solve for vibrational wavefunctions.

An alternative approach is to solve first for vibrational energies independent of rotation. Rotation can then be solved as an additional degree of freedom which perturbs vibrational energies slightly, resulting in energy splitting of the vibrational levels into rotational bands. The best approach depends on the energy levels being studied and the computational methods used.

Feshbach resonances, for reasons discussed later, only populate specific rotational states. The resonances we use conveniently populate only the R=0 states, and because the ground states of alkali atoms have electron orbital momentum L=0, they adiabatically connect to L=0 molecular states. This greatly simplifies the rotational behavior of Feshbach molecules, as the only angular momentum comes from electron spin, which is strongly coupled to the magnetic field, and nuclear spin, which has little effect on molecular dynamics but produces a manifold of hyperfine states for each BO

wavefunction. These details will be addressed in chapter III.

2.3.2 Spectroscopy notation for molecular states

I have put this off until now, but we must review spectroscopic notation of molecular energy levels, if only for completeness and translating the literature. Like in many fields of quantum mechanics, the patterns of molecular transitions were cataloged by distinguishing the largest energy splittings first, followed by smaller and smaller splittings as the experimental apparatus improved, with the theory explaining the connection of molecular spectra to physical structure being developed later[57]. For this historical reason, the naming of energy levels has the rather unwieldy format:

16 $$N^{2S+1}\Lambda_{\Omega}^{(+/-)}(v, J, m_j)$$

where N is replaced with X for the ground electronic states and 2, 3, 4 for excited electronic states. Λ is replaced with Σ for states with zero orbital angular momentum projection, Π for states with projection of 1, etc. (similar to S, P, D states for atoms). The +/- in the superscript denotes whether wavefunctions are symmetric or antisymmetric in a plane containing the nuclei. Homonuclear molecules also have symmetry upon reflection normal to the internuclear axis, which is labeled by another subscript g/u (from the German terms gerade and ungerade). As an example, the states expected to be populated by the 796 NaLi resonance is the ground, triplet (S=1), sigma state and is labeled by $X^3\Sigma_0^+(v=14, J=1, m_j=+1)$.

At this point, we abandon further adventures into the theory of diatomic

molecules. As can be expected, under many circumstances the approximations will be invalidated to some degree. Because the theory is far from exact, models of the molecular energies have to be informed by spectroscopy experiments, but those experiments require accurate theories to interpret the results and to anticipate where to look for new interesting transitions.

2.4 Important considerations for experiments:

2.4.1 Molecular transitions

One aspect of molecular dynamics that is very important in experiments is the strength of transitions between two molecular states. The matrix element for driving such transitions with photons are similar to the matrix elements of atomic transitions:

17 $$\left\langle \Psi_g \middle| \boldsymbol{d}\cdot\boldsymbol{E}\, e^{i\omega t} \middle| \Psi_e \right\rangle = \hbar \Omega_R e^{i\omega t}$$

where ΩR is the Rabi frequency. It is convenient to express the strength of transitions in terms of Rabi frequencies, because for resonant driving, the Rabi frequency is the rate at which ground state atoms are transferred into the excited state. For Na and Li optical transitions, several mW/cm2 of laser light will provide Rabi frequencies of order 10 MHz. This is called the saturation intensity for alkali atoms, where the atoms undergo spontaneous decay at the same rate as they are driven into the excited state, giving the maximum steady state excited population and maximum fluorescence[75,92].

In molecules, however, the nuclear wavefunctions have to be considered. It is not enough that the electrons are driven to a new state; the nuclear wavefunctions must also

evolve into the target state.

Once again the separation of energy scales, and therefore time scales, simplifies things. The nuclei are charged particles, so they will respond to electromagnetic forces, but the greater mass and lower energy of vibrational motion make them rather insensitive to the optical frequencies responsible for driving electronic transitions. Therefore, the matrix element for molecular transitions can be separated to give:

18 $$\left\langle \Phi_g \chi_g \left| \boldsymbol{d}\cdot\boldsymbol{E}\, e^{i\omega t} \right| \Phi_e \chi_e \right\rangle = \left\langle \Phi_g \left| \boldsymbol{d}\cdot\boldsymbol{E}\, e^{i\omega t} \right| \Phi_e \right\rangle \left\langle \chi_g \middle| \chi_e \right\rangle = \hbar \Omega_R e^{i\omega t} Q(v_g, v_e) S(J_g, J_e)$$

where Q is the Franck-Condon factor depending on the vibrational states, and S is the Hönl-London factor depending on the rotational states[58]. For weakly bound molecules, the matrix element containing the electronic wavefunctions is similar to the transition matrix element of the atomic states to which they adiabatically connect. This is not surprising, as the electron wavefunctions of such atoms are only somewhat perturbed.

The second part, which calculates the overlap of the initial and final nuclear wavefunctions, provides a factor which can be multiplied with the atomic matrix element. The factor can be close to 1 for strong molecular transitions, but can be vanishingly small for transitions between very different nuclear vibrational states. The Franck-Condon factors will sum to 1 for all possible nuclear transitions to a given electronic state. Therefore, molecular transition matrix elements, and thus radiative lifetimes, saturation intensities, and other experimentally relevant quantities, can be estimated from atomic processes (which are readily studied in bi-alkali systems), as long as the numerical factors are known.

The Frank-Condon factor, which is simply a unitless number, can be calculated numerically, obtained from empirical data, or estimated using one or more techniques

developed by molecular physicists. One simple technique is the use of turning points. This only requires knowledge of the approximate binding energy and an adequate pseudo-potential for the initial and final states. See figure 4 for a schematic explanation of the turning point method.

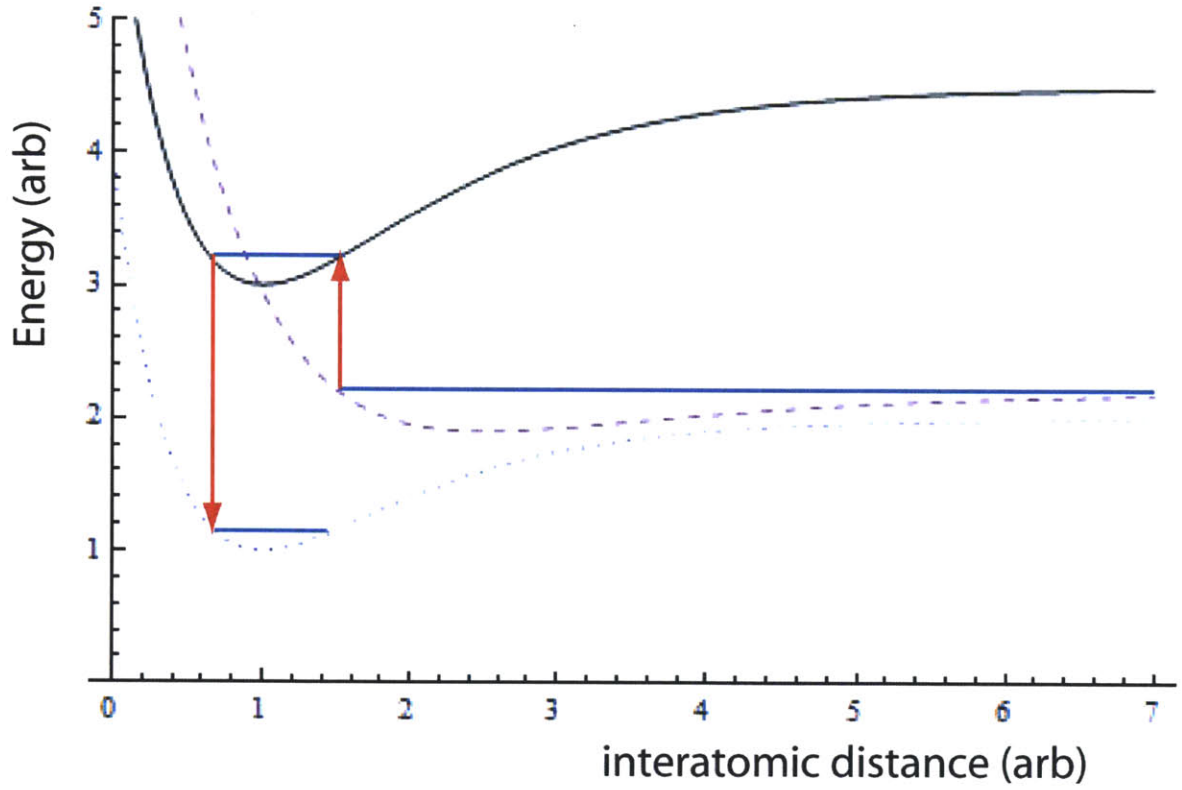

figure 4: The Turning point method allows identifying transitions with good Franck-Condon factors. If states have similar classical turning points, they are likely to have good Franck-Condon factors.

The turning point method works because most of the wavefunction amplitude of nuclear vibrational states occurs at the classical turning points, where the kinetic energy is small and the local wavelength is large. This implies that for two nuclear states with

classical turning points at similar values of R, the Franck-Condon factor can be large (close to 1), but for two states with vastly different turning points, the factor is probably very small. For any two particular states, this is a rough estimate, but given the uncertainty of exact vibrational energies and the challenge of setting up a new experiment covering particular transitions (and therefore finding the appropriate lasers, initial state preparation, etc.), the turning point method has guided the hands and minds of many molecular physicists[65].

2.4.2 Molecules in an electric field:

The major motivation for producing ultracold heteronuclear molecules is to take advantage of their electric dipole moments. Ultracold electric dipoles can be used to search for an electron EDM, create quantum computing platforms, or study many body systems with long-range, anisotropic interactions[98]. To understand the advantages of using heteronuclear molecules for this, we first consider the Stark shift in neutral atoms.

When an atom is placed in a DC Electric field $\boldsymbol{E}=\varepsilon\hat{z}$, the following perturbation is introduced to the atomic Hamiltonian:

19 $$\boldsymbol{H}'=\boldsymbol{d}\cdot\boldsymbol{E}=e\,\varepsilon\,z$$

Because the coupling term has odd parity, the matrix element will be non-zero only when coupling states of opposite parity. For atoms, this means coupling states of odd L to states of even L.

If we consider a ground state alkali atom, the most important coupling (to first

order), is from the ground S state to the first excited P-state. Simplifying to the 2-level problem, we have:

20 $$\begin{bmatrix} \langle \Psi_S | \boldsymbol{H}' | \Psi_S \rangle & \langle \Psi_S | \boldsymbol{H}' | \Psi_P \rangle \\ \langle \Psi_P | \boldsymbol{H}' | \Psi_S \rangle & \langle \Psi_P | \boldsymbol{H}' | \Psi_P \rangle \end{bmatrix} = \begin{bmatrix} E_S & e\langle z \rangle \varepsilon \\ e\langle z \rangle^* \varepsilon & E_P \end{bmatrix}$$

where <z> is shorthand for matrix element $\langle \Psi_S | z | \Psi_P \rangle$. This is just a 2-level Hamiltonian with well-known eigenvalues:

21 $$E\pm = \frac{1}{2}(E_S + E_P) \pm \frac{1}{2}\sqrt{(E_S - E_P)^2 + 4|\langle z \rangle|^2 (e\varepsilon)^2}$$

As seen in figure 5, for small values of the coupling term, the energy of the eigenstate changes quadratically. This is interpreted as an induced dipole, meaning that the electric dipole moment (defined as dE/dε) goes from zero and increases linearly with E-field. For large fields, the energy of the eigenstate becomes linear with E-field. This means the atom has been fully polarized; the eigenstate is an balanced superposition of two states of opposite parity and has maximum charge asymmetry.

As an example, in a lithium atom, this requires the coupling term to exceed the energy splitting between 2S and 2P, or in other words:

22 $$\varepsilon e a_0 \geqslant E_p - E_s = 1.85\ eV \ \rightarrow\ \varepsilon \geqslant 3.6 x 10^8\ V/cm$$

Where the Bohr radius a_0 is used for an estimate of <z>. By comparison, the largest DC electric fields routinely produced in a lab are about 10^4 V/cm. This means that, in practice, atoms cannot be polarized by DC lab fields.

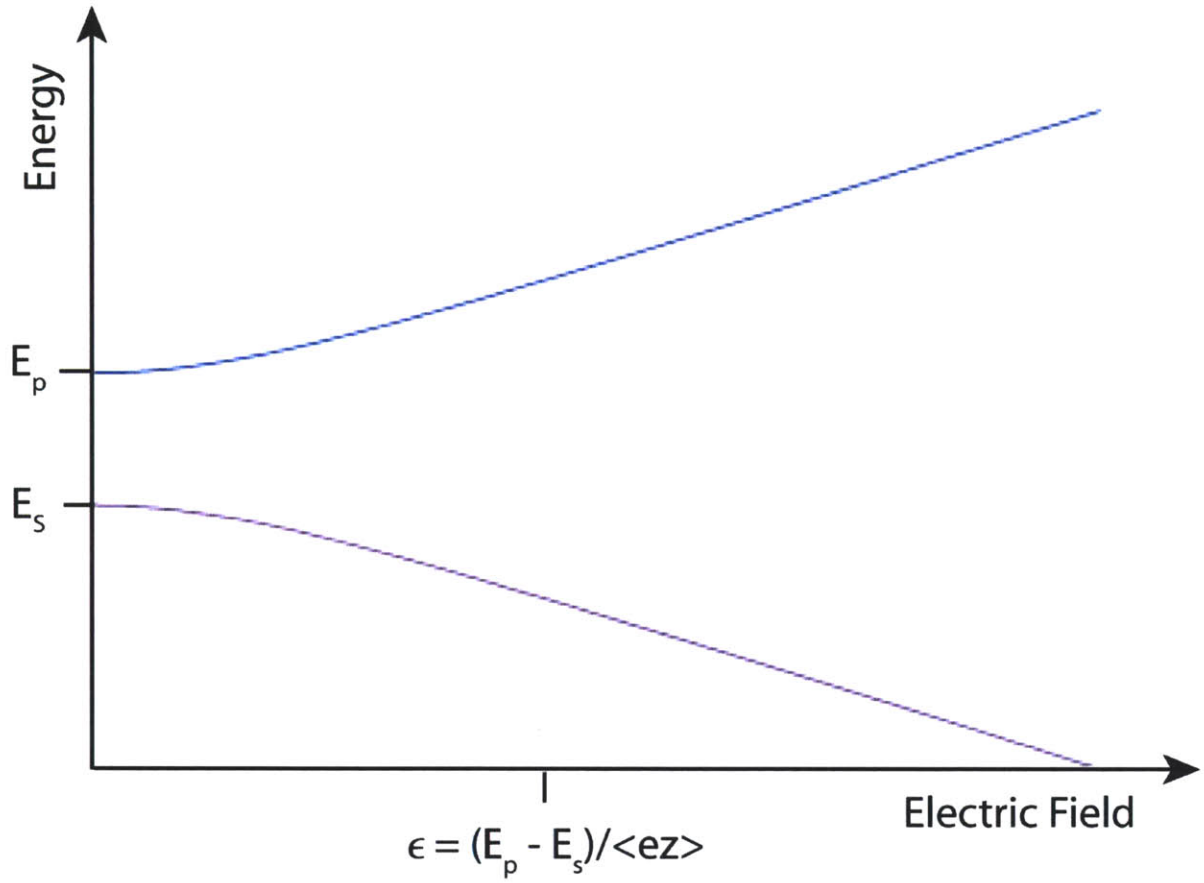

figure 5: Plot of Stark shifted energies of the lowest S and P states of an alkali atom. As discussed in the text, the field where the energies become linear (i.e. the atom is polarized) is of order 10^8 V/cm.

Molecules have similar maximum ground state dipole moments as atoms (KBr, an ionic molecule with relatively large dipole moment, has a moment of only 10.5 Debye = 4.2 ea_0)[99]. The major difference in a heteronuclear molecule in an E-field is that the charge imbalance between the two nuclei couples to the E-field, allowing a nonzero coupling Hamiltonian between nuclear states of differing rotational angular momentum. Because these states are spaced by 10-100 MHz rather than 1014 Hz,

practical lab fields can readily polarize the molecule. Some molecules, for example PbO, can be polarized with only 10 V/cm[46].

The very small E-fields required to polarize some molecules have lead chemists to define "permanent" electric dipole moments. To a physicist, dipole moments are not permanent; when E = 0, the true eigenstates are eigenstates of rotational kinetic energy, not dipole moment orientation, and these states have zero expectation value of <z>. However, the perturbation felt by another nearby molecule with "permanent" electric dipole moment is strong enough to polarize both molecules. Similarly, if in the experiment of interest, a polarizable system stays in the linear regime of energy vs. external E-field, it can be considered to have a well-defined dipole moment, and the full coupling dynamics can be ignored. This is the case for bi-alkali molecules in 10 kV/cm laboratory fields, for PbO held between low voltage capacitor plates, or for polar chemical compounds while they are being dissolved by the "permanent" dipole moment of water molecules.

3
Molecule Formation: Collisions and Feshbach Resonances

3.1 Atomic collisions and molecule formation

Traditionally, molecules for scientific study have been formed by atomic and molecular collisions in the form of chemical reactions, either reactions occurring in a lab specifically to produce the molecule of interest, or naturally occurring reactions which produce stable compounds that can be refined to obtain samples of the desired molecules.

On a microscopic level, chemical reactions are inelastic collisions. Reactant particles approach each other with finite kinetic energy and move close enough together that the electron clouds are strongly perturbed from the initial states. These perturbed reactant configurations can couple to other possible combinations of bound states with the same total atomic constituents. As the wavefunctions evolve, the system has a finite probability to transition to a different state that can satisfy energy conservation and momentum conservation. In high energy conditions (here meaning room temperature or higher), many possible final states will be populated.

The actual processes can involve any number of initial reactant particles, can leave the product particles with more or less kinetic energy (exothermic and endothermic reactions), and can result in the emission or absorption of photons (sometimes called photochemical reactions, such as photosynthesis). The history of chemistry has been dedicated to identifying and predicting patterns of these processes, and modern physical chemistry has been quite successful in using physics to describe the origins of many of these patterns[99].

3.1.1 Inelastic collisions

At ultracold temperatures, such inelastic collisions are still significant, but for many atomic physics experiments, they are considered undesirable sources of decoherence and trap loss. When experiments require temperatures of less than 1 μK, the absorption or emission of optical photons will result in recoil energy in the atoms, which leads to heating of the clouds. Even without photochemistry, the kinetic energy released from differences in binding energies of initial and final states can be equally significant. If the trap has finite depth (meaning high energy particles can escape completely), or only traps specific quantum states (such as any magnetic trapping field), the high-energy products of such reactions will at best leave the trap immediately. At worst, they will undergo further collisions with other ultracold particles, possibly depositing kinetic energy into the cloud or knocking many additional particles out of the trap.

At ultracold temperatures, endothermic reactions or exothermic reactions requiring activation energy are almost impossible due to the low initial kinetic energy. Also, by working with the proper states of the initial atoms, it is possible to eliminate two-body inelastic collisions. To show this, consider an inelastic collision where two atoms collide and bind into a molecule. Simultaneous conservation of center-of-mass momentum and kinetic energy requires:

23 $$m_1 v_1 + m_2 v_2 = (m_1 + m_2) V$$

24 $$\frac{1}{2} m_1 v_1^2 + \frac{1}{2} m_2 v_2^2 = 1/2 (m_2 + m_2) V^2 - E_b$$

Where V is the molecule velocity and E_b the molecular binding energy which is greater than 0 for a bound state. After changing to the center-of-mass frame, V=0, so the second equation cannot be satisfied unless $v_1 = v_2 = E_b = 0$. This trivial zero-energy, perfectly resonant case is technically elastic (with no transfer of kinetic into internal energy), so two-body inelastic collisions cannot result in a bound state.

3-body collisions have an extra particle to carry away the kinetic energy, but at low densities, they occur much less frequently than 2-body collisions. By choosing the lowest hyperfine state of the two colliding atoms, the system can also avoid inelastic collisions where the atoms leave with lower internal energy.

For low energy collisions where the de Broglie wavelength is large and the interaction is short-range (see section 3.3.1 for a discussion of "short-range" interactions) collisions will not cause relative rotation of the atoms, and total angular momentum of electrons and nuclei will be preserved. This can be demonstrated by analyzing collisions in terms of partial waves of definite angular momentum, but can be

intuitively understood by the fact that over interaction length scales, the atomic wavefronts are very flat and thus do not undergo "glancing" collisions which would put them in a rotating state. This is often referred to as the "freezing out" of P-wave and higher order collisions[1].[100]

Thus, the lowest hyperfine states are not even necessary; angular momentum conservation means that the initial state must only be lower in energy than other states with the same total m_f and the atoms will be safe from inelastic 2-body collisions.

3.1.2 Useful inelastic collisions in ultracold atoms

Inelastic collisions can be used to the ultracold physicist's advantage. For example, when properly detuned from a Feshbach resonance in Li-6, atoms were seen to reach a thermal equilibrium of free atoms and molecules through inelastic 3-body collisions. Energy considerations dictated that they populated almost exclusively the nearly resonant state. The finite trap depth meant that energetic free atoms tended to escape the trap, but the bound molecules remained as the mixture continuously evaporated. Thus, the desired chemical reaction ($Li + Li \rightarrow Li_2$), occurred with great efficiency, the cloud was sufficiently ultracold, and the final quantum state of the molecules was well controlled[13].

A type of controlled inelastic collision which relies on photochemistry is

1 Mathematically, higher partial waves have scattering amplitudes and phase shifts that depend on the product (kr), and therefore become insignificant for small values of k (low kinetic energy) and small values of r (short interaction range).

photoassociation. Ultracold photoassociation involves preparing a large, cold sample of atoms, either in long-lived states in a conservative atom trap, or in a continuously replenished trap such as a magneto-optical trap[65,101]. A laser is then used to drive a specific transition to an excited molecular state. At this point, the excited molecule will decay spontaneously, releasing fluorescence photons and populating deeply bound ground state molecules. Alternatively another transition can be driven to ionize the molecule or reach a specific molecular state. These processes are generally incoherent, but can still result in a large population of molecules in a desired quantum state.

If the downward transition is stimulated with a laser (thereby making the whole process a Raman transition), it can preferentially populate a specific quantum state and also avoids the random emission of a photon, preserving the low temperature. Furthermore, adiabatic transfer from the colliding states to the target state through STIRAP processes[102], could allow the reversible transfer of quantum degenerate gases to deeply bound molecular states. This technique has not yet been demonstrated in photoassociation.

3.2 Collisions and losses in dilute ultracold gases

In a dilute, cold atomic cloud, inelastic collisions can be severely restricted by the low kinetic energy available, the low atomic density, and the symmetry of low energy collisions. However, there are always finite inelastic collision rates, and near Feshbach resonances, the rates can be enhanced to the point that they prevent (or enable) the

success of a proposed experiment.

In particular weakly-bound molecules can always decay to more deeply bound vibrational states. These vibrational decays are slow when the molecule is isolated[103], as weakly-bound molecules and homonuclear diatomic molecules in general will not undergo radiative decay. Even heteronuclear bi-alkali molecules have slow radiative decay; lifetimes are typically many milliseconds and isolated deeply bound RbK has been observed with greater than 100 ms lifetimes.

However, collisions with another molecule or a free atom can cause strong coupling between different vibrational states, leading to rapid "quenching" to lower energy states and depositing the energy released into the relative motion of the molecule and atom[104,105].

Ranges for the forces between neutral atoms (less than 50 a_0) are much shorter than typical interatomic spacing (typically 1 μm in our experiments), so collisions become less and less likely (by roughly na^3) for each additional particle involved in the collision. This motivates us to consider only few-body collisions.

3.2.1 3-body atomic losses

If hyperfine states are selected as recommended in chapter 3.1, 2-body collisions will be elastic. Near a Feshbach resonance, the matrix elements in the scattering process can be greatly enhanced, but they remain elastic collisions. This is often used to enhance thermalization[106], hydrodynamic behaviors[107], or many-body phenomena[11,108].

The chief loss process of correctly chosen mixtures of ultracold atoms are then 3-body processes. The same arguments invoking conservation of center-of-mass momentum and angular momentum apply to collisions resulting in a bound trimer or three atoms, so we consider collisions where two atoms become a bound molecule, and one atom remains free.

These collisions can be interpreted as a 2-body interaction occurring for a finite time with a third particle colliding during the interaction time. This gives an intuitive picture of the way three-body losses are enhanced near a Feshbach resonance. The duration of the 2-body interaction can become very large close to resonance (where the lifetime $h/\delta E$ becomes large for the near resonant molecular state with small binding energy δE), allowing ample time for a third particle to become involved and cause an inelastic collision. The collision quenches the weakly-bound molecular state coupled with the Feshbach resonance, causing it to decay to a tightly bound state, and depositing the remaining energy in the resulting molecule and atom.

This motivates the claim that enhanced atom loss near a Feshbach resonance implies that the target molecules have been produced, although in virtual, weakly bound states. However, the molecules may be produced with substantial kinetic energy in a random deeply bound molecular state, making them useless for further experiments in quantum phenomena.

3.2.2 2-body molecular losses

Not to be confused with the previously mentioned 3-body atomic losses, molecular losses are those that occur once molecules have been produced and remain in the trap, colliding with each other and remaining atoms. Feshbach association produces molecules in weakly-bound states. In these states the atoms are well-separated and are bound mostly by the Van-der-waals forces rather than through typical covalent electronic bonds. Such states are called "Halo dimers" in the literature[65].

Because the molecule can always decay farther down the vibrational ladder, 2-body collisions with other atoms or molecules can always be inelastic unless the molecule is in the true ground state of the system. Furthermore, near the Feshbach resonance the bound atoms still experience resonant interactions with remaining free atoms.

One special case worth mentioning is a 2-state mixture of indistinguishable fermions. If molecules are formed with one particle in each state and the molecule remains a long-range Halo dimer, each constituent fermion resembles a free atom with long deBroglie wavelength. If a third fermion (indistinguishable from one of the constituent fermions), participates in a collision, an inelastic decay to a deeply bound state would require indistinguishable fermions to suddenly enter a tightly bound state much smaller than their initial deBroglie wavelength; and such collisions are greatly suppressed by the Pauli-exclusion principle[109,110]. Once the molecule becomes more deeply bound, however, the wavefunctions and internal states of the bound atoms become less like the free atoms inelastic collisions can occur rapidly.

Another unique situation occurs if the molecules themselves are composite fermions (i.e. a bound state of one bosonic atom and one fermionic atom). S-wave

collisions are forbidden by the symmetry of the collision. If P-wave collisions are frozen out, this should allow the fermionic molecules to be long-lived. However, this only applies when the molecules are tightly bound; the weakly bound Halo dimers can still experience resonant collisions between constituent atoms[103,111,112].

3.2.3 Scattering coefficients

The likelihood of a given particle undergoing a 2-body collision is proportional to the probability that a second particle is nearby. This is therefore proportional to the density of the collision partner. 2-body collision rates (per particle) can be written as

25 $$\Gamma_{12} = \beta_{12} n_2$$

Where the coefficient (beta) has units (cm^3/s), and the subscript 2 on density reflects the fact that it is the density of the species of the collision partner, not the species whose collision rate is being measured. To clarify, $\Gamma_{Na\,Li}$ gives the rate at which a particular Na atom collides with any Li atom, and depends on Li density, not Na density. One would correctly expect that $\beta 12 = \beta 21$.

3-body collisions require yet another particle present, leading to another factor proportional to density, and can be written

26 $$\Gamma_{123} = K_{123} n_2 n_3$$

In ultracold atomic physics, these coefficients are often reported separately for elastic and inelastic collisions. This is because in finite-depth state-selective traps, elastic collisions lead to thermal equilibrium while inelastic collisions lead to atom loss.

Elastic collisions can also create losses by thermally populating motional states which can escape from the trap. Determining elastic collision rates requires careful measurements of thermodynamic processes combined with accurate theories. Inelastic collision rates, on the other hand, can be measured by simply counting the atoms remaining in the trap for varying amounts of hold time.

As atoms are lost, density drops and collisions slow down. This gives typical curves for particle numbers in the presence of inelastic 2-body and 3-body collisions. See figure 6 for a simple plot of the different processes. If a system is known to experience both types of processes, a single lifetime measurement can be used to identify both coefficients[113], although it requires high-quality data to distinguish between the two curves, especially in the presence of one-body processes such as background gas collisions or heating in a finite depth trap.

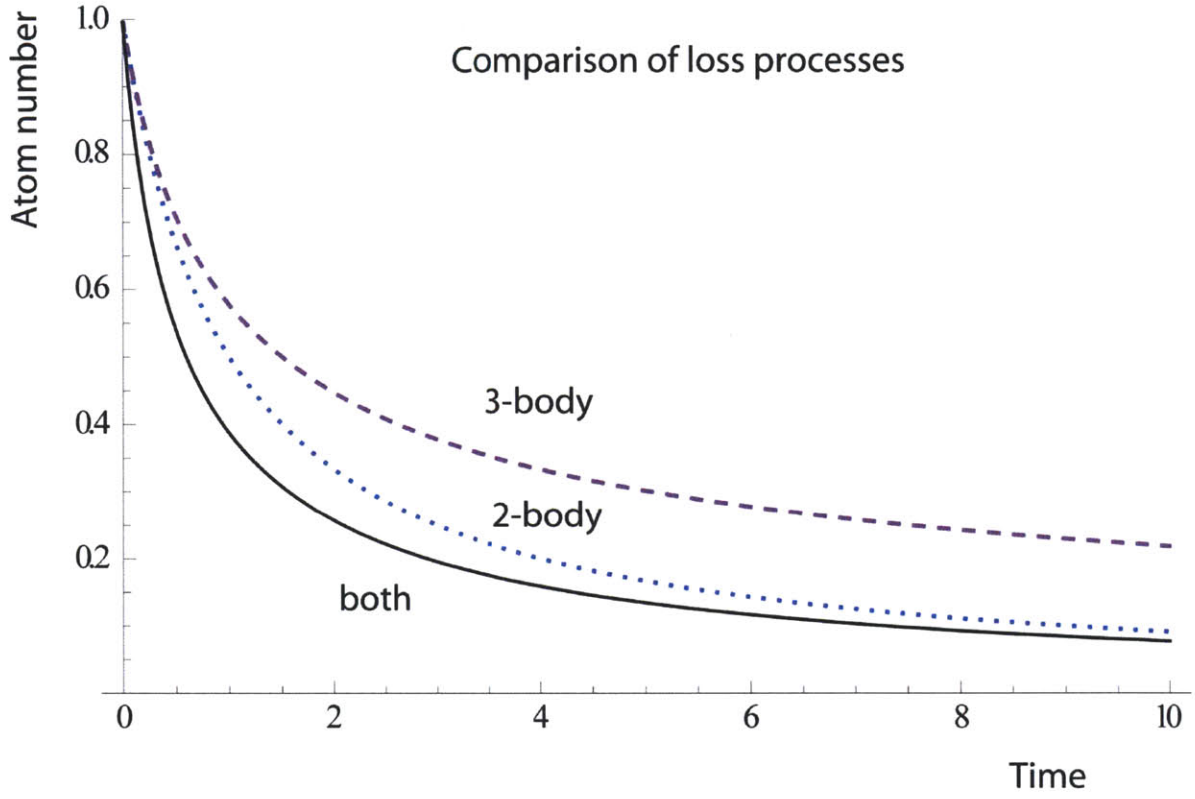

figure 6: A plot of 2-body and 3-body losses for a homogeneous gas. All units are arbitrary. The coefficients were chosen so that losses were equally significant initially.

These curves are not exponential as expected from density independent processes (such as radiative decay, light scattering, or collisions with background particles in the apparatus), but the term lifetime is often applied colloquially to 2-body or 3-body losses as the inverse rate Γ^{-1} at which atoms are lost at a given density.

The scattering coefficients can be calculated if all the decay channels and collisional matrix elements (coupling free atomic states to potential decay states). A priori calculations of these rates require exact wavefunctions for the bound states, which

as discussed in chapter 2 are generally not well known. As such, the rates are generally found empirically.

2-body collision rates are often presented as a cross-section σ with units of area, defined as

27 $$\sigma = \Gamma / nv$$

This is partly historical, as collisions were often studied with beams of particles colliding with other beams or with stationary targets[85]. The velocity v shows up because it identifies the distance through a homogeneous density n that a particle can move in unit time. This interpretation is consistent with many physical systems where collision rate is proportional to v, but cross section is rather constant with v.

The cross-section interpretation also offers intuition about another important result. Consider particles with finite spatial extent, such as thermal atoms extended over DeBroglie wavelength $\lambda_{DB} = h/\sqrt{2\pi m k_B T}$[114]. For short-range interactions with $r_o << \lambda_{DB}$, a collision will not occur if the wavefunctions never overlap, leading to a maximum cross section for $a \geq \lambda_{dB}$ which depends on temperature (or another relevant energy scale, such as T_f for a degenerate Fermi gas), but not on the details of the interaction. This is called the unitarity limit[115], and can be stated simply as

28 $$\sigma \leqslant 4\pi/k^2 = 16\pi^3 \lambda_{DB}^2$$

where the numerical factor can be found with a more careful theoretical treatment[85]. This leads directly to the unitarity limited 2-body coefficient

29 $$\beta = \sigma v \leqslant \frac{16\pi^2 h^2}{m^{3/2}\sqrt{3 k_B T}}$$

For 100 nK and collisions between Na and NaLi (with reduced mass of 13.7amu), the

unitarity limited 2-body loss coefficient is 3.1×10^{-7} cm^3/s.

Measured loss rates in ultracold gases are generally much lower than the unitarity limit, but near a Feshbach resonance or when dealing with weakly-bound molecular states, inelastic losses can come close to this limit.

3.3 Feshbach resonances

The current method of choice to produce ultracold molecules in well-defined quantum states uses Feshbach resonances[31]. Mentioned previously, a Feshbach resonance occurs when a free atomic state and a bound molecular state have different magnetic moments. At a specific magnetic field B_0 the states become degenerate, and even very weak coupling between the two states can result in strong interactions, adiabatic transfer between states, and enhanced inelastic collisions.

3.3.1 Coupling between atomic and molecular states

For low kinetic energy and short range potentials ($k << 1/r_0$, where r_0 is an appropriate cutoff range of the potential), the exact form of the potential is unimportant for asymptotic properties. Intuitively, this is similar to the way that P-wave collisions are frozen out at low energies; the atoms cannot "see" the details of the potential. The range r_0 is determined by requiring that the kinetic energy of a particle confined within

that range is larger than the potential energy outside the range:

30 $$T(r_0) > V(r_0) \rightarrow \frac{\hbar^2}{\mu r_o^2} > |V(r_0)|$$

This means that potentials that fall off faster than $1/r^2$ may considered short-range. Because the longest range components of neutral atomic interactions are Van der Waals terms (which fall off at least as fast as $1/r^3$), we can ignore the details of the potential when calculating scattering properties. Applying condition 30 to typical interatomic potentials, the length r_0 is of order 2-5 nm (sometimes referred to as the Van der Waals length l_{vdw} in the literature[116-118]). Therefore we can model interatomic interactions with square wells of width r_0 and depth adjusted to match empirical results.

The initial atomic state has kinetic energy $\varepsilon = k^2/2\mu$, where μ is the reduced mass of the atom pair. The atomic state experiences an interaction potential

31 $$V_a = \begin{cases} -V_{bg} & for\ r < r_0 \\ 0 & r \geq r_0 \end{cases}$$

Where V_{bg} is chosen to give the appropriate non-resonant scattering properties. The molecular state has binding energy E_m (relative to dissociation). The molecular potential to which the atom couples is:

32 $$V_m = \begin{cases} -V_c + \Delta E & for\ r < r_0 \\ \Delta E & r \geq r_0 \end{cases}$$

where $\Delta E >> \varepsilon$ is the energy of the free atomic state asymptotically coupled to the molecular potential, relative to the initial atomic state, and V_c is adjusted to give the correct binding energy E_m of the weakly bound molecular state. For brevity we will define the molecular energy relative to the atomic energy as the detuning $\delta = \Delta E - E_m$. See figure 7 for clarification on these potentials and energies.

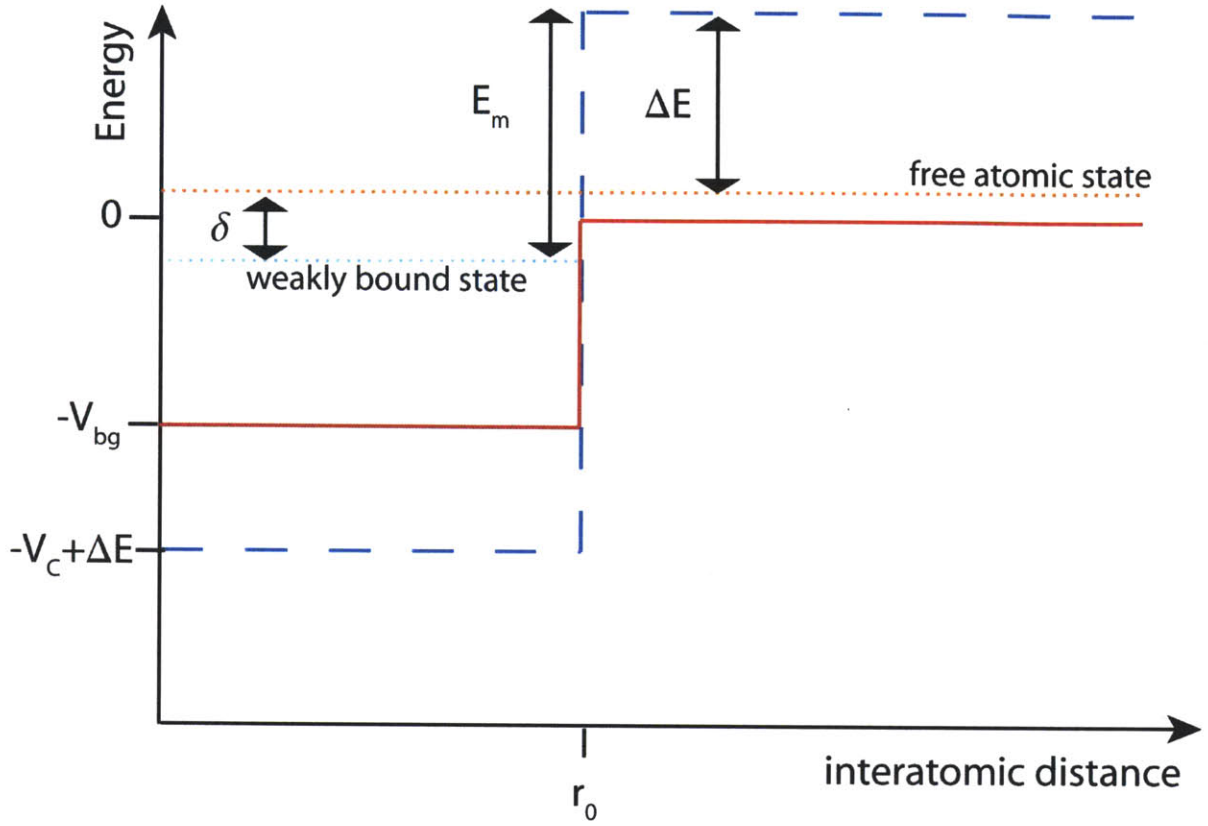

figure 7: Illustration of energies defined in the coupled square wells analysis. The solid line is the open channel potential V_a, the dashed line the closed channel potential V_m, and the dotted lines depict energies of the coupled states.

For our atomic system, V_a corresponds to the initial state, which generally has both atoms in one of the lowest hyperfine states at high magnetic field. These states are always triplet states (because both electrons are anti-aligned to the magnetic field). V_m can be a singlet state or another triplet state with different m_s. Therefore the coupling between the two potentials is related to singlet-triplet coupling (or coupling between different triplet states), which occur because of the hyperfine interaction.

For a Feshbach resonance, ΔE is given by the difference in Zeeman energies of the states, and can be changed by adjusting the magnetic field. If $\Delta E \approx E_m$, ($\delta \approx 0$) the bound state is nearly resonant with the free atomic state with small energy ε. When the molecular state is lower in energy than the dissociation energy (magnetic fields where this occurs are said to be on the molecular side of the resonance), a true bound molecule will exist. When the molecular state is higher in energy than the dissociation energy, the molecules will very quickly dissociate into the continuum of available free atomic states. Molecules in this situation (at magnetic fields on the atomic side of the resonance), are metastable, and are sometimes called quasi-bound or virtual-bound molecules.

The wavefunction of a free atom, without any coupling to the molecular state, is

33 $$|\psi_a\rangle = \left\{ \begin{array}{ll} \dfrac{\sin K_+ r}{K_+ r} & for \quad r < r_0 \\ \dfrac{\sin(kr+\eta_0)}{kr} & for \quad r > r_0 \end{array} \right\}$$

where K_+ and η_0 are determined by requiring the wavefunctions to satisfy the Schrodinger equation and meet boundary conditions at r_0. Similarly,

34 $$|\psi_m\rangle = \left\{ \begin{array}{ll} \dfrac{\sin K_- r}{K_- r} & for \quad r < r_0 \\ 0 \quad for & r > r_0 \end{array} \right\}$$

where the molecular wavefunction outside the well is approximated as 0 because the potential $V(r) = \Delta E >> \varepsilon$ in that region.

If we allow a coupling term of energy $\langle \psi_m | V'(\varepsilon) | \psi_a \rangle \ll V_{bg}, V_c$, the eigenenergies and wavefunctions within the well will be strongly perturbed when $|\delta| < V'(\varepsilon)$. When $|\psi_a\rangle$ within the well changes, the phase shift η_0 will have to change drastically to

maintain the boundary condition at r_0. For brevity, I will not show the math, but an interested reader can refer to the thesis of Martin Zweirlein[100] for detailed results.

This changing phase shift can be interpreted as a changing scattering length. In fact, if the condition $k << 1/r_0$ is met, the major effects of the resonance on the atomic collisional states can be parametrized entirely by the scattering length a. This is possible because the short-range potential can accurately be replaced by a hard-sphere potential with radius that grows large and becomes negative (i.e. the wall occurs at negative r) when the resonance is crossed. The interpretation breaks down when the radius becomes larger than the DeBroglie wavelength at which point the dynamics can be described by unitary physics.

The adiabatic ground state of the system connects the atomic state (on the atomic side of the Feshbach resonance) to the molecular bound state as the magnetic field is varied. A straightforward 2-level analysis would put the energy at

35 $$E^{(1)}=\frac{1}{2}(\varepsilon+\delta)-\frac{1}{2}\sqrt{[\varepsilon+\delta]^2+V'(\varepsilon)^2}$$

but this ignores the fact that the real problem couples the molecular state to the continuum of atomic states.

For an accurate treatment, the coupling element $(V'(\varepsilon)^2/2\,\varepsilon)$ should be integrated over all possible incoming states, and the coupling $V'(\varepsilon)$ will vary with atomic kinetic energy, although it is expected to be constant for low energy[32]. Summarizing the results from theory, make the substitution:

36 $$V'(\frac{k^2}{2\mathrm{m}})=\frac{g_k}{\sqrt{\Omega}} \quad g_k=\begin{cases} g_0 \text{ for } k<1/r_0 \\ 0 \text{ for } k>1/r_0 \end{cases}$$

where Ω is the volume of the effective potential well. The integrations over all possible coupling states give the energies:

37 $$\delta_0 \equiv \sum_{\varepsilon} \frac{V'(\varepsilon)^2}{2\varepsilon}$$

38 $$E_0 \equiv \left[\frac{g_0^2}{2\pi} \left(\frac{m}{2\hbar^2} \right)^{3/2} \right]^2$$

With these energies, the ground state energy below resonance (the binding energy of the molecule) is given by

39 $$E = -E_0 + \delta - \delta_0 + \sqrt{E_0^2 - 2E_0(\delta - \delta_0)}$$

3.3.2 Experimental parameters of Feshbach resonances

If the total angular momentum of the atomic and molecular states are equal, the interactions can occur with S-waves, and the resonance is referred to as an S-wave Feshbach resonance. Feshbach resonances can occur when the atomic state couples to a molecular state with different total angular momentum, but in these cases the collision must involve higher partial waves. Although these waves are "frozen out", when resonantly enhanced they can still be observed and used to couple to molecular states[119]. In Cesium, S, P, D, F, and even G-wave resonances have been observed in various spin states[120].

For S-wave resonances, as previously mentioned, the perturbation of the plane waves can be described by the S-wave scattering length a, where the scattering length is the radius of a hard sphere potential which would have the same effect on the

asymptotic long-range wavefunction.

At magnetic fields away from resonance, the scattering length will have a constant value a_{bg}, known as the background scattering length. This is the net effect of coupling to all the possible non-resonant collisional states, and can have a positive or negative value. The value of the scattering length at any field generally represents the strength of interactions between particles.

Near resonance, the scattering length diverges. A detailed analysis of the wavefunctions in the last section can be performed, but in the end the result can be parametrized by

40 $$a_{resonant} = \frac{m g_0^2}{2\hbar^2}\left(\frac{1}{2\pi}\right)\frac{1}{\delta - \delta_0}$$

and total scattering length is

41 $$a = a_{bg} + a_{resonant} = a_{bg}\left(1 - \frac{\Delta B}{B - B_0}\right)$$

42 $$\Delta B = \sqrt{\frac{2\hbar^2}{m}}\frac{\sqrt{E_0}}{\Delta\mu a_{bg}}$$

Where ΔB is commonly called the resonance width, and Bo is the magnetic field at which the (shifted) resonance occurs. $\Delta\mu = \mu_m - \mu_a$, the difference in magnetic moments of the atomic and molecular states. The signs of ΔB and a_{bg} determine where scattering length diverges to $+\infty$, which occurs on the molecular side of the resonance, and where it diverges to $-\infty$, the atomic side of the resonance.

For very small detunings on the molecular side of the resonance, the molecules are Halo dimers, which resemble two atoms on a stick weakly bound by the effective interaction. Such states have a universal binding energy given by

43 $E=-\hbar^2/ma^2$

This is only consistent in the region where binding energy remains quadratic with magnetic field. Beyond this region, the molecules resemble the bound molecular state and the binding energy follows the relative Zeeman energies.

The sign of the scattering length determines whether the interactions are repulsive or attractive. In ultracold gases, it determines mean-field interaction energy, so a positive scattering length, corresponding to repulsive interactions, causes the gas to expand.

A weakly-bound state causing repulsive interactions may seem counter-intuitive. Coupling to a weakly-bound state always pushes the energy of the colliding pair up, unless they can inelastically decay into the actual molecular state. Conversely, coupling to virtual-bound state (with negative binding energy) will push the energy of the atoms down, causing attractive interactions, even though the atoms will not form a bound state.

3.3.3 Scaling of loss coefficients with scattering length.

At low temperature the scattering length (see Chapter 3.2.2) for an S-wave collision gives the 2-body collisional cross section simply as $\sigma=4\pi a^2$. This is not surprising, as by construction a scattering length is the radius of a hard-sphere potential which gives the same collisional properties as the true potential, and for a true hard-sphere potential the classical interpretation is valid. The factor of 4 arises from the fact

that the critical impact parameter is twice the hard sphere radius.

The enhancement of a near a Feshbach resonance can be used to enhance elastic collisions and improve thermalization[106]. It can also lead to enhanced inelastic collisions, particularly causing large 3-body losses very close to resonance. The large losses are generally the way Feshbach resonances are identified experimentally.

3-body collisions have a more complex dependence on scattering length. General scaling behaviors can be calculated[105], but the absolute value of K_3 is not so easily determined. In the Bose-Fermi mixture of RbK, the 3-body loss coefficient was found to scale as a^4, as expected.

Resonant 2-body molecular collisions have similarly complex dependence on scattering length[112], which is not surprising due to the conceptual similarity to 3-body atomic collisions.

Even if the loss coefficients are known exactly from scattering length, there is a further complication in a real experiment. The interactions (elastic and inelastic) produce mean-field energy from the average effect of collisions at the local density, leading to expansion or contraction of the gas[121] when the scattering length changes due to a Feshbach resonance. This change in local density leads to deviations from the losses expected in a uniform gas at the same density. Furthermore, a quantum degenerate gas can demonstrate collective motion and hydrodynamic effects[11] which can further complicate the prediction of loss rates in a real experiment.

Josh Zirbel and coworkers measured many collision rates in strongly interacting samples of RbK near a Feshbach resonance [103]. Their results show that although quantitative agreement with simple theories is hard to observe, many of the expected

trends can be seen. One particularly interesting measurement is the loss rates due to RbK-Rb collisions, which are assumed to be the most significant near resonance. See figure 8 for a reproduction of the figure from the paper.

Note that losses are increasing near resonance, but also increase until similar to losses due to distinguishable atoms away from resonance. This can be understood by the fact that away from resonance, the hyperfine state in the molecules is no longer similar to the hyperfine state of the resonantly interacting atoms, and the remaining atoms are all distinguishable.

The loss behavior of distinguishable atoms (the dashed line in figure 8) is predicted from[112]. The suppression of losses near the Feshbach resonance is due to the fact that Halo dimers have poor wavefunction overlap with the deeply bound vibrational states to which they would decay. This suppresses the decay in the same way as a Franck-Condon factor suppresses transitions between molecular states with very different nuclear wavefunctions.

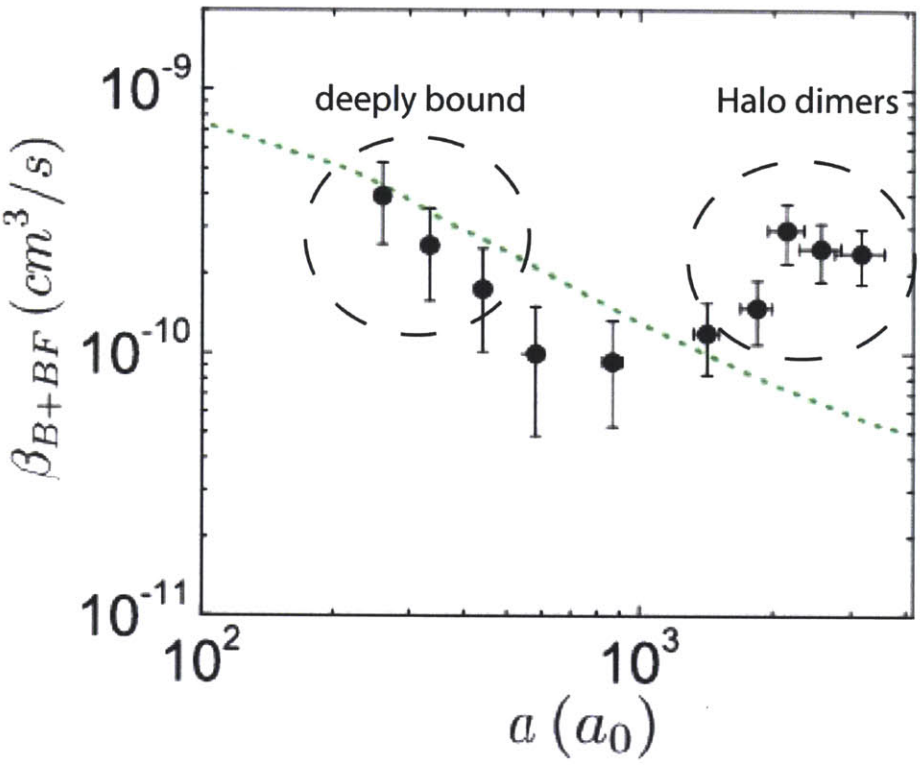

figure 8: Measured coefficient for inelastic losses of RbK molecules colliding with bosonic Rb as scattering length is resonantly enhanced. Circles with error bars are measured loss rates, and the dashed line gives the coefficient for collisions with distinguishable particles, for comparison. Reproduced from Zirbel et. al, PRL 100, 143201 (2008).

3.3.4 Comparison of energy scales

In terms of experimentally useful parameters, the binding energy can be written as

$$E=-E_o+\Delta\mu(B-B_0)+\sqrt{E_0^2-2E_0\Delta\mu(B-B_0)}; \quad \left(E_0=\frac{m(\Delta B\Delta\mu a_{bg})^2}{2\hbar^2}\right) \tag{44}$$

If E_o is smaller than the typical energy spread of the gas (such as k_BT, E_f or mean-field interaction energy in a BEC), not all atom pairs with relative kinetic energy ε will be uniformly perturbed by the resonance. This is often referred to as a narrow resonance. If E_o is larger than this energy, all atom pairs are affected, and the resonance is called a broad resonance. The distinction is important in estimating the effect of the resonance on the thermodynamics of the atom cloud[31]. However, the distinction depends on the atomic density and temperature, and is not intrinsic to the particular Feshbach resonance.

A more intrinsic distinction can be made by considering binding energy vs. magnetic field. For large detuning, the ground state energy will be linear with magnetic field, as it represents the energy of the magnetic dipole moment for either the free atoms or the bound molecule. For small detunings, the energy varies quadratically, and can be interpreted as the magnetic moment changing from the free atom case to the molecule case. This can be used to estimate the molecular character admixed with the the atomic character for the true ground state wavefunction at a given magnetic field.

Comparing the range of magnetic fields where the scattering length is enhanced (the resonance width ΔB, which is 2.2G for NaLi), to the range of fields where the resonant binding formula $E=\hbar^2/ma^2$ still predicts a magnetic moment closer to the

atomic state than the molecular state, we can make an important distinction among different Feshbach resonances. The magnetic moment near resonance is

45 $$\mu - \mu_{atom} = \frac{\partial}{\partial B}\frac{\hbar^2}{ma^2} \approx \frac{2\hbar^2(B-B_0)}{m(a_{bg}\Delta B)^2}$$

where the approximation holds while a >> a_{bg}. This approximate formula gives highly unphysical magnetic moments at large values of ($B-B_o$), so by finding the magnetic field detuning where it gives a prediction equal to $\Delta\mu$, we can estimate the point at which the molecules are no longer mostly open-channel.

46 $$\frac{2\hbar^2(B-B_0)}{m a_{bg}^2(\Delta B)^2} < \Delta\mu \;\rightarrow\; \delta B_{open} = \frac{\Delta\mu m(a_{bg}\Delta B)^2}{2\hbar^2} = \frac{E_0}{\Delta\mu}$$

For the NaLi resonance at 796G (1594G), this range is about 3 mG (17 mG). If the ratio $\delta B_{open}/\Delta B$ is greater than 1, the resonance is open-channel dominated; that is the closed channel admixture is very small for most magnetic fields that enhance atomic scattering. If the quantity is much less than 1, the resonance is closed-channel dominated, meaning the atoms have significant molecular character across the resonance.

The binding energy of the 796G resonance is shown in figure 8. Compare this to the similar situation for RbK, and it becomes clear that although the resonances have very similar resonance widths (ΔB_{NaLi} = 2.2 G vs. ΔB_{RbK} = 3.6 G)[30], the range of fields where binding energy remains quadratic is very different, since for RbK δB_{open} = 5.3G.

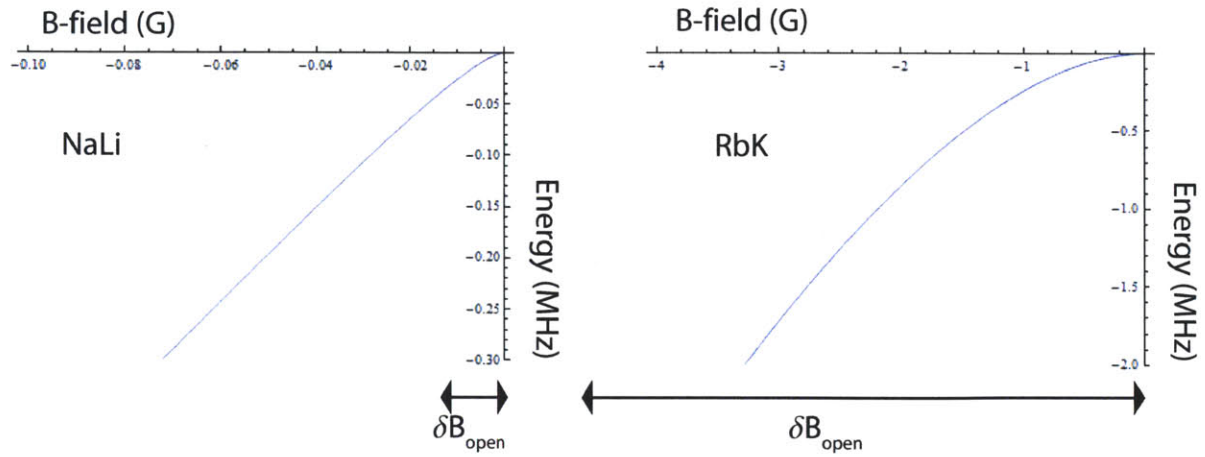

figure 9: Binding Energies of NaLi molecules compared to RbK molecules. Note the difference in scales of both axes.

Other expressions representing the open-channel dominated character of a resonance can be constructed invoking the behavior of the coupled wavefunctions or the characteristic length scales of the Van der Waals potential[31,32], but this construction is based only on the experimentally important quantities of scattering length, magnetic moments, and ΔB, and it identifies the range where binding energy is quadratic, which is useful for RF spectroscopy. In fact, RF transitions become weak outside the range δB_{open}, because the transition from free atomic state to bound molecular state is greatly suppressed by poor wavefunction overlap.

The behavior of the molecular state near resonance is determined by the net coupling to all possible free atomic states. However, many phenomena, such as scattering and adiabatic association, depend instead on the coupling of a particular atomic state to the molecular state. Such single-channel coupling depends on $V'(\varepsilon)^2/2\varepsilon$, which, for low energy, is proportional to the quantity:

47 $$\frac{\sqrt{E_0}}{m^{3/2}} = \frac{a_{bg}\Delta B \Delta \mu}{m}$$

3.4 Adiabatic molecule formation

In Chapter 3 we discussed how a Feshbach resonance results from coupling free atomic states to bound molecular states when the electronic and nuclear magnetic moments differ. The internal states are coupled with the hyperfine interaction, and the ground state of the coupled channels calculation then resembles a molecular vibrational state with exactly zero binding energy.

When the magnetic field is far away from resonance, the states are no longer strongly coupled, and the atoms will be in a true molecular state with finite binding energy or a truly free atomic state with normal collisional properties. See figure 10 for an illustration.

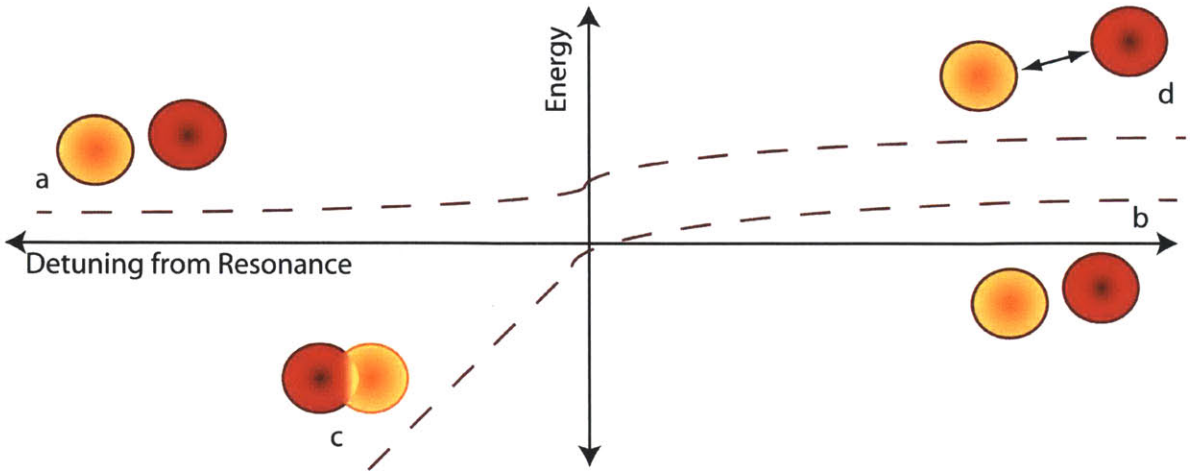

figure 10: The states coupled by a Feshbach resonance. Far from resonance, the atoms are unbound and weakly interacting (states (a) and (b). As the resonance approaches, state (b) couples to the molecular state (c). The free atomic state (a) adiabatically couples to a free state with slightly higher kinetic energy (d).

If the energies are changed very quickly, the wavefunctions cannot follow the eigenstates, and the state makes a transition from one eigenstate to another. This can be interpreted in many ways: the coupling is too weak to affect the wavefunction in the limited perturbation time, the rapidly changing environment does work on the system, and the interactions that define the uncoupled energies of the system determine the "good" quantum numbers while the coupling interaction does not.

On the other hand, if the energies change very slowly, the atom will follow the eigenstates, with the wavefunction adiabatically changing from the initial state to the final state. This is an extremely powerful experimental tool; in fact, we use it constantly to guarantee complete transitions between atomic hyperfine states.

3.4.1 Effects of phase-space density on molecule formation

The atomic and molecular states are coupled by the hyperfine interaction, so by sweeping slowly they will adiabatically transfer from atom to molecules or back. However, there is a major complication in that it is not just a two level system, but a continuum of free atomic states coupled to a single molecular state. In the center-of-mass frame, a molecule can potentially dissociate to any number of possible atomic states, especially if the sweep is not perfectly adiabatic and can deliver some extra kinetic energy to the atoms[25].

Some intuition of the full problem can be gained from two atoms with the same mass in a quantum harmonic oscillator. The problem can be decomposed into center-of-mass and relative coordinates:

48 $$H=\frac{p_1^2}{2m}+\frac{1}{2}m\omega^2 q_1^2+\frac{p_2^2}{2m}+\frac{1}{2}m\omega^2 q_2^2$$

49 $$P=p_1-p_2,\ Q=q_1-q_2,\ p_0=(p_1+p_2),\ q_0=(q_1+q_2)/2$$

50 $$H=\frac{P^2}{4m}+\frac{1}{4}m\omega^2 Q^2+\frac{p_0^2}{4m}+m\omega^2 q_0^2$$

Here the coordinates have been replaced with the combinations that are intuitively associated with relative and center of mass motion. It is clear that the problem is equivalent to independent QHOs for the relative and center-of-mass coordinates, but with different effective mass and frequency.

The molecule will inherit the center-of-mass motion of the atoms, so only the relative coordinates will be affected. But the molecule has no relative motion (apart from vibration and rotation, which are determined completely by the resonance used), so it connects to the ground state of the relative motion[32]. Other relative motion states do not adiabatically connect to the molecular state. See figure 11 for a diagram of what happens to the atomic states as the resonance is crossed.

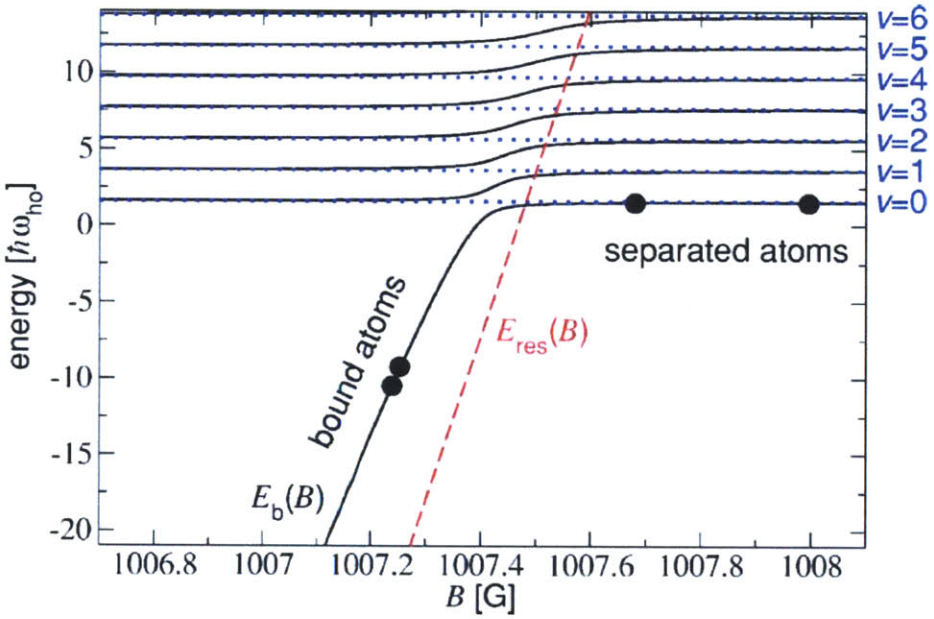

figure 11: Coupling of eigenstates of relative motion in a harmonic oscillator across a feshbach resonance. Image reproduced from Kohler et al, RMP 78, 1311 (2006).

If starting with two uncorrelated atoms in the harmonic oscillator at a finite temperature, the motion can be decomposed into COM and relative coordinates, and the particles will have a finite probability to be in the ground state of relative motion, and

therefore can still adiabatically connect to the molecular state, but with reduced efficiency. The higher the temperature, the smaller the ground state component of the wavefunction, and the smaller the probability to form molecules. Rather than following this idealized system to exact solutions, I will instead refer to a paper by Shohei Watabe and Tetsuro Nikuni[122], which studies a situation more applicable to experiments.

The authors perform thermodynamic calculations of uniform density atomic and molecular systems, calculating the entropy at varying magnetic fields and finite initial temperature. By assuming perfectly adiabatic sweeps, they calculate the maximum formation efficiency of molecules by connecting states of equal entropy across the Feshbach resonance. They apply the method to Bose-Bose, Bose-Fermi, and Fermi-Fermi mixtures with various population imbalances. As expected, molecule formation efficiency is optimum for zero temperature and drops as temperature increases. Not surprisingly, the result does not take a simple analytic form. See figure 12 for a few results from their paper applied to Bose-Fermi mixtures.

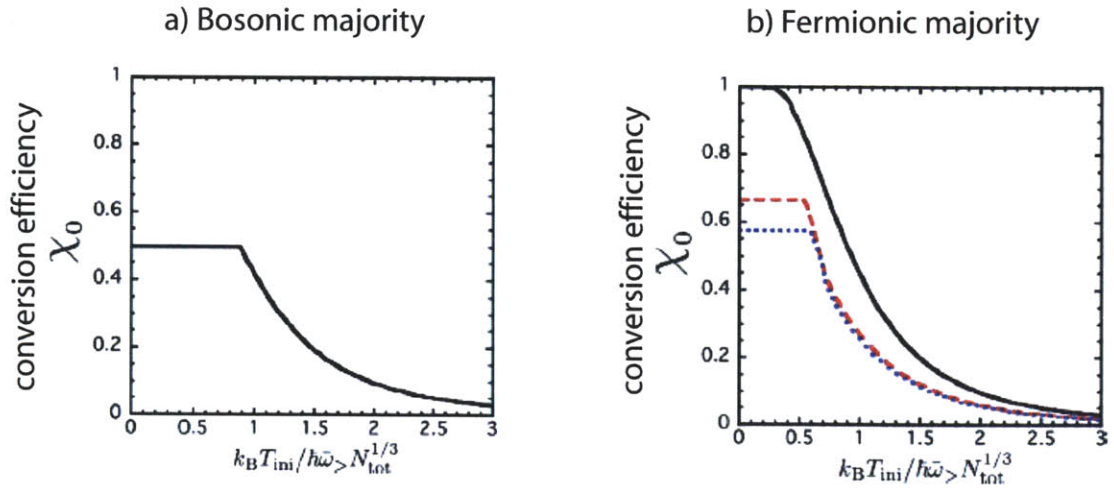

figure 12: Maximum adiabatic molecule formation efficiency (defined as the ratio of molecules to minority atoms) for Bose-Fermi mixtures at finite temperature. In a), the ratio of bosons to fermions is 15:2, in b), it is 2:15 (solid line), 3:4 (dashed line) or 13:15 (dotted line). Note that the x axes are similar to reduced temperatures T/T_f or T/T_c. Figures reproduced from Watabe and Nikuni, PRA 77, 013616 (2008).

These figures show two things of interest. One, is that molecule formation can be maximized (relative to minority atom number) by having more fermions than bosons. The authors suggest this occurs because a boson majority gas will always have a finite condensation temperature, stimulating bosons to join the condensate rather than form molecules, while a fermion majority gas can pair all the bosons into molecules, eliminating the possibility of a condensate.

Second, the molecule formation efficiency is relatively constant at low temperature, but falls off above a specific temperature. The x axis is very similar to reduced temperature, because T_f or Tc are proportional to $\hbar\omega N^{1/3}$, so it can be

considered a function of phase space density. The temperature where the conversion efficiency plateaus is near Tc for boson majority and near $T/T_f = 0.5$ for fermion majority.

The theoretical results give fair agreement with experiments[23,123], apart from fudge factors which could be justified because of non-adiabatic sweeps or losses. In our experiments, we generally use nearly balanced mixtures, as it is hard to have stable ratios of Na and Li with large imbalance. For sake of producing a simple analytic formula to analyze experimental efforts, I propose the function:

51 $$\chi_a \equiv \left\{ \begin{array}{ll} \dfrac{T_f^{3/2}}{8\,T^{3/2}} & for \quad T > 0.5\,T_f \\ 0.5 & for \quad T < 0.5\,T_f \end{array} \right\}$$

I give no justification for this particular function other than rough agreement with figure 12, and the fact that it's proportional to phase space density, which has an intuitive appeal. Because the authors did not present a plot for boson to fermion ratio of 1:1, I assume the trend of zero temperature χ_0 would continue and the balanced mixture would have approximately 50% efficiency. The $1/T^{3/2}$ dependence seems to agree rather well with the figure over the temperature range provided (note that $T = T_f$ occurs around 1.4 for the dotted line in the figure).

3.4.2 Landau-Zener formula for non-adiabatic formation

To analyze fast ramps which are not adiabatic, we return to the idealized two level problem. Starting with the Hamiltonian:

52 $$\begin{bmatrix} -\Delta E/2 & \hbar V' \\ \hbar V' & +\Delta E/2 \end{bmatrix}$$

and allowing ΔE to vary with time, the solutions for linear ramps of speed d(ΔE)/dt across resonance are exactly solvable. The formula for the probability of making the transition to the other basis state is the well known Landau-Zener formula:

53 $$P_{transfer} = 1 - \exp[\frac{-2\pi\hbar V'^2}{|\dot{E}|}]$$

which is valid for any 2-level Hamiltonian.

This formula has been applied to Feshbach association between two zero temperature atoms in a harmonic oscillator[24,118,124], where they found

54 $$\delta_{LZ} = \frac{\sqrt{6}\hbar}{\pi m a_{ho}^3}\left|\frac{a_{bg}\Delta\mu\Delta B}{\Delta\mu\dot{B}}\right|$$

Note that this formula depends only on experimentally relevant quantities mass, scattering length, and ΔB. Also, the numerator is proportional to the energy scale of single channel coupling, which makes intuitive sense.

Equation 51 assumes two distinguishable particles at zero temperature in a harmonic well. The authors extend the analysis to N particles at uniform density in a volume V for fast sweeps (very low formation efficiency so the probability remains linear with $\dot{B}$) and different quantum statistics. Quoting their results applicable to distinguishable particles:

55 $$N_{mol} = 2\pi N_1 N_2 \frac{4\pi\hbar}{mV}\left|\frac{a_{bg}\Delta B}{\dot{B}}\right|$$

By replacing N/V with local particle density n

$$56 \qquad n_{mol} = 2\pi n_1 n_2 \frac{4\pi\hbar}{m}\left|\frac{a_{bg}\Delta B}{\dot{B}}\right|$$

we can apply these formulas to experimental circumstances.

It is worth pointing out that the constant 4π in equation 56 has not been observed to accurately match experiments, and experiments which apply this formula often choose a different constant which matches the data[23,27,123]. In our own experiments, we were to able to find reasonable agreement with data from two NaLi, one Li_2 and one Na_2 resonance by using the constant 0.31 instead of 4π, although the other experiments reported used other constants. There is currently no good explanation for this in the literature or consistent agreement over the ideal value of this constant[31]. However, the general dependence on density and resonance parameters has been observed in those experiments which apply the formula.

These linear formulas could be extended to slow sweeps by simply using them as the argument of the function 1-exp[x]. This would cause formation efficiency to approach 1 rather than increasing without bound, and is the obvious extension to recover a formula more similar to the standard Landau-Zener result. However, the results of section 3.4.1 showed that even at zero temperature formation efficiency won't necessarily approach unity, so we need to incorporate those results as well for a realistic formula.

3.4.3 Combined formula for non-adiabatic, finite temperature sweeps

The formulas of section 3.4.2 still assume zero-temperature gases. However, they are all related to two-body processes, for which temperature is irrelevant apart from determining the probability distribution of relative kinetic energy of the two-particles. But we already considered the effects of finite temperature in Section 3.4.1. Invoking the intuitive notion that molecules will form if and only if an atom encounters a zero-energy collision partner, we present the following hypothesis:

For fast sweeps in finite temperature gases, every pair of potential molecular components have an independent probability to form a molecule. This probability is the product of the probability of the pair to form molecules under adiabatic sweeps χ_a and the Landau-Zener probability that a non-adiabatic sweep results in a transition to the molecular state. For nearly balanced Bose-Fermi mixtures, the function:

57 $$n_{mol} = n_{minority} \frac{T_f^{3/2}}{8\,T^{3/2}} \left(1 - \exp 2\pi \left[\alpha\, n_{majority} \frac{\hbar}{m} \left| \frac{a_{bg}\,\Delta B}{\dot{B}} \right| \right]\right)$$

should give a reasonable estimate of molecule formation. Note that the T dependence applies only at temperatures larger than 0.5 T_f; below that temperature, the formation is constant.

This hypothesis assumes that the small fraction of atoms which form molecules does not affect further molecule associations (an assumption already implicit in the many particle extension of equations 55 and 56), that association at finite energy (which necessarily occurs in the analysis of section 3.4.1), is reduced by a Landau-Zener like

formula in the same way as zero-energy collisions, and that many body collisions can be ignored.

All of these assumptions will be violated to some degree in a real experiment. However, the real advantage of equation 57 is that it requires neither of the experimentally unfeasible situations that the sweep be adiabatic or the gas be highly degenerate, but agrees with the appropriate theories in the appropriate limits.

3.4.4 Application to NaLi experiments

The preceding analysis suggests that molecule formation will be maximized by minimizing temperature, and predicts the optimum balance for a specific mass ratio and quantum statistics of the pairing partners. It provides solid theoretical footing for the intuitive notion that molecules will only form if they can find an appropriate partner to meet in a low energy collision.

However, it assumes completely adiabatic sweeps, which are rarely useful in practice. Near resonance, fast inelastic collisions lead to vibrational quenching of the molecules. Therefore the field must be swept quickly through resonance, reducing the formation efficiency but ensuring that a large fraction of the formed molecules can survive the sweep. This was readily observed in Na_2 gases[25], where maximum formation efficiency was achieved at sweeps much too fast to be adiabatic. This effect will be considered in the next section.

One exception to this rule is in 2-state Fermi mixtures, such as Li-6[13,110]. This

occurs because the third atom would be in the same state as one of the constituents of the molecule (at least when they are well separated and still resemble free atoms), but the collisional wavefunction must be antisymmetric and has low probability to reach the short collision ranges necessary for inelastic collisions. Combined with the very wide resonance in Li-6, near adiabatic formation occurred readily, even to the point that it was difficult to ramp across resonance without forming molecules[100].

For inhomogeneous trapped mixtures of Li-6 and Na-23, another effect must be considered. If the temperature drops below T_c, Na atoms will Bose-condense. The condensed part of the cloud will be much smaller and denser than the Li cloud, while the thermal cloud will become more and more dilute as atoms move into the condensate. Furthermore, gravitational sag will pull the condensate away from the trap center, so the densest part of the Na cloud has poor spatial overlap with the densest part of the Li cloud. In RbK mixtures, these effects resulted in poor empirical formation efficiency when the temperature dropped below T_c[125].

Inelastic collisions and realistic association experiments will be addressed in Chapters 6 and 7 when the formulas from this chapter are applied to our experiments with ultracold Na and Li.

4

Experimental Apparatus for Ultracold Molecules

4.1 Ultracold atomic physics in the science chamber

The methods of producing and studying ultracold atoms represent decades of impressive scientific endeavors, astounding theoretical and experimental creativity, and uncountable hours of graduate student labor. Many excellent review papers and Ph.D theses[74,75,78,79,100,126] offer detailed blueprints and histories of ultracold physics. Rather than presenting another review here, I will concentrate on the specific technical demands of cooling multiple atomic species, studying Feshbach resonances, and creating ultracold samples of molecules.

The studies of Na and Li presented in this thesis took place in Rm. 26-248B at MIT, a laboratory affectionately named "the Science Chamber", or less colorfully, BEC3. The thesis of Ananth Chikkatur[127] presents the most comprehensive account of the design and construction of the apparatus in 2001 and 2002, and the theses of Aaron

Leanhardt, Yong-Il Shin, Tom Pasquini, and Gyu-boong Jo describe subsequent experiments and modifications that have made the Science Chamber the machine it is today[128-131].

The Science Chamber, illustrated in figure 13, consists of several ultra-high vacuum chambers making up the oven, the slower, the main chamber, and the science chamber. The oven produces the hot atomic vapor and the Zeeman slower cools the atoms so they can be initially trapped. The main chamber has many windows and magnetic coils packed very close to the atoms, where the atoms are cooled in a magneto-optical trap and then magnetically trapped for further cooling and experiments. We can direct imaging beams and optical dipole traps from many directions into the main chamber, but for better optical access or unique experiments, the atoms can be transferred via an optical tweezers[132] to the science chamber, which has been used for projects ranging from extremely weak single-coil magnetic traps[42,133], to micro fabricated chip traps used to load atoms into a hollow-core optical fiber[134-136]. The Science chamber is designed to be easily replaced without affecting the rest of the machine. The ability to readily modify the apparatus in major ways has encouraged the Science Chamber to pursue experiments with uncertain but potentially exciting outcomes that would discourage investing the years and dollars required to build a dedicated apparatus.

The lab contains two optical tables for generating laser light for sodium and lithium, computers for orchestrating the many electrical devices controlling the experiment, the cameras used for collected images of the atoms and dedicated PCs for analyzing the images. Every corner of the room is filled with power supplies of all shapes and sizes and countless electronic devices, both commercial and custom-built.

The experiment is controlled by the word generator software written by Aviv Keshet consisting of the Atticus hardware server and the Cicero user interface to create precisely timed procedures with dozens of independent analog and digital control channels.

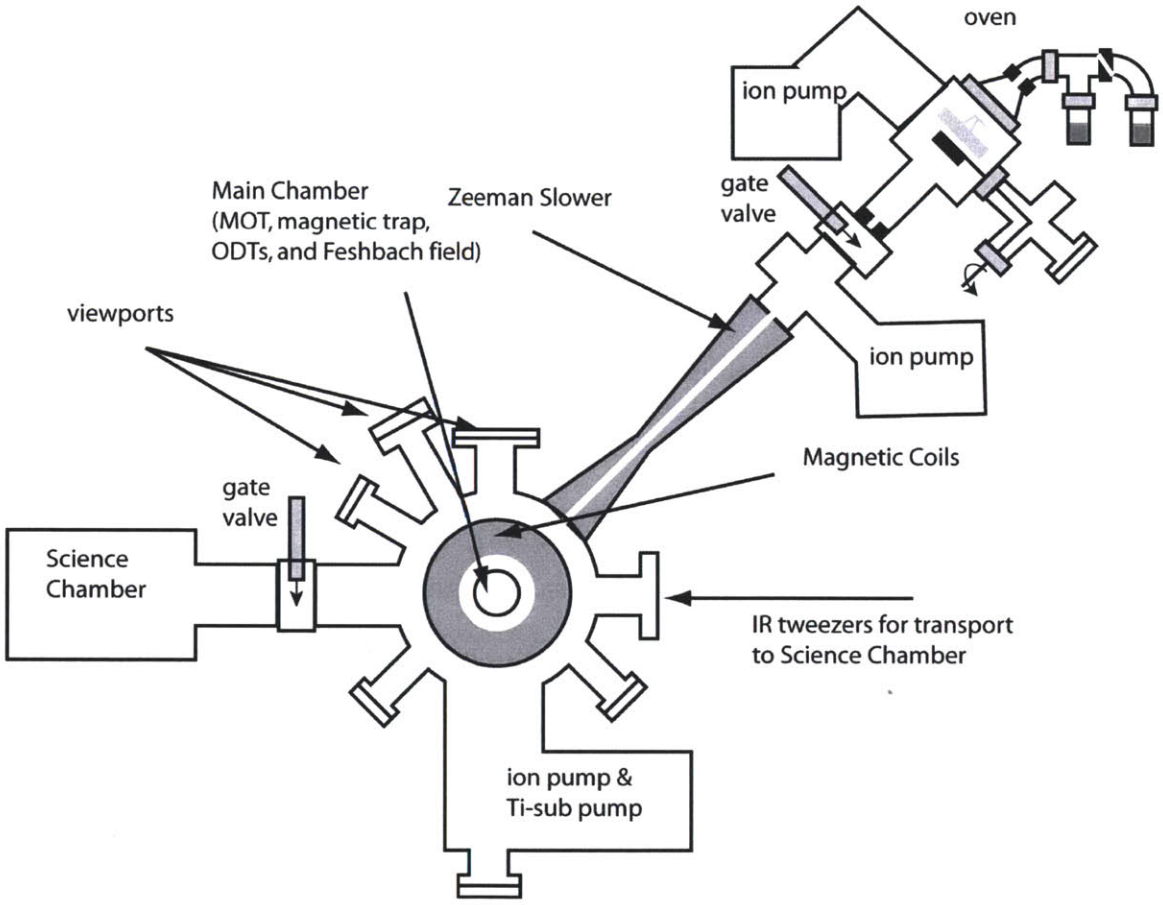

figure 13: The BEC3 apparatus. The diagram is neither to scale or complete, but rather gives an overview of the functional elements mentioned in this chapter

The science chamber was originally designed to use sodium only. When we decided to modify the apparatus to use lithium as well, we needed to make the

necessary changes to give adequate performance with both species without disrupting the working machine more than necessary. Luckily, BEC1 and BEC2 (located in rooms adjoining the Science Chamber) were sodium machines already modified to incorporate lithium, so we had good examples to work from[137]. However, every lab presents unique challenges to overcome and opportunities to improve on previous designs, so I will briefly describe the particular changes which were necessary to incorporate lithium into the Science Chamber.

4.1.1 Slowing atomic beams

The Science Chamber produces a collimated beam of atoms from a heated oven which melts and evaporates masses of pure alkali metal. The oven temperature and geometry of the nozzle and collimating apertures must be chosen to produce a sufficient flux of hot atoms needed for the experiment without consuming alkali faster than necessary[138,139]. Because the experiment takes place under ultra-high vacuum conditions, which requires long periods of baking and pumping out residual gases, the oven must be designed for minimal maintenance. It should be easy to replenish the reservoir of alkali, and accumulations of atoms should be easy to clean and should not cause permanent damage to any vacuum components.

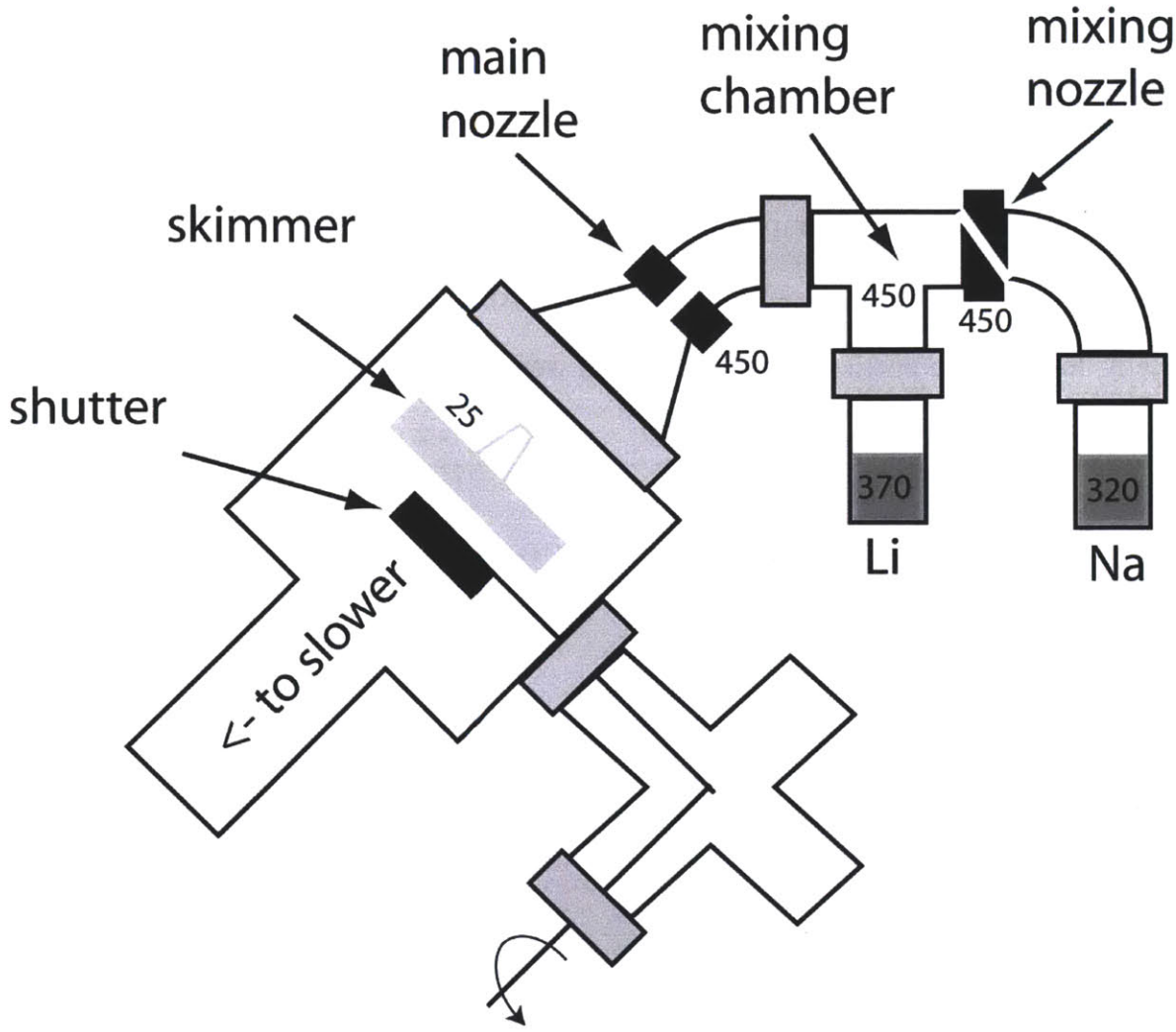

figure 14: Dual-species oven. Numbers indicate temperature, in celcius. The mixing nozzle allows reduced Na pressure to enter the mixing chamber, where it matches the lower Li pressure. Beams of both atoms exit through the main nozzle and are collimated by the skimmer.

Through years of trial and error, a reliable oven design for sodium was developed for our group's BEC machines[139]. Modifying the oven for Li presented two particular

challenges.

First, the vapor pressure of Li is much lower than the vapor pressure of sodium at a given temperature, preventing us from using a single oven chamber to heat both atoms. A temperature high enough to give good Li flux would evaporate all of the sodium within 10 hours[140], and the normal Na operating temperature of 250 C would barely even melt the Li. This problem was solved by using a separate chamber for each species with an mixing nozzle in between the chambers, as shown in figure 14. The mixing nozzle restricts the flow of Na from the oven but not Li. This allowed balancing the flux of the two species while reducing the temperature gradient required between the two reservoirs.

A second challenge is the tendency of Li vapor to adversely interact with vacuum components, especially glass windows. This property had already been observed in BEC1, where they learned the hard way that windows become irreversibly opaque when bombarded with lithium. The fact that baking didn't reverse the process suggests that the Li diffuses into or chemically reacts with the glass. Although the problem can't be fixed, it can be largely prevented by heating all susceptible windows to 100 C.

The atomic beams are brought from thermal velocities of 1000 m/s down to 30 m/s with a Zeeman slower[75]. In a Zeeman slower, a changing magnetic field keeps the atoms in resonance with an intense counter-propagating laser beam as thousands of photon collisions slow the atoms down one recoil velocity (~5cm/sec) at a time. The proper length and geometry of the slower coils is different for every atom, but luckily a slower optimized for Na works rather well for Li[137,138].

Many decisions during the modification favored sodium over lithium. The reason

for this ultimately comes from the quantum statistics of the two species. Na-23, a boson, has a finite collision rate down to zero temperature, due to the symmetry of s-wave collisions discussed in Chapter 3. Li-6, a fermion, can only collide with P-wave collisions, so thermalization and evaporation become impossible as all collisions and relaxation processes freeze out. This means that sodium can be evaporatively cooled to reach ultracold temperatures, but lithium simply cools by remaining in equilibrium with sodium. This sympathetic cooling requires much more sodium atoms than lithium atoms, even if balanced ultracold mixtures are desired in the end. In practice, we often intentionally reduce the amount of lithium in order to reduce the heat load, but we always work diligently to maximize the amount of sodium that can be cooled and trapped.

Some recent experiments have used only Li-6, prepared in a mixture of spin states with collisions enhanced by a Feshbach resonance[106]. This allows evaporative cooling because the different spin states are distinguishable and have no restrictions on allowed partial-waves, and Feshbach enhanced elastic collisions allow for efficient evaporation of the atoms. This method requires a deep, large volume optical trap, as the useful Li states are not magnetically trappable and must be held at very high magnetic field during evaporation.

4.1.2 Dual magneto-optical traps

Another complication of a two species machine is the need to produce

simultaneous magneto-optical traps (hereafter referred to as MOTs). A MOT requires 6 carefully aligned lasers converging on the center of a magnetic quadrupole field. The cooling lasers are tuned to just below resonance so that only atoms with shifted resonance frequency will scatter photons. This occurs if atoms are moving with thermal velocity into the laser beams (and giving a Doppler shift) or if they drift away from the trap center (where the magnetic field Zeeman shifts the atoms). The atoms are pushed into a dense, cold cloud at the center of the trap, where they minimize scattering from the MOT lasers[70].

The frequency and polarization of the cooling lasers must be optimized, and repumping beams at different frequencies must optically pump atoms which decay into other hyperfine levels of the ground state. In addition, the Zeeman slower laser requires repumping, and imaging and state preparation of the atoms requires additional laser frequencies which depend on magnetic field and quantum state[75]. In the end, a typical laser cooling experiment requires 5-10 distinct lasers with stable frequency, power, and polarization converging on a target a few millimeters in diameter at the center of a UHV chamber packed with magnetic coils. Not only must this be repeated for the second species, but it must be done with limited optical access and commercially available optical elements.

If the two species used are two isotopes of the same element, the light can be produced and manipulated with the same devices (possibly even the same laser, depending on the circumstances), and any optical components that work for one species will work for the other. With sodium requiring a 1 watt 589 nm dye laser and lithium requiring a grating stabilized 671 nm diode laser with amplifier stages to produce 400

mW, we had to design and operate two completely different laser systems, each with it's own unique challenges. See Yong-il Shin's Ph.D thesis for a layout of the Na table[129], and Appendix A for a layout of the Li table. Also, many optical components (particularly wave plates and single mode optical fibers) have significantly different performance at 671 nm than at 589 nm. The laser wavelengths are far enough apart to separate and combine beams with dichroic beam-splitters. These can be custom ordered from CVI; for example; we ordered long wave pass beamsplitters which, at 45 degree incidence, reflect S-polarized 589 nm and transmit P polarized 671 nm. However, a single type of optic cannot perfectly separate arbitrary polarizations of 589 nm and 671 nm, so beams must be polarized and optics selected carefully to meet the design goals.

One final complication of a two species experiment is the interspecies collisional properties. Collisions in ultracold mixtures of alkali gases were not well known prior to the first attempts at multi-species experiments, and required some trial and error and some luck. Na and Li turn out to be particularly cooperative, with a good ratio of elastic to inelastic collisions in the appropriate quantum states[41]. However, strong photo-assisted collisions in the excited states of the atoms have an effect on MOT performance, requiring the MOTs to be slightly misaligned to avoid too much overlap in the clouds while maintaining good magnetic trap loading of each species[141].

4.1.3 Quantum states of Na and Li

The hyperfine energies of Na and Li in their ground states is shown in figure 22.

Li-6 has nuclear spin I = 1, Na-23 has nuclear spin I = 3/2, and both atoms have one unpaired electron. In the ground states with L = 0, the total angular momentum is then F = 1/2 or 3/2 for Li and F = 1 or 2 for Na. At low field, the electron and nuclear spins couple and the largest energy splitting is the hyperfine splitting between states with different values of F, and the projection m_f along the magnetic field determines the magnetic moment and low field Zeeman shift. States can be labeled by $|S\,I\,F\,m_f\rangle$.

At the magnetic fields of interest (around 1000 G), the nuclear and electron spins align independently to the B-field, so atomic hyperfine states can be described by quantum numbers $|S\,m_s\,I\,m_i\rangle_{Na}$ and $|S\,m_s\,I\,m_i\rangle_{Li}$. The magnetic moment and the major energy splittings are determined by the electron spin, with small additional splittings determined by the nuclear spin.

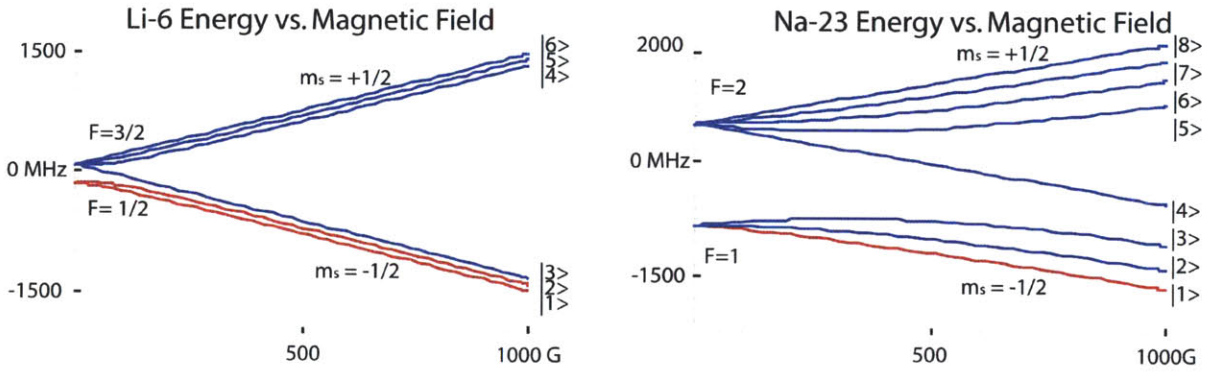

figure 15: Hyperfine States of Na and Li. Although the good quantum numbers change from low field to high field as described in the text, we unambiguously label the states from 1-6 (1-8) for Li (Na), starting at the lowest energy state and moving up. The states indicated in red are the ones used for Feshbach science.

For brevity and clarity, for the rest of this thesis the states will be labeled with a single number in order of increasing energy as illustrated in figure 15. This number refers to a clear state at low field or at high field, and an atom prepared in state 1 will remain in state 1 as the magnetic field is ramped up and down. Therefore, to describe the lowest hyperfine state of Na and the second lowest hyperfine state of Li, we will write $|1\rangle_{Na}$ and $|2\rangle_{Li}$, or simply $|1\,2\rangle$, always listing the Na quantum number first.

In the molecule, the indistinguishable electrons form triplet or singlet configurations, but nuclear hyperfine states remain coupled independently to the field, so molecular hyperfine states are described by $|S\, m_s I_{Na} m_{i,Na} I_{Li} m_{i,Li}\rangle$ where S = 0 for singlet or 1 for triplet states.

The singlet and triplet states correspond to completely different electronic curves, but the three projections m_s = 0, ±1 of the triplet state are simply shifted by the Zeeman energy. Electron spin magnetic moments are 1 μ_b = 1.4 MHz/G giving splitting of order 1 GHz at the magnetic fields of interest. The nuclear magnetic moments provide additional splittings (with energies of order 100 MHz), and coupling occurs if different states with the same total $m_f = m_s + m_{i,Li} + m_{i,Na}$ cross.

For experimental reasons, we use Li and Na atoms in the $|1\rangle_{Na}$, $|1\rangle_{Li}$, or $|2\rangle_{Li}$ states at fields of several hundred Gauss. These states adiabatically connect to the ms = -1 triplet manifold because both electron magnetic moments (anti-parallel to the spin angular momentum) are aligned with the magnetic field. The Feshbach resonances used occur at fields around 800 G and 1600 G, where this state crosses bound vibrational states in the ms = +1 triplet and most likely the ms = 0 singlet potential[2].

2 The 1600 G resonance was only observed in the last few months in our lab, and it was not exactly in

Further resonances are predicted at a variety of fields[4,5], but they have not been extensively studied because of fast inelastic decay of the atomic states or difficulty in attaining the required magnetic fields.

4.1.4 State preparation and evaporation of Na and Li

Once laser-cooled clouds of Na and Li are obtained, they have to be prepared in the correct states, evaporatively cooled, and transferred to states appropriate for the goals of the experiment. Previous experiments[41], had identified the procedures necessary to achieve good numbers, so we were able to follow their example.

Na-23 and Li-6 have the best collisional properties in the stretched states |86>. However, the sodium dark-spot MOT[142] produces 99% F=1 atoms ($|1\rangle_{Na}$, $|2\rangle_{Na}$, and $|3\rangle_{Na}$ states), and the Li MOT produces atoms distributed among all ground hyperfine states. The first step in obtaining pure clouds of |86> is to optically pump the atoms released from the MOT, as shown in figure 16. Note that we do not pump out of unwanted F=2 Na hyperfine ground states; this is a decision reached after noting that the additional pumping beams produced no significant improvement in final BEC number.

---

the expected location of the singlet resonance, but the width seems to match the expectation. Further experimental or theoretical tests would be required to be absolutely certain of the molecular state involved.

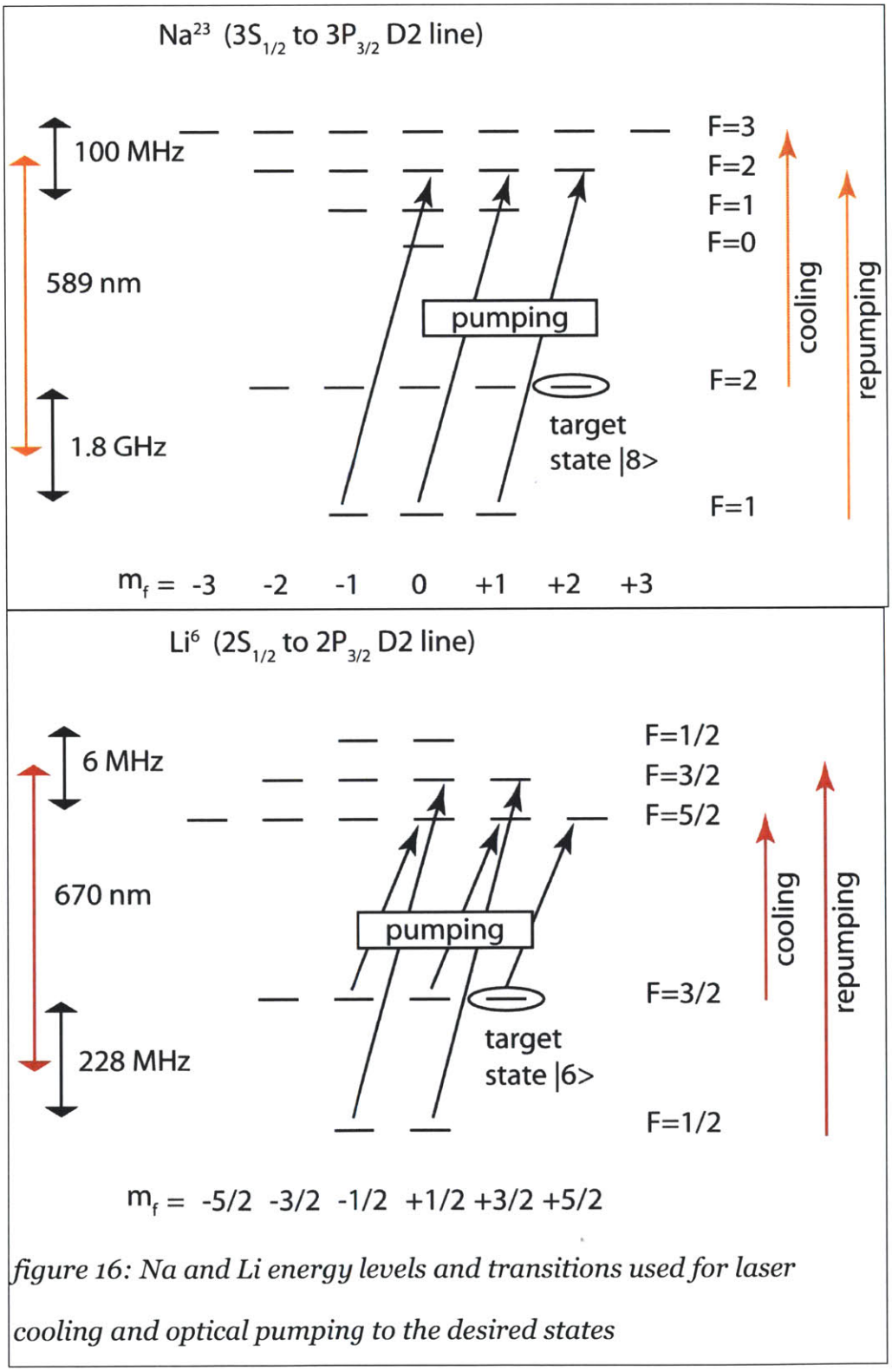

figure 16: Na and Li energy levels and transitions used for laser cooling and optical pumping to the desired states

The atoms are then caught in a Ioffe-Pritchard magnetic trap[121]. See Dan Stampur-Kurn's Ph.D. thesis[126] for an excellent explanation of the design and operation of this type of trap. The trap acts an a non-isotropic 3-D harmonic potential well, so atoms with magnetic moments anti-parallel to the local bias field (called weak-field seekers) are confined to the trap minimum. Once the optically pumped cloud from the MOT is loaded into the magnetic trap (by turning off the MOT lasers and turning on the IP trap before they escape), only the weak-field seekers remain. Any remaining atoms which are not in the desired state are removed with RF transitions to untrapped states.

The atoms are then evaporated by driving microwave transitions between the sodium $|8\rangle$ state to the anti-trapped $|1\rangle$ state. By tuning the microwave frequency so that only the most energetic atoms undergo spin flips (since only they can explore the highest magnetic fields at the edge of the trap), the high-energy atoms are selectively removed from the trap and the remaining atoms thermalize to lower temperatures[74]. The microwave frequency is gradually ramped downwards until the desired temperature is reached.

The previously described procedures allow us to produce MOTs containing around 10^{10} sodium atoms and 10^8 Li atoms. It is possible to optically pump and load the atoms into the magnetic trap with about 30% efficiency. During evaporation, sodium number drops by orders of magnitude while Li number is approximately conserved. In the end, we can trap 10^7 atoms of either species at temperatures below 1 μK at a density of 10^{13} cm^{-3}. This is cold enough for quantum degeneracy of either

species, although in our recent experiments we do not study degenerate gases in the magnetic trap.

4.1.5 Optical dipole traps

The target Feshbach resonances are between the states $|1\rangle_{Na}$ and $|1\rangle_{Li}$, which are strong-field seekers and can't be magnetically trapped, because a local magnetic field maximum is not allowed by Maxwell's equations. Also, it requires impractically large electric currents to produce tight magnetic traps at high bias fields. Therefore, an optical dipole trap (hereafter referred to as an ODT) is necessary to hold the mixtures while producing the required magnetic fields.

An ODT traps the atoms due to the AC stark shift[75]. A far detuned laser with frequency lower than the resonance frequency is brought to a tight focus, and the sign of the stark shift lowers the atoms energy. Since the magnitude of the shift is proportional to intensity, atoms will converge at the focus of the laser. The trap parameters for a Gaussian beam are obtained from

58 $$\Delta E_{Stark} = \frac{-\hbar \Omega_R^2}{4\delta} = \frac{-\hbar \Gamma^2}{8\delta I_s} I_0 e^{-r^2/w_0^2}$$

59 $$F = \nabla(\Delta E) = \frac{\hbar \Gamma^2 I_0}{r \delta I_s} r/w_0^2 e^{-r^2/w_0^2}$$

The trap depth is obtained from the maximum stark shift at r=0, and trap frequencies by identifying $\partial F/\partial r$ at r=0 as a spring constant.

Note that the above formulas invoke the rotating wave approximation, which is

not entirely valid for far detuned light. A full quantum treatment would give exact results, but the relative importance of the counter-rotating terms is equal to $(\omega_a-\omega_l)/(\omega_a+\omega_l)$, where the frequencies are the laser frequency and atomic frequency. For 1064 nm trapping light, we can multiply the results of equations 58 and 59 by 1.23 for Li and 1.29 for Na to account for this approximation.

The beam profile changes along the direction of beam propagation by simply changing the waist as

60 $$w(z)=w_0\sqrt{1+(\frac{z}{z_R})^2},\quad z_r=\pi w_0^2/\lambda$$

By using several watts of 1064 nm light brought to a focus between 30 and 100 μm, we can obtain ODTs with up to 10 μK depth for both species. The different beam sizes allow for trap frequencies ranging from 100 Hz to 2 KHz. The axial trapping is much weaker (with trapping frequencies of a few Hz), so we usually arrange that there is a small amount of appropriate magnetic field curvature to trap the atoms axially with frequencies of 10 to 50 Hz.

We use an IPG 30W 1064 fiber laser (IPG YLR-30-1064-LP-SF), to provide light for the ODTs. It is single frequency and single mode which is important for possible use in optical lattices. However, we have encountered several issues with failure of electrical components. This is possibly due to the fact that we purchased it shortly after the model became available, as IPG lasers purchased later by other labs seem to perform admirably. However, it does provide a lesson in cutting edge technology; if you don't want downtime troubleshooting and repairing devices, don't buy the newest model unless absolutely necessary.

4.1.6 Density distributions and imaging

The |11> states of sodium and lithium have similar magnetic moments (both near -1.4 MHz/G = -1 μ_b), and similar response to 1064 light:

61 $$\Gamma^2/\delta I_s = 3.48\,Hz/(mW/cm^2)_{Na}\ vs\ 3.91\,Hz/(mW/cm^2)_{Li}$$ (accounts for RWA)

so the magnetic and optical fields provide similar potentials for both atoms. This means that for thermal clouds with equal atom number and temperature, the ideal gas in-trap density distributions:

62 $$n_{th}(\vec{r}) = \frac{N}{(2\pi)^3/2\,\sigma_x\sigma_y\sigma_z} e^{-x_i^2/2\sigma_i^2};\ \ \sigma_i^2 = \frac{k_b T}{m\omega_i^2}$$

are very similar, since $m\omega^2 = k$, so thermal width σ_i is independent of mass. This is expected, as the thermal width is determined by balancing thermal energy with potential energy, which depends on fields, polarizability, and magnetic moment. As the temperatures approach quantum degeneracy the differences in quantum statistics and interactions will eliminate this symmetry. Also, trap frequencies simply scale with the mass ratio, so lithium trap frequencies are approximately $\sqrt{23/6} \approx 2$ times higher than sodium trap frequencies. After considering the exact mass ratio, magnetic moment, and polarizability, the high-field trap frequencies satisfy

63 $$\frac{\omega_{mag}^{Li}}{\omega_{mag}^{Na}} = 1.96\ ;\ \ \frac{\omega_{1064}^{Li}}{\omega_{1064}^{Na}} = 2.06$$

One significant effect of having different trap frequencies is gravitational sag, which pulls the center-of-mass of the cloud away from the potential minimum. By

adding the force of gravity to the vertical harmonic potential:

64 $$V=\frac{1}{2}m\omega_z^2 z^2+mgz=\frac{1}{2}m(\omega_z z+\frac{g}{\omega_z})^2-(\frac{g}{\omega_z})^2 \rightarrow \frac{1}{2}m\omega_z^2(z+\frac{g}{\omega_z^2})$$

which, after dropping a constant term, is a vertically shifted harmonic potential with the same frequency. The shift of g/ω^2 will be different for the two species of atoms.

The smallest radial trap frequencies we use in the ODTs are 100 (200) Hz or higher for sodium (lithium), so the sodium clouds sag by up to 25 μm, and are offset from the Li clouds which sag less (up to 7 μm). Because typical diameters of clouds in a trap with these frequencies are 60 microns or more, the clouds stay overlapped to a large degree. However, if sodium is allowed to condense into a BEC, the poor overlap of density profiles could be significant. For this reason, we generally keep the temperature of the clouds close to, but just above, Tc.

The different masses of Na and Li mean that in order to reduce density to a level appropriate for absorption imaging, the two species require different amounts of expansion time, and the analysis of time of flight images requires appropriate algorithms. If both species are above degeneracy temperatures (T_c or T_f), both clouds will have a Gaussian profile, with temperature given by.

65 $$k_B T=\frac{m}{2}(\sigma(t)/t_{of})^2$$

Absorption images involve taking at least 3 images: one with atoms present, one with no atoms present, and one without any laser illumination to account for background light and dark counts on the CCD. The intensity of light measured at each pixel can be used to obtain the transmission profile

66 $$T(x,y)=\frac{probe\ with\ atoms-dark\ count}{probe\ without\ atoms-dark\ count}$$

which gives the fraction of light which is transmitted through the cloud of atoms at each pixel. This fraction is determined by the integrated optical density, giving a measure of the number of atoms in a column with cross section equal to the pixel area. The actual numbers of atoms in each pixel is given by

67 $$N(x,y)=\frac{pixel\ \text{size}*magnification}{\sigma_{photon}}[-\ln T(x,y)]$$

where σ_{photon} is the cross section for photon absorption (references). For photons with perfect polarization and exactly resonant frequency driving a cycling transitions (where the excited state has nonzero Clebsch-Gordon coefficients with only one ground state), $\sigma_{photon} = 6\pi/k^2$, but in practice this is generally reduced by 20% to 50%, and will be further reduced by the Clebsch-Gordon coefficient for non-cycling transitions[75].

If the temperatures drop below degeneracy (which occurs at $T_f=1.8\bar{\omega}N^{1/3}$ or $T_c=0.94\bar{\omega}N^{1/3}$, the profiles will change to the finite temperature degenerate Fermi gas or a bimodal profile of a BEC within a dilute thermal cloud[76].

Because of uncertainties in photon cross section and smaller uncertainties in trap frequency, several formulas should be used to check for consistency. In our experiment where the gases were above or only slightly below degeneracy temperature, a good consistency check was to find the point where degeneracy occurs and compare measured T (depends only on pixel size), to Tc (which depends on total number and trap frequency).

To obtain good mixtures of Na and Li atoms, we stop RF evaporation when the

temperature in the magnetic trap is around 10 μK, and we still have a large number of both species of atoms. We then adiabatically ramp the ODT up to full intensity and ramp down the magnetic trap. The ODT intensity is then lowered, evaporating atoms to lower temperatures. Typically, this leaves us with around 10^6 atoms of each species at temperatures around 1 μK and densities of at least 10^{12} atoms/cm^3.

From day to day, the relative size of the MOT clouds change, so we often adjust our loading procedure to keep a properly balanced mixture of roughly equal numbers of atoms. We have found that the best way to reliably change the relative balance of atoms in the ODT is to let the MOT of one species reach equilibrium alone (typically taking 3 seconds for sodium or 8 seconds for lithium) before loading the other MOT for a variable time. Another option is to make small changes to the evaporation time or final RF frequency to evaporate more (or less) sodium in exchange for lower (or higher) temperatures, which increases (decreases) the amount of Li loaded into the ODT.

4.2 RF techniques for preparation and study of Feshbach resonances

Once the nearly degenerate mixture is obtained in the ODT, we use RF and microwaves to transfer the atoms to the desired states. At low field, this requires 1.8 GHz for the sodium transition and 228 MHz for the lithium transition (appropriately tuned to match the magnetic field, of course). In order to avoid possible 2-body losses, the sodium should make the transition first, because $|81\rangle \rightarrow |16\rangle$ is energetically

allowed but $|18\rangle \rightarrow |61\rangle$ is not. The frequencies are held constant while the magnetic field is ramped, allowing adiabatic Landau-Zener transfer between the states. Changing the RF frequency is equivalent, as long as the frequency step size is smaller than the Rabi frequency, but in practice it is more complicated to control simultaneous RF sweeps. The Na and Li frequencies cannot use the same synthesizers, amplifiers, or antennas, so we have independent RF systems for low frequency (1-500 MHz), and high frequency (up to 2 GHz).

The Science chamber was originally designed to study F=1 Na condensates at low field, where the spin flips required ($|3\rangle \rightarrow |1\rangle$) were at frequencies of 30 MHz and lower[127,128]. An internal antenna was built for this purpose when the chamber was designed. This allowed efficient evaporating and state control using medium power (no more than 5W) RF amplifiers and standard RF components.

However, when we decided to work on Feshbach resonances in both Na and Li, we had to retro-fit the machine to drive transitions at a much wider variety of RF and microwave frequencies. This involved straightforward replacement of most components and signal generators, but the bigger problem turned out to be delivering the power to the chamber. The internal antenna works efficiently only up to 10 MHz, and then performance falls off noticeably.

Attempts to tune the antenna with external circuits failed to improve Rabi frequency, likely due to parasitic capacitance to short the high frequency RF past the antenna. Also, the electromagnetic wavelength even at 2 GHz is 15 cm, which is already larger than the view port dimensions (typically no more than 5 cm) in the stainless steel vacuum chamber, so waves can't be effectively radiated into the chamber from outside

sources.

4.2.1 High power RF amplifiers

The eventual solution turned out to be brute force. By using 100W RF amplifiers, we achieved up to 1 kHz Rabi frequencies for the 70 to 80 MHz hyperfine transitions in Li atoms. For high frequencies, we created a 6 cm loop antenna which rests inside a view port as close to the atoms as possible. We deliver frequencies below 100 MHz to the internal antenna. We then use broadband high-power amplifiers (Minicircuits ZHL-100W-52 (100W, 500 MHz) and Empower RF model 1107 (25 W 2.5 GHz)), which we have discovered are expensive, have long lead times when ordered, and are very easy to break.

Protecting high-power RF amplifiers has proven to be a very important part of operating the Science Chamber. Experience has revealed a few simple rules:

First, never have an amplifier running without sufficient cooling. Air cooling is probably good enough, but even with zero input or output power, a type A (common high power amps are type A) RF amplifier constantly draws and dissipates it's full electrical load. Either turn off amplifiers when not in use (in case of cooling failure), or use modular RF amps like those made by Empower that have built in temperature monitoring and protection.

Second, never exceed the rated input power. It is always tempting to crank up the signal generator or remove attenuators to try to improve transition rates, and the

amplifier will probably survive this a few times, but it will not last long when overdriven. Also, amplifiers are already nearly saturated at this input power, so the power gained by overdriving the amplifier will be minimal.

Third, make sure the amplifier has a load attached and is powered on before applying any input signal. The reason for the second and third rules is that high power amplifiers put out more than enough energy to fry their own internal components, and without operating the device cautiously, the extra energy can dissipate within the chassis rather than being transmitted down the line as intended.

These rules can also be extended to switches and power meters, which similarly have to dissipate RF energy to do their jobs. Good RF power meters are just as expensive and fragile as amplifiers, and equally important for working with RF and microwaves. RF switches are cheaper, but they are essential parts of any circuit and 9 times out of 10 are the cause of RF equipment malfunctions.

4.3 Precision control of high magnetic fields

4.3.1 High current hardware

The magnetic coils for our Ioffe-Pritchard traps were designed to handle hundreds of amps. This is was not specifically to provide large magnetic fields, but to create strong gradients and curvatures at the center of the vacuum chamber for tight magnetic traps. By wiring additional high current power supplies, we were able to use the original coil packages to produce high bias fields.

Using such large currents requires the proper electrical components. IGBTs and high power diodes are standard, although expensive, components for fast switching of large currents and protection of power supplies, but they must be implemented with care. When a large current is running through a large inductor, turning it off creates large voltage spikes (since $V = L\ dI\ /\ dt$). The more abrupt the attempted change, the larger the voltage spikes until the voltage can find a current path which can dissipate the energy.

One technique is to use a diode which is reverse-biased during normal operation, as in figure 17. The diode technique directs the current across a high-power resistor, which allows the current to ring down exponentially with time constant $\tau = LR$. If the ring-down path was not in place, the voltage spike of hundreds or thousands of volts would be applied across the wires, power supply and IGBT until something fails and allows the current to flow. The failing component could be the insulation of the coil package, the power supply, or an inquisitive grad student's body, all of which are expensive and time-consuming to replace.

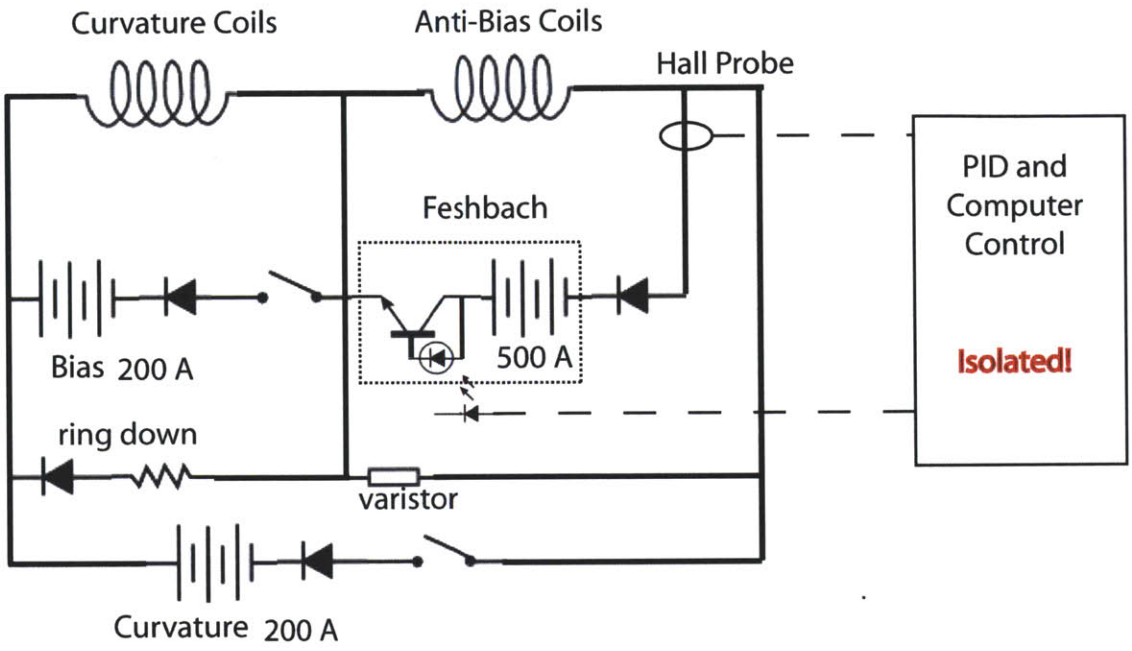

figure 17: High current circuitry for generating large, stable magnetic fields. Dashed lines indicated galvanic isolation which is essential for precision and safety

The diode technique won't work for the anti-bias coils, which need to allow current to flow both ways and ring down both ways. Because the diode/resistor path has higher resistance than the coils (typically a few ohms in the resistor vs. 0.1 ohm or less in the coil), two anti-parallel diode paths could be used to allow bi-directional ring down. However, one resistor will then continually conduct a few amps, requiring it to constantly dissipate tens of watts rather than just the infrequent energy pulse during ring-down. The amount of leakage current will also depend on resistor temperature and power supply voltage, affecting current stabilization.

A better solution is a varistor. A varistor can be interpreted as two diodes wired

back to back. Minimal current will flow until one diode undergoes reverse-breakdown, at which point current can flow freely. The physical construction of a varistor is actually a large number of tiny ceramic grains between electrode plates, the grains act like a vast array of randomly oriented diodes, giving the entire structure a predictable bi-directional breakdown voltage but high-current capabilities.

Upon reaching the threshold voltage V_t, the current flows through the varistor. Because of the non-linear relationship of current to voltage, the varistor voltage stays relatively constant near V_t, causing a linear ring-down of current instead of an exponential one. V_t should be selected to be safely higher than the operating voltage of the power supply (so it never allows leakage current to flow), but lower than the voltage at which the weakest component will fail.

The disadvantage of using varistors is that they have a finite lifetime. Varistors, typically used for emergency circuit protection, are rated by pulse energy; at the rated pulse energy, they may survive thousands of pulses. This is good for avoiding irregular power surges, but not for routine operation of a BEC machine, which can easily perform a few thousand runs in a busy week. By choosing varistors with much higher energy ratings than necessary, they can survive exponentially more pulses.

Alternatively, many varistors can be used in parallel, thereby sharing the energy load. However, as varistors degrade, the threshold voltage drops, causing the least healthy varistor to carry more and more of the energy load as its V_t drops further and further below that of its neighbors. Eventually it will catastrophically fail or conducts leakage current under normal operation (probably failing from overheating in the process).

The failure mode can be diagnosed by measuring the ring down time of the circuit, which rings down at a rate $dI/dt = V_t/L$. If V_t has changed significantly from the value when the varistors were new, they should be replaced. In our lab we use 10 Raychem ROV20-220M varistors in parallel to ring down our Feshbach currents, and we have observed the ring down time to stay within 20% of it's initial value even after 2 years (and of order 100,000 ring-down cycles).

The IGBT must also be carefully selected, as it performs the high-current switching and is used for precise current stabilization. High-current IGBTs (such as the Powerex CM1000HA-24H that we use) are large, heavy bricks with good heat sinks, but they still have a minimum voltage drop of a few volts (corresponding to roughly two semiconductor band-gaps), and because they conduct hundreds of amps continually, they dissipate hundreds of watts. They are designed to safely dissipate this energy, so if used as a simple on-off switch, this is fine. It will either conduct no current (and dissipate no power), or it will conduct at it's minimum voltage, safely operating as intended. This is not the case if it used for stabilizing current, however.

4.3.2 Precision control of current

The Feshbach resonances used for molecule formation are rather narrow, with ΔB of a few Gauss on top of 1000 G, but more importantly the magnetic field range for good mixing of the molecular state is $\delta B_{open} = 20$ mG. This requires current stability of at least 10^{-5}. Unfortunately, commercial high-current power supplies cannot provide

this stability out of the box.

Standard regulated high-current power supplies, such as the 500 amp ESS 30-500 (from Lambda EMI) used to power our coils, are always switch mode power supplies, which are intrinsically noisy. This is a matter of efficiency; linear power supplies have fixed transformer voltage and can only regulate current by burning unused power (up to the full output of 15 kW) internally. Switch mode supplies operate by alternately charging and discharging capacitor arrays at high frequency (typically tens of kHz), and by simply changing the duty cycle to build up less charge, they can regulate output power while drawing less input power. This eliminates the need to burn up the extra power, allowing switch-mode supplies to operate up to 95% efficient, no matter the output current.

However, the high-frequency switching is also a source of noise both at the output and on the input mains line. This noise directly affects the current stability, but also affects precision communication between the power supply and other devices, like an analog control voltage from a computer. Combine this with the fact that commercial high-current supplies are rarely intended for precision use, and it becomes clear why it is difficult to find off-the shelf solutions for precision magnetic field stabilization. As precision magnetic field control is becoming important for many scientific experiments, there may be commercial solutions available, but we never found proven solutions appropriate for our application.

The performance can be greatly improved by external current stabilization. Like any feedback circuit, this requires accurate measurement, an accurate set point, a good PID controller, and fast control[143]. We use a closed-loop hall probe (F.W. Bell CLN-

300), which can accurately measure the current at any point in the circuit while remaining electrically isolated from the power supply. This avoids possible problems of crosstalk directly from the noisy power supply to the hall probe while allowing accurate measurements of current through the coil even if there is noise introduced elsewhere in the circuit. Internal stabilization at the power supply cannot account for such external noise or drifts.

The hall probe outputs a current which precisely and accurately reflects the current flowing through the conductor. It is important that no additional noise or uncertainty is introduced when turning this into a voltage for the PID controller. This requires a very accurate current to voltage converter. I have often searched for commercial products with good specifications for this task, but never found anything better than precision resistors with very small thermal coefficients. The resistors must be selected so that they don't respond to room temperature variations or their own ohmic heating while in use. Active stabilization and heat sinks could be used, but we found satisfactory performance by using a network of Vishay-Dale PTF series resistors with thermal coefficients of less than 5 ppm/K. We calculated and measured less than a 10^{-6} drift of the Hall probe Voltage reading under normal operating conditions. The measurement was performed by watching the reading from a Hall probe while independently stabilizing the current with a different Hall probe of a different model and resistor design.

The set point must be provided by the word generator, but analog outputs from the computers and National Instruments PXI-6733 control cards (with 16 bit analog outputs and digital I/O ports) have finite resolution and show noise and shot to shot

instability of order 10^{-4}. One could try to find better analog cards and troubleshoot all possible sources of analog noise, but it is almost always easier and more reliable to use digital control signals than to maintain extreme precision in analog signals.. The SIM960 PID controller from Stanford Research Systems provides reliable, easy to tune PID control as well as accepting RS232 digital commands to accurately establish an internal set point.

The part of a feedback loop that actually controls the process does not require the extreme precision of the measurement and set point, because the feedback loop will naturally compensate for it's own noise as long as the measurement and set point are reliable. However, the actuator must have the fast response and dynamic range necessary to correct for errors. This is where the IGBT comes in.

An insulated gate bipolar transistor is like a hybrid of a field-effect transistor (FET), and a bipolar junction transistor (BJT). It draws almost no current from the gate like a FET, but has the reliable, high-power performance of a BJT. They make good on-off switches as mentioned earlier, but they are analog devices capable of handling a wide range of voltage and current conditions.

By driving the gate with an opto-isolator and an amplifier stage with enough current to quickly charge/discharge the gate capacitance, all the sensitive components of the feedback loop are electrically isolated from the high-current circuitry. The IGBT has a non-linear response to applied voltage, but that causes no problems for the loop. The non-linear response does change the open-loop gain of the circuit depending on current and voltage, so PID constants must be tuned under conditions matching the condition where stabilization is most needed.

The IGBT can be used as a current throttle with a voltage controlled power supply as in our experiment, or it can be used to shunt some current away from the coil by running it in parallel. The throttle setup is simpler, as one component can both switch and stabilize, and no current from the power supply is discarded. However, the shunt configuration may provide better stability depending on the particular components of the system[144]. If the power supply has better relative voltage stability, the throttle method would be best; if it has better relative current stability, the shunt configuration can be used.

Using an IGBT as a throttle for the full current is dangerous, however. If it is nearly saturated (maximum current with minimum voltage drop), it only has to dissipate a few hundred watts and has no problems. However, if the power supply voltage is set higher than necessary, the IGBT will present the voltage drop necessary for the target current. In an extreme example, the power supply could be supplying 30V, with the IGBT transmitting 250 A, with a drop across the coil of ~15V. This means the IGBT has to burn the rest of the power, amounting to almost 4 kW rather than a few hundred watts. To protect against this, we use a scaling amplifier that adjusts the power supply voltage to be only slightly higher than needed for a give current.

In the end, our circuit can produce fields up to 1620 G with ~10 mG RMS noise. At 1620G, the power supply is voltage limited, and the 10 mG noise is mostly at 60 Hz and harmonics, which are notoriously hard to track down and eliminate. The bandwidth of the feedback is limited by the inductance of the coil to 100 Hz, but the coil inductance also acts to filter high-frequency noise before it affects the magnetic field, so this is not a bad situation. For fast, small changes to the magnetic field, we use an

additional trim coil wound outside the chamber to provide an extra 10 G. The trim coil is powered by a 15 amp Kepco ATE 15-15DM, a commercial linear power supply with off-the-shelf current stability of 0.01% RMS, more than sufficient for our demands.

4.4 Techniques to measure ultracold molecules

Once a Feshbach resonance is located and resonant losses are observed, it can be claimed that molecules have been formed. Resonant losses near a Feshbach resonance always involve collisions which produce molecules. Properties of scientific interest include molecule collision rates, binding energy or kinetic energy, electric or magnetic moments, or density distributions. However, unless the molecules can measured and distinguished from the atoms in some way, these quantities cannot be studied.

Before molecules have been isolated and measured, the only relevant data that can be obtained are atomic loss rates. These can be used to estimate the parameter B_0 to within the width of the loss feature (for our measurements this can be a few hundred mG), but because of the difficulty in mapping 3-body losses directly to scattering length, B_0 cannot be identified more accurately than this. Magnetic fields can be measured very accurately with atomic RF transitions, but knowledge of B_0 is never more accurate than the best available empirical data, so the true resonance position is still unknown.

The best way to determine the true resonance location is to look for the moment where molecules dissociate or to perform RF spectroscopy and extrapolate the binding energy of the molecules[30]. However, if molecules have not yet been isolated and

measured, these techniques cannot be used. To escape this catch-22, an experimental method must be devised to blindly search for a molecular signal without precise knowledge of B_0 or molecular properties.

4.4.1 Adiabatic sweeps for molecule formation

Adiabatic sweeps across the resonance can form molecules without precise knowledge of the resonance location, although such methods require that the atom density and sweep rate will form molecules that can survive long enough to isolate and measure. These processes are studied in detail in chapters 6 and 7. If molecules can be formed this way, they can be separated from the atoms and imaged.

One way to achieve this separation is to blast the atoms away, then dissociate the molecules and image the cloud[29]. See figure 18 for an illustration of this method. If the blasting is known to eliminate the majority of a pure atomic cloud, but a significant number of atoms are imaged after dissociation, it can be concluded that they were molecules. The blasting must be effective at quickly removing the atoms by optically pumping to non-resonant states or transferring enough momentum to kick them out of the trap. This serves the dual purpose of removing the atomic background signal from the image and also avoids inelastic collisions between free atoms and molecules. However, the blasting beam must not affect the molecules, so it must occur away from resonance where the molecules are detuned from the blasting laser.

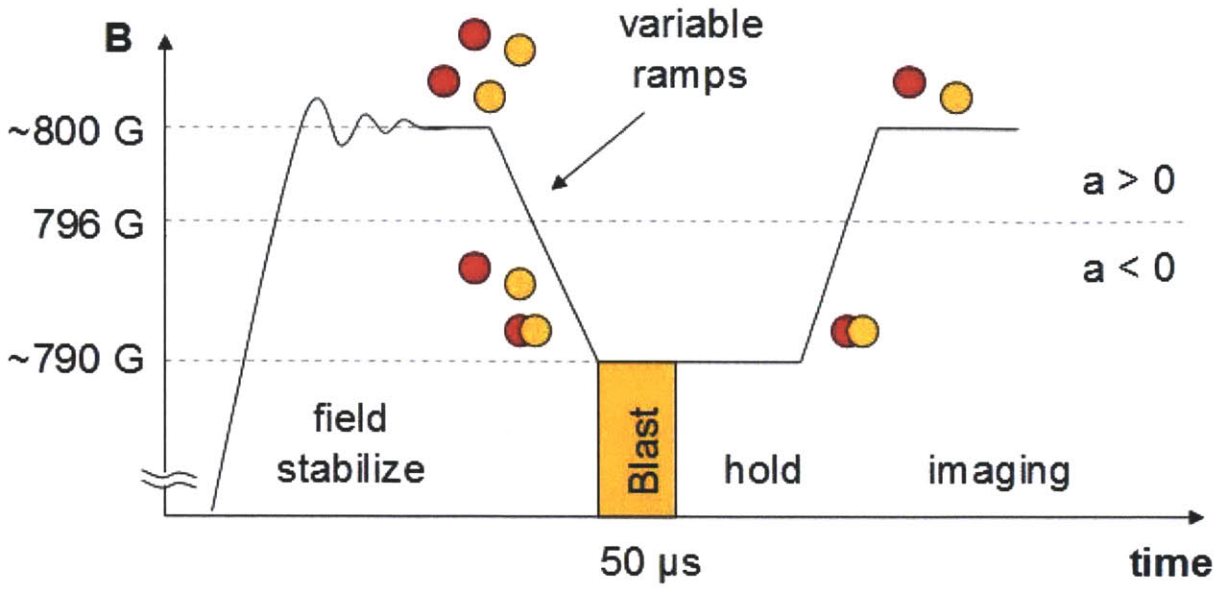

figure 18: Blasting method of isolating and measuring molecules. If atoms remain at the end, but the blast beam is effective at fully removing a cloud of free atoms, one can conclude that the remaining atoms were molecules during the hold time.

This method is very effective for homonuclear molecules, where the ground state molecular potential varies mostly as 1/R^3 but the excited state potential varies as 1/R^6 (refer to chapter 2.2.3 for a discussion). This causes the transition for even weakly bound molecules to be well detuned from the atomic resonance[13]. Heteronuclear molecules have an R^6 dependence in both the ground and excited states (although with different coefficients), so they may remain sensitive to the blasting beam even with moderate detuning[35].

Another way to separate the molecules is with a Stern-Gerlach procedure[29]. By applying a magnetic field gradient, the atoms and molecules will separate if the trapping potential is weak or turned off. This separation will occur whenever the particles have

different values of μ/m. Here there is no danger of accidentally blasting the molecules, but the separation is slower and inelastic collisions can continue for longer. Also, the molecular cloud is expanding during separation, which can dilute the absorption image of a molecular cloud which might already be small.

Both of these processes take a finite amount of time, both for the actual separation or blasting and for ramping the field back and forth across the resonance. The amount of time to separate the atoms and molecules are determined by the maximum acceleration of the method and the cloud dimensions. For blasting, the acceleration is given by:

68 $$a_{blast} = \Gamma \hbar k / 4\mathrm{m}$$

Since Γ/2 (the saturated resonant scattering rate) is the maximum rate at which photons can deliver their momentum kicks to the atoms. For Stern-Gerlach separation, the acceleration is given by

69 $$a_{SG} = B'(\delta\mu)/m_{reduced}$$

for magnetic field gradient B', where δμ is the difference in magnetic moments of the molecules and atoms.

As expected the time required to separate the clouds is just $\sqrt{2w/a}$ for clouds of width w, but with the added complication that strong gradients must act parallel to the large bias field (for transverse gradients, the B-field magnitude changes in quadrature with distance) while blasting beams can push from any direction. In our experiment, we were able to separate atoms within 100 μs along the short cloud dimension with blasting, but had to separate magnetically along the long cloud dimension, which took about 1 ms for gradients of order 10 G/cm. In chapter 6 this will be addressed more

quantitatively and applied to practical formation procedure.

The association itself requires a specific ramp speed, but once safely across the resonance the magnetic field can be quickly ramped for blasting and imaging or strong gradients quickly turned on. If the molecular lifetime is not long enough to survive the procedure, this technique will fail to give a clear signal even if some molecules have been formed.

4.4.2 RF association of molecules

Another possibility which has shown some success is RF association[30,100,125]. Here the atoms are prepared with one species in a non-resonant hyperfine state and the magnetic field is brought to the molecular side of the resonance. The non-resonant species is then driven to make the transition to the resonant atomic state. See figure 19 for an illustration of this method.

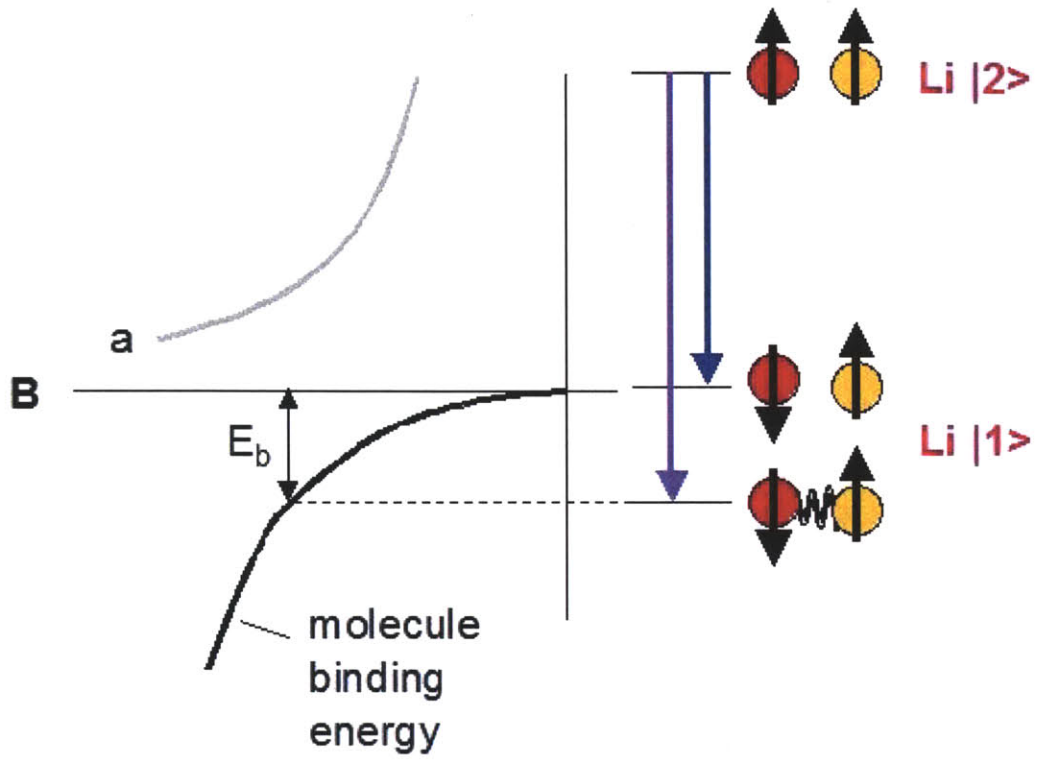

figure 19: Rf association of molecules. The correct frequency for associating molecules is determined by the binding energy, making this technique sensitive to the magnetic field.

The bare atomic transition frequency gives a good reference value corresponding to zero binding energy, although the spectroscopy may be broadened by interactions[12]. If a distinct peak can be found which is shifted from the atomic peak, it can be assumed that molecules have been associated with the RF transition. If the peak shifts with magnetic field in the expected way, it can be concluded that molecules have indeed formed and the binding energy curve can be fit to theory to determine the exact resonance location. This method has an advantage over adiabatic sweeps and

separation in that even if molecules are immediately destroyed, the RF signal can be obtained by looking for atomic depletion. See figure 20 for such a spectrum.

Practically, there are several challenges to this method. One is that the molecular peak will be much weaker than the atomic peak. Not only must the atom undergo the normal spin flip, but it must be near a partner atom to associate and the overlap of the free atomic wavefunction with the bound molecular state will reduce the Rabi frequency by a Frank-Condon factor Q. The value of the overlap integral depends on the open-channel fraction in the molecular state, which is small for finite detuning in closed-channel dominated resonances.

Also, the magnetic binding energy depends strongly on magnetic field. Because the magnetic field fluctuates in any real experiment, the binding energy will be inhomogeneously broadened. If this broadening is larger than the already reduced Rabi frequency, the transition will be incoherent and the transition rate will be further reduced by $Q\Omega_R/(\delta B \delta\mu)$.

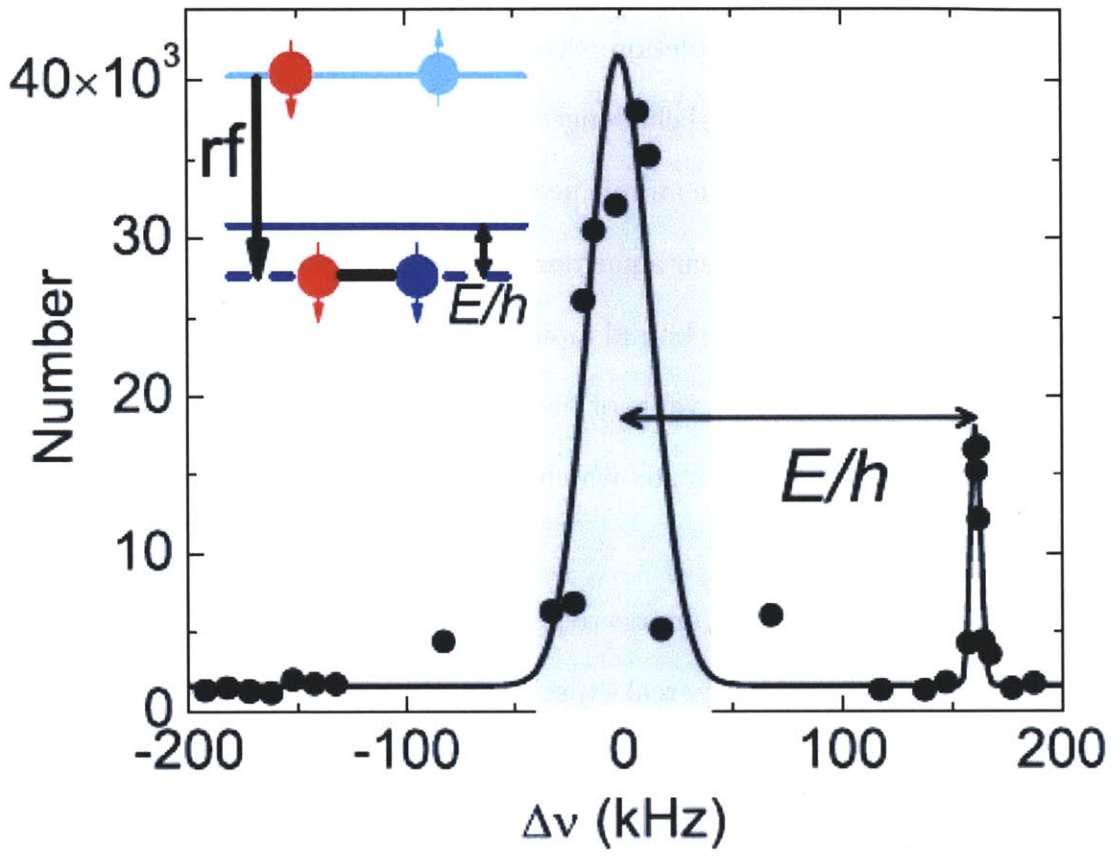

figure 20: RF spectrum taken from a gas of Rb and K near a Feshbach resonance. The atoms are driven into the target atomic or molecular state, the magnetic field is ramped to dissociate molecules, and the resulting atomic population is measured. Image reproduced from Zirbel et. al, Phys Rev A 78, 013416 (2008)

Summarizing these effects, The rate of RF association is given by

$$P_{pair}(n,T)\,Q\,\Omega_R\,\frac{Q\,\Omega_R}{\delta B\,\delta\mu} \qquad (70)$$

Where P_{pair} is a probability that reflects the likelihood of a given atom finding a partner.

For good values of Q this is not so bad, for example in RbK and Li_2 where the Feshbach state remains open-channel dominated (with small $\delta\mu$ and large Q) for a wide range of fields. However, for NaLi, it paints a grim picture.

For NaLi molecules, we can drive a maximum atomic Rabi frequency of about 1 kHz. With the generous assumptions Q = 0.01, P_{pair} = 1 and $\delta\mu$ = 1 MHz/G (which already occurs less than 20 mG from the exact resonance), our inhomogeneously broadened molecular transition rate would be 0.5 Hz. Without rebuilding the experiment or using kW RF amplifiers (which are very expensive and possibly dangerous to our lab and nearby labs), we would have to drive the transition for seconds to get a good signal. With the maximum experiment time of about 4 seconds (after which most of the atoms have been lost from the trap and the magnetic coils are overheating) we would barely produce a 20 kHz wide feature. However, even using the fantasy parameters given earlier, the binding energy of the molecules is around 10 kHz this close to the resonance, making it a tough experiment to distinguish the signal from a inhomogeneously broadened atomic peak.

Gleaning such a small, broad peak from an atomic spectra is difficult, if not impossible. In fact, the experiment is as sensitive to RF sidebands and noise as it is to real transitions, and for some time we were distracted by distinct features which turned out to be weak sidebands, 60 dB smaller than the carrier, produced by an Agilent 33250A arbitrary waveform generator. After replacing the generator with a cleaner Tektronix AFG3101, the features vanished, but we still failed to observe molecular transitions.

Proper experimental design can overcome many challenges, but a given Feshbach

resonance will have some hard limits imposed by nature, and it takes a little luck and careful experimental choices to glean useful data from an experiment.

5

Feshbach Resonances in Sodium and Lithium

5.1 Feshbach resonances in Na and Li gases

My experiments on ultracold molecule formation have been performed with dilute gases of Na-23 and Li-6. This choice of atoms is partly historical, as they are the atoms that have given our research group great results in experiments with quantum degenerate gases. This is largely due to the fact that gases of Na and Li have a favorable ratio of elastic to inelastic collisions, which has lead to efficient evaporative cooling and long lifetimes of trapped mixtures[41]. It would be nice if molecules made up of Na and Li would inherit this good fortune, although there is no solid scientific reason to expect it[3]. Even if this is not the case, any ultracold formation experiment benefits from large

3 One could appeal to the fact that the light mass of Na and Li compared to other alkalis means that the vibrational and rotational spacing of possible molecular states is larger. Because inelastic collisions generally involve decaying to bound molecular states, this would suggest (with much hand-waving and little rigor) that the atoms are less likely to find an energetically appropriate decay channel.

initial numbers of component particles and long lifetimes during preparation procedures.

Another motivation for studying Na and Li is the existence of several Feshbach resonances, both homonuclear and heteronuclear, at experimentally attainable magnetic fields. Prior to the start of my research in NaLi, Na2 molecules had been isolated and measured[25,29], and Li2 molecules have been studied under a wide variety of circumstances[14,27,145]. NaLi resonances had been identified and cataloged[4], but the molecules had never been isolated or measured for lifetime or formation efficiency.

The effective potentials of NaLi (refer back to figure 3 in section 2.2.2) are developed from molecular spectroscopy on hot vapors or beams of molecules[3,93-97]. The molecules were formed in a hot gaseous mixture of Na and Li vapors, and are therefore distributed among the quantum states in thermal equilibrium. The strong spectroscopic lines produced by these samples are mostly among low vibrational and rotational nuclear states. This gives accurate knowledge of the bottoms of molecular wells (the short range parts), but less accuracy in calculating the exact potentials near dissociation (the long-range parts).

In our experiment, we use a Feshbach resonance to populate only the R=0 rotational state in the most weakly bound vibrational states of the ground electronic potentials. Calculating the exact fields for these resonances was impossible from the hot spectroscopy data; however, once the resonances were found experimentally, many more could be predicted as the long-range potentials were refined[4,5].

5.1.1 New heteronuclear resonances between Na and Li

Prior to the start of my research, Claudiu Stan had located three NaLi Feshbach resonances and predicted the locations of several more[4,138]. A more detailed analysis by Marko Gacesa and co-workers refined the predictions, by fitting their calculations to the observed locations of the 3 verified resonances[5]. The following table summarizes Feshbach resonances we have located, and lists the fields where they were predicted to occur prior to observation.

Observed B_0	Predicted B_0	Atomic States	Molecular State	ΔB (G)	$\Delta\mu$ (μ_b)
746	746	$\|1\rangle_{Na} + \|1\rangle_{Li}$	$\|1\ 1\ 1\ -1/2\rangle$	0.04	4
760	760	$\|1\rangle_{Na} + \|1\rangle_{Li}$	$\|1\ 1\ 0\ 1/2\rangle$	0.31	4
795	795	$\|1\rangle_{Na} + \|1\rangle_{Li}$	$\|1\ 1\ -1\ 3/2\rangle$	2.18	4
787	780	$\|1\rangle_{Na} + \|2\rangle_{Li}$	$\|1\ 1\ 1\ -3/2\rangle$	1*	4
824	820	$\|1\rangle_{Na} + \|2\rangle_{Li}$	$\|1\ 1\ 0\ -1/2\rangle$	2*	4
851	872	$\|1\rangle_{Na} + \|2\rangle_{Li}$	$\|1\ 1\ -1\ 1/2\rangle$	4*	4
1594	1186?	$\|1\rangle_{Na} + \|1\rangle_{Li}$	$\|0\ 0\ 0\ 3/2\rangle$?	8.7	2

Table 1: Feshbach resonances in NaLi. Molecular states are listed in the $|S\ m_s\ m_{i,Na}\ m_{i,Li}\rangle$ basis. The last resonance has not yet been incorporated into the model, so the molecular state is not certain. ΔB values marked with a star are estimates from loss measurements. Predictions are taken from Gacesa et. al. PRA 78, 010701 (2008)

The first three Feshbach resonances listed (the ones observed by Stan et. al.) are close together because for the same molecular electronic state, there are three combinations of nuclear magnetic moment that give the same total m_f as the atomic

states. The predicted resonances in the |12> state were an obvious place to look for new resonances. The atomic states are still safe from 2-body inelastic collisions, have the same electronic configuration, and also couple to three nuclear configurations.

The resonances were predicted at 787 G, 820 G, and 870G. We were able to measure the three body losses experimentally and found the resonances at 787G, 824G, and 851G. Typical results of loss measurements near a Feshbach resonance are shown in figure 21.

The measurement occurs by holding the atoms at different magnetic fields for a fixed amount of time and measuring the remaining atoms. In our NaLi experiments, the ratio of Na to Li atoms varied from shot to shot, so we used a normalization scheme to obtain reliable measurements of atoms. We would take a series of data and also take several images with out crossing the resonance, so we could find the average initial atom number for Na and for Li. We would normalize the atom numbers for each measurement to the initial numbers. We would then take the geometric average of the normalized Na and normalized Li numbers to obtain a single number representing normalized atom number. Mathematically, this result is given by

$$\textit{Normalized atom number} = \sqrt{\frac{\text{Na \#}}{\text{initial Na \#}}\frac{\text{Li \#}}{\text{initial Li \#}}} \tag{71}$$

This number showed much less shot to shot and day to day instability than raw atom numbers.

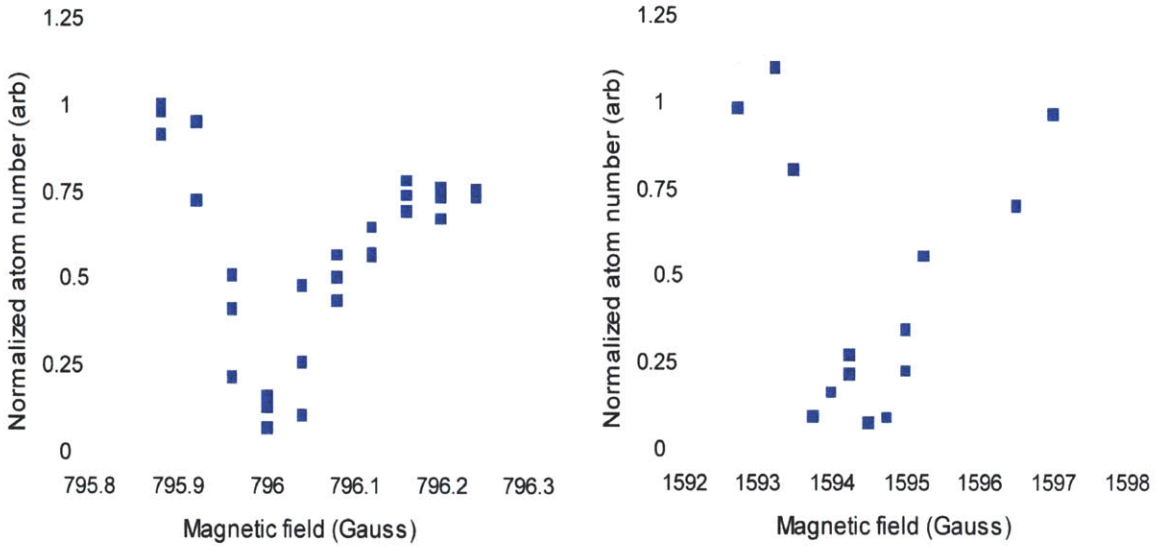

figure 21: Loss measurements near two Feshbach resonances between Na |1> and Li |1>. The atom numbers are normalized as described in the text. The resonance at 1594 Gauss was identified by a blind search described below in the text.

The search for specific Feshbach resonances is a good example of the importance of combining experiment and theory in molecular work. Blind experimental searching for any possible Feshbach resonances can miss narrow, weak resonances and takes a long time. On the other hand, numerical theories have some uncertainty for resonance locations even when most of the relevant data is known accurately.

5.1.2 Search for the wide singlet NaLi resonance

The UConn group predicted an 8 G wide Feshbach resonance at 1186 G in the |11> state. The width of the resonance made it an interesting target for experimental

efforts, and the resonance couples to the singlet molecular manifold, thereby avoiding the need for singlet/triplet coupling to drive transitions to populate the true molecular ground state $X^1\Sigma^+(v=0, j=0)$. However, a few attempts to search all fields up to 1300 G failed to locate the resonant losses.

The fact that all known resonances involved the triplet manifold gives a clue to the difficulty here. The known resonances provided no direct information on weakly bound states of the singlet manifold. However, to get the theory to accurately match the observed resonances, coupling between the singlet and triplet molecular states was invoked, so indirect knowledge of the singlet states was obtained.

A simplified calculation of the magnetic fields where resonances occur is possible by using a simple Hamiltonian[146-148]. The Asymptotic Bound State Hamiltonian is

72 $$\boldsymbol{H} = \boldsymbol{H}_{rel} + \boldsymbol{H}_Z + \boldsymbol{H}_{hf}$$

where $\mathbf{H_{rel}}$ includes the kinetic energy and effective potentials from the electronic motion, $\boldsymbol{H}_Z = \gamma_e \boldsymbol{S}\cdot\boldsymbol{B} - \gamma_1 \boldsymbol{i}_1\cdot\boldsymbol{B} - \gamma_2 \boldsymbol{i}_2\cdot\boldsymbol{B}$ is the Zeeman energy of electrons and nuclei in the magnetic field, and $\boldsymbol{H}_{hf} = (a_{hf1}/\hbar^2)\boldsymbol{i}_1\cdot\boldsymbol{s}_1 + (a_{hf2}/\hbar^2)\boldsymbol{i}_2\cdot\boldsymbol{s}_2$ is the hyperfine interaction for each atom. If we use a basis $|S, m_s, m_{i1} m_{i2}\rangle$, we can rewrite the Hamiltonian

73
$$\boldsymbol{H} = \boldsymbol{H}_0 + \boldsymbol{H}_Z + Q(\boldsymbol{H}^+_{hf} + \boldsymbol{H}^-_{Hf})$$
$$\boldsymbol{H}^+_{hf} = \sum_k (a_{hfk}/2\hbar^2)\{S_z i_{kz} + \frac{1}{2}[S_+ i_{k-} + S_- i_{k+}]\}$$
$$\boldsymbol{H}^-_{hf} = \sum_k (-1)^{(k-1)}(a_{hfk}/2\hbar^2)\{(s_{1z} - s_{2z})i_{kz} + \frac{1}{2}[(s_{1+} - s_{2+})i_{k-} + (s_{1-} - s_{2-})i_{k+}]\}$$

Two simplifications have occurred here. First, the relative motion has been "solved" to give a binding energy H_0 for a given basis state. The open channel has zero binding energy and is considered completely uncoupled from the molecular states. Coupling

between atomic states and molecular states can be invoked to find the resonance width as described earlier, but it is ignored in this method when finding the resonance locations. The singlet binding energy and triplet binding energies are adjustable parameters to match experimental locations of Feshbach resonances. The relative motion has also provided the Franck-Condon factor Q for coupling among different molecular states.

The hyperfine interaction has been separated into two parts, the + term couples only among singlet or among triplet states, the – term couples between singlet and triplet states. The first two terms are diagonal among basis states, only the hyperfine terms have off-diagonal elements. If Q can be approximated, the problem no longer involves solving any wave equations and simply involves diagonalizing a N x N Hamiltonian (for N basis states) whose diagonal matrix elements depend on B through the Zeeman term.

To solve for NaLi Feshbach resonances, we choose a single atomic state for Na and for Li, and the Hamiltonian reproduces the standard Breit-Rabi formula for the energy of the atoms in a magnetic field.

We then consider all molecular states with the same total m_f as the atomic state. There will probably be several coupled states, some singlet, some triplet. The hyperfine constants $a_{hf,Na}$ and $a_{hf,Li}$ can be looked up[149]. The remaining unknown is the Franck-Condon factor. This is possible to estimate because the singlet and triplet potentials are very similar at long range. Invoking the turning point method, we assume that Q=1 for states with the same binding energy (particularly for all diagonal terms), and for different binding energies, make the approximation

74 $$Q = 2\frac{(E_s E_t)^{1/4}}{\sqrt{E_s}+\sqrt{E_t}}$$

where E_s and E_t are the singlet and triplet binding energies[146]. These two binding energies are the only free parameters in the Hamiltonian, and they can be adjusted to match experimental Feshbach resonance locations.

See figure 22 for the results of such a calculation. Here we used the atomic state | 11> and all possible molecular states with the same total $m_f = 3/2$ (there are 8 such states) . The relevant constants were looked up and used to find the diagonal and off-diagonal terms of the Hamiltonian. The Hamiltonian was diagonalized using Mathematica, and then E_s and E_t were found through a built-in optimization routine.

Numerical treatment of the molecular wavefunctions shows that this simplified coupling scheme is not the whole story[5,148]. After a conversation with Marko Gacesa about the NaLi potential, we learned that by independently adjusting multiple parameters of the effective molecular potential, the coupling terms do not follow the binding energies as predicted in the simple model. He suggested that the singlet state could be much more deeply bound than initially predicted, moving the predicted 1186 G resonance to much higher magnetic fields.

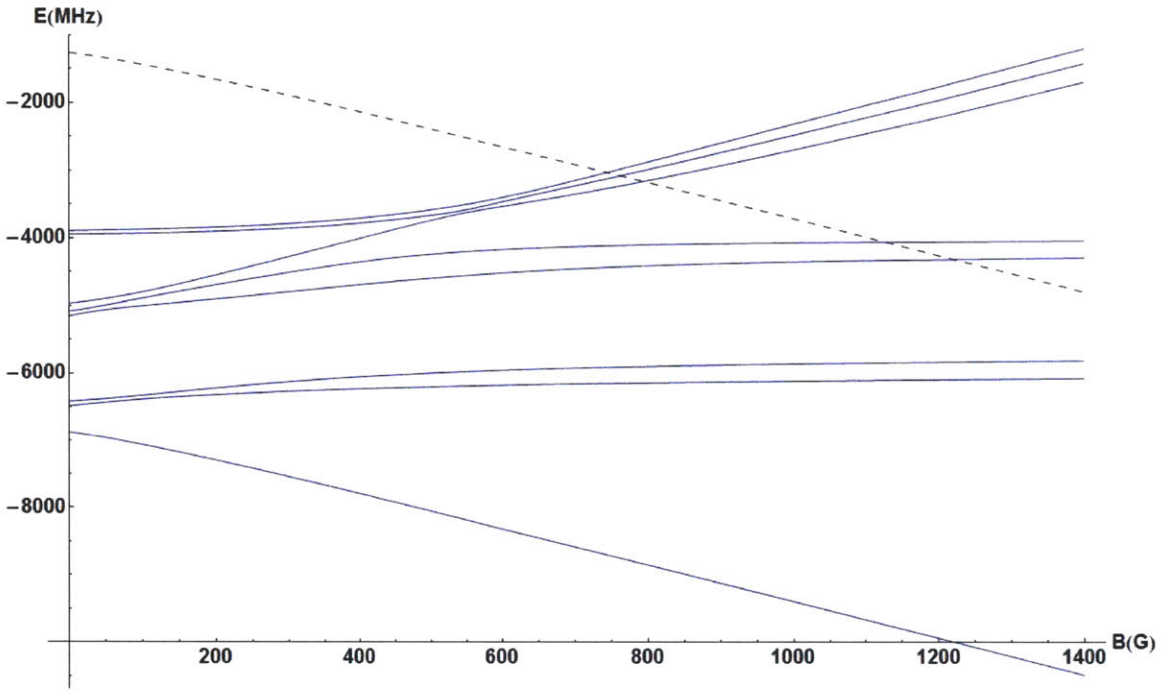

figure 22: Energies of the atomic state |11> (dashed line) and the eight molecular states with the same projection of total angular momentum, calculated with the coupled channels method. The singlet and triplet binding energies are adjusted to give good agreement with the experimental positions of the three highest energy molecular states. Note the prediction of two resonances near 1200 G. Image provided by Tout Wang.

Hoping that the field wasn't too far off, we pushed our search to the absolute limit of our apparatus around 1620G, and located a broad resonance at a field of 1594 G (see figure 9). As of the writing of this thesis, I have not heard if this field has been matched with revised molecular potentials, but it is almost certainly due to the

coupling to the singlet state, and should allow refining both singlet and triplet potentials of the NaLi molecules.

5.1.3 Homonuclear resonances in Na and Li

Homonuclear Feshbach resonances can occur in a gas of Na-23 and Li-6. If the trapped fermionic Li-6 is all in the same internal state, S-wave collisions between atoms cannot be anti-symmetric upon exchange of particle labels, so S-wave resonances do not occur at all. P-wave collisions have the correct symmetry (as will any odd partial wave), but at ultracold temperatures where the probabilities of higher partial-wave collisions are vanishingly small, the fully polarized Fermi gas has no interactions. Feshbach resonances can certainly occur with P-wave character, and several are known[119] for Li-6, but they are narrow and easily avoided.

A fully polarized Bose gas, on the other hand, allows even partial wave collisions (S, D etc.) and forbids odd collisions. Combined with the tendency of ultracold Bosons to condense or bunch, this increases the likelihood for two atoms to be close enough to interact by a factor of 2. Na2 S-wave Feshbach resonances can have a major effect on experiments in NaLi. Some Na2 Feshbach resonances are known[150]; in fact, we found resonant sodium collisions at 1590 G by surprise during our studies of the 1596 G NaLi resonance. These additional Feshbach resonances cause undesired inelastic losses, and interfere with preparing NaLi mixtures at desired magnetic fields unless they can be crossed very quickly to avoid losses or unwanted association.

5.2 Measured loss rates in Na and Li mixtures

5.2.1 3-body atomic losses near NaLi Feshbach resonances.

The most straightforward measurement of a Feshbach resonance is measuring three-body loss rates. See figure 23 for the results of measuring atom numbers with varying hold times near a Feshbach resonance.

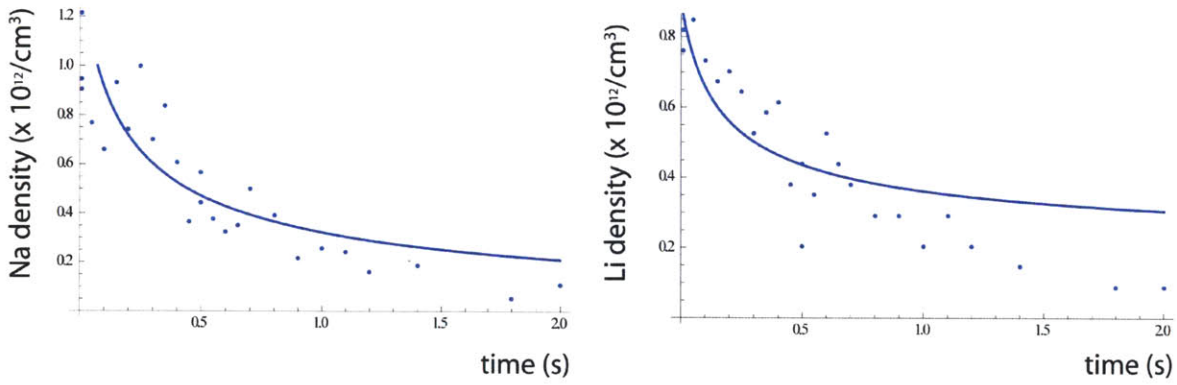

figure 23: 3-body trap loss in a strongly interacting gas of Na and Li near the 796G Feshbach resonance. The lines are obtained by numerically solving coupled differential equations for a homogenous gas assuming only Na-Na-Li collisions (with K3 = 5 x 10^{-24} cm^6/s) cause losses.

The most likely loss process in a resonant NaLi mixture is the 3-body collision of two Na atoms and one Li atom, because Pauli exclusion will suppress the 3-body

collision of two fermionic Li atoms and one Na atom, and a Na-Na-Na collision is not resonantly enhanced. In the figure we fit a line to the data assuming all losses occur due to Na-Na-Li collisions. As can be seen in the figure, this assumption fails to give exact agreement for low atom numbers, possibly because of other mechanisms dominating losses once the Na density is low, such as density independent background gas collisions or heating in the finite depth ODT.

5.2.2 2-body molecular losses near a Feshbach resonance.

Without producing and isolating NaLi molecules, we have not been able to measure their loss rates, although a lower bound can be predicted by applying a model with some assumptions explained in chapter 7. However, the Na_2 and Li_2 molecules have been produced using the exact same procedures in our lab. Although we were not the first to study either of these molecules or measure their loss rates, it was reassuring to see that our general procedures were sound. In this section, I am providing results from earlier work, as their experiments were more extensively optimized and analyzed than our brief forays into these bosonic molecules.

In the papers describing earlier work on Na_2 molecules from the Ketterle group[25,29], molecules could be readily formed and imaged. Lifetimes were limited to hundreds of microseconds if free Na atoms were present, but by blasting away atoms shortly after molecules were formed, about 5% of the initial atom number would remain

in molecules with lifetimes of up to 20 ms.

Our attempts gave very similar results to those reported in the paper, including a ~5% molecule formation, short lifetimes with atoms present, and ~10 ms lifetimes without free atoms present.

The Na_2 loss rates are informative because there is no reason to expect that NaLi losses should be more severe. In fact, because Na_2-Na collisions involve indistinguishable bosons, where NaLi-Na collisions have one distinguishable particle present, quantum statistics would suggest NaLi losses should be less severe. We have not observed this to be the case, however, and we will address this issue again in Chapter 7.

In Li_2, much work has been done with the exceptionally broad Feshbach resonance centered at 834 G. This broad resonance may not be a good comparison because of the very different dynamics expected between broad and narrow Feshbach resonances discussed in Chapter 3. However, there is a narrow Li_2 resonance in Li-6 at 543 G, which was investigate by[27].

Strecker and colleagues were able to observe up to 50% of the Li atoms disappear after a ramp across resonance to form molecules, but also see the atoms recovered if the molecules were dissociated with the reverse ramp. They were able to recover up to 85% of the initial atom cloud, suggesting at least the remaining 35% of the atoms adiabatically associated into molecules. The molecules displayed a very long lifetime of up to 1 second, even in the presence of the remaining Li atoms.

Our attempts to repeat these results were unsuccessful. We were able to see only a few percent molecule formation, although part of the problem was our trapping

configuration at the time. Atoms were trapped in an ODT radially, but axially held by a harmonic magnetic field. The molecular state, which is a singlet state with very small magnetic moment, can expand in the axial direction, thereby limiting the time-scales we could use for molecule formation. However, we were able to form a small fraction of molecules with a relatively fast sweep, but these molecules seemed to decay very quickly. Because of the trapping issues, we can't make any firm conclusions regarding the long lifetime reported in the paper.

The trapping problem was not an issue for observing Na2, because the higher atom density and wider resonance allowed faster sweeps to be used. It is also unlikely that the trapping was the only issue preventing good clouds of NaLi to be formed, as the 796 G and 850 G NaLi resonances are of similar width to the Na_2 resonance, and the 1596 G resonance is not only much wider but has less difference in magnetic moment between the atomic and molecular states. However, resolving this problem would certainly improve the procedure and allow better imaging of remaining molecules, therefore making the experiment able to detect smaller fractions of molecules.

6

Ultracold Molecule Formation Experiments

6.1 Requirements for long-lived molecules

The discussion of the previous chapters should make it clear that inelastic collisions are bad for ultracold molecule experiments, and collisions between atoms and weakly bound molecules near the Feshbach resonance are likely to cause inelastic vibrational decay. This suggests that once molecules are formed, they should be separated from the atoms as quickly as possible.

6.1.1 Stern-Gerlach separation

Magnetic field separation will separate particles with different values of μ/m, and is simple to implement if magnetic field gradients can be applied. As in a Stern-Gerlach

measurement if a magnetic field gradient is applied, all particles will be accelerated by the field according to their masses and magnetic moments. The time it takes to separate the molecules is determined by the size of the cloud in the gradient direction and the acceleration as

$$\tau = \sqrt{2w/a} = \sqrt{\frac{2wm}{\delta\mu B'}} \qquad (75)$$

where m is the reduced mass and $\delta\mu$ the difference in magnetic moments. For the Gaussian clouds produced by typical traps, if using the 2σ radius (the radius which contains 95% of the total population) for the width, the overlap of the clouds is reduced to 1/e after this time.

Because our experiment starts with a Magneto-Optical Trap, it has quadrupole coils capable of producing a large gradient. Even if if such quadrupole coils are unavailable, the Helmholtz coils used to produce a bias field for Feshbach studies can be modified to produce a gradient as well by shunting some of the current from one coil. Our experiment can readily produce gradients of up to 39 G/cm by running 30 amps in the MOT quadrupole coils. A practical limit of a few 10s of amps is encountered because of the switching hardware used for the MOT control, but with further modifications and high current power supplies, hundreds of amps could be used, producing much larger gradients.

39 G/cm gradients apply accelerations of 942 m/s^2 (or $\mu m/ms^2$) for sodium, so our clouds of a few hundred microns in length can be separated in less than 1 ms. To be able to distinguish a small molecular cloud from the tail of the atomic distribution, it takes about twice the separation time (by then, the clouds are 4 radii apart).

Care should be taken with this method to avoid allowing the local magnetic field of the molecules from crossing the resonance. If the initial trap location does not match the zero of the gradient field, the local magnetic field will jump when it is switched on, possibly dissociating the molecules or driving them to deeper binding energies than desired. In our experiment, the zero of the field is well matched, and the gradient is turned on only when the magnetic field is a few Gauss past the resonance.

6.1.2 Resonant processes for separation

RF spectroscopy can be useful for preparing or identifying molecules, but the momentum transfers and transition rates are far too small to produce a noticable acceleration. More useful for separating atoms from molecules are resonant optical beams, which can deliver forces of

76 $$F_{blast} = p_{recoil} * \Gamma / 2 \rightarrow a_{blast} = 9 x 10^5 m/s^2$$

Where the sodium recoil velocity of 3 cm/s and spontaneous emission rate of 10 x 2π MHz (divided by 2 for the saturated transmission rate) was used. Note that this is about 1000 times larger than the Stern-Gerlach acceleration. The blasting method can also optically pump atoms to non-resonant states, possibly allowing it to protect molecules faster than the acceleration alone would suggest.

Because the blasting method uses the same technology as imaging near the resonance (only with much more optical intensity), for us it was only a trivial modification to enable the method. Another advantage is that if the molecules are not

resonant with the blasting beam, they will be unaffected by the beam and can remain in the trap. This is probably not the case for Stern-Gerlach separation.

Until a molecular signal has been obtained, it is hard to be certain that the molecules are truly unaffected. Because of the previously mentioned difficulties of predicting binding energies of weakly bound molecules, the molecular excited states may be unknown. However, in general there will be a combination of magnetic field and optical frequency that blasts atoms sufficiently quickly without affecting the molecules adversely.

6.1.3 Unwanted resonant processes affecting molecules

Even if the blasting beam is not affecting the molecules, the red-detuned laser used in the ODT could possibly drive transitions to molecular excited states. This effect was reported in Josh Zirbel's Ph.D thesis on RbK molecules[125], and could be a concern for any molecular experiment. Because of the high intensities used in trapping lasers (our trapping laser can be 10^8 times above saturation intensity for 10 W focused down to 30 μm), even a far detuned molecular transition can allow unacceptable scattering rates. To calculate the likelihood of such an event, we used predictions of excited state energy levels from Marko Gacesa (see figure 24), but because they had not been measured, assumed that the vibrational states could be randomly displaced by any amount while keeping the same level spacing.

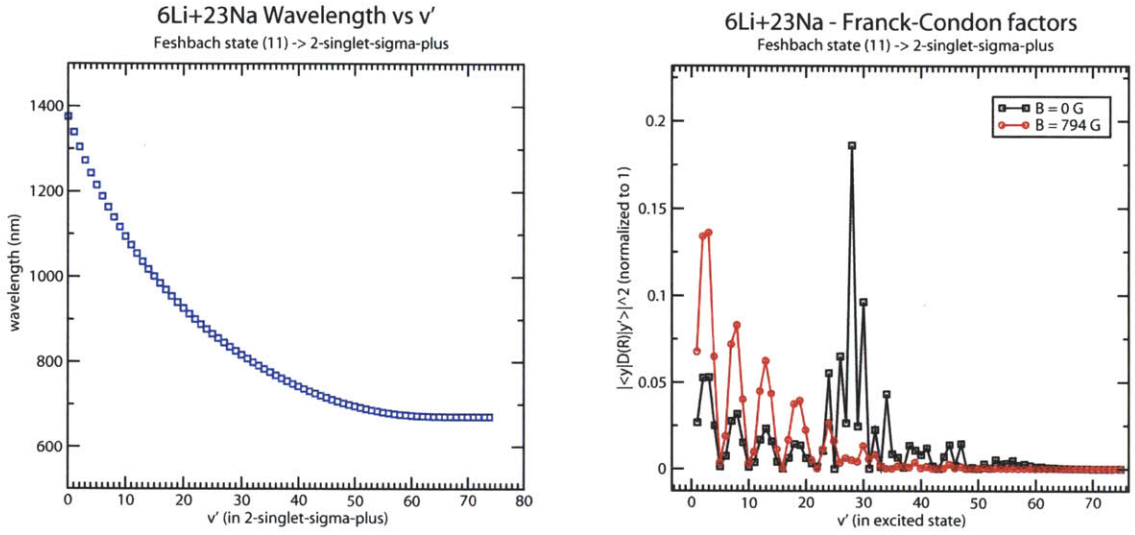

figure 24: Predicted transition wavelengths and Franck-Condon factors for transitions from the molecularFeshbach state to the lowest lying NaLi excited state. Note in particular that near 1064, FC factors are less than 0.1 and transitions are spaced by 20 nm. In fact, transitions are predicted to occur at 1054 and 1074 nm. Images provided by Marko Gacesa.

Assuming a Franck-Condon factor of 0.1 (likely an overestimate as seen in figure 27), to cause scattering lifetimes of less than 10 ms the IR laser must be within 10 GHz. Because molecular excited states are spaced by a few THz, there is less than a 1% chance for this to occur. The only guaranteed protection from these transitions is to chose a trapping laser that is red detuned beyond even the lowest energy transition from ground state dissociation to an excited state, which would require a laser at 1370 nm or longer wavelength for the case of NaLi.

6.2 Experimental results for Na and Li gases

The formulas of section 3.4 gives a probability to form molecules during a magnetic field sweep, but ignore the likelihood of the molecules being lost to collisions during the sweep. A simple experiment can be used to measure molecule formation, even if all the molecules are promptly destroyed before they can be directly measured.

A direct measurement of atom loss after a magnetic field sweep cannot be used to calculate molecule formation. A few papers have defended this assumption on the grounds that other loss processes are insignificant during the experiment[23,27], and have backed up the assumption with estimates of 3-body atomic losses. However, even if the atomic mixture is long-lived on resonance, every inelastic collision involving a molecule likely removes free atoms from the trap. This is because the major inelastic loss process is a molecule colliding with a free atom, being quenched to a lower vibrational state, and releasing the excess energy to both collision partners as kinetic energy[103]. The high-energy particles can then potentially undergo further collisions as they leave the trap. Also, in experimental conditions, sweeps slow enough to form a significant fraction of molecules may also be slow enough to experience non-negligible 3-body losses, even before the molecules are formed.

A better estimate of molecule formation can be obtained by comparing losses due to a sweep across resonance with losses due to the same sweep across resonance but in the reversed direction. In this way all possible atomic loss processes that do not involve

adiabatic molecule formation are measured under an identical experimental procedure, and any asymmetry between the two sweep directions can be assumed to reflect adiabatic molecule formation, which only occurs for one direction. We will refer to the sweep which can form molecules as the forward sweep, and the reversed sweep which does not form molecules as the backward sweep.

77 $$fraction\ of\ atoms\ lost\ to\ molecular\ processes = 1 - \frac{forward\ atom\ number}{backward\ atom\ number}$$

The total number of extra atoms lost does not immediately give the number of molecules formed, but is proportional to the number of molecules formed. The proportionality factor reflects the fact that every molecule formation and loss causes the loss of the pairing partners, the free atom which collided with them, and possibly more atoms that undergo subsequent collisions as the high energy collision products leave the trap. Because molecule formation and loss can occur very close to resonance, where collisions are frequent and the proportionality factor can be larger than 3, and can only be known for sure if the molecules can be isolated and their original population extrapolated from lifetime measurements.

We have performed these measurements in our experiment for Na-Na, Li-Li, and Na-Li Feshbach resonances. See figure 27 for a plot of results for a few experiments. You can see that in each case, it was possible to observe at least 30% more loss in forward sweeps than backward sweeps, and we can assume that this part of the atomic cloud is lost due to collisions involving molecules.

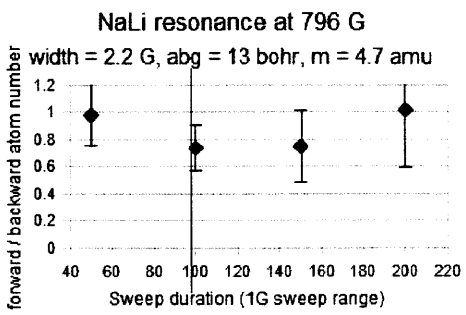

(density = 1 x 10^{12}, T/T_f = 0.7)
Shallow trap, 796G, freq(Na) = 215 x 22 Hz, T = 400 nK

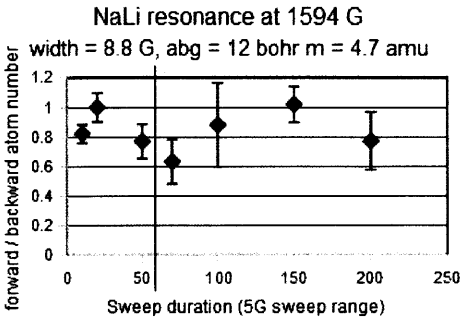

(density = 3 x 10^{12}, T/T_f = 1)
Deep trap, 1594G, freq(Na) = 281 x 46 Hz, T = 1.0 μK

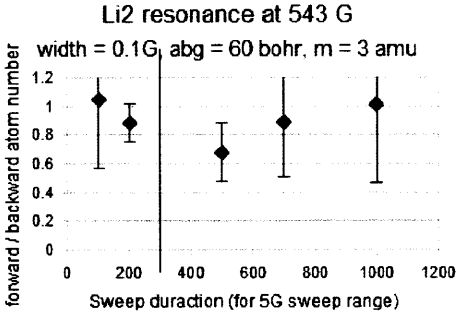

(density = 5 x 10^{12}, T/T_f = 0.2)
Shallow trap, 543G, freq(Li) = 420 x 35 Hz, T = 400 nK

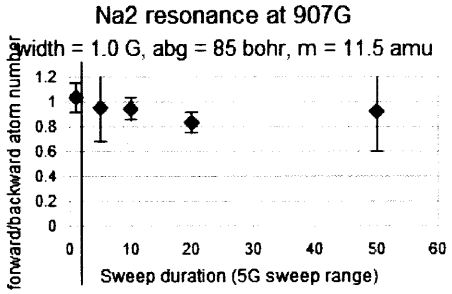

(density = 1 x 10^{12}, T/T_c = 2)
Shallow trap, 907G, freq(Na) = 215 x 23 Hz, T = 400 nK

figure 25: Results of comparing forward and backward sweeps across several feshbach resonance. The y axis displays the ratio of atoms remaining after forward sweeps to atoms remaining after backward sweeps. The vertical blue lines show the sweep rate which corresponds to δLZ = 2 with the constant α=0.31 for all sweeps, and a factor of 2 included in the Na2 resonance for identical bosons. The Na and Li atom numbers are first independently normalized to average initial atom numbers, and then normalized as described in section 5.1.1

The Landau-Zener formation formula (equation 57 from section 3.4.3) can be compared to these results. In figure 25 a vertical line in each plot shows the point where

the Landau-Zener parameter $\delta_{LZ} = 2$ while using the constant 0.31 for α.

In chapter 7 we present a numerical method for modeling these asymmetric sweep formulas, but we have not extensively tested a wide range of parameters for each plot, so we do not draw any definite conclusions about this value of α. However, the correspondence of the $\delta_{LZ} = 2$ sweep rate with the fastest sweep rates showing significant molecular losses for several different resonances is reassuring.

6.2.1 Results from Na_2 and Li_2

In our experiments on Na and Li, we have explored the following Feshbach resonances in detail

Species	B_0 (G)	ΔB (G)	a_{bg} (a_0)	m_{red} (amu)
Na-Na	907	1	63	11.5
Li-Li	543	0.1	59	3
Na-Li	796	2.2	13	4.8
Na-Li	870	4*	13.5	4.8
Na-Li	1594	8.7	12.5	4.9

Table 2: Experimentally investigated resonances in Na and Li. Numbers for Na-Na and Li-Li was taken from Chin et. al RMP 82, 1225 (2010)

Data on asymmetric sweeps were obtained for all resonances except 870, and a variety of formation techniques have been attempted for all of these resonances. Na_2 and Li_2 Molecules have been successfully isolated, but we have not succeeded in isolating NaLi.

An example image from our successful Na_2 procedures can be seen in figure 26.

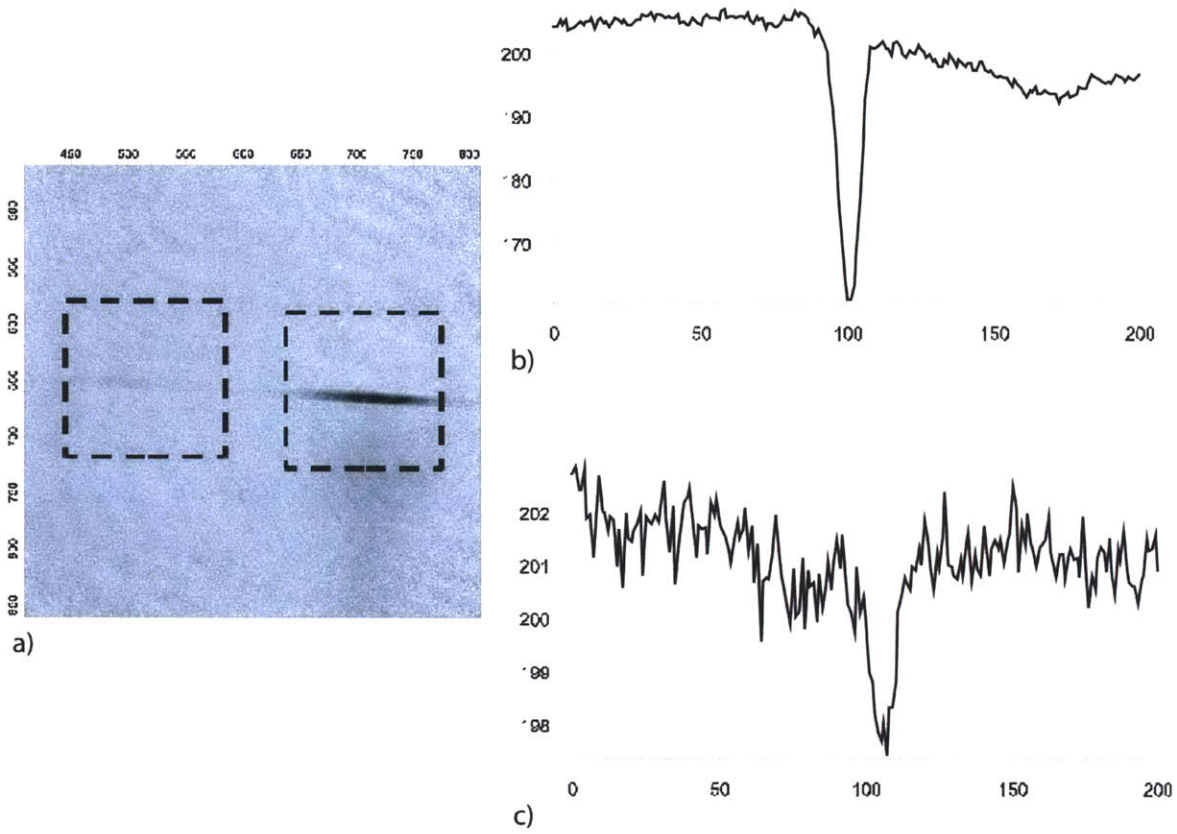

figure 26: Image of Na atoms and molecules separated by the Stern-Gerlach method. In (a), the cloud on the right is remaining atoms, and the left cloud is the surviving molecules. The molecules contain about 4% of the original atom number. b) and c) are 1-D profiles obtained by integrated the region around the atomic and molecular clouds, respectively.

These images should give an idea of the real limit of molecule studies; enough molecules must be formed and isolated to produce clear images of the molecular cloud. This means the molecule cloud must be distinct from the tail of the atomic cloud (if

using Stern-Gerlach separation, as in these images), or the surviving molecules must be distinguished from possible remaining atoms (if blasting is used without Stern-Gerlach). The particular procedure and imaging setup used impose limits on the minimum molecule fraction that can be measured. For our imaging, we can visually distinguish 4% molecule formation. After some integration and performing Ncounts in the region of interest, we could observe down to 1% formation, but any smaller fraction and the molecular peak is lost in imaging noise. Because we could not observe NaLi molecules in images, even after integrating over the expected location of molecules, we conclude that the surviving molecule fraction is less than 1% of the initial atom number.

Slightly smaller fractions might be observed by combing through many images with a fine-toothed analysis algorithm. However, shot to shot instability in atoms numbers, imaging beam fluctuations, and fringes make it likely that such an algorithm will give false positives. We did not attempt such methods to pick out procedures which might have been "barely successful" at forming NaLi molecules, instead devoting our experimental time and creative energies to improving systematic methods in the hopes of getting unmistakable signals of molecule formation.

6.3 Further considerations for molecule experiments

6.3.1 Empirical optimization of molecules

A few techniques of currently successful molecule formation experiments must be mentioned to allow this thesis to be a useful guide to Feshbach molecule formation.

They have not been mentioned yet because they are the result of optimization through trial and error, but cannot be systematically applied to an experiment that has not yet produced any image of surviving Feshbach molecules, such as NaLi.

To optimize the surviving fraction in a successful experiment, search for the balance of atomic densities, temperature and ramp rate that give maximum molecule numbers. This can involve changing trap geometries, or even releasing the atoms in ballistic expansion before attempting formation[33].

Another important technique worth mentioning is carefully shaped magnetic field profiles. Rather than a simple linear sweep across resonance, the field is jumped abruptly from one field to another. This has the advantage of avoiding the portions of the ramp where molecules do not form but losses are nevertheless enhanced. In our experience, we improved the surviving fraction of Na_2 molecules by a factor of 2 by changing from linear ramps to shaped ramps. However, this method involves many more free parameters, and only makes sense if a signal has already been obtained and the procedure is being empirically optimized for surviving molecule fraction. It is unlikely to allow significant formation in a system where linear sweeps yield no measurable results.

Another technique, which has been previously mentioned, is to wait at a field with finite molecular binding energy and to allow thermal equilibrium to populate the molecular state[145]. This method has only been demonstrated in the unusual case of the broad Li_2 resonance, and relies on the long-lifetimes and very strong coupling unique to that resonance.

6.3.2 Molecular transitions in weakly bound NaLi

The molecules formed are in the most weakly bound vibrational states. If large electric dipole moments are desired, more deeply bound states are required. The only currently feasible way to achieve this is through Raman transitions, where the upward transition is driven with a laser and the downward transition is stimulated with a laser tuned to populate the desired state. The only way to do this coherently is by two photon transitions with shaped laser pulses in a technique known as STIRAP[67]. The exact locations of excited states with good Frank-Condon overlap with the Feshbach molecule is unknown (again, these tend to be highly vibrational levels with strong dependence on the uncertain long-range potentials), but with cooperation between experimental spectroscopy and theoretical refinements of the molecular potentials, the appropriate transitions can be found.

The downward transitions also require good Frank-Condon factors, and if the atoms start in the triplet manifold, to end up in the true ground state some singlet-triplet coupling is required. This can occur in the excited states of the molecules in one of the previously mentioned violations of the Born-Oppenheimer approximation.

In the NaLi system, some estimates have been made regarding these molecular transitions. Based on potentials incorporating data from our group on NaLi Feshbach resonances, the research group of Robin Cote from the University of Connecticut has calculated estimates of the required transitions as seen in figure 24.

If long-lived molecules can be formed, some spectroscopic measurements can be

performed on the most weakly bound states by simply detuning the lasers already used to drive resonant atomic transitions. Because these states are typically a few GHz below dissociation, the transition frequencies are well within the tuning range of lasers, and might even be within the range of standard AOM or EOM frequency shifters. This allows some immediate improvement in spectroscopic knowledge the moment an atomic physicist can form measurable molecules[68].

7

Modeling Practical Molecule Formation

7.1 Model of real Feshbach association procedures

7.1.1 Assumptions of model

Incorporating the material from previous chapters, we can now construct a numerical model for real Feshbach Association procedures. This will be useful in interpreting data from NaLi where we cannot measure molecule populations directly. The model requires the following assumptions:

First, the system is prepared at a boson phase space density of 1. This is done to optimize association with large phase space density while avoiding Bose-Einstein Condensation at phase space density of 2.6[77]. It also simplifies the system dynamics, as collective motion of the BEC and other effects of quantum degeneracy can be avoided. The Fermion phase space density is less of a concern as it gets automatically capped at 1

from Pauli Exclusion[76], and the degenerate density profile remains qualitatively similar to the thermal profile at $T=T_f$. For our balanced mixtures of NaLi, Na phase space density ≤ 1, Li phase space density would be as high as 4 assuming a thermal distribution, but degeneracy limits it to 1.

Second, collision and formation rates are calculated using the uniform density equations of Chapters 5 and 6. This means hydrodynamic effects and correlations are ignored, and densities are not allowed to redistribute during the formation sweep. The results should be reasonably accurate as long as the mean free path is greater than the interatomic spacing, which is the case except for unitarity limited collisions in fully degenerate gases.

Third, molecule formation efficiency and atom loss should total less than 50%. This will limit the effects of depleting the high-density portions of the cloud faster than the low density portions. The modified exponential Landau-Zener formation formula will be used (equation 57), so molecule formation will automatically be restricted to less than 50%, and sweep times of interest are generally much faster than those that will severely deplete the atom cloud, so this assumption will definitely hold.

Fourth, the only formation and collision processes considered are adiabatic formation, 3-body atomic loss and 2-body molecular loss. In each collision only the particles participating in the collision are lost from the trap, but they are assumed to be lost from the trap immediately. These circumstances will cover the most relevant processes near resonance.

7.1.2 Description of model

The model begins with a trapped gas held away from resonance. If the magnetic field is at least 2 ΔB away from resonance, the scattering length is within 50% of a_{bg} and the atoms will have their equilibrium non-resonant density distribution. For our experiments, these distributions are roughly thermal distributions, as T > Tc and T/T_f ~ 0.5 or higher.

A linear sweep is used to cross resonance. This causes the heteronuclear scattering length to vary with time as

78 $$a(t)=a_{bg}(1-\frac{\Delta B}{B(t)-B_0})=a_{bg}(1-\frac{\Delta B}{2\Delta B-\dot{B}t-B_0})$$

Only resonant collisions are considered. Other collisions should cause minimal loss during the experiment duration. Collision rates are incorporated in the coupled differential equations.

79 $$\dot{n_{Na}}=-K'_3 a^4 n_{na}^2 n_{li}-\beta(a) n_{Na} n_{mol}$$

80 $$\dot{n_{Li}}=-K'_3 a^4 n_{na}^2 n_{li}$$

81 $$\dot{n_{mol}}=-\beta(a) n_{Na} n_{mol}$$

These equations are numerically solved to obtain surviving atomic and molecular densities. The coefficients may be known or may be treated as the free parameters of the model. The a^4 dependence of 3-body loss agrees with losses observed in RbK[103], but we apply a cutoff when scattering length exceeds the deBroglie wavelength. The function β(a) probably does not have a simple analytical form, as seen in the RbK loss paper (refer back to figure 25 in chapter 6). For the results presented in this chapter, we use a constant value for β(a), which can be interpreted as the average value across

resonance.

The peak density alone can be used for rough calculations, but each point in a 3-D density distribution can be independently solved at it's local density for a more thorough treatment. Redistribution of densities in the trap are ignored. This can remain accurate for fast sweeps (where total experiment time is less than a quarter trap period), but slower sweeps may have quantitative errors.

No molecules are present at the beginning of the sweep, but as the sweep crosses the resonance, the molecule density is calculated with the formula from chapter 5:

$$n_{mol} = n_{minority} \frac{T_f^{3/2}}{8\,T^{3/2}} \left(1 - \exp 2\pi \left[\alpha\, n_{majority} \frac{\hbar}{m} \left| \frac{a_{bg}\,\Delta B}{\dot{B}} \right| \right]\right) \qquad (82)$$

using the densities present at the time the resonance is crossed. The molecular and atomic densities are all abruptly changed at this time by forming molecules with density n_{mol}, and removing this same density from both species of atom.

The constant α is a fudge factor invoked by all experiments which have compared the formula to experimental results. In our experiments, we found $\alpha = 0.31$ to give adequate agreement with observations, but this value should not be considered conclusive, as we have not done careful numerical modeling fitted to the many experiments we have performed with various temperatures, densities and Feshbach resonances.

The simulation is then completed by allowing the linear sweep to continue for a specific time after crossing resonance. This time represents the extra time required to separate and measure any potential molecules. The densities at the end of this time are used as the final atom/molecule density and number.

7.2 Application to Na_2 experiments

We first test the modeling on the case of Na_2, where we are able to directly measure molecule formation. Optimized Na_2 experiments require Bose-Einstein Condensation for maximum molecule formation, but we can still obtain measurable molecule fractions in a thermal gas, which has a more repeatable peak atom density and thus provides more reliable data to compare to the model.

We use the measured density and temperature of the cloud ($n = 1 \times 10^{13}$ cm^{-3}, $T = 400$ nK), and the molecular loss rate $\beta = 5.5 \times 10^{-11}$ presented in Mukaiyama et. al[25]. We find the constant $K'3 = 5 \times 10^{5}$ gives good agreement with backward sweep data. At this point all parameters are fixed, and we model atom numbers surviving forward and backward sweeps, as well as molecule numbers surviving forward sweeps. See figure 27 for the results and a comparison of asymmetric sweep data to experiment.

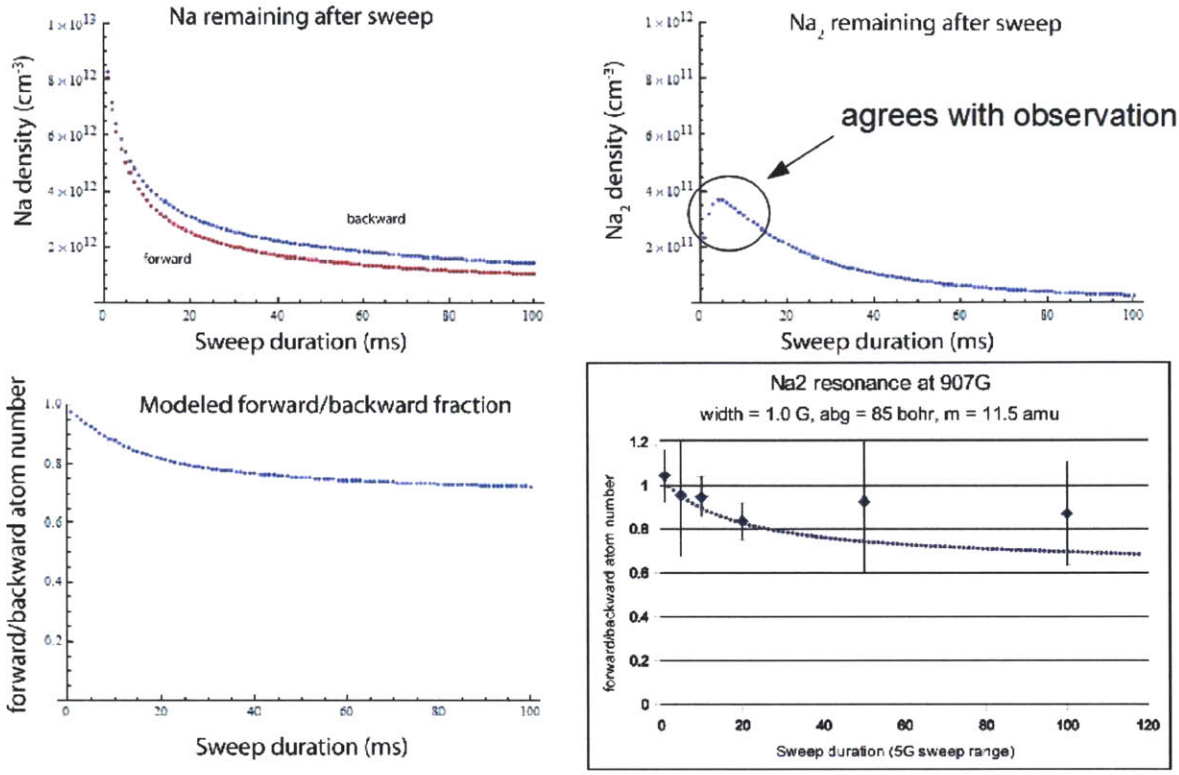

figure 27: Numerically modeled results for experiments near the Na2 Feshbach resonance. the bottom right compares experimental data to the model. Note the maximum molecule formation corresponds to 4% efficiency for sweeps between 2 and 10 ms, which roughly agrees with our observations.

Note the fair agreement with experiments, both the forward/backward ratio and also the maximum molecule formation of about 4%, which drops for sweeps which are faster than 1 ms or slower than 10 ms, which roughly agrees with experiments.

7.3 Application to NaLi experiments

See figures 28 and 29 for results obtained for the 796G NaLi resonance by using measured 3-body loss (see figure 25 in chapter 5) and typical initial atomic densities which match those used in the asymmetric sweep experiment shown in figure 27. This analysis and the figures were provided by Gregory Lau.

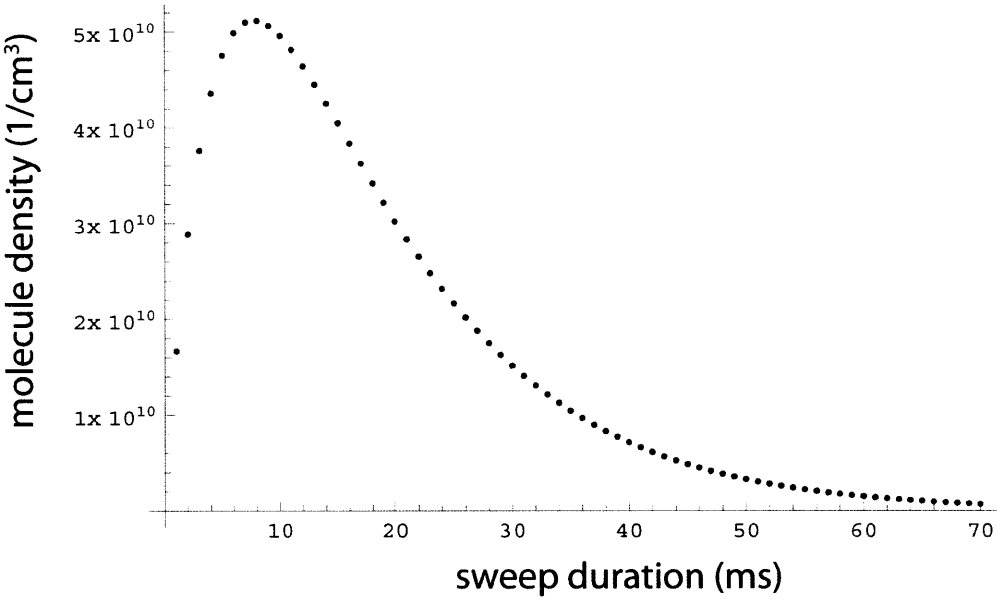

figure 28: Surviving molecule density calculated using the numerical model described in the text, and a constant 2-body loss coefficient $\beta = 10^{-10}$ cm³/s. The maximum surviving density near 5 x 10^{10} is 2.5% of the initial atomic densities (2x10^{12} for each species). Data provided by Gregory Lau.

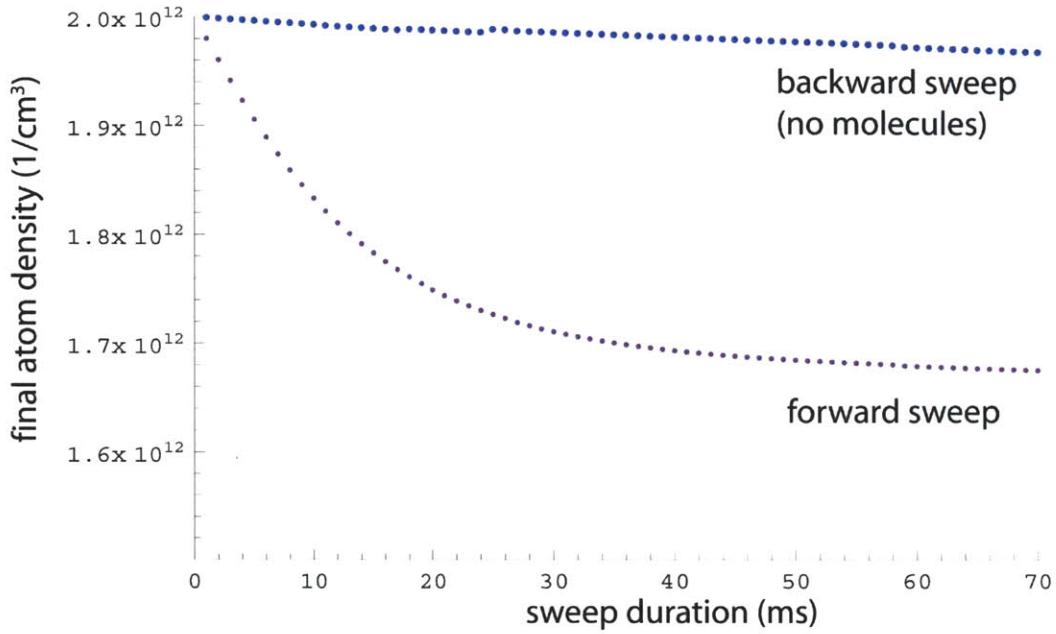

figure 29: Atoms remaining after asymmetric sweeps across the Feshbach resonance, calculated using numerical modeling. These results are similar to measured atom numbers after asymmetric sweeps. Data provided by Gregory Lau.

The results use initial atom densities that match the peak densities in our experiments, measured 3-body loss rates and known values for resonance parameters. The atom loss results are consistent with asymmetric sweep experiments. The atom loss results were obtained using a conversion efficiency $\chi_a = 0.1$, which corresponds to $T/T_f = 1.2$. Temperature measurements indicate that our system is colder than this (around $T/T_f = 0.5$ or 0.7), but considering that the conversion efficiency is approximate, this is not a major concern.

The results assume a 2-body molecular loss coefficient $\beta = 10^{-10}$ cm^3/s, and using this value produces a molecular density that would be barely observable in our

experiment. Assuming that only molecular losses are preventing us from isolating molecules (and not possible technical difficulties), this value can be interpreted as a lower bound. Because this is a constant value, the real loss coefficient may be higher or lower than this value at different stages of the experiment, in which case the bound would apply to the average value. Furthermore, we have tried a wide variety of experimental parameters and magnetic field sweeps beyond those simulated in this and never observed molecules, this lower bound is conservative.

Because this is a 2-body inelastic collision process, a unitarity limit can be applied to find an upper bound for the possible coefficient. The rate calculated in chapter 6 is 3.1×10^{-7}, 3000 times larger than the lower bound. Thus it is certainly possible that 2-body molecule losses could prevent us from observing NaLi molecules.

Unitarity limits apply to the total elastic and inelastic collision rate, so a loss rate close to this limit implies that almost every collision results in vibrational quenching. The ratio of elastic to inelastic collisions can be modified by the existence of nearby resonant trimer states, details of the vibrational wavefunctions, and other molecular properties that are not widely studied for NaLi at this time.

7.4 Conclusions regarding NaLi molecules

Our non-observation of surviving NaLi molecules should not be interpreted as hard evidence of physical limitations of the NaLi system. I believe no experimental physicist should ever claim that their experiment is indisputable. However, experience

and observation leads me to believe that our statements regarding the 2-body loss coefficient are accurate, and 2-body collisional losses are the most likely reason for our difficulties in isolating and studying these molecules.

One additional possibility is the narrow magnetic field range of strong mixing of the atomic and molecular states δB_{open} = 18 mG is not large enough compared to magnetic field noise, although the narrow Li2 resonance has δB_{open} = 0.1 mG and molecules were isolated, so that cannot be the whole story.

Our success at forming Na2 and Li2 molecules using identical procedures and atomic properties serves as an "idiot check" that we are not making obvious mistakes. We cannot rule out technical problems specific to NaLi such as the ODT laser driving resonant molecular transitions. However, I also believe no experimental physicist should blame such unlikely "boogeymen" for problems before searching for logical and likely explanations.

7.4.1 Comparison to RbK

If the theories presented in chapter 3 are to be believed, a few general statements can be made comparing the NaLi system to the highly successful heteronuclear Bose-Fermi mixture of Rb-K[35,67,103,151]. The adiabatic molecule formation efficiency (equation 57) gives the following results for the resonances

$$83 \quad P(RbK, 546\text{G}) \approx \frac{2\pi T_f^2 n_{majority}}{8T^2} \frac{4\pi\hbar}{m} \left| \frac{a_{bg}\Delta B}{\dot{B}} \right| = \frac{2\pi 10^{12}}{2} \frac{4\pi\hbar}{(27.4\,amu)} \left| \frac{-185\,a_0(3.6\,G)}{\dot{B}} \right|$$

84 $$P(NaLi, 796G) \approx \frac{2\pi 10^{12}}{2}\frac{4\pi\hbar}{(4.8\,amu)}\left|\frac{+12\,a_0(2.2G)}{\dot{B}}\right|$$

85 $$P(NaLi, 1594G) \approx \frac{2\pi 10^{12}}{2}\frac{4\pi\hbar}{(4.8\,amu)}\left|\frac{+14\,a_0(\sim 8G)}{\dot{B}}\right|$$

The only parameters that can depend on a particular procedure are temperature, density and sweep rate. I have used 0.5 T_f as the temperature for both experiments, and 10^{12} for the densities. These are consistent with the published numbers[103] and with the values measured in our experiment, so quantum statistics are likely to have the same effect on the two systems.

The different masses, widths, and scattering lengths of the systems put these probabilities, for a given sweep rate $\dot{B}$, nearly equal for RbK and 1594G NaLi, and 796G NaLi would be lower by a factor of 4. However, sweep rate is a readily changed parameter in the lab, so this ratio is not meaningful on it's own.

The RbK experiment measured two-body molecule loss coefficients of around 10^{-9} cm^3/s near resonance. In this case the unitarity limited collision rate (for reduced mass of 51.3 in a Rb-RbK collision) would be 4×10^{-8} cm^3/s, 40 times higher than observed losses. They also observed losses being enhanced with scattering length as the resonance was approached (refer back to figure 8 in section 3.3.3). If NaLi losses were this close to the unitarity limit, it would be impossible to isolate molecules in this way.

These collision rates are calculated based on specific experimental parameters, but a more fundamental comparison can be performed by assuming a density of λ_{DB}^{-3} which corresponds to phase space density of 1. The unitarity limited loss rate would be

86 $$\Gamma = n\sigma v = \lambda_{atom}^{-3} 16\pi^3 \lambda_{red}^2 \sqrt{\frac{3k_bT}{m_{red}}} = \frac{\sqrt{6\pi}k_BT}{h}\left(\frac{m_{atom}}{m_{red}}\right)^{3/2}$$

The final dependence on the ratio of boson mass to reduced mass of the molecule/boson system does not cause a significant difference (this ratio is 4.9 for Na-NaLi and 3.2 for Rb-RbK). The difference in the unitarity loss coefficients reported above reflects differences in the particular experimental values reported, but this formula uses only definitions of phase space density and the unitarity limit.

We can also compare theoretical formation efficiency to loss probability in any sweep experiment. Theoretical predictions[111] suggest that loss coefficients would scale as a^4. The hard sphere interpretation would say cross section should scale as a^2, but inelastic processes would probably get even worse as the resonance is approached. By using a loss rate with power law dependence on scattering length:

87 $$\beta = \sigma v_{therm} = (constant)\, a^n v_{therm} = (constant)\left(a_{bg}\left(1+\frac{(\Delta B)}{(B(t))}\right)\right)^n \sqrt{\frac{3k_bT}{m}}$$

and integrating the 2-body collision rate across resonance:

88 $$\int_0^\infty \beta n_i dt = (constant)\sqrt{\frac{3k_bT}{m}}\, n_i \int_0^\infty \left(a_{bg}\left(1+\frac{(\Delta B)}{(B(t))}\right)\right)^n dt$$

we can find an analytical expression for total fractional molecular loss across resonance. We will ignore the background term in the scattering length expression. This part will be insignificant near resonance, although it will be important for molecule losses while separating and imaging the atoms. This leaves the resonant part

89 $$\int_0^\infty \beta n_i dt = (constant)\sqrt{\frac{3k_bT}{m}}\, n_i \int_0^\infty \left(\frac{(a_{bg}\Delta B)}{(B(t))}\right)^n dt$$

which cannot be avoided, as the molecules and atoms will experience this for any

experiment which crosses the Feshbach resonance. For a linear sweep, this integral takes the form:

90 $$(constant)\sqrt{\frac{3k_bT}{m}}n_i[\int_{Tc}^{\infty}(\frac{(a_{bg}\Delta B)}{(\dot{B}t)})^n dt+\int_0^{Tc}(2\pi\lambda_{dB})^2 dt]$$

where the unitarity limited scattering length is used as a cutoff to make the integral finite. The cutoff was implemented by defining a time Tc where the scatting length formula gives the same results as the unitarity limit, and evaluating the integral in a piecewise fashion before and after Tc. It turns out the two parts of the piecewise integral give similar contributions. After solving the integral and ignoring constants, the result is proportional to

91 $$n_i\sqrt{\frac{3k_BT}{m}}\frac{a_{bg}\Delta B}{\dot{B}}(2\pi\frac{h}{\sqrt{2\pi m k_bT}})^{2-2/n}$$

The precise implementation of the cutoff will affect the exact results, but the factor of $(2\pi\lambda_{dB})^{2-2/n}$ will always show up. This is significant, as it implies that while formation efficiency depends inversely on mass, integrated losses depend at least inversely on mass (for n = 2), but more severely for loss rates scaling with a higher power of scattering length. This could be one clue as to why the lightweight NaLi molecules have been more difficult to isolate than in the very similar case of RbK.

Note that this formula contains the same factor of $n/\dot{B}$ as the formation efficiency, implying that one does not gain significantly by changing atom density because changing the sweep rate compensates for both formation and losses. By taking the ratio of losses to molecule formation, almost all experimental parameters cancel:

92 $$\frac{P_{loss}}{P_{form}} = \frac{n_i \sqrt{\frac{3k_B T}{m}} \frac{a_{bg}\Delta B}{\dot{B}} \left(2\pi \frac{h}{\sqrt{2\pi m k_b T}}\right)^{2-2/n}}{\frac{2\pi T_f^{3/2} n_i}{8T^{3/2}} \frac{4\pi\hbar}{m} \left|\frac{a_{bg}\Delta B}{\dot{B}}\right|} \propto (mT)^{\frac{1}{n}-\frac{1}{2}} \frac{T^{3/2}}{T_f^{3/2}}$$

The T dependence in this result is not quite reliable, as formation saturates at $T/T_f = 0.5$ and the unitarity limited loss rate will likely saturate in the low-temperature limit as well. Therefore, if the temperature is near degeneracy, there is little else to do to optimize sample preparation in the hopes of obtaining good molecule formation and low loss.

In practice, the maximum surviving fraction is known to depend on density, perhaps due to the fact that if the density is high, losses during the time spent separating and imaging the molecules can become as important as the resonant processes. This makes it important to attempt a variety of methods and procedures.

In summary, there is no specific theoretical reason to assume that RbK should have a huge advantage over NaLi. Because we have explored a wide variety of experimental parameters and Feshbach resonances, it is unlikely that small variations in density, sweep rate, or temperature of any specific experiment can account for the difference either.

One significant difference could be the fact that RbK uses an open-channel dominated resonance while NaLi is closed-channel dominated, but there is no known reason that this should affect association through magnetic sweeps. A technical issue might be that the magnetic field noise of 10 mG is similar to δB_{open} for 796G, which would not be an issue for RbK. However, this is probably not the whole story as mentioned earlier in relation to the narrow Li_2 resonance.

Without the ability to measure NaLi lifetimes, we cannot be sure that the inelastic collisions tell the whole story of poor molecule production. Precise knowledge of the wavefunctions and matrix elements for NaLi molecules, combined with knowledge of trimer and tetramer states involved in the inelastic collisions, could be used to predict the loss coefficients and the ratio of elastic to inelastic collisions at unitarity. Such analysis requires extensive experimental spectroscopy and the concentrated efforts of talented theorists. However, if these valuable resources were readily available, what would be the fun of such challenging experiments as ultracold heteronuclear molecule formation?

7.5 General procedure for optimized molecule formation

In addition to motivating the model, the previous assumptions suggest a method for optimizing sweep rates for forming molecules if nothing is known about collisions or adiabatic formation. By modeling the asymmetric sweeps discussed in chapter 5, the coefficients for loss and formation can be found, and a time scale can be found where a significant amount of atom loss is attributed for molecule formation rather than just 3-body atomic loss.

By running the simulation for a range of time scales, the surviving molecule fraction is found to be optimum at somewhat faster sweeps than where molecule formation saturates (compare figures 28 and 29). This result agrees with intuition that molecule losses are very fast, so it is better to err on the side of inefficient formation

than to allow additional time for destructive molecular collisions.

These results suggest the following procedure to form and isolate molecules:

1. Perform backward sweeps (sweeps which cannot form molecules), finding the point at which 3-body losses result in 50% depletion of remaining atoms.
2. Perform forward sweeps at that rate and faster, looking for the fastest sweep that gives saturated formation efficiency, calculated from the atoms remaining after forward and backward sweeps:

   93 $$loss\ fraction\ due\ \text{to}\ molecules = \frac{backward\ fraction - forward\ fraction}{backward\ fraction}$$

3. Try isolating molecules using sweep rates that are 3-5 times faster than the sweep with maximum molecule formation.
4. If no molecules are formed, try sweeps that are up to 10 times faster or slower.
5. If there are still no results, begin looking for technical errors in the experiment or improving isolation and imaging techniques.

Once molecules are formed, they should be optimized empirically. The major advantage of this systematic method is that it requires no prior knowledge of collision rates, exact atom densities, exact resonance location, or any knowledge at all of the nature of the resonance beyond a rough idea of the location and width.

8

Many-body Physics Near a Feshbach Resonance

At many points in the previous chapters, we have mentioned that correlations, collective motion, and many-body effects complicate the dynamics near a Feshbach resonance. However, what causes confusion in one experiment can lead to great insight in another. As interactions become very strong, correlations and many-body effects can become as important as local two or three body processes.

This property, along with the tunability of strong interactions, the ability to measure complete density or momentum distributions, and the very low thermal energy allows unprecedented preparation and measurement of strongly correlated, non-equilibrium, and many body states. Ultracold atomic physics, especially with tunable interactions near a Feshbach resonance, has become a proving ground for complex condensed matter theories which cannot be directly tested in any other experiments[16,152-154].

8.1 Ferromagnetism vs. molecule formation in Li mixtures

As one example, consider what occurs in a sample of atoms, initially on the side of the Feshbach resonance with large positive scattering length, as it approaches the resonance. As the scattering length becomes large, the repulsive interactions create mean-field interaction energy. If the interaction is an interspecies interaction in a two-component gas, and intraspecies interactions remain constant, the gas may be able to lower it's energy by locally separating the two species. This is the logic behind the Stoner model for ferromagnetism[155], where the energy saved by segregating magnetic moment orientations in domains is greater than the energy required to establish the domains, leading to spontaneous long-range ordering of spins.

Recall that near a Feshbach resonance, large positive scattering lengths occur between free atoms only when there exists a weakly bound molecular state. This means that the repulsive state is not the ground state, but is only a metastable state which is susceptible to inelastic decay to molecules. Viewed in this way, the molecule association is the unwanted property in an experiment designed specifically to produce unique correlated states and inhomogeneous density with long-lived, long-range ordering.

8.1.1 Itinerant ferromagnetism in a Fermi gas of ultracold atoms

The material in the section is taken from the paper of the same name published

by our lab[11].

The Stoner model, first proposed in 1938[155], provides an intuitive argument for the tendency of electron spins to locally align in ferromagnetic materials. This textbook model for ferromagnetism requires no band structure or microscopic correlations to understand, but is a simple matter of balancing energies.

The energies to be balanced are the interaction energy, which occurs when wavefunctions from unlike spins overlap, and the kinetic energy, which is minimized by distributing both species homogeneously throughout the available volume.

We define the magnetization of the gas as:

94 $$\eta=\frac{(n_1-n_2)}{(n_1+n_2)}$$

This is 0 for a balanced mixture and +1 or -1 for a fully polarized mixture. The energy of the system takes the form:

95 $$E_f 2V(n_1+n_2)\{\frac{3}{10}[(1+\eta)^{5/3}+(1-\eta)^{5/3}]+\frac{2}{3\pi}k_f a(1+\eta)(1-\eta)\}$$

The term dependent on the dimensionless interaction parameter $k_f a$ is the interaction energy, and the term in square brackets is the kinetic energy (from the independent Fermi energies of the two spin states).

Two possible states of the system are shown in figure 30. Comparing the energy for the cases of zero magnetization:

96 $$E_f 2V(n_1+n_2)\{\frac{3}{5}+\frac{2}{3\pi}k_f a\}$$

and the case of maximal magnetization (+1 or -1):

97 $$E_f 2V(n_1+n_2)\{\frac{3}{10}[2^{5/3}]+0\}$$

we can see that maximal magnetization is favored for strong interactions (large $k_f a$), but zero magnetization is favored for weak interactions (small $k_f a$). Specifically, at $k_f a > \pi/2$ total energy is minimized at nonzero magnetization. An accurate treatment should take into account that the density of the gas changes with $k_f a$, so for a trapped atomic gas the critical value of $k_f a$ is reduced by about 15%, and a treatment which considers second order corrections predicts a critical value of 1.054[156].

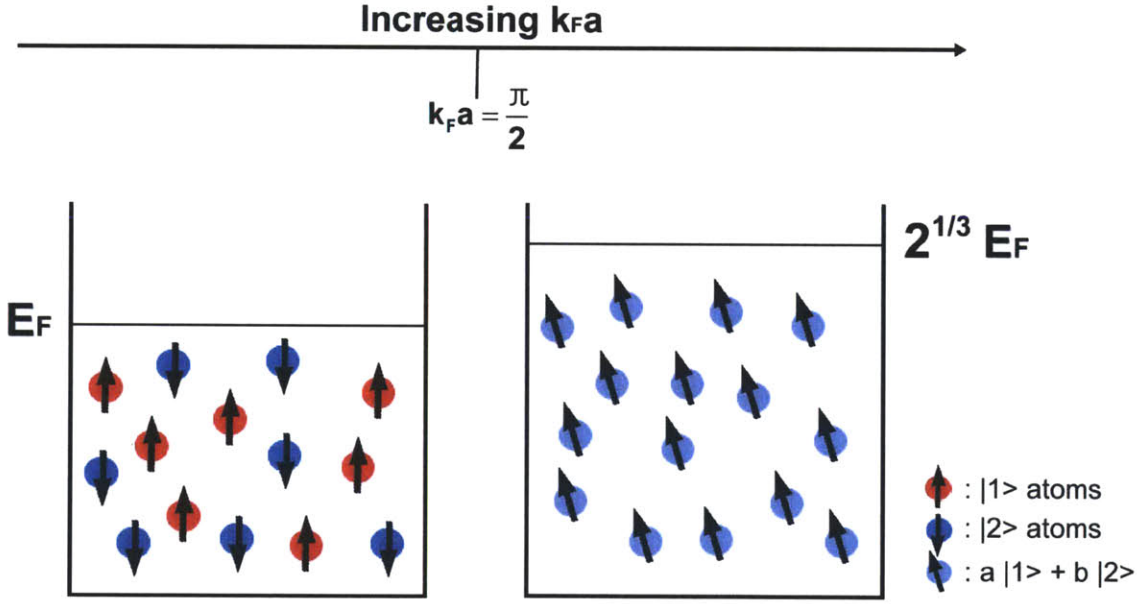

figure 30: The two many-body configurations considered in the Stoner model. At low interaction strength to the left, the atoms will stay mixed. At high interaction strength, the atoms can lower their energy by polarizing into one state, which can be a superposition of the initial states.

If the scattering length is tuned to be larger than this value, the separated state is energetically favorable to the mixed state. This is called the Stoner criterion. Note that

it does not depend on the fixed volume V, so it will apply even if only small parts of the cloud satisfy the criterion. There is a narrow window from

$k_f a = \pi/2$ to $k_f a = 3\pi/(2^{7/3}) \approx 1.19*\pi/2$ in the zero order theory, where the energy is minimized at intermediate values between zero and +1 or -1, but for larger $k_f a$ the system is predicted to fully magnetize.

Although intuitively appealing, the Stoner model has been in contention among theorists for some time[157]. The previous situation does not take into account metallic band structure or electron-electron correlations, which are important in any natural ferromagnet. Furthermore, it only suggests two possible states and calculates which has lower energy; this is far from a proof that the segregated state is the true ground state of the system under strong interactions.

Our experiment allows an idealized realization of the Stoner model. Li-6 atoms in an incoherent mixture (as opposed to a superposition) of the hyperfine states |1> and |2> are prepared in a harmonic trap with weak interactions by holding the mixture at 590 G. This weakly interacting mixture is known to assume the idealized fully mixed state shown on the left in figure 30. The magnetic field is then quickly ramped to a new field near the very wide Feshbach resonance centered near 834 G. Although the trapped gas is inhomogeneous, in the region of peak density we can readily achieve large $k_f a$, and studied values of $k_f a < 10$ in this experiment.

As mentioned numerous times in this thesis, many-body effects which affect the density distributions can have a major effect on collision rates. In this case, the inelastic collisions which cause decay into the molecular state require that both species

participate in the collision. Obviously, complete separation of the two species will prevent such collisions, greatly reducing the rate of atom loss. If the species remain mixed, on the other hand, collision rates will be enhanced as the magnetic field is brought close to resonance.

In the experiment, the collision rate gave a clear sign that there was a qualitative change in collision dynamics once a certain interaction strength was reached (see figure 31). The loss rate increased as the scattering length grew, but at $k_f a = 2.2$, the loss rate suddenly dropped. The critical interaction parameter is not the expected 1.054 of second order theory, or even $\pi/2$ as in the simple formula shown earlier. This shift of the observed critical interaction parameter has not been explained as of the writing of this thesis.

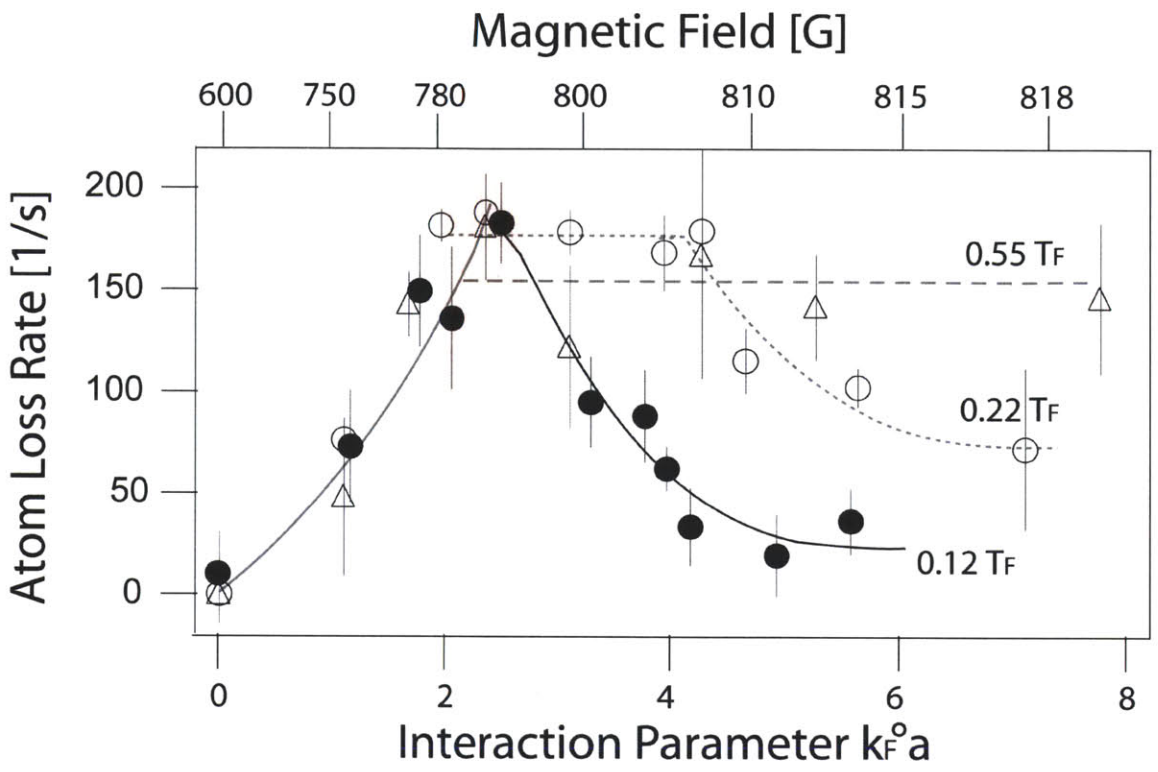

figure 31: Atomic loss rate in a repulsively interacting Fermi mixture. Because loss rate in such a mixture requires collisions between different spin states, this serves as a test of microscopic properties of the gas.

More evidence of a qualitative change in the system can be seen by studying thermodynamic quantities. By taking images of the atom cloud in the trap and after some ballistic expansion, we measured kinetic energy and cloud size (which reflects total energy of the gas, including interaction energy) finding that they also showed changes around $k_fa = 2$. (see figure 32) These changes qualitatively agree with mean-field predictions, suggesting our experimental results are compatible with the ferromagnetism interpretation, if not in quantitative agreement. The broadening of the

transitions can be attributed to inhomogeneous density of the trapped gas.

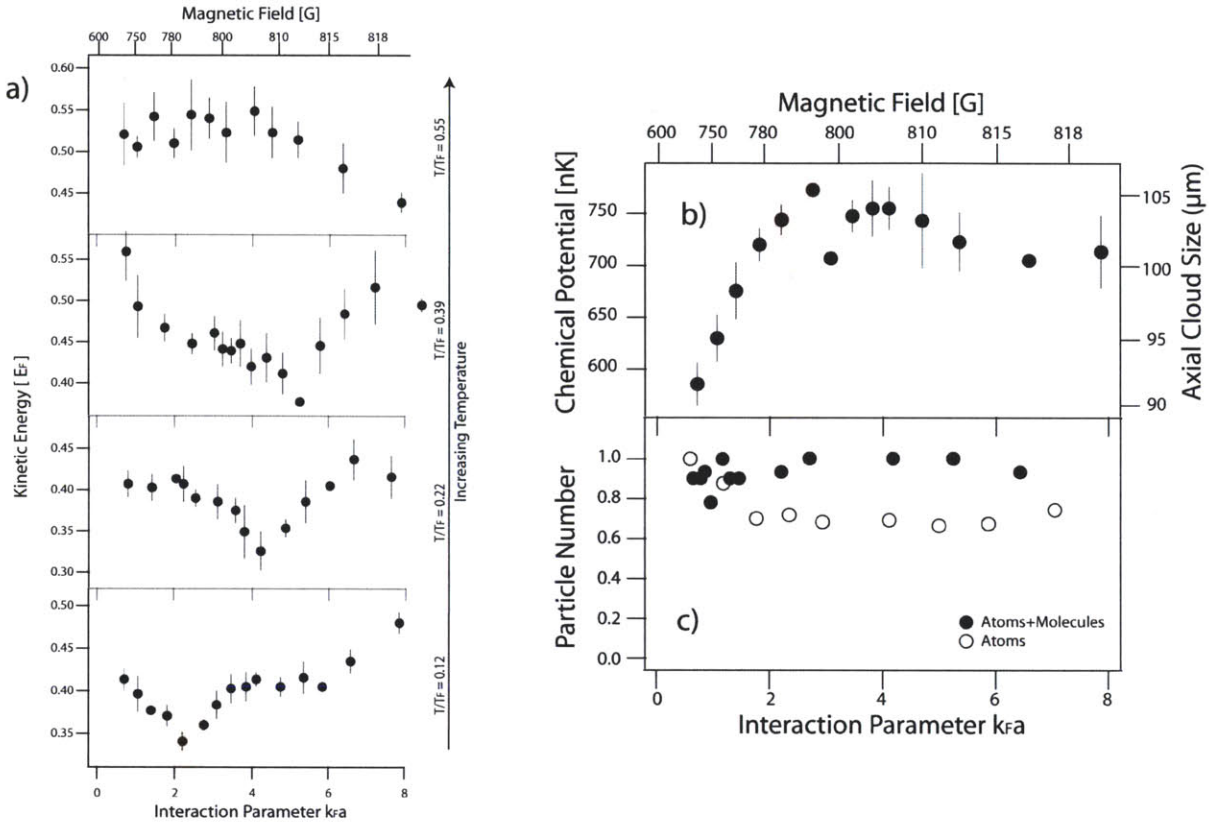

figure 32: More data from the repulsively interacting gas. a) shows the kinetic energy of the cloud at different temperatures and interaction parameters. b) shows cloud size, which reflects total energy. c) Shows the relative numbers of atoms and molecules for different experimental parameters.

These effects can be understood by the fact that when the gas polarizes, the kinetic energy increases with the Fermi energy of the polarized state, which would have twice the density per spin state as the unpolarized mixture if it did not expand. The cloud size, which normally increases with repulsive interactions, reaches a plateau because interaction energy is eliminated as kinetic energy increases, leading to a similar

value of total energy. An accurate thermodynamic treatment does predict a modest decrease (around 15%) in cloud size at the transition[11].

One major limitation of the experiment is the limited time for which the sample shows these properties. After more than a few ms, losses have reduced the density and produced a fair population of molecules (around 20%) in the trap, and the sample no longer resembles the idealized model. We were unable to observe ferromagnetic domains in images, possibly because they would be expected to take a finite amount of time to grow to a resolvable size.

8.1.2 Comparison of molecule formation and ferromagnetic ordering

Our maximum atomic lifetimes of 10 or 20 ms may be too short for domain formation. The experimental signatures suggest that something is happening; one would expect that domains must have macroscopic size to modify the thermodynamics and collisions in the observed way. Domains would be expected to form with small sizes and to grow as atoms near the boundaries migrate into domains with spin orientations matching their own.

Based the signal to noise of our images and our camera resolution (around 2 μm), and imaging a random arrangement of uniform sized domains in the sample, we should have observed domains if they were larger in volume that 5 μm^3. Domains smaller than this would contain fewer than 50 atoms, and the significance of the thermodynamic

effects expected from such small domains is a open question.

A rigorous study of the competition between molecule formation and ferromagnetic ordering was undertaken by David Pekker and colleagues[158]. The rates of both processes increase as the interaction parameter increases, and by theoretically calculating these rates, they calculated that pairing of atoms into molecules with finite kinetic energy was always faster than ferromagnetic ordering according to Stoner theory, but that ferromagnetic domain formation was fastest near $k_f a = 2$.

The decay of atoms into molecules could possibly be suppressed by using a closed-channel dominated Feshbach resonance. With such a resonance, there is a region of magnetic fields which are within ΔB (so interactions are enhanced), but outside δB_{open}, so coupling between the molecular state and the atomic state is small. As an example, with the narrow Li-6 resonance at 543G, for density of 10^{12} cm^{-3}, $k_f a = 4$ at a detuning $B-B_0 = 20\ \delta B_{open}$. At this detuning, decay into closed-channel molecules is likely slow, but the Stoner criteria is satisfied. However, this detuning corresponds to 3 mG, demanding better magnetic field stability than readily achievable in our lab (it would require magnetic shielding against environmental fields and 10^{-6} current stability). Also, the resonance is narrow, so only atom pairs in a narrow range of relative energies are strongly coupled, which may prevent system-wide thermodynamic signatures.

Other Feshbach resonances may have an experimentally accessible regime where thermodynamic effects are observed without fast decay into molecules. However, the fact that the interacting atomic state is only a metastable state on the repulsive side of the resonance means that the experiment will always involve competition between

inelastic decay and many-body ordering.

8.1.3 Further study

A vigorous debate exists among theorists about the true ground state of a two-state system of fermions with repulsive interactions, and without observing domains, our experiment has not conclusively settled the debate. There are open questions about the significance of correlations[159,160], the effects of the exact interaction potential[161], and the possible configurations that a harmonically trapped ferromagnetic system would adopt if it did exist[162,163].

A full review of the many proposed theories of itinerant ferromagnetism is beyond the scope of this chapter, but it is interesting to consider a few that have been applied to our system.

Hui Zhai and Xiaoling Cui have studied an alternative state similar to that originally proposed by Gutzweiler[157,159]. This state can be described as being macroscopically homogeneous (meaning zero magnetization everywhere in the cloud), but with microscopic correlations of the particles causing them to avoid collisions.

In one paper[160], Zhai studies the thermodynamic properties of an atomic Fermi system in such a state, and shows qualitatively similar signatures as were observed in our experiment. In another paper[159], Cui and Zhai study the energy of a single particle in a polarized Fermi sea undergoing a spinflip into a state possessing correlations similar to a Gutsweiler state, finding it can reduce total energy under some

circumstances.

These results do not attempt to prove that such correlated states are the true ground state, but rather show that such a state is a viable alternative to a proper ferromagnetic state with macroscopic domains. Without imaging domains, advances will be required both from theory and in experiment to obtain enough accuracy to conclusively distinguish between correlated states and ferromagnetism.

A theory group from Ohio State University has studied the importance of the form of the interaction potential in many-body studies[161]. A common choice is to use a hard-sphere potential with the same scattering length, as mentioned many times in this thesis and used in many theories, including those of Cui and Zhai. Such a potential ignores the existence of the bound state, however, so it may be better to use an accurate potential where the atoms are in the upper branch of a Feshbach resonance.

By performing quantum Monte Carlo calculations they observed that both potentials lead to similar criteria for the transition to the ferromagnetic state, but that collisions and short-range correlations are very different for hard-spheres than for the upper-branch of a Feshbach resonance. Because collisions and correlations play an important role in interpreting the experiment, this suggests that the proper potential is important for accurate conclusions about the existence of Stoner-type ferromagnetism.

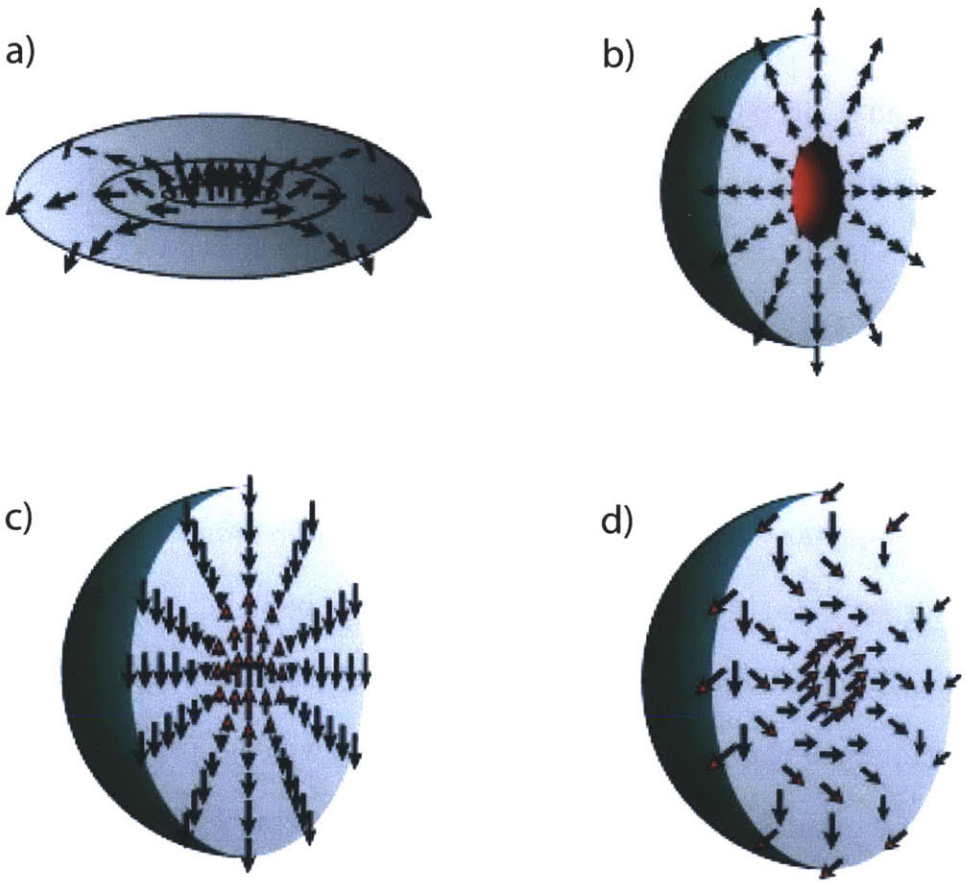

figure 33: Possible configurations of spins in a ferromagnetic Fermi gas. Images adapted from Berdnikov et. al. Phys Rev B, 79, 224403 (2009). The authors name these configurations a) skyrmion, b) hedgehog, c) domain wall, and d) single-axis twist

It is also important to understand the possible spin profiles of a trapped ferromagnetic gas. The picture of many randomly oriented small domains is one possibility, but for strong, many-body interactions, the trapped gas could take many possible configurations. Papers by research groups at University of Toronto[163] and Rutgers[162] suggest several possible spin configurations. See figure 34 for some images

from the Rutgers paper. These equilibrium configurations would had been evident in the experiment, although the growth rates and stability against inelastic collisions may be different than in the picture of small random domains.

The variety of approaches and results is indicative of the challenges of studying many-body, strongly correlated systems. Until it is possible to conduct a massive numerical Monte-Carlo analysis with realistic atom numbers and exact interaction potentials, any tractable many-body theory must make some approximations and work within current computational limits.

Overcoming the experimental limitations has proven difficult as well. Eddy currents limit the speed at which our magnetic field can be stabilized after large ramps, preventing us from instantaneously jumping from the weakly interacting mixed state to the strongly interacting regime. Molecule formation inevitably occurs until the atoms are fully separated, so the limit of preparation speed prevents us from observing idealized short-time dynamics of the system. Furthermore, pushing our resolution higher would require major changes to the apparatus, as we already operate close to the diffraction limit for our imaging system.

We also considered preparing the state by driving RF transitions from a weakly interacting hyperfine mixture to a strongly interacting one, which avoids the eddy current problem. Unfortunately the intermediate strongly interacting three-state mixture causes rapid decoherence and losses, leaving us no better off than the previous procedure which allows some molecule formation while the fields stabilize.

We are currently pursuing other methods of measurements on the repulsively interacting Fermi gas. By obtaining high quality images of imbalanced Fermi mixtures,

the inhomogeneous profile of the cloud can be used to extract thermodynamic quantities[164] such as pressure $P=\frac{\partial(n_1+n_2)}{\partial(\mu_1+\mu_2)}$ and spin susceptibility $\chi=\frac{\partial(n_1-n_2)}{\partial(\mu_1-\mu_2)}$. These quantities have well-known behaviors in weakly interacting ideal gases, but strong interactions can cause perturbations from many-body phenomena, such as ferromagnetism.

This method requires the system to reach a thermodynamic equilibrium, so it cannot probe the unstable regions studied in the previous experiment, but may give clues to the many-body dynamics even before a phase transition occurs. However, studies are still preliminary, and the reader will have to wait for further reports from our lab to hear the details and the outcome of those experiments

8.2 Interesting phases of Bose-Fermi mixtures

Although NaLi molecules may have very short lifetimes due to inelastic collisions, we have seen very long lifetimes in the Na and Li mixture even on resonance (recall figure 23 in chapter 5). As these lifetimes are many times the trap periods, and elastic collisions are known to be very strong on resonance, this offers us a chance to study the thermodynamics of a strongly interacting mixture of Bosons and Fermions, both in equilibrium and as it approaches equilibrium after some perturbation.

In the following sub-sections I provide a review of some interesting theoretical proposals which might be tested in an experiment such as ours. As we haven't seriously

addressed the feasibility of observing any specific phenomena, I do not go into great detail about possible experiments to accomplish these feats. However, similar to the ferromagnetism experiment, it can be assumed that a combination of long lifetime, fast, accurate magnetic field control, and high-quality imaging will be necessary in any study of these theories.

8.2.1 Bose-mediated Fermi-Fermi interactions

One physical system in which Bose-Fermi interactions are known to be relevant is in the early theories of superconductivity[165]. Although electrons in free space are known to be repulsive, in a lattice the coulomb repulsion is heavily screened. As an electron moves through the lattice, it attracts the positively charged ions in it's wake, causing regions of net positive charge. Because other electrons will be attracted to positive charges, this effect can be though of as weak electron-electron attraction, or more specifically, as attractive interactions mediated by phonons.

Phonons observe bosonic statistics, so this interaction is a three-body interaction where fermions interact indirectly via bosons. A system of non-interacting fermions (such as the Li in our NaLi mixtures), with tunable interspecies interactions with bosons (provided by the Feshbach resonances), would be an ideal situation to study such Boson-mediated Fermi-Fermi interactions[166]. However, initial predictions place the transition temperature for realistic experimental parameters as sub-nanokelvin temperatures, which is a challenge (but not an insurmountable one)[42,167].

8.2.2 Quantum phases of Bose-Fermi mixtures

The previous example is a situation which occurs in known materials, but examples of Bose-Fermi mixtures with conserved total particle number (such as our atomic mixtures), are not readily observed in nature. Ultracold gases with tunable interactions are thus a unique opportunity to study a novel system.

Francesca Marchetti and her collaborators developed a theory of the strongly interacting Bose-Fermi mixture and predicted possible quantum states which might arise[168]. Their model uses a mean-field theory that explicitly includes the molecular state in the Hamiltonian rather than only considering effective atom-atom interactions. The molecular state proves to be relevant to the quantum phases whether it is a real bound state or a quasi-bound state.

One particularly interesting prediction of the paper is the existence of a phase separated state when Bose-Femi interactions are strong and attractive. It is a well known fact that a low temperature cloud of bosons will undergo a "Bose-nova" and collapse if there are attractive effective interactions[169]. This is because the attractive interactions increase the density of the gas, which increases the attraction, which further increases the density, causing positive feedback where a BEC will contract to high density until it becomes unstable to many-body relaxation processes.

However, when coupling to the molecular state is considered, these interactions are accompanied by association with the fermions, which cannot increase to higher and

higher density because of Pauli-exclusion. The result of the analysis is a state where the bosons undergo a partial collapse, but are stopped once the Fermi pressure balances the attractive interaction. It's almost as if the bosons inherit some fermionic character because of molecular coupling to the Fermions.

A real study of such systems would be affected by inelastic decays when there is strong coupling to the molecular state, but a brief estimation in the paper suggests that the Na and Li system, with weak repulsive background interaction and long inelastic lifetimes, might be uniquely suited to observing the predicted dynamics. An additional paper from the group predicted the effects that could be seen by placing such a Bose-Fermi mixture in an optical lattice of one-dimensional tubes, with the reduced dimensionality producing further signatures of new quantum phases[170].

Another study predicts dynamics intermediate between Bose gases and Fermi gases by studying collective oscillation in an interacting Bose-Fermi mixture[171]. A BEC can undergo collective oscillations (sometimes referred to as hydrodynamic "breathing modes") at $\sqrt{5}\omega$ and $\sqrt{14}\omega$ where ω is the frequency of a single boson in the harmonic trap. On the other hand, a trapped Fermi gas can have similar collective oscillations at 2ω and 4ω. By varying the relative population of Fermions and Bosons, the theory predicts that frequencies of collective oscillations will vary continuously between the two cases, as if the mixture has hydrodynamic properties intermediate between those of bosons and fermions.

Dynamics in a Bose-Fermi mixture with arbitrary strong interactions is a very difficult problem for condensed-matter theorists. The fact that strongly interacting Bose-Fermi mixtures are rare in nature (the only quantum degenerate example is a

superfluid mixture of He3 and He4)[172] has further prevented physicists from developing intuition or even knowing what kind of interesting quantum phases might arise in such a system. The existence of Bose-Fermi atomic mixtures with tunable interactions allows the precise preparation and measurement techniques of atomic physics to be applied to these novel many-body systems, and may lead to a variety of interesting results in the future.

9

Conclusions

"Success is failure with no loss of enthusiasm" -

a fortune cookie

I have spent nearly 3 years of my Ph.D. studies working to form NaLi molecules, and during that time I have scrutinized existing research on ultracold atoms, molecular theory, Feshbach resonances, and inelastic collisions. I have been in frequent personal contact with other scientists, experimental and theoretical, and I have worked closely with several other talented students and post-docs.

Yet in that time, I have not succeeded in isolating a sample of NaLi molecules from their constituent atoms, nor have I succeeded in performing specific measurements to calculate exact collisional properties. The motivations for such measurements are many, not the least of which is to develop techniques which will help other groups perform similar experiments with molecules.

But no scientific labor is completely without fruit, and the only way to truly fail in science is to abandon a project before gaining any understanding of it. My efforts have not yet solved the problems I set out to solve, but my determination and perseverance

have brought me from utter confusion to some degree of understanding.

9.1 Choosing the right molecules for the right reasons

A large part of the difficulty in any new experiment is the fact that much is unknown. This is rather obvious; there is little scientific motivation to study systems which do not hold any mysteries. Perfect knowledge of one's field of study is an exciting prospect, but a scientist would quickly become bored without unanswered questions.

When I began my Ph.D studies, the only thing that was known about ultracold NaLi molecules were the locations of a few Feshbach resonances and decades old spectroscopy data on deeply bound molecular states. Details about the collisional properties, formation efficiency in quantum gases, or the influence of strong interactions at heteronuclear Feshbach resonances were guessed at, but not proven in experiments or rigorous theories.

In spring and summer of 2006, shortly after I came to MIT, Silke and Christian Ospelkaus, working in the research lab of Klaus Sengstock in Hamburg Germany, performed some groundbreaking experiments on Rubidium and Potassium in an optical lattice, and showed some of the first interesting results regarding heteronuclear molecules[26,173,174]. It was not too long after this that we decided to try out our favorite atoms, Sodium and Lithium, in a heteronuclear molecule experiment. We had had great success using these atoms to produce large degenerate gases, and they were known to have good atomic collision properties.

Looking back, it is easy to say that I could have found more exciting results and written more papers if I had chosen another goal. I can also say that we have always had promising leads and exciting new ideas that spurred us forward. To abandon the project at any point during my thesis work would have been the wrong decision at the time.

However, the particular methods and goals of our NaLi work could have been much more focused and informed if I knew then what I know now. For any ultracold physicist looking to start a new experiment on molecules, I think the most important results from this thesis are the formulas and experimental methods which require only the experimentally relevant parameters of atomic masses, a_{bg}, B_0 and ΔB. It is helpful to know the quantum state and magnetic moment of the target molecule for some formulas as well, although these can be guessed at in most circumstances.

First, the resonance should be identified as broad or narrow. Find the coupling energy scale

98 $$E_0 = \frac{m(\Delta B \Delta \mu a_{bg})^2}{2\hbar^2}$$

and comparing it to the typical energy spread of an ultracold gas.

If the coupling is much larger than thermal energies, Fermi energy, or the chemical potential of a BEC, the resonance is broad, and is useful for studies of thermodynamics and unitarity limited quantum behavior. The very broad Li_2 resonance has produced spectacular results along these lines.

However, if the resonance is narrow, such as in NaLi (where E_0 = 3 kHz, which corresponds to a temperature of around 150 nK, lower than typical temperatures in our experiments), it will be useful for studying few body physics, such as molecule formation

and collisions. In such a gas, only a limited fraction of the particles are resonantly interacting; this could simplify the interpretation of few body physics (such as collisions or molecule formation), without system-wide effects such as thermodynamic phase transitions complicating the interpretation of the data.

The narrow/broad distinction depends on the density and temperature of the gas. The resonance should also be identified as open-channel or closed-channel dominated, which depend only on the resonance and not on the experimental details of the system. The range of strong mixing of the atomic and molecular states

$$\delta B_{open} = \frac{E_0}{\Delta \mu} \qquad 99$$

should be compared to the ΔB, the range of field-dependent interactions. An open-channel dominated resonance allows strong transitions between atomic and molecular states even away from the strongly interacting regime, making it a good candidate for RF association and spectroscopy. It also gives a large range of fields to study the dynamics of Halo dimers, where the molecules resemble strongly interacting atoms more than deeply bound molecules.

If the resonance is closed-channel dominated, on the other hand, it resembles a molecule for nearly all fields in the vicinity of the Feshbach resonance. In our experiment, this has prevented RF association or spectroscopy of the binding energy (unfortunately I didn't come to this conclusion until spending quite some time on RF spectroscopy), but if long-lived close-channel molecules can be created, they may offer a good system to study dynamics which rely on the molecules behaving like true molecules with limited atomic character.

The broad/narrow distinction and the open-channel/closed-channel distinction are closely related (they both depend on the energy scale E0), but the distinctions do not exactly coincide, and the broad/narrow distinction, which depends on temperature and density, may vary from experiment to experiment even when the same resonance is used.

With a goal in mind, the measurement techniques described in chapters 6 and 7 can be performed even with no additional knowledge of the resonance or the molecules. Using the formulas and models described in chapter 7, the results of these measurements can be used to identify the importance of collisional losses in the system, even if no molecules have been isolated yet. Also, the formulas used in the model can compare experiments involving completely different atomic species, so existing knowledge can be applied to a newly discovered Feshbach resonance.

With some critical thinking before beginning the difficult task of studying ultracold molecules, one can be sure to choose appropriate goals and avoid methods which will be difficult or impossible. The successes of groups studying ultracold molecules prove that there are many interesting possibilities for such experiments, yet there are few suggestions in the literature of systematic ways to approach a new experiment. Hopefully the knowledge I've obtained dealing with the frustrations of forming NaLi can inform scientists embarking on a new project in Feshbach resonances

9.2 Possibilities for NaLi

We have not yet exhausted possible techniques for obtaining useful results from strongly interacting mixtures of Na and Li. There is a chance that with a few tweaks the same techniques described in this thesis will produce and isolate sufficient NaLi for interesting experiments. These methods include improvements in imaging, the introduction of a crossed dipole trap which will strongly confine all molecular states and assist in separation of atoms and molecules, and improving sample preparation and magnetic field control at the high-field 1594 resonance (with my apologies to the magnetic coils of the science chamber).

However, these changes are at best incremental improvements in the methods used up until this point. It is my conclusion that the most significant challenge in forming NaLi molecules is large inelastic losses with 2-body loss coefficients larger than $\beta = 10^{-10}$ cm3/s. If the loss coefficient is close to this value, factors of 2 or 4 in formation efficiency or detection techniques could be all that is required. However, if the coefficient is an order of magnitude higher, drastic changes are necessary.

It is also possible that magnetic field noise of order δB_{open} could be inhibiting efficient molecule formation. The use of the broader 1594 resonance (with δB_{open} ~ 100mG) could help protect against this possibility.

One option to drastically improve the survivability of molecules is to put the atoms in an optical lattice. Although operating an optical lattice requires time, patience and experience, many groups (including two of the Ketterle labs), have succeeded, and the techniques are becoming routine for atomic physics. A lattice will make it possible to isolate a few atoms at each lattice site, and any sites which hold exactly one of each pairing partner can form a molecule which is immediately isolated from further

collisions.

If molecules can be successfully formed, the cooling lasers can be used for spectroscopy among the most weakly-bound molecular states. Measurements of transitions among these states can provide useful information on the long range molecular potentials. This knowledge is valuable to molecular theorists simply because it can't be obtained with other methods. But it will also be useful for performing Raman or STIRAP transitions to more deeply bound states of the molecules, which could be used to study dipolar physics or quantum chemistry.

Even if ultracold NaLi molecules are never formed, the long atomic lifetimes on resonance suggest that strongly interacting NaLi is a good proving ground for theories about Bose-Fermi interactions and quantum phases. Some examples of such experiments were mentioned in Chapter 8; in fact the papers by Francesca Marchetti specifically predict the 796G resonance in NaLi to be a good candidate to observe their predictions[168]. These experiments do not require isolated, long-lived molecules, but do require large samples of long-lived samples of atoms which can reach thermal equilibrium, which has been the advantage of Na and Li mixtures all along.

9.3 Coda: the motivations of a scientist

The pursuit of science is an uncertain business, and success in research can hardly be quantified in terms of satisfied and unsatisfied goals. Through careful work, continuous review of theory and experimental methods, and determination, the growth

of knowledge is guaranteed. Although the outcome of any particular experiment is never certain, the net result of my countless small experiments on NaLi has been a steady crawl from confusion to understanding; hopefully my labor and this thesis will assist future scientists in their endeavors.

I have always loved working with complicated machines, solving mysterious problems in science or in engineering, and consuming obscure and confusing texts for no reason other than to broaden my intellectual horizons. I have become elated with successes in the lab, however small they may have been, and felt a strong sense of satisfaction upon understanding a theory which had previously left me baffled.

Although one must choose goals based on their potential benefits, whether for all of humanity or just for a small scientific sub-field, I believe results can not be the sole motivation of a scientist. Neither can the only motivation be fame, glory, or a job security in a tenured position at a respected university. There are other career paths that can provide these benefits with more certainty and less effort.

I think the most important motivation of a scientist should be curiosity. It is curiosity that pushes the frontiers of knowledge, it is curiosity that guides the mind of a young student learning a new field, and it is curiosity that keeps a grad student awake through the evening, night and morning in an attempt to finally complete an important set of data. It was certainly curiosity that kept me searching for new ideas and new data without ever catching a glimpse of an isolated molecule of NaLi.

Every experiment involves long periods of confusion before final data can be collected and papers written. Science is hard, but scientists know it and expect it. Curiosity, combined with patience (or stubbornness), is what kept me optimistic

through the inevitable frustration of the difficult experiments that I have performed in order to write this thesis.

Now, in the last paragraph of the longest paper I hope to ever write, I am happy to say that I have enjoyed my time in the MIT Physics department, and my efforts to advance physics have been successful. As I move on with my career in science, I can say with confidence that my curiosity is a strong as it was on the day I started school over 22 years ago, and it will continue to guide me in all my future adventures.

Appendix A

Diode laser system for Lithium-6

The following page contains a diagram of the laser table we use to produce light for cooling and manipulating Lithium-6. The heart of the table is a DL-100 grating stabilized diode laser producing 25 mW of 671 nm light which is locked to an atomic reference cell. An interested reader can refer to the Ph.D. thesis of Zoran Hadzibabic for a comprehensive review of the motivations and techniques for the Lithium laser system. I give Tout Wang full credit for the layout of this diagram.

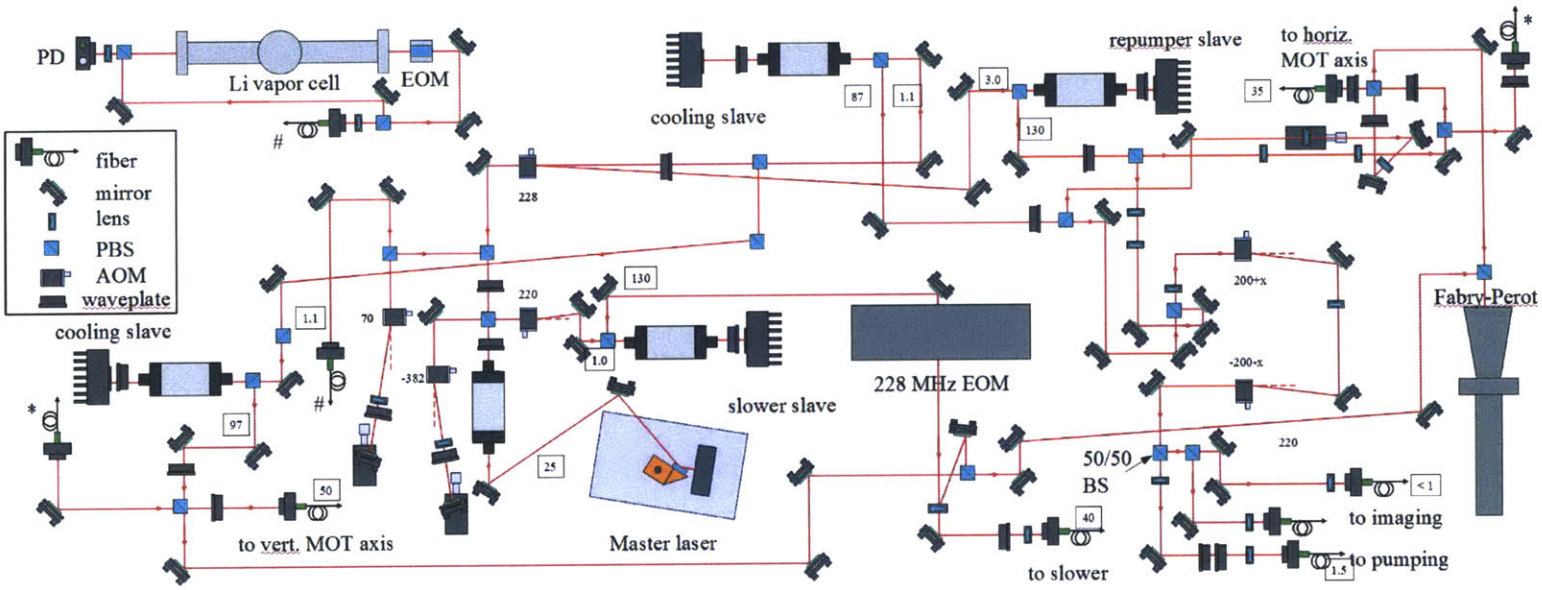

figure 34: Overview of the Li laser system. Numbers in boxes give laser power, in mW, with power next to fibers indicating the coupled power, and MOT fibers having a balance of cooling:repumper light of about 3:2. Numbers without boxes give AOM frequency shifts. Also note that the fibers labeled * and # connect from one part of the table to another, rather than travelling to the experiment.

Appendix B

Phase Sensitive Recombination of two Bose-Einstein Condensates on an Atom Chip

The recombination of two split Bose-Einstein condensates on an atom chip is shown to result in heating which depends on the relative phase of the two condensates. This heating reduces the number of condensate atoms between 10% and 40% and provides a robust way to read out the phase of an atom interferometer without the need for ballistic expansion. The heating may be caused by the dissipation of dark solitons created during the merging of the condensates.

PRL 98, 180401 (2007) PHYSICAL REVIEW LETTERS week ending 4 MAY 2007

Phase-Sensitive Recombination of Two Bose-Einstein Condensates on an Atom Chip

G.-B. Jo, J.-H. Choi, C. A. Christensen, T. A. Pasquini, Y.-R. Lee, W. Ketterle, and D. E. Pritchard*
MIT-Harvard Center for Ultracold Atoms, Research Laboratory of Electronics, Department of Physics, Massachusetts Institute of Technology, Cambridge, Massachusetts 02139, USA
(Received 28 February 2007; published 30 April 2007)

The recombination of two split Bose-Einstein condensates on an atom chip is shown to result in heating which depends on the relative phase of the two condensates. This heating reduces the number of condensate atoms between 10% and 40% and provides a robust way to read out the phase of an atom interferometer without the need for ballistic expansion. The heating may be caused by the dissipation of dark solitons created during the merging of the condensates.

DOI: 10.1103/PhysRevLett.98.180401 PACS numbers: 03.75.Dg, 03.75.Lm, 39.20.+q

Most experiments in atom interferometry use freely propagating atom clouds [1–3]. Alternative geometries are confined-atom interferometers where atoms [3] are guided or confined in trapping potentials [4], often realized by using atom chips [5]. These geometries are promising in terms of compactness and portability, and also offer the prospect of extending interrogation times beyond the typical 0.5 s achievable in the atomic fountains. Such interferometers can be used to study atom-surface interactions [6] and Josephson phenomena [7].

Many discussions of confined-atom interferometers propose a readout by merging the two separated clouds [8–10]. These discussions usually assume noninteracting atoms [8,11] and do not address the deleterious effects of atomic interactions, including dephasing, collisional shifts, and phase diffusion [12–17]. A recent study showed that the recombination process is much more sensitive to atomic interactions than the splitting process since merging clouds with the opposite phase involves excited modes of the recombined potential and can lead to exponential growth of unstable modes [18]. To circumvent these problems, previous realizations of confined-atom interferometry used ballistic expansion of the two spatially independent condensates, which decreases the atomic density before overlap [4,19–21] or worked at very low atom densities and pushed the clouds into each other with photon recoil [22,23]. While this avoids the deleterious effects of atom-atom interactions during the recombination, it lacks the inherent simplicity and robustness of in-trap recombination. Furthermore, in-trap recombination, combined with dispersive, *in situ*, imaging [24], could make it possible to recycle the condensate for the next measurement cycle after resetting the temperature through evaporating cooling. The detection optics for *in situ* imaging may even be integrated onto the atom chip [25]. Moreover, a trapped sample at high optical density can be read out with subshot noise precision using cavity-enhanced atom detection [26].

In this Letter, we show that in-trap recombination leads indeed to heating of the atomic cloud. However, this heating is phase dependent and can be used as a robust and sensitive readout of the atom interferometer. The resulting oscillations of the condensate atom number are dramatic (typically ~25% contrast), occur over a wide range of recombination rates, and permit high signal to noise ratios since they simply require a measurement of the total number of condensate atoms in the trap.

The implications of phase-sensitive recombination extend beyond atom interferometry. Recombination with uncontrolled phase was used to replenish a continuous Bose-Einstein condensate (BEC) [27] or to create vortices [28]. An extreme case of the merge process, where two condensates are suddenly connected, has been studied by optically imprinting a dark soliton into a single trapped condensate [29,30]. Here we use methods of atom interferometry to prepare two condensates with well-defined relative phase and study the merging process for variable recombination times.

Two special cases of the merging process can be exactly described (Fig. 1). Two noninteracting separated condensates with the same phase should adiabatically evolve into the ground state of the combined potential, whereas a π-relative phase should result in the lowest lying antisymmetric state with excitation energy $N\hbar\omega$, where N is the total number of atoms in a trap and ω is the transverse frequency of the trapping potential. The other limiting case is a merging process where a thin membrane separates two interacting condensates until the potentials are merged, and then is suddenly removed. For the 0-relative phase, the merged condensate is in its Thomas-Fermi ground state. For a π-relative phase, however, the merged condensate contains a dark soliton. Although the wave function differs from the ground state only in a thin layer, the total energy of this excited state is proportional to $N\hbar\omega$, as the lowest antisymmetric state in the noninteracting case [31].

Our working assumption is that the phase-sensitive excitation of the cloud decays quickly, on the order of ~1 ms in our system, and leads to an increase in temperature on the order of $\hbar\omega/k_B \simeq 100$ nK for the case of $\Delta\phi = \pi$, and less for other values of $\Delta\phi$, where k_B is the Boltzmann constant. The parameters of our experiment were intermediate between limiting cases of suddenness or adiabaticity, and we found a window of recombination times for

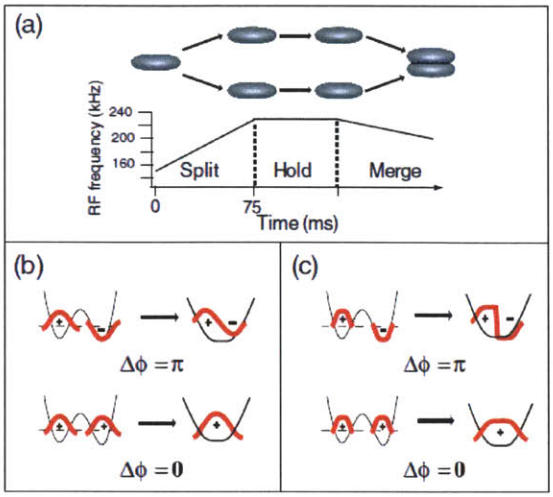

FIG. 1 (color online). Schematic of the in-trap recombination with a well-defined relative phase. (a) The phase-coherent condensates were prepared using a radio frequency induced double-well potential on an atom chip [21]. The splitting was done within 75 ms by ramping up the rf frequency from 140 to 225 kHz. During the hold time, the relative phase of two independent condensates evolved with time at ~500 Hz. After a variable time, the double-well potential was deformed into a single well and the two trapped condensates were merged by decreasing the rf frequency by 33 kHz over a variable "recombination time." The condensates started to spill over the barrier after ≤10% of the recombination time or ~3 kHz decrease of the rf frequency. (b),(c) The merged matter-wave functions are shown for the cases of an adiabatic merger of noninteracting condensates and for a sudden merger of interacting condensates.

the phase-sensitive readout to which none of these descriptions apply.

Bose-Einstein condensates of $\sim 4 \times 10^5$ ^{23}Na atoms in the $|F = 1, m_F = -1\rangle$ state were transferred into a magnetic trap generated by the trapping wire on an atom chip and an external bias field [19]. The cloud had a condensate fraction $\simeq 90\%$ and the temperature was $\sim 1/2$ of the BEC transition temperature, well above 0.1 when axial phase fluctuations are excited. Using adiabatic rf-induced splitting [20,32], a double-well potential in the horizontal plane was formed. Typically, the separation of the two wells was $d \sim 6\ \mu$m, the height of the trap barrier was $U \sim h \times 10$ kHz, and the chemical potential of the condensates, measured from the trap bottom, was $\mu \sim h \times 6$ kHz, where h is Planck's constant. In the experiment, the coherence time of two separated condensates was at least ~50 ms [21]. The recombination of two split condensates was realized by reducing the rf frequency as described in Fig. 1(a), which decreases the trap barrier height. The merging occurred slowly compared to the time scale determined by the radial trap frequency (~1 kHz) to minimize mechanical excitation.

To monitor the energy increase after recombination, we measured the central atom density during ballistic expansion. Phase-sensitive collective excitations, in addition to mechanical excitations from the splitting and merging processes, heat the cloud and lower the condensate fraction and, therefore, reduce the central density. In the experiment, the split condensates were held in the double-well potential for varying hold times, merged into a single potential, and released by turning off the trapping potential within 30 μs. After 8 ms time of flight, we measured the number of atoms in a fixed area which is comparable to the size of (expanded) Thomas-Fermi radius [dotted box in Fig. 2(c)]. While the total atom number was conserved, the number within the fixed area decreased, indicating that the temperature had increased. The fractional loss of condensate atoms was obtained as the ratio of atom number after recombination to the atom number before splitting.

The fractional loss of condensate atoms was reproducible for a given hold time, and observed to oscillate between 15% and 35% as a function of hold time at a rate of 500 Hz (Figs. 2 and 3). The observed oscillations are sinusoidal, although the nonlinear interactions can give rise to nonsinusoidal variations [16]. To confirm that this oscillatory heating was associated with the relative phase of the split condensates, we measured the relative phase as the spatial phase of the interference pattern when the split condensates were suddenly released and interfered during ballistic expansion [Fig. 2(a)] [4]. The strong correlation between the two measurements [Fig. 2(b)] is the central result of this Letter. As the relative phase increased from 0 to π, the atom loss after recombination increased [Fig. 2(b)]; the π-relative phase (0-relative phase) difference leads to maximum (minimum) loss of condensate atoms.

The use of phase-sensitive recombination as a readout for an atom interferometer is demonstrated in Fig. 3. The separated condensates accumulate relative phase for an evolution time of up to 6 ms which is read out after in-trap recombination. The phase-sensitive recombination signal showed high contrast over a wide range of recombination times [Figs. 3 and 4(a)]. The observed largest amplitudes of condensate atom loss correspond to a change in temperature on the order of ~100 nK, in agreement with the estimate in the introduction. This is testimony to the insensitivity of the energy of phase-dependent excitations against changes in the exact recombination parameters, and is promising for further applications of chip-based atom interferometry.

The dependence of the condensate atom loss on the recombination time allows us to speculate about different excitations caused by the merging process. The 1 ms recombination time shows little contrast [Fig. 3(d)]. This time scale is comparable to the period of radial oscillations, and one would expect breakdown of adiabaticity and excitation of collective excitations independent of the relative phase. Significant loss (~30%) was observed for all relative phases and masked or suppressed any phase-sensitive signal. The loss of contrast for the long recombination

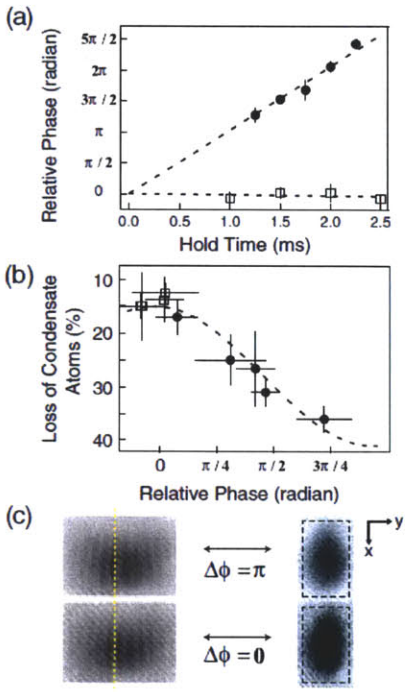

FIG. 2 (color online). Phase-sensitive recombination of two separate condensates. (a) The relative phase of two split condensates was monitored for various hold time after splitting by suddenly releasing the two condensates and observing interference fringes. For the independent condensates (solid circle), the evolution rate of the relative phase was determined from the linear fit to be ~500 Hz. For the weakly coupled condensates (open square), the relative phase did not evolve. At 0 ms hold time, the relative phase was set to zero for both cases. (b) For the same range of delay times as in (a), the condensate atom loss after in-trap recombination was determined. The relative phase (x axis) was obtained from interference patterns as in (a). The merging time was 5 ms. (c) The matter-wave interference patterns (after 9 ms time of flight) and absorption images of merged clouds (after 8 ms time of flight) show the correlation between phase shift and absorption signal. The field of view is 260×200 μm and 160×240 μm for matter-wave interferences and merged clouds, respectively.

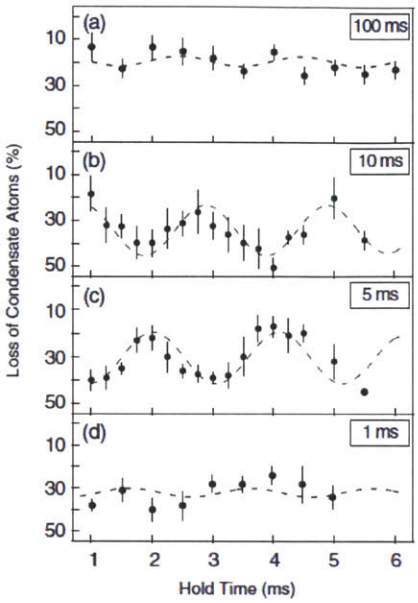

FIG. 3. Oscillations of condensate atom loss after recombination reflecting the coherent phase evolution. The condensate atom loss was monitored during a variable hold time for the two split condensates whose relative phase evolved at ~500 Hz. The merging was done for different values of the recombination time: 100 (a), 10 (b), 5 (c), and 1 ms (d). The dotted lines are sinusoidal curves fitted with fixed frequency ~500 Hz. The reproducible phase shift for the 5 and 10 ms data occurred during the recombination process. The data points represent the average of 6 measurements.

times could be caused by relaxation of the phase-sensitive collective excitation during the merging process when the condensates are connected only by a region of low density, and solitonlike excitations have lower energy. An alternative explanation is the evolution of the relative phase (at ~500 Hz) during the effective recombination time. In a simple picture assuming a thin membrane being slowly pulled out between the condensates, a phase evolution during this time would create local solitons with phases varying between 0 and π. This could wash out the phase-sensitive signal to an average value. Since the data for 100 ms recombination time show low loss [comparable to the zero relative phase loss for faster recombination times, Fig. 3(d)], we favor the first explanation. Furthermore, it is not clear during what fraction of the ramp time of the rf frequency (called the recombination time) the effective merging of the condensates and the creation of a phase-sensitive collective excitation occurs. The time between when the barrier equals the chemical potential and when the barrier reaches ~70% of the chemical potential is 10% of the recombination time. Another open question is what the rate of phase evolution is at the moment of the merger. It is plausible that during splitting, the condensates have the same chemical potential, and that the observed difference is created only when the condensates are further separated by ramping up the barrier. This would imply that during recombination, the situation reverses, the chemical potential difference is reduced and reaches near zero when the condensates merge. In any case, our work raises intriguing questions for further experimental and theoretical studies: What kind of phase-sensitive excitations are created during a merger process? How and when do they dissipate, and what would happen when two condensates with different chemical potentials are merged?

The present work demonstrates that interactions between atoms and collective excitations are not necessarily deleterious to direct recombination of separated trapped

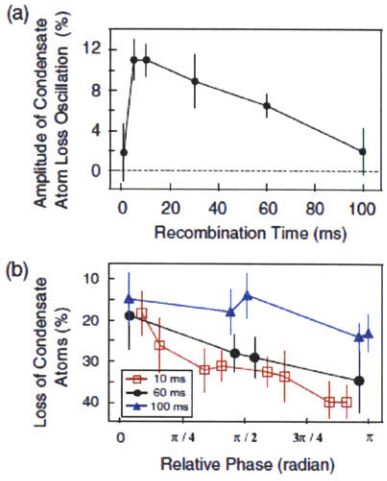

FIG. 4 (color online). Recombination time and atom loss. (a) The amplitude of atom loss oscillations was determined for various recombination times. (b) Assuming that minimum atom loss occurs at 0-relative phase of the two condensates, relative phases were obtained from the fitted atom loss oscillations in Fig. 3.

condensates that have acquired a relative phase in atom interferometry. In contrast, the phase-sensitive generation of collective excitations is used to monitor the relative phase. This complements our previous work where atomic interactions were shown to enhance the coherence time by preparing a number squeezed state with the help of atomic interactions during the beam splitting process [21]. So the merger between condensed matter and atomic physics goes both ways. In recent years, atomic physics has developed powerful tools to study many-body physics [33], and, as we have shown here, many-body physics provides methods and tools to atom optics.

This work was funded by DARPA, NSF, and ONR. G.-B. Jo and Y.-R. Lee acknowledge additional support from the Samsung Foundation. We would like to acknowledge Y. Shin for useful discussions, and M. Vengalattore and M. Prentiss for atom chip fabrication.

*Electronic address: http://cua.mit.edu/ketterle_group/

[1] D. W. Keith, C. R. Ekstrom, Q. A. Turchette, and D. E. Pritchard, Phys. Rev. Lett. **66**, 2693 (1991).
[2] M. Kasevich and S.Chu, Phys. Rev. Lett. **67**, 181 (1991).
[3] P. Berman, *Atom Interferometry* (Academic, New York, 1997).
[4] Y. Shin, M. Saba, T. A. Pasquini, W. Ketterle, D. E. Pritchard, and A. E. Leanhardt, Phys. Rev. Lett. **92**, 050405 (2004).
[5] J. Fortagh and C. Zimmermann, Rev. Mod. Phys. **79**, 235 (2007).
[6] J. D. Perreault and A. D. Cronin, Phys. Rev. Lett. **95**, 133201 (2005).
[7] M. Albiez, R. Gati, J. Folling, S. Hunsmann, M. Cristiani, and M. K. Oberthaler, Phys. Rev. Lett. **95**, 010402 (2005).
[8] W. Hänsel, J. Reichel, P. Hommelhoff, and T. W. Hänsch, Phys. Rev. A **64**, 063607 (2001).
[9] J. A. Stickney and A. A. Zozulya, Phys. Rev. A **66**, 053601 (2002).
[10] A. Negretti and C. Henkel, J. Phys. B **37**, L385 (2004).
[11] E. Andersson, T. Calarco, R. Folman, M. Andersson, B. Hessmo, and J. Schmiedmayer, Phys. Rev. Lett. **88**, 100401 (2002).
[12] Y. Castin and J. Dalibard, Phys. Rev. A **55**, 4330 (1997).
[13] M. Lewenstein and L. You, Phys. Rev. Lett. **77**, 3489 (1996).
[14] E. M. Wright, D. F. Walls, and J. C. Garrison, Phys. Rev. Lett. **77**, 2158 (1996).
[15] J. Javanainen and M. Wilkens, Phys. Rev. Lett. **78**, 4675 (1997).
[16] A. J. Leggett and F. Sols, Phys. Rev. Lett. **81**, 1344 (1998).
[17] J. Javanainen and M. Wilkens, Phys. Rev. Lett. **81**, 1345 (1998).
[18] J. A. Stickney and A. A. Zozulya, Phys. Rev. A **68**, 013611 (2003).
[19] Y. Shin, C. Sanner, G.-B. Jo, T. A. Pasquini, M. Saba, W. Ketterle, D. E. Pritchard, M. Vengalattore, and M. Prentiss, Phys. Rev. A **72**, 021604 (2005).
[20] T. Schumm, S. Hofferberth, L. Andersson, S. Wildermuth, S. Groth, I. Bar-Joseph, J. Schmiedmayer, and P. Krüger, Nature Phys. **1**, 57 (2005).
[21] G.-B. Jo, Y. Shin, S. Will, T. A. Pasquini, M. Saba, W. Ketterle, D. E. Pritchard, M. Vengalattore, and M. Prentiss, Phys. Rev. Lett. **98**, 030407 (2007).
[22] O. Garcia, B. Deissler, K. J. Hughes, J. M. Reeves, and C. A. Sackett, Phys. Rev. A **74**, 031601(R) (2006).
[23] E. Su, S. Wu, and M. Prentiss, physics/0701018.
[24] M. R. Andrews, M.-O. Mewes, N. J. van Druten, D. S. Durfee, D. M. Kurn, and W. Ketterle, Science **273**, 84 (1996).
[25] T. Steinmetz, A. Balocchi, Y. Colombe, D. Hunger, T. Hänsch, R. Warburton, and J. Reichel, physics/0606231.
[26] I. Teper, Y.-J. Lin, and V. Vuletic, Phys. Rev. Lett. **97**, 023002 (2006).
[27] A. P. Chikkatur, Y. Shin, A. E. Leanhardt, D. Kielpinski, E. Tsikata, T. L. Gustavson, D. E. Pritchard, and W. Ketterle, Science **296**, 2193 (2002).
[28] D. R. Scherer, C. N. Weiler, T. W. Neely, and B. P. Anderson, cond-mat/0610187.
[29] S. Burger, K. Bongs, S. Dettmer, W. Ertmer, K. Sengstock, A. Sanpera, G. V. Shlyapnikov, and M. Lewenstein, Phys. Rev. Lett. **83**, 5198 (1999).
[30] J. Denschlag, J. E. Simsarian, D. L. Feder, C. W. Clark, L. A. Collins, J. Cubizolles, L. Deng, E. W. Hagley, K. Helmerson, and W. P. Reinhardt *et al.*, Science **287**, 97 (2000).
[31] In a layer on the order of the healing length ξ, the soliton has a kinetic energy per atom proportional to $(1/\xi)^2$. With the Thomas-Fermi radius proportional to $\hbar/(\omega\xi)$, the number of atoms covered by the soliton is proportional to $N\omega\xi^2$, and the total energy to $N\hbar\omega$. If the condensates were merged along their long axis, the soliton energy would be smaller by the aspect ratio, that is, ~200.
[32] O. Zobay and B. M. Garraway, Phys. Rev. Lett. **86**, 1195 (2001).
[33] J. R. Anglin and W. Ketterle, Nature (London) **416**, 211 (2002).

Appendix C

Matter-wave Interferometry with Phase Fluctuating Bose-Einstein Condensates

Elongated Bose-Einstein condensates (BECs) exhibit strong spatial phase fluctuations even well below the BEC transition temperature. We demonstrate that atom interferometers using such condensates are robust against phase fluctuations; i.e., the relative phase of the split condensate is reproducible despite axial phase fluctuations. However, larger phase fluctuations limit the coherence time, especially in the presence of some asymmetries in the two wells of the interferometer.

PRL 99, 240406 (2007) PHYSICAL REVIEW LETTERS week ending 14 DECEMBER 2007

Matter-Wave Interferometry with Phase Fluctuating Bose-Einstein Condensates

G.-B. Jo, J.-H. Choi, C. A. Christensen, Y.-R. Lee, T. A. Pasquini, W. Ketterle, and D. E. Pritchard*
MIT-Harvard Center for Ultracold Atoms, Research Laboratory of Electronics, Department of Physics, Massachusetts Institute of Technology, Cambridge, Massachusetts 02139, USA
(Received 26 June 2007; published 14 December 2007)

Elongated Bose-Einstein condensates (BECs) exhibit strong spatial phase fluctuations even well below the BEC transition temperature. We demonstrate that atom interferometers using such condensates are robust against phase fluctuations; i.e., the relative phase of the split condensate is reproducible despite axial phase fluctuations. However, larger phase fluctuations limit the coherence time, especially in the presence of some asymmetries in the two wells of the interferometer.

DOI: 10.1103/PhysRevLett.99.240406 PACS numbers: 03.75.Dg, 03.75.Lm, 39.20.+q

A noninteracting zero temperature Bose-Einstein condensate is the matter-wave analogue to the optical laser, and therefore the ideal atom source for atom interferometry. Finite temperature and atomic interactions profoundly change the coherence properties of a condensate and introduce phase fluctuations and phase diffusion. Those phenomena are of fundamental interest [1–6], but also of practical importance because they may limit the performance of atom interferometers [7–9]. This applies, in particular, to magnetic microtraps and waveguides (e.g., atom chips) [10] since tight confinement and elongated geometry enhances phase diffusion and phase fluctuations.

Phase *diffusion* is a quantum effect associated with the coherent splitting of the condensate. Number fluctuations lead to density fluctuations, which, due to interactions, cause fluctuations of the energy and cause diffusion of the relative phase proportional to the chemical potential times $\Delta N/N$, the amount of fluctuations in the relative atom number. In our previous work [11,12], we showed that such phase diffusion could be dramatically reduced by number squeezing, increasing the coherence time. In this paper, we characterize and discuss the role of spatial phase *fluctuations* in an atom interferometer.

Phase *fluctuations* cause the condensate to break up into several quasicondensates with random phase; i.e., long range coherence is lost. This usually happens in elongated geometries when the temperature is sufficiently high to excite such modes [1,2], or in interacting one-dimensional condensates even at zero temperature due to quantum fluctuations [13]. Spatial phase fluctuations have two major consequences for atom interferometry. First, they speed up phase diffusion, since $\Delta N/N$ refers now to the atom number in a single quasicondensate. Second, they make the atom interferometer much more sensitive to random relative displacements of the split condensates, which have to be smaller than the coherence length, which, for condensates with phase fluctuations, can be much smaller than the size of the condensate.

A typical elongated trap geometry, realized by an atom chip, has an aspect ratio of ~200 [8,11,14], sufficient to induce phase fluctuations in a quasicondensate along the axial direction [1] already at very low temperatures (or in the 1D case, even at zero temperature). When the temperature of a condensate is above the characteristic temperature, $T^* = 15N(\hbar\omega_z)^2/32\mu$, where μ is the chemical potential, N total atom number, ω_z axial trap frequency, and $\hbar$ the Planck's constant divided by 2π [1], then thermal excitations of low energy axial modes lead to longitudinal phase fluctuations. For temperatures above T^*, the coherence length L^* of a phase-fluctuating condensate is shorter than the length L of the condensate $L^*/L = T^*/T$ [1].

Previous experiments [8,11,14] on atom interferometry have operated in a regime where phase fluctuations are predicted to be present. However, their presence has not been observed because the interferometer was read out by integrating the interference fringes along the axial direction. Other experiments characterized phase fluctuations by interferometric techniques [15] and Bragg spectroscopy [16], but did not study the effect of phase fluctuations on an atom interferometer.

In this Letter we observe the axial phase fluctuations spatially resolved and characterize their effect on the coherence time of the atom interferometer. We show explicitly that atom interferometry can be performed in the presence of phase fluctuations. This has been expected [13], since for sufficiently short times after splitting, those fluctuations are identical for both condensates and therefore do not affect the measurement of the relative phase. For the same reason, atom interferometry is possible with thermal clouds of atoms [17]. However, already at short times, phase fluctuations degrade the contrast and can limit the coherence time. As we discuss below, we believe that this degradation is not due to the quantum effect of the increased relative number fluctuations in each quasicondensate because of the high degree of number squeezing, but is rather caused by asymmetries in the double-well potential leading to relative motion of the condensates.

Bose-Einstein condensates of $\sim 4 \times 10^5$ ^{23}Na atoms in the $|F = 1, m_F = -1\rangle$ state were transferred into a magnetic trap generated by the trapping wire on an atom chip and external bias field [14]. Using adiabatic rf-induced splitting [8,18], a double-well potential in the vertical plane (paral-

lel to the gravity direction) was formed as illustrated in Fig. 1(a) [19]. Gravity was compensated by a magnetic field gradient from the trapping wire. Typically, the separation of the two wells was $d \sim 6$ μm, the height of the trap barrier was $U \sim h \times 10$ kHz, and the difference of the trap bottom between two wells $\sim h \times 300$ Hz. The trapping frequencies were ~2 kHz (radial) and ~10 Hz (axial). The absorption imaging light for data acquisition was resonant with the $|F=2\rangle \rightarrow |F'=3\rangle$ cycling transition for the trapped atoms and was aligned perpendicular to the condensate axis [side imaging in Fig. 1(c)]. The atoms were optically pumped into the $|F=2\rangle$ hyperfine level with a pulse resonant with the $|F=1\rangle \rightarrow |F'=2\rangle$ transition.

First, we characterized the presence of phase fluctuations in the condensate before splitting by observing density modulations of the expanded atomic cloud after 7 ms time of flight (Fig. 2 inset). In trap, the mean-field interaction energy suppresses density fluctuations, but ballistic expansion converts phase fluctuations into density modulations [2] since the initial velocity field is proportional to the gradient of the phase. The number of observed density striations of around ten is consistent with the ratio of the measured temperature of ~650 ± 100 nK and the calculated value of $T^* \simeq 60$ nK. Since the barrier height is comparable to the temperature, we assume that both condensates interact with the same heat bath. However, we do not expect any difference to the case of two separated thermal clouds.

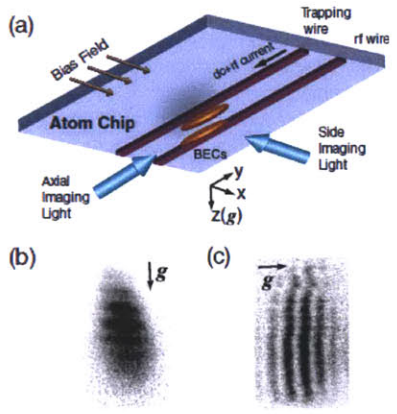

FIG. 1 (color online). Geometry of the atom chip interferometer. (a) Atoms were confined radially by the combined magnetic potential of a current-carrying wire and an external bias field. A pair of end cap wires (not shown) provided axial confinement. The single well was deformed into a vertical double well within 15 ms by adding rf current into the trapping wire dressing the atoms with oscillating rf fields. Absorption image was taken by a probe beam directed along the condensate axis [(b), axial imaging] and perpendicular to the condensate axis [(c), side imaging]. All data in this Letter were obtained using side imaging. The fields of view are 160×260 μm and 180×100 μm for axial and side imaging, respectively.

The longitudinal phase fluctuations were quantified by measuring the root-mean-square average of the density fluctuations as described in Fig. 2 [20]. The amount of phase fluctuations was controlled by changing the atom number and the temperature with rf-evaporation. The rf field generated by the rf wire [Fig. 1(a)] was swept down from ~20 kHz above the Larmor frequency at the trap center to a variable final value, leading to a variable chemical potential and temperature of the condensate (Fig. 2 inset) [21]. The variation of the spatial phase fluctuations with chemical potential is shown in Fig. 2.

Having firmly established the presence of phase fluctuations, we can now demonstrate the robustness of an atom interferometer against longitudinal phase fluctuations. For this, we split the condensates and observe the reproducibility of ten interference fringes obtained by recombining the condensates during ballistic expansion. The regular, almost straight interference fringes (Figs. 1 and 3) show that the spatial phase fluctuations are common mode and do not affect the relative phase in a major way.

However, when we increase the amount of phase fluctuations, we observe an increasing blurring or waviness of the interference fringes (Fig. 3). The number of wiggles of the waviness is comparable to the modulation pattern observed in the ballistic expansion of single condensates (Fig. 2). Of course, without any technical imperfection in

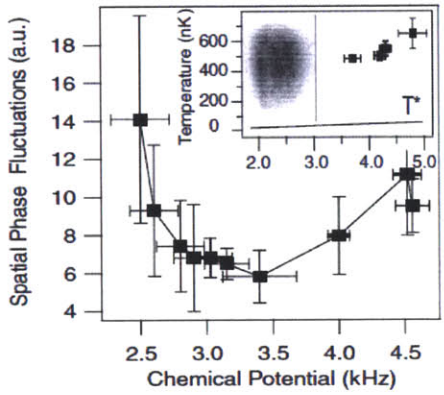

FIG. 2. Spatial phase fluctuations in a single condensate. The phase fluctuations were characterized by observing the density modulations in an absorption image of the expanded cloud after 8 ms time-of-flight (see inset) and calculating the rms fluctuations as described in Ref. [2]. The chemical potential (or atom number) was controlled by additional rf-evaporative cooling. The temperature of the condensate is shown in the inset graph. For chemical potentials less than 3.5 kHz, we could not measure the temperature of a condensate due to the lack of discernible thermal atoms. The observed phase fluctuations do not decrease monotonically, but show a minimum at the chemical potential of ~3.5 kHz, probably because the effect of the lower temperature was more than offset by the loss in the atom number. In the inset graph, T^* displays the characteristic temperature for the onset of the phase fluctuations.

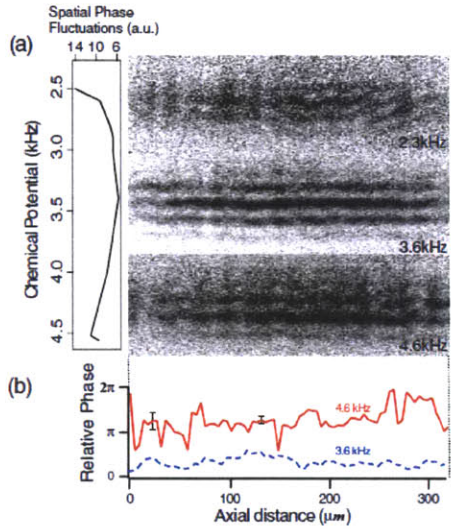

FIG. 3 (color online). Effect of spatial phase fluctuation on the waviness of interference fringes. (a) Interference fringes obtained right after splitting a condensate. For large spatial phase fluctuation (e.g., 4.6 kHz), the fringe pattern shows more significant wiggles than for smaller phase fluctuations (e.g., 3.6 kHz). (b) From the fringes for 3.6 kHz (dashed line) and 4.6 kHz (solid line) chemical potentials, relative phases are obtained along the axial direction. In both cases, the overall relative phase can be well determined by averaging along the axial coordinate, but considerable axial variations of the relative phase were observed in the regime of large longitudinal phase fluctuations (solid line). The error bars indicate the statistical uncertainty in the phase determination.

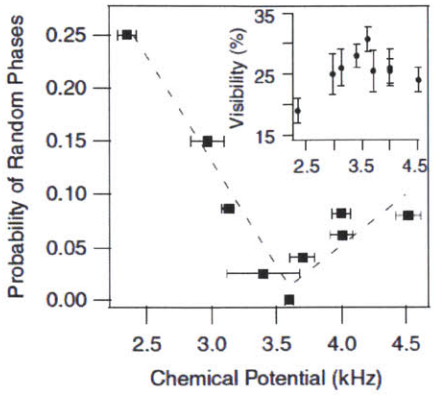

FIG. 4. Effect of spatial phase fluctuations on the reproducibility of the relative phase right after splitting. The probability of random phases was measured with variable longitudinal phase fluctuations immediately after splitting (0 ms hold time). The phase was determined by analyzing the central ~40% of the axial length of the interference pattern. In the inset graph, the visibility of the integrated interference fringe over the central ~40% is shown.

the splitting process, phase fluctuations would be common mode and not lead to any observable effects right after the splitting. For the smallest amount of spatial phase fluctuations, the relative phase is almost constant along the axial direction [dashed line in Fig. 3(b)]. The effect of larger phase fluctuations is displayed by the solid line. However, an average relative phase can still be determined.

To quantify the reproducibility of the relative phase, we determine the probability of the ten measurements of the relative phase being random (called randomness) [11] (Fig. 4). For values of the chemical potential larger than 3.0 kHz, the randomness is less than 0.1 which implies a reproducible phase with 90% confidence. However, by comparing Figs. 2 and 4, one clearly recognizes the degradation of reproducibility of the relative phase with increasing spatial phase fluctuations. We cannot rule out that the condensate had some weak collective excitations after preparation. However, the amount of the excitation should not depend on the final temperature. Therefore, we attribute the temperature dependence of the fringe contrast to phase fluctuations.

By introducing a variable hold time after the splitting, we can examine how spatial phase fluctuations limit the coherence time of a matter-wave interferometer. Figure 5 shows the increase of randomness with hold time. For the smallest amount of phase fluctuations (chemical potential ~3.4 kHz, black squares in Fig. 5), the phase coherence time is ~23 ms. As the spatial phase fluctuations increase (solid circles and open squares in Fig. 5), the phase coherence time becomes shorter [22]. It should be noted that in the absence of spatial phase fluctuations, for a condensate with zero temperature, the rate of phase diffusion decreases with chemical potential, proportional to $\sim\mu^{-1/4}$ [3,4], which is also valid at finite temperature [3]. Our observed *increase* of decoherence with increasing chemical potential is therefore attributed to the increase of spatial phase fluctuations. The increasing waviness of the interference fringes show that the decoherence is caused by randomization of the relative phase along the axial direction [Fig. 5(b)].

By which mechanism do the spatial phase fluctuations affect the interferometer signal? For our experimental parameters, the rate of phase diffusion (assuming Poissonian number fluctuations after the splitting) is ~20 ms [3,4]. For our value of T/T^*, the condensate fragments into ~10 quasicondensates which should decrease the coherence time by a factor of $\sqrt{10}$ to about 7 ms. Our observation of much longer coherence times implies strong squeezing of the relative number fluctuations, as already observed in Ref. [11]. In Ref. [11] we inferred a reduction of the number fluctuations below shot noise by a factor of 10. However, having now established the presence of strong phase fluctuations, we should reinterprete our previous result. Those data were taken at a value of T/T^* of about 7, which implies that the number fluctuations for each quasicondensate was squeezed by a factor of ~25. Our current experiments were carried out in a rotated geometry (in

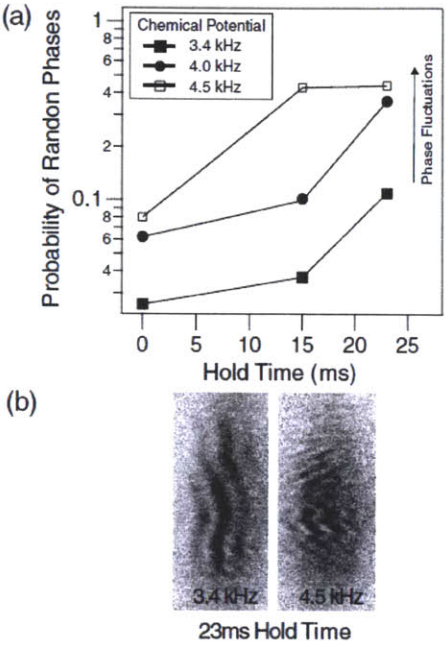

FIG. 5. Effect of longitudinal phase fluctuations on the coherence time between the split condensates. (a) The probability for a random phase for ten measurements of the relative phase is shown for three different amounts of the longitudinal phase fluctuations. (b) For condensates in the regime of large longitudinal phase fluctuations (~4.5 kHz), interference fringes show more wavy patterns, which led to the increased randomness of the measured relative phase.

order to be able to observe along a radial direction), but the value of $T/T^* \sim 10$ is similar. If we assume that the squeezing factor is the same, then we should have observed phase coherence times comparable to the 200 ms observed previously [11].

We therefore conclude that the shorter coherence times observed in this Letter are not limited by the fundamental quantum phase diffusion of quasicondensates because of strong number squeezing, but rather reflect the interplay of spatial phase fluctuations and some relative motion of the two condensates. This is probably due to some asymmetries in the current trapping potential [23] and/or technical noise. The loss of coherence due to phase fluctuations starts already during the splitting process (Figs. 3 and 4), and increases with hold time.

The main conclusions of this Letter are that matter-wave interferometers are robust against spatial phase fluctuations, especially when strong number squeezing mitigates the fragmentation into smaller quasicondensates (which show faster phase diffusion than a single condensate) resulting in coherence times of up to 200 ms [11]. However, spatial phase fluctuations make the interferometer much more sensitive to residual relative motion of the two split condensates and therefore require a highly symmetric double-well potential.

This work was funded by DARPA, NSF, and ONR. G.-B. Jo and Y.-R. Lee acknowledge additional support from the Samsung foundation. We thank H. Kim for experimental assistance and Y. Shin for critical reading of the manuscript. We also thank E. Demler for stimulating discussions.

*http://cua.mit.edu/ketterle_group/

[1] D. S. Petrov, G. V. Shlyapnikov, and J. T. M. Walraven, Phys. Rev. Lett. **87**, 050404 (2001).
[2] S. Dettmer *et al.*, Phys. Rev. Lett. **87**, 160406 (2001).
[3] M. Lewenstein and L. You, Phys. Rev. Lett. **77**, 3489 (1996).
[4] Y. Castin and J. Dalibard, Phys. Rev. A **55**, 4330 (1997).
[5] D. S. Petrov, M. Holzmann, and G. V. Shlyapnikov, Phys. Rev. Lett. **84**, 2551 (2000).
[6] D. S. Petrov, G. V. Shlyapnikov, and J. T. M. Walraven, Phys. Rev. Lett. **85**, 3745 (2000).
[7] Y. Shin *et al.*, Phys. Rev. Lett. **92**, 050405 (2004).
[8] T. Schumm *et al.*, Nature Phys. **1**, 57 (2005).
[9] S. Hofferberth *et al.*, Nature (London) **449**, 324 (2007).
[10] J. Fortagh and C. Zimmermann, Rev. Mod. Phys. **79**, 235 (2007).
[11] G.-B. Jo *et al.*, Phys. Rev. Lett. **98**, 030407 (2007).
[12] G.-B. Jo *et al.*, Phys. Rev. Lett. **98**, 180401 (2007).
[13] R. Bistritzer and E. Altman, Proc. Natl. Acad. Sci. U.S.A. **104**, 9955 (2007).
[14] Y. Shin *et al.*, Phys. Rev. A **72**, 021604(R) (2005).
[15] D. Hellweg *et al.*, Phys. Rev. Lett. **91**, 010406 (2003).
[16] S. Richard *et al.*, Phys. Rev. Lett. **91**, 010405 (2003).
[17] T. Gustavson, P. Bouyer, and M. Kasevich, Phys. Rev. Lett. **78**, 2046 (1997).
[18] O. Zobay and B. M. Garraway, Phys. Rev. Lett. **86**, 1195 (2001).
[19] S. Hofferberth *et al.*, Nature Phys. **2**, 710 (2006).
[20] For quantitative analysis of the spatial phase fluctuations, the density profile obtained from an absorption image is Fourier transformed. After filtering out high and low momentum components, the profile is transformed back and its root-mean-square average is determined (Fig. 2).
[21] In the final stage of the evaporation, the ratio of trap depth to temperature was rather small (≈ 2), possibly due to heating from the atom chip potential.
[22] We did not study the temporal evolution for chemical potentials smaller than 3.4 kHz due to the large fluctuations in the evaporation process.
[23] In our trap geometry, the two condensates in vertically separated potential wells feel different magnetic fields from a pair of end cap wires. The slightly asymmetric axial confinement leads to some quadrupolar relative motion of the two separated condensates. For the determination of the relative phase, we select the central region where the fringes were parallel to the axial direction.

Appendix D

Trapping of Ultracold Atoms in a Hollow-core Photonic Crystal Fiber

Ultracold sodium atoms have been trapped inside a hollow-core optical fiber. The atoms are transferred from a free-space optical dipole trap into a trap formed by a red-detuned Gaussian light mode confined to the core of the fiber. We show that at least 5% of the atoms held initially in the free-space trap can be loaded into the core of the fiber and retrieved outside.

PHYSICAL REVIEW A 78, 033429 (2008)

Trapping of ultracold atoms in a hollow-core photonic crystal fiber

Caleb A. Christensen,[1] Sebastian Will,[2] Michele Saba,[3] Gyu-Boong Jo,[1] Yong-Il Shin,[1] Wolfgang Ketterle,[1] and David Pritchard[1]

[1]*MIT-Harvard Center for Ultracold Atoms, Research Laboratory of Electronics, Department of Physics, Massachusetts Institute of Technology, Cambridge, Massachusetts 02139, USA*

[2]*Institut für Physik, Johannes Gutenberg-Universität, 55099 Mainz, Germany*

[3]*Dipartimento di Fisica, Università di Cagliari, Cagliari, Italy*

(Received 29 July 2008; published 25 September 2008)

Ultracold sodium atoms have been trapped inside a hollow-core optical fiber. The atoms are transferred from a free-space optical dipole trap into a trap formed by a red-detuned Gaussian light mode confined to the core of the fiber. We show that at least 5% of the atoms held initially in the free-space trap can be loaded into the core of the fiber and retrieved outside.

DOI: 10.1103/PhysRevA.78.033429 PACS number(s): 37.10.Gh, 03.75.Be, 42.70.Qs

I. INTRODUCTION

Ultracold atoms in waveguides are being used for studying quantum optics [1], performing atom interferometry [2–5], and implementing schemes for quantum-information science [6]. Of particular interest is the ability of waveguides and microtraps to strongly confine atoms, providing high optical densities, strong interactions with light, and mechanisms for transporting atoms for further experiments.

Hollow-core optical fibers can guide and confine both atoms and light. Previous experiments have reported guiding atoms in optical dipole traps (ODTs) formed by light guided in hollow fibers [7–10]; these experiments used capillaries which guide light in multiple modes in the cladding or core. Such fibers are susceptible to speckle or inhomogeneous fields causing uncontrolled guiding, heating, or loss due to local absence of confinement. Recently developed alternatives are photonic crystal fibers which propagate a single Gaussian mode confined to a hollow core [11,12]. If ultracold atoms are efficiently loaded into such a mode using red-detuned light, the atoms might be held for long times or controllably transported along the fiber. The first experiments have succeeded in trapping ultracold atoms [13] or guiding thermal [14] or laser-cooled atoms [15] through hollow-core photonic band gap fibers.

This paper presents results [13] on the transfer of trapped ultracold sodium atoms into a hollow-core fiber, and the retrieval of a significant fraction (at least 5%) back in the external trap.

II. EXPERIMENTAL PROCEDURE

We produce sodium Bose-Einstein condensates (BECs) using laser cooling and rf evaporation in a dc Ioffe-Pritchard magnetic trap, then load the BEC into a red-detuned ODT formed by a focused laser. The ODT focus can be moved by translating the focusing optics outside the vacuum chamber [16]. This procedure typically delivers a condensate of 10^6 atoms to a separate vacuum chamber holding a fiber. The ODT is positioned 1 mm from the end of a hollow-core photonic crystal fiber (2 cm long, Blaze Photonics HC-1060-02) which supports a red-detuned Gaussian mode in the core, hereafter called the hollow-core trap (HCT). The fiber has a 10 μm hollow core that atoms can enter. By adjusting the intensities of the two traps, the atoms can be controllably transferred between them.

The light for the ODT and the HCT is produced by a 1064 nm Spectra-Physics J201-BL-106C diode pumped solid state multimode laser. Intensities are controlled by using acousto-optical modulators. The beams are frequency shifted such that they have 50 MHz relative detuning in order to prevent static interference fringes in regions where the traps overlap. The laser is coupled to the core mode by focusing the beam onto the fiber tip from outside the vacuum chamber (Fig. 1). Using a retractable mirror, the light exiting the other end of the fiber can be observed to determine how well the core mode is coupled, as well as how much light has coupled into other modes that can propagate in the cladding or on the surface of the fiber.

Because the 1064 nm trapping light is far detuned from the 589 nm ^{23}Na D_2 line, the light scattering rate, which scales as $1/\delta^2$, is less than 10^{-3} Hz. Therefore radiation pressure, heating, and trap loss associated with scattering are negligible in the experiment. In the far-detuned limit where $\delta \gg \Omega_R, \Gamma$, the potential is given by

$$U(r) = \frac{\hbar[\Omega_R(r)]^2}{4}\left(\frac{1}{\omega_L-\omega_0}+\frac{1}{\omega_L+\omega_0}\right) = \frac{\hbar\Gamma^2 I(r)}{8I_{\mathrm{sat}}}\left(\frac{1}{\delta}+\frac{1}{2\omega_0+\delta}\right), \quad (1)$$

where $[\Omega_R(r)]^2$ is the squared Rabi frequency, proportional to the position-dependent beam intensity $I(r)$, $\delta=\omega_L-\omega_0$ is the laser detuning in rad/s, and Γ is the natural linewidth. For the sodium D_2 line, the saturation intensity $I_{\mathrm{sat}}=6$ mW/cm^2 and $\Gamma=2\pi\times 10$ MHz. Note that the counter-rotating term accounts for 25% of the potential.

The focus of the ODT has a waist $w_0=20$ μm, approximated by a Gaussian profile of

$$I(\rho,z) = \frac{2P}{\pi w(z)^2} e^{-2r^2/w(z)^2} \quad (2)$$

where ρ is the radial coordinate, z is the axial distance from the focal plane, $w(z)$ is the beam radius

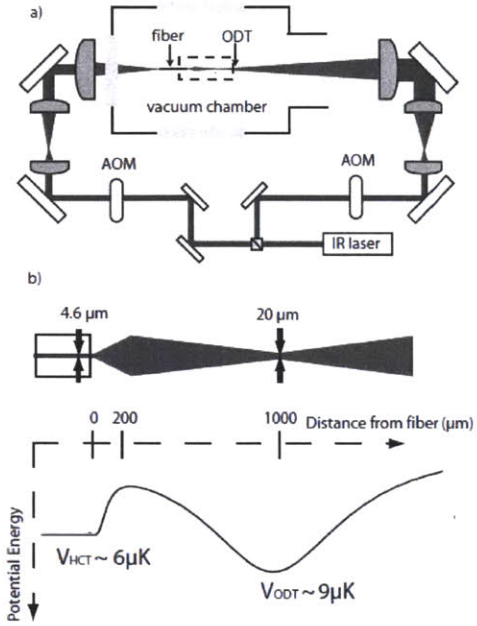

FIG. 1. (a) Diagram of the optics setup. Note that both beams used for trapping are first-order-diffracted beams from acousto-optic modulators. (b) Closeup of the region near the fiber where the atoms are held and transferred. The combined potential of the traps with 150 mW in the ODT and 5 mW in the HCT is sketched.

$w(z)=w_0\sqrt{1+(\lambda z/\pi w_0^2)^2}$, and P is the beam power. The HCT mode is approximately Gaussian in the radial direction with a waist of 4.6 μm. Assuming only the core mode is excited, the mode is axially constant along the fiber and diverges at the fiber tip according to the Gaussian formula, with the appropriate P and w_0.

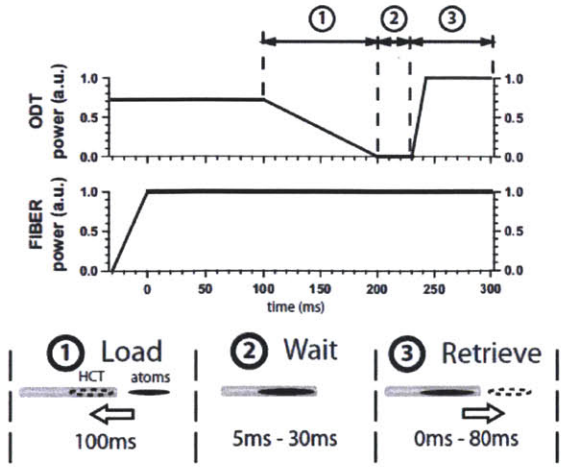

FIG. 2. Time line for transferring atoms by ramping laser power. The fiber light is ramped up while the atoms are in the ODT, and the ODT is ramped down to transfer to the HCT (1), turned off for holding (2), and ramped up to retrieve the atoms (3).

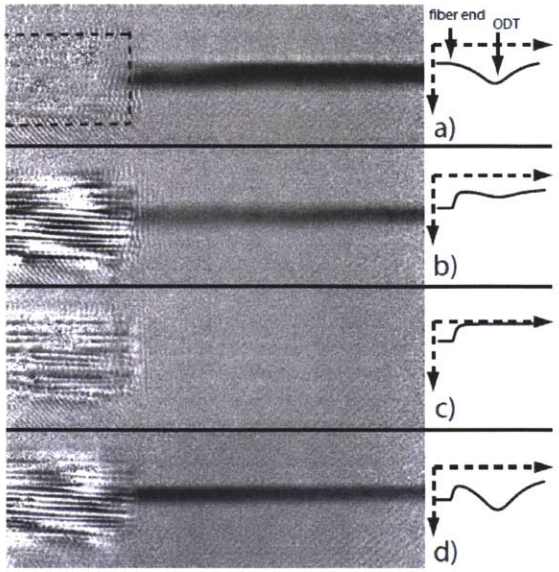

FIG. 3. Images of atoms in the ODT during the experiment. Also shown are sketches of the corresponding combined potential of the HCT and ODT. (a) Atoms are held in the ODT near the fiber, with no light coupled into the fiber. The dashed line indicates the position of the 100 μm thick fiber. (b) Light is coupled to the fiber, and as the ODT intensity is ramped down, atoms are depleted from the ODT until (c) no atoms remain outside the fiber when the ODT power reaches zero. (d) After ramping the ODT back up, atoms that were trapped in the HCT return to the ODT.

The calculated depths of the ODT and HCT are 5.8×10^{-2} and 1.2 μK/mW, respectively [Fig. 1(b)]. The maximum power in the ODT is 150 mW. Potentials are qualitatively consistent with our observations if we assume a maximum power of 5 mW in the core mode of the fiber. Bench tests suggested that three times more power could couple through the fiber, but we believe that the extra power was in surface or cladding modes and did not contribute to the core intensity.

The ODT is positioned in front of the fiber, and the laser intensities in the two traps are ramped to perform the transfer (Fig. 2). As the ODT depth is reduced (step 1 in the figure), atoms are pulled out of the trap and are accelerated into the potential well of the HCT. The ODT is turned off completely while the atoms are held within the HCT (step 2). After some hold time the ODT is ramped up and atoms transfer back to the ODT (step 3).

Absorption images are obtained during the loading and retrieving process to measure the atom number in the ODT (Fig. 3). From the final ODT number we determine the overall efficiency of the process.

III. RESULTS

Based on the analysis of absorption images we measure 5×10^4 atoms in the ODT after retrieval, corresponding to about 5% of the 10^6 atoms initially delivered at the start of

the experiment. The successful transfer of atoms into the HCT and their retrieval is the main result of this paper.

Images recorded while the ODT power is ramped down reveal that the number of atoms is gradually reduced until the ODT power reaches zero [see Figs. 3(b) and 3(c)]. Once the ODT power drops to zero, any remaining atoms either fall into the HCT potential well, or are lost from either trap.

The atoms are then held in the trap for up to 30 ms, several hundred radial trapping periods. After this time, the ODT intensity is ramped back up, and the atom number outside the fiber increases over 80 ms [Fig. 3(d)] until a maximum is reached. In varying the hold time, the retrieved number changed by at most 30%, indicating a lifetime longer than 50 ms. Longer hold times were not explored in the current setup. To rule out alternate trapping mechanisms, we performed some experimental runs under identical parameters except with no light in the HCT, and found that no atoms are recovered, indicating that the atoms indeed are loaded into and retrieved from the HCT.

The initial and final cloud sizes were similar, implying similar temperatures before and after the transfer. This temperature may be estimated at a few microkelvins by assuming evaporation continually occurs in the finite-depth optical trap, leading to temperatures at a fraction of the trap depth.

IV. DISCUSSION

Our experimental scheme for transferring atoms between the two traps was guided by the concept of adiabatic transfer in a double-well potential, where the atoms always occupy the deeper well. Our results are consistent with this picture. We do not know whether the transfer of atoms involves tunneling, spilling over the barrier, or sloshing. This reflects that the potential between the two traps is likely to be affected by spurious modes traveling along the fiber surface or in the cladding and interfering with the light in the core. In fact, we frequently observed light coupled into the cladding leading to distortions in the mode after the fiber. Without proper alignment, the cladding modes prevented atoms from being loaded into the fiber or trapped atoms in local maxima outside the fiber. The successful transfer was possible only with great care in coupling to minimize light in the cladding modes. In the future, a coupling lens inside the vacuum could replace the final lens (which was 10 cm away from the fiber), resulting in more controlled and stable coupling of light. We do not try to describe the exact dynamics of the transfer without better knowledge of the potential between the two wells.

Observation of the atoms inside the fiber would reveal the dynamics of the loading and trapping process. Although the fiber is transparent to resonant light, absorption imaging from the side was not possible due to severe scattering and refraction. However, resonant light could be propagated along the core mode to provide information on the integrated density of atoms inside the fiber.

We were unable to observe atoms being guided completely through the fiber, probably because of low atom density and the lack of an appropriate trap in which to collect them after the fiber. It may turn out to be difficult to control the light intensity along the fiber core sufficiently to avoid undesirable accelerations of the atoms, to localize them inside the fiber, or to propagate them through the fiber in a controlled way. In this case, it may be advantageous to use the fiber mode for strong transverse confinement but add magnetic confinement for the axial direction. This could be accomplished with a quadrupole trap, where, by changing the balance of currents in anti-Helmholtz coils, the axial minimum could be swept across the fiber to controllably propagate the atomic cloud. With this setup, one could obtain detailed information on atom lifetime at different positions within the fiber. Originally, we had the intention to take more quantitative data with such an improved setup, but the priorities of the laboratory changed. Therefore, we have presented our qualitative results in this paper.

In conclusion, we have shown that optical dipole traps are well suited to load ultracold atoms into a hollow-core photonic crystal fiber. The reported retrieval efficiency of 5% is a lower bound for the transfer efficiency, and can probably be substantially increased with an improved setup.

ACKNOWLEDGMENTS

This work was funded by DARPA, NSF, and ONR. G.-B.J. and S.W. acknowledge additional support from Samsung Foundation and the Studienstiftung des Deutschen Volkes, respectively.

[1] I. Teper, Y.-J. Lin, and V. Vuletic, Phys. Rev. Lett. **97**, 023002 (2006).

[2] G.-B. Jo, J.-H. Choi, C. A. Christensen, T. A. Pasquini, Y.-R. Lee, W. Ketterle, and D. E. Pritchard, Phys. Rev. Lett. **98**, 180401 (2007).

[3] S. Wu, E. Su, and M. Prentiss, Phys. Rev. Lett. **99**, 173201 (2007).

[4] E. Andersson, T. Calarco, R. Folman, M. Andersson, B. Hessmo, and J. Schmiedmayer, Phys. Rev. Lett. **88**, 100401 (2002).

[5] Y.-J. Wang, D. Z. Anderson, V. M. Bright, E. A. Cornell, Q. Diot, T. Kishimoto, M. Prentiss, R. A. Saravanan, S. R. Segal, and S. Wu, Phys. Rev. Lett. **94**, 090405 (2005).

[6] P. Treutlein, T. W. Hänsch, J. Reichel, A. Negretti, M. A. Cirone, and T. Calarco, Phys. Rev. A **74**, 022312 (2006).

[7] M. J. Renn, D. Montgomery, O. Vdovin, D. Z. Anderson, C. E. Wieman, and E. A. Cornell, Phys. Rev. Lett. **75**, 3253 (1995).

[8] H. Ito, T. Nakata, K. Sakaki, M. Ohtsu, K. I. Lee, and W. Jhe, Phys. Rev. Lett. **76**, 4500 (1996).

[9] R. G. Dall, M. D. Hoogerland, K. G. H. Baldwin, and S. J. Buckman, J. Opt. B: Quantum Semiclassical Opt. **1**, 396 (1999).

[10] D. Müller, E. A. Cornell, D. Z. Anderson, and E. R. I. Abraham, Phys. Rev. A **61**, 033411 (2000).

[11] R. F. Cregan, B. J. Mangan, J. C. Knight, T. A. Birks, P. S. J. Russell, P. J. Roberts, and D. C. Allan, Science **285**, 1537 (1999).

[12] P. Roberts *et al.*, Opt. Express **13**, 236 (2005).

[13] S. Will, diploma thesis, Universitat Mainz, 2006.

[14] T. Takekoshi and R. J. Knize, Phys. Rev. Lett. **98**, 210404 (2007).

[15] M. Bajcsy, S. Hofferberth, V. Balic, T. Peyronel, M. Hafezi, A. S. Zibrov, V. Vuletic, and M. Lukin (unpublished).

[16] T. L. Gustavson, A. P. Chikkatur, A. E. Leanhardt, A. Gorlitz, S. Gupta, D. E. Pritchard, and W. Ketterle, Phys. Rev. Lett. **88**, 020401 (2001).

Appendix E

Itinerant Ferromagnetism in a Fermi Gas of Ultracold Atoms

Can a gas of spin-up and spin-down fermions become ferromagnetic because of repulsive interactions? We addressed this question, for which there is not yet a definitive theoretical answer, in an experiment with an ultracold two-component Fermi gas. The observation of non-monotonic behavior of lifetime, kinetic energy, and size for increasing repulsive interactions provides strong evidence for a phase transition to a ferromagnetic state. Our observations imply that itinerant ferromagnetism of delocalized fermions is possible without lattice and band structure, and our data validate the most basic model for ferromagnetism introduced by Stoner.

ble spectra could easily push this effect to higher frequencies that are beneficial for a variety of practical applications (*30*).

References and Notes

1. D. Schurig, J. B. Pendry, D. R. Smith, *Opt. Express* **15**, 14772 (2007).
2. A. V. Kildishev, W. Cai, U. K. Chettiar, V. M. Shalaev, *N. J. Phys.* **10**, 115029 (2008).
3. J. B. Pendry, D. Schurig, D. R. Smith, *Science* **312**, 1780 (2006).
4. Z. Liu, H. Lee, Y. Xiong, C. Sun, X. Zhang, *Science* **315**, 1686 (2007).
5. H.-T. Chen *et al.*, *Appl. Phys. Lett.* **93**, 091117 (2008).
6. J. N. Gollub, J. Y. Chin, T. J. Cui, D. R. Smith, *Opt. Express* **17**, 2122 (2009).
7. H.-T. Chen *et al.*, *Nature Photon.* **2**, 295 (2008).
8. I. Gil *et al.*, *Electron. Lett.* **40**, 1347 (2004).
9. M. M. Qazilbash *et al.*, *Appl. Phys. Lett.* **92**, 241906 (2008).
10. W. J. Padilla, A. J. Taylor, C. Highstrete, L. Mark, R. D. Averitt, *Phys. Rev. Lett.* **96**, 107401 (2006).
11. A. Degiron, J. J. Mock, D. R. Smith, *Opt. Express* **15**, 1115 (2007).
12. T. Driscoll *et al.*, *Appl. Phys. Lett.* **93**, 024101 (2008).
13. I. V. Shadrivov, N. A. Zharova, A. A. Zharov, Y. S. Kivshar, *Phys. Rev. E Stat. Nonlin. Soft Matter Phys.* **70**, 046615 (2004).
14. T. Driscoll *et al.*, *Appl. Phys. Lett.* **91**, 062511 (2007).
15. M. Di Ventra, Y. V. Pershin, L. O. Chua, *Proc. IEEE* **97**, 1371 (2009).
16. Materials and methods are available as supporting material on *Science* Online.
17. A. Zylbersztejn, N. F. Mott, *Phys. Rev. B Solid State* **11**, 4383 (1975).
18. B. G. Chae, H.-T. Kim, D.-H. Youn, K.-Y. Kang, *Physica B* **369**, 76 (2005).
19. S. Lysenko *et al.*, *Appl. Surf. Sci.* **252**, 5512 (2006).
20. M. M. Qazilbash *et al.*, *Science* **318**, 1750 (2007).
21. T. Driscoll, H. T. Kim, B. G. Chae, M. Di Ventra, D. N. Basov, *Appl. Phys. Lett.* **95**, 043503 (2009).
22. R. Lopez, L. A. Boatner, T. E. Haynes, R. F. Haglund Jr., L. C. Feldman, *Appl. Phys. Lett.* **85**, 1410 (2004).
23. G. V. Eleftheriades, O. Siddiqui, A. K. Iyer, *Microwave Wireless Compon. Lett. IEEE* **13**, 51 (2003).
24. J. D. Baena *et al.*, *Microwave Theory Tech. IEEE Trans.* **53**, 1451 (2005).
25. S. Tretyakov, http://arxiv.org/abs/cond-mat/0612247 (2006).
26. J. J. Yang *et al.*, *Nat. Nanotechnol.* **3**, 429 (2008).
27. Y. Muraoka, Z. Hiroi, *Appl. Phys. Lett.* **80**, 583 (2002).
28. H.-T. Kim *et al.*, *N. J. Phys.* **6**, 52 (2004).
29. I. Shadrivov, *SPIE Newsroom* doi:10.1117/2.1200811.1390 (2008).
30. V. M. Shalaev, *Nature Photon.* **1**, 41 (2007).
31. This work is supported by the U.S. Department of Energy (DOE), the Air Force Office of Scientific Research (AFOSR), and ETRI. Work at UCSD on VO_2 was supported by DOE–Basic Energy Sciences and the metamaterials work was supported by AFOSR and ETRI. M.D. acknowledges partial support from NSF. H.K. acknowledges research support from a project of the Ministry of Knowledge Economy in Korea.

Supporting Online Material

www.sciencemag.org/cgi/content/full/1176580/DC1
Materials and Methods
Fig. S1
Table S1
References

20 May 2008; accepted 4 August 2009
Published online 20 August 2009;
10.1126/science.1176580
Include this information when citing this paper.

Itinerant Ferromagnetism in a Fermi Gas of Ultracold Atoms

Gyu-Boong Jo,[1]* Ye-Ryoung Lee,[1] Jae-Hoon Choi,[1] Caleb A. Christensen,[1] Tony H. Kim,[1] Joseph H. Thywissen,[2] David E. Pritchard,[1] Wolfgang Ketterle[1]

Can a gas of spin-up and spin-down fermions become ferromagnetic because of repulsive interactions? We addressed this question, for which there is not yet a definitive theoretical answer, in an experiment with an ultracold two-component Fermi gas. The observation of nonmonotonic behavior of lifetime, kinetic energy, and size for increasing repulsive interactions provides strong evidence for a phase transition to a ferromagnetic state. Our observations imply that itinerant ferromagnetism of delocalized fermions is possible without lattice and band structure, and our data validate the most basic model for ferromagnetism introduced by Stoner.

Magnetism is a macroscopic phenomenon with its origin deeply rooted in quantum mechanics. In condensed-matter physics, there are two paradigms for magnetism: localized spins interacting via tunneling and delocalized spins interacting via an exchange energy. The latter gives rise to itinerant ferromagnetism, which is responsible for the properties of transition metals such as cobalt, iron, and nickel. Both kinds of magnetism involve strong correlations and/or strong interactions and are not yet completely understood. For localized spins, the interplay of magnetism with d-wave superfluidity and the properties of frustrated spin materials are topics of current research. For itinerant ferromagnetism (*1*–*7*), phase transition theories are still qualitative.

We implemented the Stoner model, a textbook Hamiltonian for itinerant ferromagnetism (*8*), by using a two-component gas of free fermions with short-range repulsive interactions, which can capture the essence of the screened Coulomb interaction in electron gases (*8*). However, there is no proof so far that this simple model for ferromagnetism is consistent when the strong interactions are treated beyond mean-field approaches. It is known that this model fails in one dimension, where the ground state is singlet for arbitrary interactions, or for two particles in any dimension (*3*). In our work, cold atoms were used to perform a quantum simulation of this model Hamiltonian in three dimensions, and we showed experimentally that this Hamiltonian leads to a ferromagnetic phase transition (*2*). This model was also realized in helium-3 (*9*), but the liquid turn into a solid phase and not into a ferromagnetic phase at high pressure. It has also been applied to neutrons in neutron stars (*10*).

To date, magnetism in ultracold gases has been studied only for spinor (*11*, *12*) and dipolar (*13*) Bose-Einstein condensates (BECs). In these cases, magnetism is driven by weak spin-dependent interactions, which nevertheless determine the structure of the condensate because of a bosonic enhancement factor. In contrast, here we describe the simulation of quantum magnetism in a strongly interacting Fermi gas.

An important recent development in cold atom science has been the realization of superfluidity and the BEC–Bardeen-Cooper-Schrieffer (BCS) crossover in strongly interacting, two-component Fermi gases near a Feshbach resonance (*14*). These phenomena occur for attractive interactions for negative scattering length and for bound molecules (corresponding to a positive scattering length for two unpaired atoms). Very little attention has been given to the region of atoms with strongly repulsive interactions. One reason is that this region is an excited branch, which is unstable against near-resonant three-body recombination into weakly bound molecules. Nevertheless, many theoretical papers have proposed a two-component Fermi gas near a Feshbach resonance as a model system for itinerant ferromagnetism (*15*–*22*), assuming that the decay into molecules can be sufficiently suppressed. Another open question is the possibility of a fundamental limit for repulsive interactions. Such a limit due to unitarity or many-body physics may be lower than the value required for the transition to a ferromagnetic state. We show that this is not the case and that there is a window of metastability where the onset of ferromagnetism can be observed.

A simple mean-field model captures many qualitative features of the expected phase transition but is not adequate for a quantitative description of the strongly interacting regime. The total energy of a two-component Fermi gas of average density n (per spin component) in a volume V is given by $E_F 2Vn\left\{\frac{3}{10}[(1+\eta)^{5/3}+(1-\eta)^{5/3}]+\frac{2}{3\pi}k_F a(1+\eta)(1-\eta)\right\}$, where E_F is the Fermi energy of a gas, k_F is the Fermi wave vector of a gas, a is the scattering length characterizing short-range interactions between the two components, and $\eta = \Delta n/n = (n_1 - n_2)/(n_1 + n_2)$ is the magnetization of the Fermi gas. The local magnetization of the Fermi gas is nonzero when the gas separates into two volumes, where the densities n_1 and n_2 of the two spin states differ

[1]Massachusetts Institute of Technology–Harvard Center for Ultracold Atoms, Research Laboratory of Electronics, Department of Physics, Massachusetts Institute of Technology, Cambridge, MA 02139, USA. [2]Department of Physics, University of Toronto, Toronto, Ontario M5S1A7, Canada.
*To whom correspondence should be addressed. E-mail: gyuboong@mit.edu

by $2\Delta n$. We studied an ensemble in which the number of atoms in each spin state is conserved. This is equivalent to a free electron gas at zero external magnetic field where the total magnetization is zero. The interaction term represents any short-range spin-independent potential. When the gas is fully polarized, it avoids the repulsive interaction but increases its kinetic energy by a factor of $2^{2/3}$. The phase transition occurs when the minimum in energy is at nonzero magnetization (Fig. 1A) at $k_F a = \pi/2$. This onset was previously discussed in the context of phase separation in a two-component Fermi gas (*15*–*18*). Figure 1B shows several consequences of the phase transition for a system at constant pressure. First, for increasing repulsive interactions, the gas expands, lowering its density and Fermi energy; kinetic energy is therefore reduced. When the gas enters the ferromagnetic phase, kinetic energy increases rapidly because of the larger local density per spin state. Furthermore, the volume has a maximum value at the phase transition. This can be understood by noting that pressure in our model is $(2/3)E_{kin}/V + E_{int}/V$, where E_{kin} is kinetic energy and E_{int} is interaction energy. At the phase transition, the system increases its kinetic energy and reduces its interaction energy, thus reducing the pressure. This maximum in pressure at constant volume turns into a maximum in volume for a system held at constant pressure or in a trapping potential. We have observed three predictions of this model: (i) the onset of local magnetization through the suppression of inelastic collisions, (ii) the minimum in kinetic energy, and (iii) the maximum in the size of the cloud. These qualitative features are generic for the ferromagnetic phase transition and should also be present in more-advanced models (*19*).

We start with an atom cloud consisting of an equal mixture of ^{6}Li atoms in the lowest two hyperfine states, held at 590 G in an optical dipole trap with additional magnetic confinement (*23*). The number of atoms per spin state is approximately 6.5×10^5, which corresponds to a Fermi temperature T_F of ~1.4 μK. The effective temperature T could be varied between $T/T_F = 0.1$ and $T/T_F = 0.6$ and was determined immediately after the field ramp by fitting the spatial distribution of the cloud with a finite temperature Thomas-Fermi profile. We define k_F° as the Fermi wave vector of the noninteracting gas calculated at the trap center. Applying the procedure discussed in (*24*) to repulsive interactions, we estimate that the real temperature is approximately 20% larger than the effective one. The effective temperature did not depend on $k_F^\circ a$ for $k_F^\circ a < 6$. At higher temperatures, additional shot-to-shot noise was caused by large fluctuations in the atom number. From the starting point at 590 G, the magnetic field was increased toward the Feshbach resonance at 834 G, thus providing adjustable repulsive interactions. Because of the limited lifetime of the strongly interacting gas, it was necessary to apply the fastest possible field ramp, limited to 4.5 ms by eddy currents. The ramp time is approximately equal to the inverse of the axial trap frequency (*23*) and therefore only marginally adiabatic. Depending on the magnetic field during observation, either atoms or atoms and molecules were detected by absorption imaging as described in fig. S1 (*25*).

The emergence of local spin polarization can be observed by the suppression of (either elastic or inelastic) collisions, because the Pauli exclusion principle forbids collisions in a fully polarized cloud. We monitored inelastic three-body collisions, which convert atoms into molecules. The rate (per atom) is proportional to $f(a,T)n_1n_2$ or $f(a,T)\,n^2(1 - \eta^2)$ and is therefore a measure of the magnetization η. For $k_F a \ll 1$, the rate coefficient $f(a,T)$ is proportional to $a^6 \max(T,T_F)$ (*26*). This rate can be observed by monitoring the initial drop in the number of atoms during the first 2 ms after the field ramp. We avoided longer observation times, because the increasing molecule fraction could modify the properties of the sample.

A sharp peak appears in the atom loss rate around $k_F^\circ a \cong 2.5$ at $T/T_F = 0.12$ (Fig. 2), indicating a transition in the sample to a state with local magnetization. The gradual decrease is consistent with the inhomogeneous density of the cloud, where the transition occurs first in the center. The large suppression of the loss rate indicates a large local magnetization of the cloud.

The kinetic energy of the cloud was determined by suddenly switching off the optical trap and the Feshbach fields immediately after the field ramp and then imaging state $|1\rangle$ atoms at zero field using the cycling transition after a ballistic expansion time of $\Delta t = 4.6$ ms. The kinetic energy was obtained from the Gaussian radial width σ_r as $E_{kin} = [(3m\sigma_r^2)/(2\Delta t^2)]$ where m is the mass of the ^{6}Li atom. A minimum of the kinetic energy at $k_F^\circ a \cong 2.2$ for the coldest temperature $T/T_F = 0.12$ nearly coincided with the onset of local polarization (Fig. 3). The peak in the atom loss rate occurs slightly later than the minimum of kinetic energy, probably because $f(a,T)$ increases with a (*22*). Because the temperature did not change around $k_F^\circ a \cong 2.2$, the increase in kinetic energy is not caused by heating but by a sudden change in the properties of the gas, which is consistent with the onset of ferromagnetism. The observed increase in kinetic energy is approximately 20% at $T/T_F = 0.12$, smaller than the value $(2^{2/3} - 1) = 0.59$ predicted for a fully polarized gas. This discrepancy could be due to the absence of polarization or partial polarization in the wings of the cloud. Also, it is possible that the measured kinetic energy of the strongly interacting gas before the phase transition includes some interaction energy if the Feshbach fields are not suddenly switched off. For the current switch-off time of ~100 μs, this should be only a 5% effect, but the magnetic field decay may be slower because of eddy currents.

Finally, Fig. 4 shows our observation of a maximum cloud size at the phase transition, in agreement with the prediction of the model. The cloud size may not have fully equilibrated, because our ramp time was only marginally adiabatic, but this alone cannot explain the observed maximum.

The suppression of the atom loss rate, the minimum in kinetic energy, and the maximum in cloud size show a strong temperature dependence between $T/T_F = 0.12$ and 0.22. The properties of a normal Fermi gas approaching the unitarity limit with $k_F^\circ a \gg 1$ should be insensitive to temperature variations in this range; therefore, the observed temperature dependence provides further evidence for a transition to a new phase.

At higher temperature (e.g., $T/T_F = 0.39$ as shown in Fig. 3), the observed nonmonotonic behavior becomes less pronounced and shifts to larger values of $k_F^\circ a$ for $3 \leq k_F^\circ a \leq 6$. For all three observed properties (Figs. 2 to 4), a nonmonotonic behavior is no longer observed at $T/T_F = 0.55$ (*27*). One interpretation is that at this temperature and

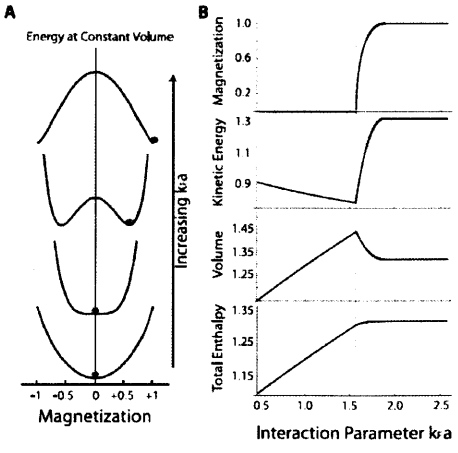

Fig. 1. Ferromagnetic phase transition at $T = 0$, according to the mean-field model described in the text. The onset of itinerant ferromagnetism occurs when the energy as a function of magnetization flips from a U shape to a W shape (**A**). (**B**) Enthalpy, volume, and kinetic energy, normalized to their values for the ideal Fermi gas, and magnetization as a function of the interaction parameter $k_F a$. k_F is defined by the density of the gas. The dotted line marks the phase transition.

above, there is no longer a phase transition. In a mean-field approximation, a ferromagnetic phase would appear at all temperatures but for increasing values of $k_F^o a$. Our observations may imply that the interaction energy saturates around $k_F^o a \approx 5$.

The spin-polarized ferromagnetic state should not suffer from inelastic collisions. However, typical lifetimes were 10 to 20 ms, which were probably related to a small domain size and three-body recombination at domain walls.

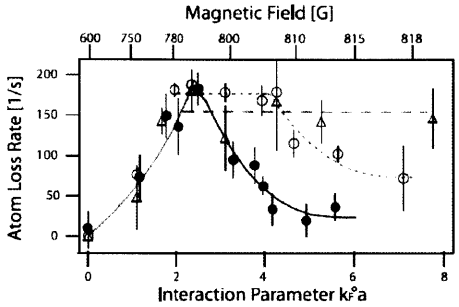

Fig. 2. Atom loss rate as a probe for local spin polarization, for different temperatures. $T/T_F = 0.55$ (triangles, dashed curve), $T/T_F = 0.22$ (open circles, dotted curve), and $T/T_F = 0.12$ (solid circles, solid black curve). The curves are guides to the eye, based on the assumption of a loss rate that saturates for increasing a in the normal state. The shaded area around the phase transition at $T/T_F = 0.12$ highlights the same region as in Figs. 3 and 4.

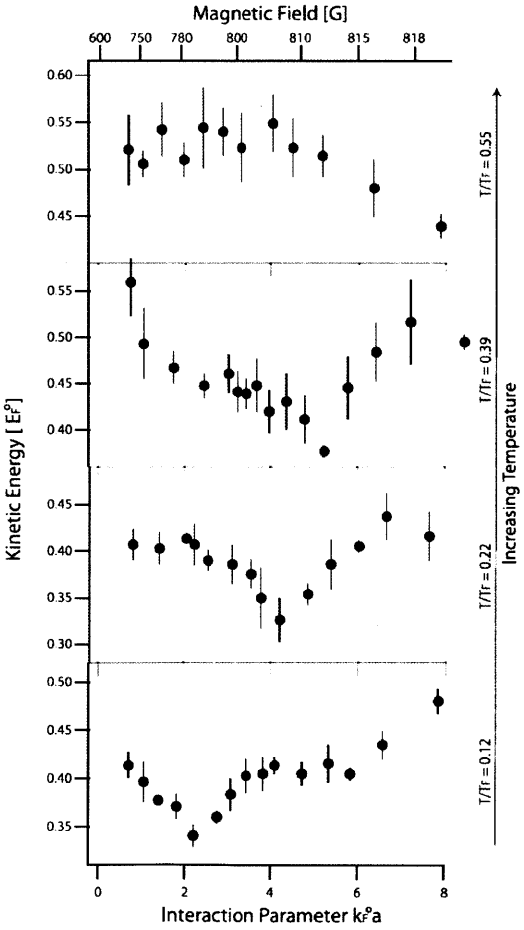

Fig. 3. Kinetic energy of a repulsively interacting Fermi gas determined for different interaction parameters $k_F^o a$ and temperatures. The measured kinetic energy is normalized by the Fermi energy E_F^o of the noninteracting Fermi gas at $T = 0$, calculated at the trap center with the same number of atoms per spin state. Each data point represents the average of three or four measurements.

We were unsuccessful in imaging ferromagnetic domains using differential in situ phase-contrast imaging (*28*). A signal-to-noise level of ~ 10 suggests that there were at least 100 domains in a volume given by our spatial resolution of ~3 μm and by the radial size of the cloud. This implies that the maximum volume of the spin domains is ~5 μm^3, containing ~50 spin-polarized atoms. We suspect that the short lifetime prevented the domains from growing to a larger size and eventually adopting the equilibrium texture of the ground state, which has been predicted to have the spins pointing radially outward, like a hedgehog (*20*, *22*). All our measurements are sensitive only to local spin polarization and are independent of domain structure and texture.

The only difference between our experiment and the ideal Stoner model is a molecular admixture of 25% (Fig. 4). The molecular fraction was constant for $k_F^o a > 1.8$ for all temperatures and therefore cannot be responsible for the sudden change of behavior of the gas at $k_F^o a \cong 2.2$ at the coldest temperature $T/T_F = 0.12$. This prediction was confirmed by repeating the kinetic energy measurements with a molecular admixture of 60%. The minimum in the kinetic energy occurred at the same value of $k_F^o a$ within experimental accuracy.

For a comparison of the observed phase transition at $k_F^o a \cong 2.2$ to the theoretical predictions, the ideal gas k_F^o has to be replaced by the value for the interacting gas, which is smaller by ~15% because of the expansion of the cloud (Fig. 4), resulting in a critical value for $k_F a \cong 1.9 \pm 0.2$. At $T/T_F = 0.12$, the finite temperature correction in the critical value for $k_F a$ is predicted to be less than 5% (*19*). The observed value for $k_F a$ is larger than both the mean-field prediction of $\pi/2$ and the second-order prediction of 1.054 at zero temperature (*19*). Depending on the theoretical approach, the phase transition has been predicted to be first or second order. This could not been discerned in our experiment because of the inhomogeneous density of the cloud.

It has been speculated (*19*) that earlier experiments on the measurement of the interaction energy (*29*) and radio frequency spectroscopy of Fermi gases (*30*) showed evidence for the transition to a ferromagnetic state at or below $k_F a = 1$. This interpretation seems to be ruled out by our experiment.

Our work demonstrates a remarkable asymmetry between positive and negative scattering length. Early work (*15*) predicted that for $k_F|a| = \pi/2$, both an attractive and a repulsive Fermi gas become mechanically unstable (against collapse and phase separation, respectively). In an attractive Fermi gas, however, the mechanical instability does not occur [due to pairing (*31*)], in contrast to our observations in a repulsive Fermi gas. This suggests that the maximum total repulsive energy [in units of $3/5(2Vn)E_F$] is larger than the maximum attractive energy $|\beta|$ of 0.59 (*32*) that is realized for infinite a (*23*).

The interpretation of our results in terms of a phase transition to itinerant ferromagnetism is based on the agreement with the prediction of simplified models [Fig. 1, (*15*–*22*)]. Future

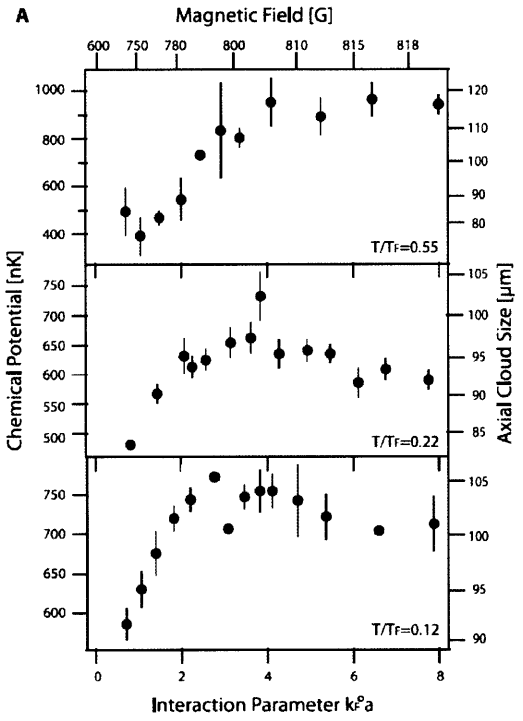

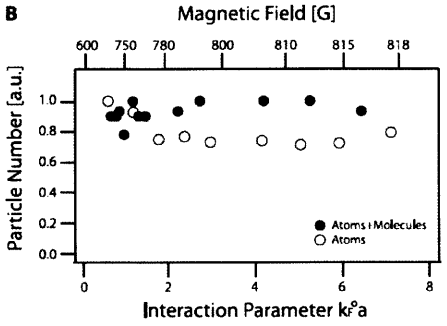

Fig. 4. Maximum in volume at the phase transition. **(A)** Axial size and chemical potential of the cloud for various temperatures. The chemical potential μ is determined from the measured cloud size, σ_z, as $\mu = [1/2]m\omega_z^2\sigma_z^2$. **(B)** Number of particles including both atoms and molecules right after the field ramp. This result shows that 25% of the atoms were converted into molecules during the field ramp, and this fraction stayed constant for $k_F^0a > 1.8$, where the phase transition was reached. This molecule fraction was independent of temperature.

work should address how the observed signatures are modified by strong interactions and correlations. Additional insight can be obtained by varying the magnetic field ramp time over a wide range and studying the relaxation toward an equilibrium state (*33*).

Heisenberg and Bloch's explanation for ferromagnetism was based on exchange energy; that is, the Pauli principle and spin-independent repulsive interactions between the electrons. However, it was unknown what other "ingredients" were needed for itinerant ferromagnetism. It was not until 1995 (*6*, *7*) that a rigorous proof was given that, in certain lattices, spin-independent Coulomb interactions can give rise to ferromagnetism in itinerant electron systems. Our finding suggests that Heisenberg's idea does not require a lattice and band structure but already applies to a free gas with short-range interactions. Our experiment can be regarded as quantum simulation of a Hamiltonian for which even the existence of a phase transition was unproven. This underlines the potential of cold atom experiments as quantum simulators for many-body physics.

References and Notes

1. F. Bloch, *Z. Phys.* **57**, 545 (1929).
2. E. Stoner, *Philos. Mag.* **15**, 1018 (1933).
3. E. Lieb, D. Mattis, *Phys. Rev.* **125**, 164 (1962).
4. P. W. Brouwer, Y. Oreg, B. I. Halperin, *Phys. Rev. B* **60**, R13977 (1999).
5. D. Vollhardt, N. Blumer, K. Held, M. Kollar, *Metallic Ferromagnetism–An Electronic Correlation Phenomenon*, vol. 580 of *Lecture Notes in Physics* (Springer, Heidelberg, Germany, 2001).
6. H. Tasaki, *Phys. Rev. Lett.* **75**, 4678 (1995).
7. A. Tanaka, H. Tasaki, *Phys. Rev. Lett.* **98**, 116402 (2007).
8. D. W. Snoke, *Solid State Physics: Essential Concepts* (Addison-Wesley, San Francisco, CA, 2008).
9. D. Vollhardt, *Rev. Mod. Phys.* **56**, 99 (1984).
10. J. Pfarr, *Z. Phys.* **251**, 152 (1972).
11. J. Stenger *et al.*, *Nature* **396**, 345 (1998).
12. L. E. Sadler, J. M. Higbie, S. R. Leslie, M. Vengalattore, D. M. Stamper-Kurn, *Nature* **443**, 312 (2006).
13. T. Lahaye *et al.*, *Nature* **448**, 672 (2007).
14. M. Inguscio, W. Ketterle, C. Salomon, *Ultracold Fermi Gases, Proceedings of the International School of Physics Enrico Fermi, Course CLXIV* (IOS Press, Amsterdam, 2008).
15. M. Houbiers *et al.*, *Phys. Rev. A* **56**, 4864 (1997).
16. L. Salasnich, B. Pozzi, A. Parola, L. Reatto, *J. Phys. At. Mol. Opt. Phys.* **33**, 3943 (2000).
17. M. Amoruso, I. Meccoli, A. Minguzzi, M. Tosi, *Eur. Phys. J. D* **8**, 361 (2000).
18. T. Sogo, H. Yabu, *Phys. Rev. A* **66**, 043611 (2002).
19. R. A. Duine, A. H. MacDonald, *Phys. Rev. Lett.* **95**, 230403 (2005).
20. I. Berdnikov, P. Coleman, S. H. Simon, *Phys. Rev. B* **79**, 224403 (2009).
21. S. Zhang, H. Hung, C. Wu, preprint available at http://arxiv.org/abs/0805.3031v4 (2008).
22. L. J. LeBlanc, J. H. Thywissen, A. A. Burkov, A. Paramekanti, *Phys. Rev. A* **80**, 013607 (2009).
23. Materials and methods are available as supporting material on *Science* Online.
24. J. Kinast *et al.*, *Science* **307**, 1296 (2005).
25. M. W. Zwierlein *et al.*, *Phys. Rev. Lett.* **91**, 250401 (2003).
26. J. P. D'Incao, B. D. Esry, *Phys. Rev. Lett.* **94**, 213201 (2005).
27. The interpretation of the loss rate is complicated because $f(a,T)$ is unknown for $k_Fa \geq 1$. The three-body rate $f(a,T)$ is expected to be unitarity saturated for $k_Fa >> 1$ (*34*). The lines in Fig. 2 indicate that the observed loss rate is consistent with unitarity saturation and a sudden drop at the phase transition, which occurs at large values of k_Fa at higher temperature.
28. Y. Shin, M. W. Zwierlein, C. H. Schunck, A. Schirotzek, W. Ketterle, *Phys. Rev. Lett.* **97**, 030401 (2006).
29. T. Bourdel *et al.*, *Phys. Rev. Lett.* **91**, 020402 (2003).
30. S. Gupta *et al.*, *Science* **300**, 1723 (2003).
31. P. Nozières, S. Schmitt-Rink, *J. Low Temp. Phys.* **59**, 195 (1985).
32. J. Carlson, S. Reddy, *Phys. Rev. Lett.* **95**, 060401 (2005).
33. M. Babadi, D. Pekker, R. Sensarma, A. Georges, E. Demler, preprint available at http://arxiv.org/abs/0908.3483 (2009).
34. T. Weber, J. Herbig, M. Mark, H.-C. Nägerl, R. Grimm, *Phys. Rev. Lett.* **91**, 123201 (2003).
35. Supported by NSF and the Office of Naval Research, through the Multidisciplinary University Research Initiative program, and under Army Research Office grant no. W911NF-07-1-0493 with funds from the Defense Advanced Research Projects Agency Optical Lattice Emulator program. G.-B.J and Y.-R.L acknowledge additional support from the Samsung Foundation. We thank E. Demler, W. Hofstetter, A. Paramekanti, L. J. LeBlanc, and G. J. Conduit for useful discussions; T. Wang for experimental assistance; and A. Keshet for development of the computer control system.

Supporting Online Material

www.sciencemag.org/cgi/content/full/325/5947/1521/DC1
Materials and Methods
SOM Text
Fig. S1
References

1 June 2009; accepted 21 July 2009
10.1126/science.1177112

Bibliography

1. Lunney, D., Pearson, J.M. & Thibault, C. Recent trends in the determination of nuclear masses. *Rev. Mod. Phys.* **75**, 1021 (2003).
2. Varshni, Y.P. Comparative Study of Potential Energy Functions for Diatomic Molecules. *Rev. Mod. Phys.* **29**, 664 (1957).
3. Fellows, C.E. The NaLi 1 1Σ+(X) electronic ground-state dissociation limit. *J. Chem. Phys.* **94**, 5855 (1991).
4. Stan, C.A., Zwierlein, M.W., Schunck, C.H., Raupach, S.M.F. & Ketterle, W. Observation of Feshbach Resonances between Two Different Atomic Species. *Phys. Rev. Lett.* **93**, 143001 (2004).
5. Gacesa, M., Pellegrini, P. & Côté, R. Feshbach resonances in ultracold^{6,7}Li+^{23}Na atomic mixtures. *Phys. Rev. A* **78**, 010701 (2008).
6. Essen, L. & Parry, J.V.L. An Atomic Standard of Frequency and Time Interval: A Cæsium Resonator. *Nature* **176**, 280-282 (1955).
7. Mohr, P.J., Taylor, B.N. & Newell, D.B. CODATA recommended values of the fundamental physical constants: 2006. *Rev. Mod. Phys.* **80**, 633-730 (2008).
8. Anderson, M.H., Ensher, J.R., Matthews, M.R., Wieman, C.E. & Cornell, E.A. Observation of Bose-Einstein Condensation in a Dilute Atomic Vapor. *Science* **269**, 198 -201 (1995).
9. Davis, K.B. et al. Bose-Einstein Condensation in a Gas of Sodium Atoms. *Phys. Rev. Lett.* **75**, 3969 (1995).
10. Chin, J.K. et al. Evidence for superfluidity of ultracold fermions in an optical lattice. *Nature* **443**, 961-964 (2006).
11. Jo, G.-B. et al. Itinerant Ferromagnetism in a Fermi Gas of Ultracold Atoms. *Science* **325**, 1521 -1524 (2009).
12. Schunck, C.H., Shin, Y., Schirotzek, A., Zwierlein, M.W. & Ketterle, W. Pairing Without Superfluidity: The Ground State of an Imbalanced Fermi Mixture. *Science* **316**, 867 -870 (2007).
13. Zwierlein, M. et al. Observation of Bose-Einstein Condensation of Molecules. *Phys. Rev. Lett.* **91**, (2003).
14. Zwierlein, M.W., Abo-Shaeer, J.R., Schirotzek, A., Schunck, C.H. & Ketterle, W. Vortices and superfluidity in a strongly interacting Fermi gas. *Nature* **435**, 1047-1051 (2005).
15. Regal, C.A., Greiner, M., Giorgini, S., Holland, M. & Jin, D.S. Momentum Distribution of a Fermi Gas of Atoms in the BCS-BEC Crossover. *Phys. Rev. Lett.* **95**, 250404 (2005).
16. Greiner, M., Regal, C.A. & Jin, D.S. Probing the Excitation Spectrum of a Fermi Gas in the BCS-BEC Crossover Regime. *Phys. Rev. Lett.* **94**, 070403 (2005).
17. Chin, C. et al. Observation of Feshbach-Like Resonances in Collisions between Ultracold Molecules. *Phys. Rev. Lett.* **94**, 123201 (2005).

18. Cubizolles, J., Bourdel, T., Kokkelmans, S.J.J.M.F., Shlyapnikov, G.V. & Salomon, C. Production of Long-Lived Ultracold Li_{2} Molecules from a Fermi Gas. *Phys. Rev. Lett.* **91**, 240401 (2003).
19. Deiglmayr, J. et al. Formation of Ultracold Polar Molecules in the Rovibrational Ground State. *Phys. Rev. Lett.* **101**, (2008).
20. Deuretzbacher, F. et al. Heteronuclear molecules in an optical lattice: Theory and experiment. *Phys. Rev. A* 77, (2008).
21. Gaebler, J.P., Stewart, J.T., Bohn, J.L. & Jin, D.S. p-Wave Feshbach Molecules. *Phys. Rev. Lett.* **98**, 200403 (2007).
22. Herbig, J. et al. Preparation of a Pure Molecular Quantum Gas. *Science* **301**, 1510 -1513 (2003).
23. Hodby, E. et al. Production Efficiency of Ultracold Feshbach Molecules in Bosonic and Fermionic Systems. *Phys. Rev. Lett.* **94**, (2005).
24. Julienne, P.S., Tiesinga, E. & Köhler, T. Making cold molecules by time-dependent Feshbach resonances. *Journal of Modern Optics* **51**, 1787-1806 (2004).
25. Mukaiyama, T., Abo-Shaeer, J.R., Xu, K., Chin, J.K. & Ketterle, W. Dissociation and Decay of Ultracold Sodium Molecules. *Phys. Rev. Lett.* **92**, 180402 (2004).
26. Ospelkaus, C. et al. Ultracold Heteronuclear Molecules in a 3D Optical Lattice. *Phys. Rev. Lett.* **97**, 120402 (2006).
27. Strecker, K.E., Partridge, G.B. & Hulet, R.G. Conversion of an Atomic Fermi Gas to a Long-Lived Molecular Bose Gas. *Phys. Rev. Lett.* **91**, 080406 (2003).
28. Thompson, S.T., Hodby, E. & Wieman, C.E. Ultracold Molecule Production via a Resonant Oscillating Magnetic Field. *Phys. Rev. Lett.* **95**, 190404 (2005).
29. Xu, K. et al. Formation of Quantum-Degenerate Sodium Molecules. *Phys. Rev. Lett.* **91**, 210402 (2003).
30. Zirbel, J. et al. Heteronuclear molecules in an optical dipole trap. *Phys. Rev. A* **78**, (2008).
31. Chin, C., Grimm, R., Julienne, P. & Tiesinga, E. Feshbach resonances in ultracold gases. *Rev. Mod. Phys.* **82**, 1225 (2010).
32. Köhler, T., Góral, K. & Julienne, P. Production of cold molecules via magnetically tunable Feshbach resonances. *Rev. Mod. Phys.* **78**, 1311-1361 (2006).
33. Danzl, J.G. et al. Quantum Gas of Deeply Bound Ground State Molecules. *Science* **321**, 1062 -1066 (2008).
34. Spiegelhalder, F.M. et al. All-optical production of a degenerate mixture of ^{6}Li and ^{40}K and creation of heteronuclear molecules. *Phys. Rev. A* **81**, (2010).
35. Ni, K.-K. et al. A High Phase-Space-Density Gas of Polar Molecules. *Science* **322**, 231-235 (2008).
36. DeMille, D., Cahn, S.B., Murphree, D., Rahmlow, D.A. & Kozlov, M.G. Using Molecules to Measure Nuclear Spin-Dependent Parity Violation. *Phys. Rev. Lett.* **100**, 023003 (2008).
37. Hudson, E.R., Gilfoy, N.B., Kotochigova, S., Sage, J.M. & DeMille, D. Inelastic Collisions of Ultracold Heteronuclear Molecules in an Optical Trap. *Phys. Rev. Lett.* **100**, 203201 (2008).
38. Kerman, A.J., Sage, J.M., Sainis, S., Bergeman, T. & DeMille, D. Production of Ultracold, Polar RbCs^{*} Molecules via Photoassociation. *Phys. Rev. Lett.* **92**,

033004 (2004).
39. Shuman, E.S., Barry, J.F. & DeMille, D. Laser cooling of a diatomic molecule. *Nature* **467**, 820-823 (2010).
40. van der Stam, K.M.R., van Ooijen, E.D., Meppelink, R., Vogels, J.M. & van der Straten, P. Large atom number Bose-Einstein condensate of sodium. *Rev. Sci. Instrum.* **78**, 013102 (2007).
41. Hadzibabic, Z. et al. Fiftyfold Improvement in the Number of Quantum Degenerate Fermionic Atoms. *Phys. Rev. Lett.* **91**, 160401 (2003).
42. Leanhardt, A.E. et al. Cooling Bose-Einstein Condensates Below 500 Picokelvin. *Science* **301**, 1513 -1515 (2003).
43. Ni, K.-K. et al. Dipolar collisions of polar molecules in the quantum regime. *Nature* **464**, 1324-1328 (2010).
44. Quéméner, G. & Bohn, J.L. Electric field suppression of ultracold confined chemical reactions. *Phys. Rev. A* **81**, 060701 (2010).
45. Idziaszek, Z., Quéméner, G., Bohn, J.L. & Julienne, P.S. Simple quantum model of ultracold polar molecule collisions. *Phys. Rev. A* **82**, 020703 (2010).
46. DeMille, D. et al. Investigation of PbO as a system for measuring the electric dipole moment of the electron. *Phys. Rev. A* **61**, 052507 (2000).
47. DeMille, D. Quantum Computation with Trapped Polar Molecules. *Phys. Rev. Lett.* **88**, 067901 (2002).
48. Yelin, S.F., Kirby, K. & Côté, R. Schemes for robust quantum computation with polar molecules. *Phys. Rev. A* **74**, 050301 (2006).
49. Kuznetsova, E., Gacesa, M., Yelin, S.F. & Côté, R. Phase gate and readout with an atom-molecule hybrid platform. *Phys. Rev. A* **81**, 030301 (2010).
50. Dalton, J. *A new system of chemical philosophy*. (London: 1808).at <http://www.archive.org/details/newsystemofchemi01daltuoft>
51. Perrin, M.J. Brownian movement and molecular reality. *Ann. Chim. Phys.* **18**, 5 (1909).
52. Dunham, J.L. The Wentzel-Brillouin-Kramers Method of Solving the Wave Equation. *Phys. Rev.* **41**, 713 (1932).
53. Dunham, J.L. The Energy Levels of a Rotating Vibrator. *Phys. Rev.* **41**, 721 (1932).
54. Franck, J. & Dymond, E.G. Elementary processes of photochemical reactions. *Trans. Faraday Soc.* **21**, 536 (1926).
55. Coolidge, A.S., James, H.M. & Vernon, E.L. On the Determination of Molecular Potential Curves from Spectroscopic Data. *Phys. Rev.* **54**, 726 (1938).
56. Hulburt, H.M. & Hirschfelder, J.O. Potential Energy Functions for Diatomic Molecules. *J. Chem. Phys.* **9**, 61 (1941).
57. Herzberg, G. *Molecular Spectra and Molecular Structure*. (Van Nostrand: Princeton, N.J., 1945).
58. Lefebvre-Brion, H. & Field,, R.W. *The spectra and dynamics of diatomic molecules*. (Elsevier Academic Press,: Amsterdam ;;Boston :, 2004).
59. Mabrouk, N. & Berriche, H. Theoretical study of the NaLi molecule: potential energy curves, spectroscopic constants, dipole moments and radiative lifetimes. *J. Phys. B: At. Mol. Opt. Phys.* **41**, 155101 (2008).
60. Fontana, P.R. Theory of Long-Range Interatomic Forces. I. Dispersion Energies

between Unexcited Atoms. *Phys. Rev.* **123**, 1865 (1961).
61. Pritchard, D.E., Carter, G.M., Chu, F.Y. & Kleppner, D. Alkali-Alkali Differential Spin-Exchange Scattering. I. *Phys. Rev. A* **2**, 1922 (1970).
62. Pritchard, D.E. & Chu, F.Y. Alkali-Alkali Differential Spin-Exchange Scattering. II. *Phys. Rev. A* **2**, 1932 (1970).
63. Pichler, G., Milosevic, S., Viza, D. & Beuc, R. Diffuse bands in the visible absorption spectra of dense alkali vapours. *J. Phys. B: At. Mol. Phys.* **16**, 4619-4631 (1983).
64. Jones, R.B., Schloss, J.H. & Eden, J.G. Excitation spectra for the photoassociation of Kr–F and Xe–I collision pairs in the ultraviolet (208–258 nm). *J. Chem. Phys.* **98**, 4317 (1993).
65. Jones, K., Tiesinga, E., Lett, P. & Julienne, P. Ultracold photoassociation spectroscopy: Long-range molecules and atomic scattering. *Rev. Mod. Phys.* **78**, 483-535 (2006).
66. Schloss, J.H., Jones, R.B. & Eden, J.G. Photoassociation of Kr–F collision pairs in the ultraviolet. *J. Chem. Phys.* **99**, 6483 (1993).
67. Ospelkaus, S. et al. Efficient state transfer in an ultracold dense gas of heteronuclear molecules. *Nat Phys* **4**, 622-626 (2008).
68. Danzl, J.G. et al. Precision molecular spectroscopy for ground state transfer of molecular quantum gases. *Faraday Discuss.* **142**, 283 (2009).
69. Ashkin, A. Acceleration and Trapping of Particles by Radiation Pressure. *Phys. Rev. Lett.* **24**, 156 (1970).
70. Chu, S., Hollberg, L., Bjorkholm, J.E., Cable, A. & Ashkin, A. Three-dimensional viscous confinement and cooling of atoms by resonance radiation pressure. *Phys. Rev. Lett.* **55**, 48 (1985).
71. Raab, E.L., Prentiss, M., Cable, A., Chu, S. & Pritchard, D.E. Trapping of Neutral Sodium Atoms with Radiation Pressure. *Phys. Rev. Lett.* **59**, 2631 (1987).
72. Bloch, I. Ultracold quantum gases in optical lattices. *Nat Phys* **1**, 23-30 (2005).
73. DeMarco, B. & Jin, D.S. Onset of Fermi Degeneracy in a Trapped Atomic Gas. *Science* **285**, 1703 -1706 (1999).
74. Pethick, C. *Bose-Einstein condensation dilute gas.* (Cambridge U.P: N.Y., 2002).
75. Metcalf, H. *Laser cooling and trapping*. (Springer: New York, 1999).
76. Ketterle, W. & Zwierlein, M.W. Making, probing and understanding ultracold Fermi gases, Proceedings of the International School of physics "Enrico Fermi."(2008).
77. Ketterle, W., Durfee, D.S. & Stamper-Kurn, D.M. Making, probing and understanding Bose-Einstein condensates, Proceedings of the International School of Physics "Ernico Fermi."(1999).
78. Leggett, A.J. Bose-Einstein condensation in the alkali gases: Some fundamental concepts. *Rev. Mod. Phys.* **73**, 307 (2001).
79. Dalfovo, F., Giorgini, S., Pitaevskii, L.P. & Stringari, S. Theory of Bose-Einstein condensation in trapped gases. *Rev. Mod. Phys.* **71**, 463 (1999).
80. Doret, S.C., Connolly, C.B., Ketterle, W. & Doyle, J.M. Buffer-Gas Cooled Bose-Einstein Condensate. *Phys. Rev. Lett.* **103**, 103005 (2009).
81. Narevicius, E. et al. An atomic coilgun: using pulsed magnetic fields to slow a supersonic beam. *New J. Phys.* **9**, 358-358 (2007).

82. Gilijamse, J.J., Hoekstra, S., Vanhaecke, N., Meerakker, S.Y.T. van de & Meijer, G. Loading Stark-decelerated molecules into electrostatic quadrupole traps. *The European Physical Journal D* **57**, 9 (2010).
83. Meerakker, S.Y.T. van de, Labazan, I., Hoekstra, S., Küpper, J. & Meijer, G. Production and deceleration of a pulsed beam of metastable NH radicals. *J. Phys. B: At. Mol. Opt. Phys.* **39**, S1077-S1084 (2006).
84. Emsley, J. *The Elements, Oxford chemistry Guides*. (Oxford Univ. Press, New York, NY: 1995).
85. Eisberg, R. & Resnick, R. *Quantum Physics of Atoms, Molecules, Solids, Nuclei, and Particles*. (Wiley: 1985).
86. Poteau, R. & Spiegelmann, F. Calculation of the Electronic Spectrum of Li2 Using Effective Core Pseudopotentials and l -Dependent Core Polarization Potentials. *Journal of Molecular Spectroscopy* **171**, 299-308 (1995).
87. Cohen-Tannoudji, C., Diu, B. & Laloe, F. *Quantum Mechanics*. (Wiley-Interscience: 2006).
88. Gottfried, K. & Yan, T.-M. *Quantum Mechanics: Fundamentals*. (Springer: 2004).
89. Hartree, D.R. *The calculation of Atomic Structures*. (Wiley & Sons: New York, 1957).
90. Morse, P.M. Diatomic Molecules According to the Wave Mechanics. II. Vibrational Levels. *Phys. Rev.* **34**, 57 (1929).
91. Morse, P.M. & Stueckelberg, E.C.G. Diatomic Molecules According to the Wave Mechanics I: Electronic Levels of the Hydrogen Molecular Ion. *Phys. Rev.* **33**, 932 (1929).
92. Cohen-Tannoudji, C. *Atom photon interactions : basic processes and applications*. (Wiley: New York [u.a.], 1992).
93. Bang, N.H., Jastrzebski, W. & Kowalczyk, P. New observation and analysis of the E(4)1Σ+ state in NaLi. *Journal of Molecular Spectroscopy* **233**, 290-292 (2005).
94. Engelke, F., Ennen, G. & Meiwes, K.H. Laser induced fluorescence spectroscopy of NaLi in beam and bulk. *Chemical Physics* **66**, 391-402 (1982).
95. Jastrzebski, W., Kowalczyk, P., Nadyak, R. & Pashov, A. Spectroscopic study of the E(4)1[Sigma]+ state in NaLi. *Spectrochimica Acta Part A: Molecular and Biomolecular Spectroscopy* **58**, 2193-2197 (2002).
96. Kappes, M.M., Marti, K.O., Radi, P., Schär, M. & Schumacher, E. Resonant two-photon ionization of LiNa. Observation and preliminary characterization of five new singlet states. *Chemical Physics Letters* **107**, 6-12 (1984).
97. Petsalakis, I.D., Tzeli, D. & Theodorakopoulos, G. Theoretical study on the electronic states of NaLi. *J. Chem. Phys.* **129**, 054306 (2008).
98. Krems, R. *Cold molecules : theory, experiment, applications*. (CRC Press: Boca Raton, 2009).
99. Barrow, G.M. *Physical Chemistry*. (Mcgraw-Hill College: 1996).
100. Zwierlein, M.W. High Temperature Superfluidity in an Ultracold Fermi Gas. Ph.D Thesis, Massachusetts Institute of Technology, Cambridge, MA (2006).
101. Sage, J.M., Sainis, S., Bergeman, T. & DeMille, D. Optical Production of Ultracold Polar Molecules. *Phys. Rev. Lett.* **94**, 203001 (2005).
102. Kuznetsova, E., Gacesa, M., Pellegrini, P., Yelin, S.F. & Côté, R. Efficient formation

of ground-state ultracold molecules via STIRAP from the continuum at a Feshbach resonance. *New J. Phys.* **11**, 055028 (2009).
103. Zirbel, J.J. et al. Collisional Stability of Fermionic Feshbach Molecules. *Phys. Rev. Lett.* **100**, (2008).
104. D'Incao, J.P. & Esry, B.D. Mass dependence of ultracold three-body collision rates. *Phys. Rev. A* **73**, 030702 (2006).
105. D'Incao, J.P. & Esry, B.D. Scattering Length Scaling Laws for Ultracold Three-Body Collisions. *Phys. Rev. Lett.* **94**, 213201 (2005).
106. Granade, S.R., Gehm, M.E., O'Hara, K.M. & Thomas, J.E. All-Optical Production of a Degenerate Fermi Gas. *Phys. Rev. Lett.* **88**, 120405 (2002).
107. Trenkwalder, A. et al. Hydrodynamic Expansion of a Strongly Interacting Fermi-Fermi Mixture. *Phys. Rev. Lett.* **106**, 115304 (2011).
108. Campbell, G.K. et al. Imaging the Mott Insulator Shells by Using Atomic Clock Shifts. *Science* **313**, 649 -652 (2006).
109. Jochim, S. et al. Pure Gas of Optically Trapped Molecules Created from Fermionic Atoms. *Phys. Rev. Lett.* **91**, 240402 (2003).
110. Petrov, D.S., Salomon, C. & Shlyapnikov, G.V. Weakly Bound Dimers of Fermionic Atoms. *Phys. Rev. Lett.* **93**, 090404 (2004).
111. D'Incao, J. & Esry, B. Scattering Length Scaling Laws for Ultracold Three-Body Collisions. *Phys. Rev. Lett.* **94**, (2005).
112. D'Incao, J.P. & Esry, B.D. Suppression of Molecular Decay in Ultracold Gases without Fermi Statistics. *Phys. Rev. Lett.* **100**, (2008).
113. Moerdijk, A.J. & Verhaar, B.J. Collisional two- and three-body decay rates of dilute quantum gases at ultralow temperatures. *Phys. Rev. A* **53**, R19 (1996).
114. Craik, A.D.D. THE ORIGINS OF WATER WAVE THEORY. *Annual Review of Fluid Mechanics* **36**, 1-28 (2004).
115. Arndt, M., Ben Dahan, M., Guéry-Odelin, D., Reynolds, M. & Dalibard, J. Observation of a Zero-Energy Resonance in Cs-Cs Collisions. *Phys. Rev. Lett.* **79**, 625-628 (1997).
116. Góral, K., Gajda, M. & Rza-cedillazdotewski, K. Multimode Dynamics of a Coupled Ultracold Atomic-Molecular System. *Phys. Rev. Lett.* **86**, 1397 (2001).
117. Góral, K., Köhler, T. & Burnett, K. Ramsey interferometry with atoms and molecules: Two-body versus many-body phenomena. *Phys. Rev. A* **71**, 023603 (2005).
118. Góral, K., Köhler, T., Gardiner, S.A., Tiesinga, E. & Julienne, P.S. Adiabatic association of ultracold molecules via magnetic-field tunable interactions. *J. Phys. B: At. Mol. Opt. Phys.* **37**, 3457-3500 (2004).
119. Schunck, C.H. et al. Feshbach resonances in fermionic^{6}Li. *Phys. Rev. A* **71**, 045601 (2005).
120. Chin, Vuletic, Kerman & Chu High resolution feshbach spectroscopy of cesium. *Phys. Rev. Lett* **85**, 2717-2720 (2000).
121. Mewes, M.-O. et al. Bose-Einstein Condensation in a Tightly Confining dc Magnetic Trap. *Phys. Rev. Lett.* 77, 416-419 (1996).
122. Watabe, S. & Nikuni, T. Conversion efficiencies of heteronuclear Feshbach molecules. *Phys. Rev. A* 77, 013616 (2008).

123. Papp, S. & Wieman, C. Observation of Heteronuclear Feshbach Molecules from a Rb85–Rb87 Gas. *Phys. Rev. Lett.* **97**, (2006).
124. Mies, F.H., Tiesinga, E. & Julienne, P.S. Manipulation of Feshbach resonances in ultracold atomic collisions using time-dependent magnetic fields. *Phys. Rev. A* **61**, 022721 (2000).
125. Zirbel, J.J. Ultracold Fermionic Feshbach Molecules. Ph.D Thesis, University of Colorado, Boulder, CO(2008).
126. Stamper-Kurn, D.M. Peeking and poking at a new quantum fluid: Studies of gaseous Bose-Einstein condensates in magnetic and optical traps. Ph.D Thesis, Massachusetts Institute of Technology, Cambridge, MA (2000)
127. Chikkatur, A. Colliding and Moving Bose-Einstein Condensates: Studies of superfluidity and optical tweezers for condensate transport. Ph.D Thesis, Massachusetts Institute of Technology, Cambridge, MA (2002).
128. Leanhardt, A.E. Microtraps and Waveguides for Bose-Einstein Condensates. Ph.D Thesis, Massachusetts Institute of Technology, Cambridge, MA (2003).
129. Shin, Y.-I. Experiments with Bose-Einstein Condensates in a Double-Well Potential. Ph.D Thesis, Massachusetts Institute of Technology, Cambridge, MA (2006)
130. Pasquini, T.A. Quantum Reflection of Bose-Einstein Condensates. Ph.D Thesis, Massachusetts Institute of Technology, Cambridge, MA (2007).
131. Jo, G.-B. Quantum coherence and Magnetism in Bosonic and Fermionic Gases of Ultracold Atoms. Ph.D Thesis, Massachusetts Institute of Technology, Cambridge, MA (2010).
132. Gustavson, T.L. et al. Transport of Bose-Einstein Condensates with Optical Tweezers. *Phys. Rev. Lett.* **88**, 020401 (2001).
133. Pasquini, T. et al. Quantum Reflection from a Solid Surface at Normal Incidence. *Phys. Rev. Lett.* **93**, (2004).
134. Christensen, C. et al. Trapping of ultracold atoms in a hollow-core photonic crystal fiber. *Phys. Rev. A* **78**, (2008).
135. Jo, G.-B. et al. Matter-Wave Interferometry with Phase Fluctuating Bose-Einstein Condensates. *Phys. Rev. Lett.* **99**, 240406 (2007).
136. Jo, G.-B. et al. Phase-Sensitive Recombination of Two Bose-Einstein Condensates on an Atom Chip. *Phys. Rev. Lett.* **98**, (2007).
137. Hadzibabic, Z. Studies of a Quantum Degenerate Fermionic Lithium Gas. Ph.D Thesis, Massachusetts Institute of Technology, Cambridge, MA (2003).
138. Stan, C.A. Experiments with Interacting Bose and Fermi Gases. Ph.D Thesis, Massachusetts Institute of Technology, Cambridge, MA (2005).
139. Stan, C.A. & Ketterle, W. Multiple species atom source for laser-cooling experiments. *Rev. Sci. Instrum.* **76**, 063113 (2005).
140. Bowles, K.J. & Rosenblum, L. Vapor Pressure of Sodium from 0.5 to 120 Atmospheres. *Journal of Chemical & Engineering Data* **10**, 321-322 (1965).
141. Auböck, G. et al. Trap loss collisions of Li6 and Li7 with Na23 in a combined magneto-optical trap. *J. Phys. B: At. Mol. Opt. Phys.* **39**, S871-S879 (2006).
142. Ketterle, W., Davis, K.B., Joffe, M.A., Martin, A. & Pritchard, D.E. High densities of cold atoms in a dark spontaneous-force optical trap. *Phys. Rev. Lett.* **70**, 2253

(1993).
143. Bechhoefer, J. Feedback for physicists: A tutorial essay on control. *Rev. Mod. Phys.* **77**, 783 (2005).
144. DeMarco, B. Quantum Behavior of an Atomic Fermi Gas. Ph.D thesis, University of Colorado, Boulder, CO (2001).
145. Zwierlein, M.W. et al. Observation of Bose-Einstein Condensation of Molecules. *Phys. Rev. Lett.* **91**, 250401 (2003).
146. Tiecke, T.G., Goosen, M.R., Walraven, J.T.M. & Kokkelmans, S.J.J.M.F. Asymptotic-bound-state model for Feshbach resonances. *Phys. Rev. A* **82**, 042712 (2010).
147. Wille, E. et al. Exploring an Ultracold Fermi-Fermi Mixture: Interspecies Feshbach Resonances and Scattering Properties of^{6}Li and^{40}K. *Phys. Rev. Lett.* **100**, 053201 (2008).
148. Tiecke, T.G. Feshbach resonances in ultracold mixtures of the fermionic quantum gases 6Li and 40K. Ph.D thesis, University of Amsterdam, Amsterdam, Netherlands (2009).
149. Arimondo, E., Inguscio, M. & Violino, P. Experimental determinations of the hyperfine structure in the alkali atoms. *Rev. Mod. Phys.* **49**, 31 (1977).
150. Inouye, S. et al. Observation of Feshbach resonances in a Bose-Einstein condensate. *Nature* **392**, 151-154 (1998).
151. Ospelkaus, S. et al. Quantum-State Controlled Chemical Reactions of Ultracold Potassium-Rubidium Molecules. *Science* **327**, 853-857 (2010).
152. Cheng, C.-H. & Yip, S.-K. Anisotropic Fermi Superfluid via p-Wave Feshbach Resonance. *Phys. Rev. Lett.* **95**, 070404 (2005).
153. Gurarie, V., Radzihovsky, L. & Andreev, A.V. Quantum Phase Transitions across a p-Wave Feshbach Resonance. *Phys. Rev. Lett.* **94**, 230403 (2005).
154. Ohashi, Y. BCS-BEC Crossover in a Gas of Fermi Atoms with a p-Wave Feshbach Resonance. *Phys. Rev. Lett.* **94**, 050403 (2005).
155. Stoner, E.C. Collective Electron Ferromagnetism. *Proceedings of the Royal Society of London. Series A. Mathematical and Physical Sciences* **165**, 372 -414 (1938).
156. Duine, R. & MacDonald, A. Itinerant Ferromagnetism in an Ultracold Atom Fermi Gas. *Phys. Rev. Lett.* **95**, (2005).
157. Gutzwiller, M.C. Effect of Correlation on the Ferromagnetism of Transition Metals. *Phys. Rev. Lett.* **10**, 159 (1963).
158. Pekker, D. et al. Competition between Pairing and Ferromagnetic Instabilities in Ultracold Fermi Gases near Feshbach Resonances. *Phys. Rev. Lett.* **106**, 050402 (2011).
159. Cui, X. & Zhai, H. Stability of a fully magnetized ferromagnetic state in repulsively interacting ultracold Fermi gases. *Phys. Rev. A* **81**, 041602 (2010).
160. Zhai, H. Correlated versus ferromagnetic state in repulsively interacting two-component Fermi gases. *Phys. Rev. A* **80**, 051605 (2009).
161. Chang, C.-C., Zhang, S. & Ceperley, D.M. Itinerant ferromagnetism in a Fermi gas with contact interaction: Magnetic properties in a dilute Hubbard model. *Phys. Rev. A* **82**, 061603 (2010).
162. Berdnikov, I., Coleman, P. & Simon, S.H. Itinerant ferromagnetism in an atom

trap. *Phys. Rev. B* **79**, 224403 (2009).
163. LeBlanc, L.J., Thywissen, J.H., Burkov, A.A. & Paramekanti, A. Repulsive Fermi gas in a harmonic trap: Ferromagnetism and spin textures. *Phys. Rev. A* **80**, 013607 (2009).
164. Navon, N., Nascimbene, S., Chevy, F. & Salomon, C. The Equation of State of a Low-Temperature Fermi Gas with Tunable Interactions. *Science* **328**, 729-732 (2010).
165. Cooper, L.N. Bound Electron Pairs in a Degenerate Fermi Gas. *Phys. Rev.* **104**, 1189 (1956).
166. Efremov, D.V. & Viverit, L. p-wave Cooper pairing of fermions in mixtures of dilute Fermi and Bose gases. *Phys. Rev. B* **65**, 134519 (2002).
167. Weld, D.M. et al. Spin Gradient Thermometry for Ultracold Atoms in Optical Lattices. *Phys. Rev. Lett.* **103**, 245301 (2009).
168. Marchetti, F., Mathy, C., Huse, D. & Parish, M. Phase separation and collapse in Bose-Fermi mixtures with a Feshbach resonance. *Phys. Rev. B* **78**, (2008).
169. Adhikari, S.K. Mean-field description of collapsing and exploding Bose-Einstein condensates. *Phys. Rev. A* **66**, 013611 (2002).
170. Marchetti, F.M., Jolicoeur, T. & Parish, M.M. Stability and Pairing in Quasi-One-Dimensional Bose-Fermi Mixtures. *Phys. Rev. Lett.* **103**, 105304 (2009).
171. Van Schaeybroeck, B. & Lazarides, A. Trapped phase-segregated Bose-Fermi mixtures and their collective excitations. *Phys. Rev. A* **79**, 033618 (2009).
172. Edwards, D.O. & Daunt, J.G. Phase Separation in He^{3}-He^{4} Mixtures near Absolute Zero. *Phys. Rev.* **124**, 640 (1961).
173. Ospelkaus, S. et al. Degenerate K-Rb Fermi-Bose gas mixtures with large particle numbers. *J. of Modern Optics* **54**, 661-673 (2007).
174. Ospelkaus, S. et al. Localization of Bosonic Atoms by Fermionic Impurities in a Three-Dimensional Optical Lattice. *Phys. Rev. Lett.* **96**, 180403 (2006).